# 論文 / 著書情報
# Article / Book Information

| | |
|---|---|
| 題目(和文) | |
| Title(English) | High-resolution positivity-preserving schemes for complex compressible flows |
| 著者(和文) | TannSiengdy |
| Author(English) | Siengdy Tann |
| 出典(和文) | 学位:博士(工学),<br>学位授与機関:東京工業大学,<br>報告番号:甲第11593号,<br>授与年月日:2020年9月25日,<br>学位の種別:課程博士,<br>審査員:肖 鋒,奥野 喜裕,青木 尊之,末包 哲也,長﨑 孝夫 |
| Citation(English) | Degree:Doctor (Engineering),<br>Conferring organization: Tokyo Institute of Technology,<br>Report number:甲第11593号,<br>Conferred date:2020/9/25,<br>Degree Type:Course doctor,<br>Examiner:,,,, |
| 学位種別(和文) | 博士論文 |
| Type(English) | Doctoral Thesis |

TOKYO INSTITUTE OF TECHNOLOGY

DOCTORAL THESIS

---

# High-resolution positivity-preserving schemes for complex compressible flows

---


*Author:*

TANN Siengdy

*Supervisor:*

Professor Feng XIAO


*A thesis submitted in partial fulfillment of the requirements*

*for the degree of Doctor of Engineering*


Department of Mechanical Engineering


August 2020

# *Abstract*

Computational fluid dynamics (CFD) has been widely used in many engineering and scientific research fields for decades. For instance, the conservative finite volume (FV) framework, one of the classical computational fluid dynamics methods is often employed to solve the compressible flow problems. Most of the classical finite volume schemes are based on polynomial reconstructions, which is further supplemented with a nonlinear limiting projection, such as the TVD (Total Variation Diminishing) limiter, WENO (Weighed Essentially Non-Oscillatory) limiter, hierarchical moment limiter, artificial viscosity, etc.

In spite of tremendous in many applications, the existing FV schemes still have some unresolved problems. For example, the excessive numerical dissipation and numerical oscillation still remain and are problematic for some applications. Furthermore, original high order schemes may generate non-physical negative density or pressure (positivity failure) because of interpolation errors in the vicinity of strong discontinuities or near-vacuum states. These problems become even more serious and challenges when simulating the compressible Euler equations with source terms (e.g., gravity, chemical reaction), or multiphase compressible flows involving moving interfaces. These non-physical fluid properties might lead to blow-up of the computation and subsequent code crash.

This thesis for doctoral degree reports my efforts and achievements made in the past years to resolve the aforementioned problems of existing finite volume method. Systematic works have carried out to develop novel numerical methods of high-order accuracy, less dissipation and preserved positivity. The major contents of this thesis are summarized as follows.

**Chapter 1: Introduction**

In Chapter 1, we describe about the general background of CFD, compressible flow, as well as the finite volume methods. The governing equations for compressible flows such

as Euler equations and extended Euler equations (source terms and multi-phase flows), are presented in this section. We introduce the conventional finite volume method for single-phase flows and finite volume wave propagation method for multi-phase flows. Furthermore, we present two popular numerical schemes under finite volume framework as MUSCL-type and WENO-type schemes, including the Riemann solvers that we implement in this work. We also present the issues of numerical methods for compressible flows and our research purposes in this chapter.

**Chapter 2: Reconstruction approach by using MOOD and THINC method**

Chapter 2 firstly introduces a novel finite volume scheme to solve hyperbolic conservation laws under the multi-dimensional optimal order detection (MOOD) framework. The concept of this method is to replace the first-order finite volume method by the tangent of hyperbola interface capturing (THINC) scheme to capture sharply the discontinuities. The MOOD algorithm consists of two criteria such as physical admissible detection (PAD) for positivity-preserving and numerical admissible detection (NAD) for suppress numerical oscillations as well as computing errors. The numerical tests show that the proposed scheme can achieve high order accuracy gained by polynomial based reconstruction in smooth regions and capture discontinuous solution without spurious oscillation and with less numerical dissipation.

**Chapter 3: Solution property preserving reconstruction: BVD+MOOD scheme**

In Chapter 3, we develop a general formulation of reconstruction in finite volume method by integrating the boundary variation diminishing (BVD) and multi-dimensional optimal order detection (MOOD) methodologies by blending of high-/low-order polynomials and hyperbolic tangent reconstructions. As a concrete example, we propose a high-resolution scheme under a three-stage cascade BVD algorithm and MOOD method to fulfill the essentially non-oscillation, shock capturing and positivity-preserving properties. This novel algorithm is a limiting-free solution property preserving scheme and it shows competitive performance compared to well-known high-order schemes. The new scheme is so-called multi-stage BVD-MOOD approach. For BVD reconstruction strategy, the linear fifth-order upwind or piecewise quartic method (PQM) on fourth-degree of polynomial (P4) is implemented as one of the candidate reconstruction functions to

capture smooth solutions. Other candidate reconstruction functions use tangent of hyperbola interface capturing (THINC) functions with different controlling the slope (jump thickness) to eliminate the numerical oscillation and to capture sharply all discontinuities. Furthermore, a MOOD algorithm performs and detects a candidate solution by PAD ensuring as such the positivity-preserving property. Verified through the numerical benchmark tests involving vacuum or near vacuum states, strong discontinuities and also smooth flows, the present scheme is effectively able to resolve both smooth and discontinuous solutions and preserve the positivity.

**Chapter 4: BVD+MOOD scheme for compressible Euler equations with source terms**

In Chapter 4, we extend our new approach (multi-stage BVD-MOOD) for the compressible Euler equations supplemented with source terms (e.g. gravity, chemical reaction). We briefly introduce the numerical methods to solve the Euler equations with source terms by operator splitting into convection operator and source term or reaction operator. One of the main challenges when simulating these models is the occurrence of negative density or pressure during the time evolution, which leads to a blow-up of computation. According to the numerical benchmark tests, the present scheme can preserve the physical properties of the numerical solution still enduring robustness and accuracy when and where appropriate. Moreover, it provides excellent solution quality competitive to other existing schemes for reactive compressible gas dynamics.

**Chapter 5: Implementation of BVD+MOOD scheme for compressible multi-phase flows**

The newly proposed scheme is applied to solve the five-equation model for interface two-phase flows in Chapter 5. This scheme is implemented in finite volume wave propagation method, which realizes the consistency among volume fraction and other physical variables. Due to the BVD principle that selects the appropriate reconstruction operator for the target cell, the dissipation error in numerical solution is effectively minimized. More importantly, this approach is able to resolve discontinuous solutions which are sharper than other existing schemes, even for a long-term computation. The numerical results demonstrate that the present scheme is able to capture sharply the material

interface without additional “anti-diffusion” or “artificial compression” treatment.

**Chapter 6: Conclusions and future work**

In Chapter 6, we make conclusions for this research work. The major contributions of the current study and discussion about the future work are highlighted. The presented novel numerical methods are able to obtain accurate solutions for both smooth and discontinuous flow structures with strong robustness for complex compressible flows, as well as interface two-phase flows. According to their algorithmic simplicity, proposed methods can be expected as very promising numerical tools for a wide range of engineering applications.

# *Acknowledgment*

This research project could not have been completed without the help, encourage, advisory and support. I would like to take this opportunity to express my immense gratitude to all those persons who have given their invaluable support and assistance.

First of all, I would like to express my deep and sincere gratitude to my supervisor, professor Feng XIAO for his guidance, instructions, help and support, so I can accomplish my thesis. His office's door is always opened. It is my great opportunity to be one of his students and under his supervision. During three years and a half, I truly enjoyed working in a good research environment that stimulates original thinking and initiative which he created. He always shares us with his research experience and knowledge during lab meeting as well as research seminar. I have gained a lot of experiences not only in academic research but also my future life in the society. Thank prof. XIAO again, and I greatly appreciate his commitment to advise me during three years and a half of my study at his laboratory. Especially, He always support and take good care of all his students during the hardest time of COVID-19 pandemic.

Secondly, I would like to offer my special thank to professor Raphaël LOUBÈRE in Université de Bordeaux for patient guidance, enthusiastic encouragement and all his efforts in research collaboration. He gave me great help, ideas and guidance during his visit in Tokyo. He also advised me to improve the quality of my research work as well as journal publications. I am so glad that I have good opportunity to get the instructions from prof. LOUBÈRE.

Then, I wish to acknowledge Dr. Jin Peng who is my senior and tutor during I am a research student for his guidance, teaching coding skills and helpful discussion on my research project. Beside of research work, he also helps me to access and guide me to some places in Tokyo to make me a comfortable daily life in Tokyo as an international student.

In addition, I must thank Dr. Deng Xi who is one of my senior for his help, guidance and support. It is impossible for me to finish the work during doctoral program without his help and guidance. He teaches me a lot about CFD. He always help me to solve many problems that I face in my research and he always give me solution when I have trouble with my coding program. Discussing with him and my advisor is also very enjoyable.

I thank all my and senior and fellow labmates in Xiao lab, Jin Jonghoon, Andrés, Saito, Hashiguchi, Shimizu, Miyakawa, Koseki, Cheng, Li, Wakimura and Hirakawa. During the finish of this thesis, they all provide me with kinds supports on both the research and daily life. We have a lot of memories in working together and have a lot of fun during these years.

I would like to thank Japanese International Cooperation Agent (JICA) for providing me the scholarship and financial support that made this research work possible. Also, I must thank to JICA's officers (Yokohama center and Tokyo center) for their support and help. They take good care of me during my study in Japan.

Last, but definitely not the least, I am greatly indebted to my family, specially to my beloved wife who always stands by me to encourage and support. It was my parents, parents-in-law and my lovely wife's unconditional love, care and tolerance which the hardship of doing research and writing thesis. Without their support and encourage, I do not think that I could overcome the difficulties and accomplish this work during these three years and a half.

# Contents

# List of Figures

# List of Tables

# Abbreviations

| | |
|---|---|
| **CFD** | **C**omputational **F**luid **D**ynamics |
| **FV** | **F**inite **V**olume |
| **EOS** | **E**quation **o**f **S**tate |
| **CFL** | **C**ourant-**F**riedrich-**L**ewy |
| **BVD** | **B**oundary **V**ariation **D**iminishing |
| **FCT** | **F**lux **C**orrected **T**ransport |
| **DG** | **D**iscontinuous **G**alerkin |
| **MUSCL** | **M**onotone **U**pstream-centered **S**cheme for **C**onservative **L**aws |
| **TVD** | **T**otal **V**ariation **D**iminishing |
| **TBV** | **T**otal **B**oundary **V**ariation |
| **PPM** | **P**iece-wise **P**arabolic **M**ethod |
| **PQM** | **P**iece-wise **Q**uartic **M**ethod |
| **PHO** | **P**olynomial-based **H**igh-**O**rder |
| **ODE** | **O**rdinary **D**ifferential **E**quation |
| **PDE** | **P**artial **D**ifferential **E**quation |
| **ENO** | **E**ssentially **N**on-**O**scillatory |
| **THINC** | **T**angent of **H**yperbola **IN**terface **C**apturing |
| **MOOD** | **M**ulti-dimensional **O**ptimal **O**rder **D**etection |
| **DMP** | **D**iscrete **M**aximum **P**rinciple |
| **RDMP** | **R**elaxation **D**iscrete **M**aximum **P**rinciple |
| **PAD** | **P**hysical **A**dmissible **D**etection |

| | |
|---|---|
| **NAD** | **N**umerical **A**dmissible **D**etection |
| **NaN** | **N**ot-**a**-**N**umber |
| **HLL** | **H**arten **L**ax van**L**eer |
| **HLLC** | **H**arten **L**ax van**L**eer **C**ontact |
| **RK3** | Third-order TVD **R**unge **K**utta |
| **SSPRK** | **S**trong **S**tability **P**reserving **R**unge-**K**utta |
| **WENO** | **W**eighted **E**ssentially **N**on-**O**scillatory |
| **CWENO** | **C**entral **W**eighted **E**ssentially **N**on-**O**scillatory |
| **VIA** | **V**olume-**I**ntegrated **A**verage |
| **VOF** | **V**olume **o**f **F**luid |

# Chapter 1

# Introduction

## 1.1 Background

When a fluid flows with a speed that Mach number is much greater than zero, it is called compressible flow which the density of fluid having significant change. The density changes the temperature, and then the temperature changes due to the kinetic energy, associated with the velocity changes, therefore it has influence the flow. Especially, the compressible flow is implemented in many fields such as modern high-speed aircraft, natural gas pipeline, gas turbine, stream turbine, rocket motors and combustion chamber for car engine. However, the knowledges of compressible fluid flows are required due to the significant effect of fluid compressibility. For example, in combustion engine, the compressible flows become more complex because they involve high compressibility, multi-components or chemical reaction. Since the complexity of the flow structures is governing by PDEs, the analytical approaches are not available and difficultly make experimental techniques in many cases. Development of numerical methods for complex compressible flows is an active and challenging research area.

Computational fluid dynamics (CFD) has been widely used in many engineering and scientific research fields for decades. CFD is the most powerful and reliable tool to solve fluid mechanics problems in scientific research and engineering applications which involve complex geometries and complex flow structures (shock waves and vortex flows), as well as compressible flows. For instance, the conservative finite volume (FV) method,

one of the classical computational fluid dynamics algorithms is often employed to solve the compressible flow problems because of its rigorous numerical conservation. According to this conservativeness, high-order accuracy both smooth and discontinuous solutions, computational efficiency, robustness and flexibility with geometries, FV methods are popularly employed in numerical solvers for real-case engineering applications. Therefore, the numerical methods have been consecutively developed over the past decades under finite volume framework including low and high order schemes. Most of the classical finite volume schemes are based on a (linear) polynomial reconstruction, which is further supplemented with a nonlinear limiter (slope limiter), (C)WENO blending, hierarchical moment limiter, artificial viscosity, etc.

The main core of CFD is to provide reliable and high efficient numerical algorithms. Thus, in CFD, the explorations of numerical methods with high-order accuracy, high efficiency and robustness are highly demanded. In the following sections, we introduce the current state of development of high-resolution numerical methods under finite volume framework, along with the issues of compressible flows that we are going to describe in this thesis.

## 1.2 Governing Equations

The fundamental equations for compressible flows are presented in this section such as Euler equations and extended Euler equations (source terms/detonations and multiphase flows).

### 1.2.1 Euler equations

The one dimensional Euler equations for compressible gas dynamics consists of conservation laws of mass, momentum and total energy as following

$$\frac{\partial U}{\partial t} + \frac{\partial F(U)}{\partial x} = 0, \quad t \geq 0, \quad x \in \mathbb{R} \tag{1.1}$$

where

$$\mathbf{U}(x,t) = \begin{pmatrix} \rho \\ \rho u \\ E \end{pmatrix}, \quad \mathbf{F}(\mathbf{U}) = \begin{pmatrix} \rho u \\ \rho u^2 + p \\ u(E+p) \end{pmatrix} \tag{1.2}$$

Here $\rho$, $u$, $p$ are the density, velocity, and pressure, respectively. $E$ is the total energy expressed as $E = e + \frac{1}{2}\rho u^2$ and $e$ is the specific internal energy. For ideal gas, the pressure can be computed by the equation of state (EOS) is defined as $p = (\gamma - 1)\rho e$ where $\gamma$ is the ratio of specific heats. The total enthalpy is computed by $H = (E+p)/\rho$.

### 1.2.2 Extended Euler equations with source terms

The general form of one dimensional Euler equations with source terms is defined as

$$\frac{\partial U}{\partial t} + \frac{\partial F(U)}{\partial x} = S(U); \quad t \geq 0, \quad x \in \mathbb{R} \tag{1.3}$$

where $U(x,t) = (\rho, \rho u, E)^T$, $F(U) = [\rho u, \rho u^2 + p, (E+p)u]^T$ and $\rho, u, p$ are the density, velocity and pressure, respectively. $E$ is the total energy expressed as $E = e + \frac{1}{2}\rho u^2$ and $e$ is the internal energy, they are linked to the pressure through an equation of state (EOS) $p \equiv p(\rho, e)$ from which we can define the sound speed $a > 0$. $S(U)$ is the source terms, i.e. gravity acceleration and detonation models of premixed reactive gases.

The time-dependent inviscid compressible flow with reaction between two chemical states in one-dimensional space is considered. The homogeneous Euler system (1.1) (i.e. with $S(U) = 0$) is supplemented with an equation on the mass fraction of the unburnt gas $\alpha$ as

$$\frac{\partial}{\partial t}(\rho\alpha) + \frac{\partial}{\partial x}((\rho\alpha)u) = K(T)\,(\rho\,\alpha), \tag{1.4}$$

where $K(T)$ is the chemical reaction rate. The pressure is obtained from an equation of state like

$$p = (\gamma - 1)\left(E - \frac{1}{2}\rho u^2 + \mathsf{R}\right), \tag{1.5}$$

where $\mathsf{R} = -q_0\,(\rho\alpha)$ models the heat released from the chemical reaction processes, and $q_0$ denotes the chemical heat release. The temperature is computed by $T = \frac{p}{\rho}$ and

we set the $\gamma$ to $1.4$, otherwise mentioned. The reaction rate $K(T)$ can be modeled with the so-called Arrhenius kinetics [109] as

$$K(T) = K_0 \exp\left(\frac{-T_{ign}}{T}\right), \tag{1.6}$$

where $K_0$ the pre-exponential coefficient and $T_{ign}$ the ignition (or activation) temperature are model parameters. When the source term becomes stiff, the reaction rate may be modeled by a Heaviside kinetics as

$$K(T) = \begin{cases} \frac{1}{\xi} & \text{if} \quad T \geq T_{ign}, \\ 0 & \text{if} \quad T < T_{ign}. \end{cases} \tag{1.7}$$

where $\xi$ represents the reaction time.

### 1.2.3 Five-equation model for compressible multi-phase flows

There are several numerical models have been proposed for simulating the compressible multi-phase flows such as four-equation model [1] and five-equation model [4], etc. The five-equation model is employed in this present work for simulating the inviscid compressible two-phase flows. In this five-equation model, the velocity and pressure of the mixture are assumed to be equilibrium for material interface. The five-equation model consists of two continuity equations for phasic mass, a momentum equation, an energy equation, and an advection equation of volume fraction as follows

$$\begin{aligned} &\frac{\partial}{\partial t}(\alpha_1\rho_1) + \nabla\cdot(\alpha_1\rho_1\mathbf{u}) = 0, \\ &\frac{\partial}{\partial t}(\alpha_2\rho_2) + \nabla\cdot(\alpha_2\rho_2\mathbf{u}) = 0, \\ &\frac{\partial}{\partial t}(\rho\mathbf{u}) + \nabla\cdot(\rho\mathbf{u}\otimes\mathbf{u}) + \nabla p = 0, \\ &\frac{\partial E}{\partial t} + \nabla\cdot(E\mathbf{u} + p\mathbf{u}) = 0, \\ &\frac{\partial \alpha_1}{\partial t} + \mathbf{u}\cdot\nabla\alpha_1 = 0, \end{aligned} \tag{1.8}$$

where $\rho_k$ and $\alpha_k$ are the $k$th phasic density and volume fraction, respectively, for $k = 1, 2$ which $\alpha_k \in [0, 1]$, $\mathbf{u}$ is the vector of mixture velocity, $p$ is the mixture pressure, and $E$ is the total energy.

This five-equation model is not closed. To close the system, a mixture of two Mie-Grüneisen fluids for equation of state [98] is considered

$$p_k\left(\rho_k, e_k\right) = p_{\infty,k}\left(\rho_k\right) + \rho_k \Gamma_k\left(\rho_k\right)\left(e_k - e_{\infty,k}\left(\rho_k\right)\right), \tag{1.9}$$

where $\Gamma_k = \left(1/\rho_k\right)\left(\partial p_k/\partial e_k\right)\big|_{\rho_k}$ is the Grüneisen coefficient, and $p_{\infty,k}, e_{\infty,k}$ are the properly chosen states of the pressure the internal energy along some reference curves (e.g., along an isentrope, a single shock Hugoniot, or the other empirically fitting curves) in order to match the experimental data of the examined material [77]. The parameters $\Gamma_k, p_{\infty,k}$ and $e_{\infty,k}$ can be simplified as functions of density only. This Mie-Grüneisen equation of state can be approximated a wide variety of materials including some gaseous or solid explosives and solid metals under high pressure.

For conservativeness constraints, the global quantities and thermodynamical parameters for the mixture can be defined as follows

$$\begin{aligned} &\alpha_1 + \alpha_2 = 1, \\ &\alpha_1\rho_1 + \alpha_2\rho_2 = \rho, \\ &\alpha_1\rho_1 e_1 + \alpha_2\rho_2 e_2 = \rho e. \end{aligned} \tag{1.10}$$

From [98] under the isobaric assumption, the Grüneisen coefficient, reference pressure $p_\infty$ and reference internal energy $e_\infty$ can be expressed as

$$\begin{aligned} &\frac{\alpha_1}{\Gamma_1\left(\rho_1\right)} + \frac{\alpha_2}{\Gamma_2\left(\rho_2\right)} = \frac{1}{\Gamma}, \\ &\alpha_1\rho_1 e_{\infty,1}\left(\rho_1\right) + \alpha_2\rho_2 e_{\infty,2}\left(\rho_2\right) = \rho e_\infty, \\ &\alpha_1\frac{p_{\infty,1}\left(\rho_1\right)}{\Gamma_1\left(\rho_1\right)} + \alpha_2\frac{p_{\infty,2}\left(\rho_2\right)}{\Gamma_2\left(\rho_2\right)} = \frac{p_\infty(\rho)}{\Gamma(\rho)}, \end{aligned} \tag{1.11}$$

then, the mixture pressure is calculated by

$$p = \left( \rho e - \sum_{k=1}^{2} \alpha_k \rho_k e_{\infty,k} \left( \rho_k \right) + \sum_{k=1}^{2} \alpha_k \frac{p_{\infty,k} \left( \rho_k \right)}{\Gamma_k \left( \rho_k \right)} \right) \Big/ \sum_{k=1}^{2} \frac{\alpha_k}{\Gamma_k \left( \rho_k \right)}. \tag{1.12}$$

These mixing rules of Eq.(1.11) and Eq.(1.12) are ensuring that the mixture pressure is free of spurious oscillations across the material interfaces[1, 2, 96, 97, 98]. Under isobaric assumption [4], the sound speed of mixture could be calculated as the volumetric average of the phasic sound speeds as

$$c^2 = \alpha_1 c_1^2 + \alpha_2 c_2^2 \tag{1.13}$$

**Note:** The time step is restricted with the local wave speed and local sound speed since sound speed is totally different from different materials.

## 1.3 Finite volume method for hyperbolic system

One of the classical CFD numerical methods, the finite volume (FV) methods are popularly used for compressible flows due to its rigorous numerical conservation. Hence, in present work, the high-solution property-preserving numerical schemes are developed under finite volume framework.

### 1.3.1 Finite volume method and finite volume wave propagation method

The one dimensional scalar conservation law under the form is considered

$$\frac{\partial U}{\partial t} + \frac{\partial F(U)}{\partial x} = 0, \tag{1.14}$$

where $U(x,t)$ is the solution variable and $F(U)$ is the flux function. Because (1.14) is hyperbolic, the characteristic speed $\alpha = F'(U)$ is a real number in 1D.

The space computational domain is defined as $\Omega = [x^L, x^R]$ and divided into $N$ cells, $I_i = [x_{i-1/2}, x_{i+1/2}]$, for $i = 1, 2, ..., N$. The grid size is uniform over the computational

domain and denoted by $\Delta x = x_{i+1/2} - x_{i-1/2}$. The time coordinate is $t$ and $t \leq T$, where $T > 0$ is the final time. The time interval $[0, T]$ is split into time steps $[t^n, t^{n+1}]$, the size of the time-step is non-uniform and denoted by $\Delta t = t^{n+1} - t^n > 0$.

For the standard finite volume semi-discretization, we employ the approximated volume-integrated average (VIA) of the solution $U(x,t)$ over a mesh cell $I_i$ at time $t$ as

$$U_i(t) = \frac{1}{\Delta x} \int_{x_{i-1/2}}^{x_{i+1/2}} U(x,t)\, dx, \qquad \text{where} \qquad i = 1, 2, \ldots, N. \tag{1.15}$$

Let us denote by $\mathsf{U} = (U_i)_{i=1,2,\ldots,N}$ the vector of discrete FV data in the mesh.

The VIA $U_i(t)$ for each cell $I_i$ is updated by

$$\frac{dU_i}{dt} = -\frac{1}{\Delta x}\left(\widetilde{F}_{i+1/2}(t) - \widetilde{F}_{i-1/2}(t)\right), \tag{1.16}$$

where $\widetilde{F}_{i+1/2}(t)$ and $\widetilde{F}_{i-1/2}(t)$ are the numerical fluxes at cell boundaries, calculated by a Riemann solver

$$\widetilde{F}_{i+1/2}(t) = F^{\text{Riemann}}_{i+1/2}(U^L_{i+1/2}, U^R_{i+1/2}, t), \tag{1.17}$$

where $U^L_{i+1/2}$ and $U^R_{i+1/2}$ are the left-side value and right-side value of cell boundary respectively, given by reconstructions over left and right potentials stencils. Particularly, the Riemann flux can be written into a canonical form as

$$F^{\text{Riemann}}_{i+1/2}(U^L_{i+1/2}, U^R_{i+1/2}, t) = \underbrace{\frac{1}{2}\left(F(U^L_{i+1/2}) + F(U^R_{i+1/2})\right)}_{\text{Central flux}} - \underbrace{\frac{|a_{i+1/2}|}{2}(U^R_{i+1/2} - U^L_{i+1/2})}_{\text{Dissipation}}, \tag{1.18}$$

where $a_{i+1/2}$ stands for the characteristic speed of the hyperbolic conservation law. The remaining main task is how to calculate $U^L_{i+1/2}$ and $U^R_{i+1/2}$ trough the reconstruction process to feed the Riemann flux as in Eq.(1.18).

Finite volume wave propagation method is known as one kind of finite volume method. The five-equation model is a quasi-conservative system of the equations. Compared to the conventional finite volume method, the wave propagation method can be approximate the five-equation model consistently and accurately [67, 68, 99]. From Eq.(1.16),

denote $\mathcal{L}(\overline{U}(t))$ as the spatial discretization operator for convection terms, then the semi-discrete version of the finite volume method can be expressed as system of ODEs (Ordinary Differential Equations)

$$\frac{\partial \overline{U}(t)}{\partial t} = \mathcal{L}(\overline{U}(t)), \tag{1.19}$$

where the spatial discretization operator for the convection terms in a cell $C_i$ is calculated by

$$\mathcal{L}\left(\overline{U}_i(t)\right) = -\frac{1}{\Delta x}\left(\mathcal{A}^{+}\Delta U_{i-1/2} + \mathcal{A}^{-}\Delta U_{i+1/2} + \mathcal{A}\Delta U_i\right), \tag{1.20}$$

where $\mathcal{A}^{+}\Delta U_{i-1/2}$ and $\mathcal{A}^{-}\Delta U_{i+1/2}$, are the right- and left-moving fluctuations, respectively, which enter into the grid cell, and $\mathcal{A}\Delta U_i$ is the total fluctuation within $C_i$. We need to solve Riemann problems to determine these fluctuations. The right- and left-moving fluctuations can be calculated using

$$\mathcal{A}^{\pm}\Delta U_{i-1/2} = \sum_{k=1}^{l}\left[s^k\left(U^L_{i-1/2}, U^R_{i-1/2}\right)\right]^{\pm}\mathcal{W}^k\left(U^L_{i-1/2}, U^R_{i-1/2}\right), \tag{1.21}$$

where moving speeds $s^k$ and jumps $\mathcal{W}^k$ of the $k$ propagating discontinuities can be solved by Riemann solvers [108] given the reconstructed values $U^L_{i-1/2}$ and $U^R_{i-1/2}$, which are computed from the reconstruction functions $\widetilde{U}_{i-1}(x)$ and $\widetilde{U}_i(x)$ to the left and right of the cell edge $x_{i-1/2}$, respectively. Normally, the notations for the quantities $s^{\pm}$ are set by $s^{+} = \max(s, 0)$ and $s^{-} = \min(s, 0)$. In similar manner, the total fluctuation can be defined by

$$\mathcal{A}\Delta U_i = \sum_{k=1}^{l}\left[s^k\left(U^R_{i-1/2}, U^L_{i+1/2}\right)\right]\mathcal{W}^k\left(U^R_{i-1/2}, U^L_{i+1/2}\right). \tag{1.22}$$

**Note:** $l$ is based on the number of propagation discontinuities in approximate Riemann solver. For instance, $l = 2$ is used in HLL-type solver and $l = 3$ is used in HLLC-type solver. However, in this work we employ the HLLC Riemann solver, then we calculate

the jump $\mathcal{W}^k\left(U^L_{i-1/2}, U^R_{i-1/2}\right)$ as

$$\begin{aligned}
\mathcal{W}^1 &= \mathbf{U}^{*L}_{i-1/2} - \mathbf{U}^{L}_{i-1/2}, \\
\mathcal{W}^2 &= \mathbf{U}^{*R}_{i-1/2} - \mathbf{U}^{*L}_{i-1/2}, \\
\mathcal{W}^3 &= \mathbf{U}^{R}_{i-1/2} - \mathbf{U}^{*R}_{i-1/2},
\end{aligned} \tag{1.23}$$

where $\mathbf{U}^L_{i-1/2}$ and $\mathbf{U}^R_{i-1/2}$ are the reconstructed values at cell boundaries, respectively. Also, $\mathbf{U}^{*L}_{i-1/2}$ and $\mathbf{U}^{*R}_{i-1/2}$ are the left-side and right-side intermediate variables, respectively.

### 1.3.2 Time integration

Given the spatial discretization, time integration scheme can be used to solve ODEs. In order to achieve high-order numerical accuracy in time, the time discretizations are made by the third-order TVD Runge-Kutta (RK3) method [43, 93] and fourth-order strong stability preserving Runge-Kutta (SSPRK) method [43, 88, 101]. More precisely, the third-order TVD Runge-Kutta (RK3) is given by

$$\begin{aligned}
U^{(1)} &= U^n + \Delta t L\left(U^n\right), \\
U^{(2)} &= \frac{3}{4}U^n + \frac{1}{4}U^{(1)} + \frac{1}{4}\Delta t L\left(U^{(1)}\right), \\
U^{n+1} &= \frac{1}{3}U^n + \frac{2}{3}U^{(2)} + \frac{2}{3}\Delta t L\left(U^{(2)}\right).
\end{aligned} \tag{1.24}$$

Similarly, the fourth-order strong stability preserving Runge-Kutta (SSPRK) is given by

$$\begin{aligned}
U^{(1)} &= U^n + 0.391752226571890\Delta t L\left(U^n\right), \\
U^{(2)} &= 0.444370493651235U^n + 0.555629506348765U^{(1)} + 0.368410593050371\Delta t L\left(U^{(1)}\right), \\
U^{(3)} &= 0.620101851488403U^n + 0.379898148511597U^{(2)} + 0.251891774271694\Delta t L\left(U^{(2)}\right), \\
U^{(4)} &= 0.178079954393132U^n + 0.821920045606868U^{(3)} + 0.544974750228521\Delta t L\left(U^{(3)}\right), \\
U^{n+1} &= 0.517231671970585U^{(2)} + 0.096059710526147U^{(3)} + 0.063692468666290\Delta t L\left(U^{(3)}\right) \\
&\quad + 0.386708617503269U^{(4)} + 0.226007483236906\Delta t L\left(U^{(4)}\right).
\end{aligned} \tag{1.25}$$

These time integration schemes are restricted by the CFL condition

$$\Delta t \leq \text{CFL} \frac{\Delta x}{\max_i \left( |u_i| , |u_i \pm a_i| \right)}, \tag{1.26}$$

where CFL $< 1$ is a safety constant.

### 1.3.3 Local reconstruction processes

The first order conservative finite volume method is known as Godunov scheme [42, 108] with piece-wise constant reconstruction or no reconstruction. The resultant scheme possesses interesting properties such as conservativeness, monotonicity, positivity-preserving and extreme robustness. Nonetheless, it generates excessive numerical dissipation and tends to smear out the flow structures. However, there is no limit for just piece-wise constant reconstruction and it can be extended to high-order reconstructions.

In order to reduce the numerical dissipation and to capture shocks exempt from spurious oscillation, high-resolution conservative schemes have been developed over the last half century. A class of non-linear schemes can effectively eliminate numerical oscillations by introducing flux or slope limiters, for instance, Flux Corrected Transport (FCT) scheme [13, 124], Total Variation Diminishing (TVD) scheme [48, 104], and Monotone Upstream-centered Scheme for Conservative Laws (MUSCL) [65, 66], which reach a nominal 2nd order accuracy, but still suffer from important numerical dissipation with a tendency to smear out flow structures, such as vortices and contact discontinuities.

Consecutively, the polynomial-based higher-order (PHO) reconstructions have been proposed to achieve higher accuracy. For example, Piecewise Parabolic Method (PPM) [27, 54], Essential Non-oscillatory (ENO) scheme [93, 94] can achieve third-order accuracy and Weighted Essential Non-oscillatory (WENO) [3, 38, 56, 86] schemes can achieve fifth-order accuracy for smooth solutions. Contrarily, when the strong discontinuity occurs, the PHO reconstructions have to be projected to lower order, non-linear scheme or piecewise constant to suppress numerical oscillations, which is limiting projection. The PHO reconstructions with limiting projection might also generate excessive

numerical dissipation and tent to smear out the discontinuities in numerical solution. These limiting projection schemes are known as *a priori* limiting projection.

Following the different path, a novel limiting projection scheme, known as the Multi-dimensional Optimal Order Detection (MOOD) technique [15, 22, 34], was recently proposed under the finite volume framework. The MOOD method is *a posteriori* limiting scheme since the limiting projection is performed after computing a candidate solution. In MOOD algorithm, some criterion were designed from constraints on computational stability and physics to detect the problematic cell which has to be recomputed by decrementing degree of local polynomial reconstruction. This procedure of MOOD algorithm can let the scheme achieve high-order accuracy for smooth solutions.

Even though these *a priori* limiting and *a posteriori* limiting projections have a great success in achieving possible highest order accuracy for smooth solutions and effectively suppressing numerical oscillations in the vicinity of discontinuities, they still suffer from numerical dissipation. On the other hand, high order schemes with conventional *priori* limiting procedure may still generate non-physical fluid properties such as negative density or pressure, which leads to the blow-up of the computation and subsequent code crash. Most of high order schemes fail to preserve positivity because of interpolation errors when near vacuum states occur or in the presence of strong shocks.

Employing polynomial reconstructions in an FV context is the ultra classical path followed by the majority of researchers to reach highly accurate FV schemes. However, when discontinuous or step-like solutions are encountered, such polynomial reconstructions become inefficient, or, worse, counterproductive. For several years, in order to capture such discontinuous solutions, some researchers rely on the tangent of hyperbola interface capturing (THINC) method which mimics a step-like function, see for instance [99, 118, 119]. It has been shown in successive researches that with a properly chosen steepness, THINC scheme works well as an advection scheme with accuracy competitive to the TVD schemes [32].

In the next subsections, we introduce two popular and well-known reconstructions of finite volume methods as MUSCL and WENO reconstructions.

#### 1.3.3.1 MUSCL reconstruction

MUSCL based reconstructions are piece-wise linear approximations constructed from volume-integrated average values by using slope limited left and right extrapolated states as follows

$$\widetilde{U}_i(x) = \overline{U}_i + \phi_i \left(x - x_i\right), \tag{1.27}$$

where $x \in \left[x_{i-1/2}, x_{i+1/2}\right]$ and $\phi_i$ is the slope defined at the cell center $x_i = \frac{1}{2}\left(x_{i-1/2} + x_{i+1/2}\right)$. To satisfy the total variation diminishing (TVD) property, a slope limiter [65, 66, 67] is needed to prevent spurious oscillations. The reconstructed values at left and right cell boundaries can be defined as

$$\begin{aligned} U^L_{i+1/2} &= \overline{U}_i + 0.5\phi(r)(\overline{U}_{i+1} - \overline{U}_i) \\ U^R_{i-1/2} &= \overline{U}_i - 0.5\phi(r)(\overline{U}_{i+1} - \overline{U}_i) \end{aligned} \tag{1.28}$$

where $\phi(r)$ is the limiter function and the difference ratio $r$ is defined as

$$r = \frac{\overline{U}_i - \overline{U}_{i-1}}{\overline{U}_{i+1} - \overline{U}_i}, \tag{1.29}$$

In literature, there are several limiters which have been developed [67]. For instance, Van Leer [111] proposed a formula of slope limiter as

$$\phi_{VL}(r) = \frac{r + |r|}{1 + r}; \quad \lim_{r\to\infty} \phi_{VL}(r) = 2. \tag{1.30}$$

The min-mod slope limiter which reported in [104] is expressed as

$$\phi_{MM}(r) = \max(0, \min(r, 1)); \quad \lim_{r\to\infty} \phi_{MM}(r) = 1. \tag{1.31}$$

In spite of its famous implementation in various numerical models, the MUSCL reconstruction generates excessive numerical dissipation with discontinuous solution and tends to smear out the flow structures.

#### 1.3.3.2 WENO reconstruction

Weighted essential non-oscillatory (WENO) reconstruction is an effective and popular reconstruction scheme in which high-order but non-oscillatory interpolation by a combination of several lower order polynomials. It is widely used method to construct left and right values at the cell boundaries from the solution available at the cell centers. We start introducing the fifth-order WENO scheme representing one in WENO family. The basic idea of WENO scheme is to choose the smoothest function from the three candidate stencils. One large stencil $S_3$ can be divided in to three sub-stencils as $S_0, S_1, S_2$. Then, we use the volume-integrated average value of each cell inside three sub-stencils $S_0, S_1, S_2$ and approximate the point value at $x_{i+1/2}$ with 3rd order accuracy to construct the solution functions. The solution function of each stencil can be recovered from the following conditions

$$\overline{U}_{i+j+k-2} = \frac{1}{\Delta x_{i+j+k-2}} \int_{x_{i+j+k-\frac{5}{2}}}^{x_{i+j+k-\frac{3}{2}}} U^{(j)}(x)dx, \quad j = 0, 1, 2, k = 0, 1, 2, \tag{1.32}$$

where $\Delta x_{i+j+k-2}$ is the mesh or cell size. For simplicity, we assume a uniform grid spacing, i.e. $\Delta x_{j-i} = x_{i+j+k-\frac{5}{2}} - x_{i+j+k-\frac{3}{2}} = \Delta x$. Thus, the third order approximation of $U_{i+\frac{1}{2}}$ is given respectively from solution function $U^{(j)}(x), j = 0, 1, 2$ as

$$U^{(0)}_{i+\frac{1}{2}} = \frac{1}{3}\overline{U}_{i-2} - \frac{7}{6}\overline{U}_{i-1} + \frac{11}{6}\overline{U}_i, \tag{1.33a}$$

$$U^{(1)}_{i+\frac{1}{2}} = -\frac{1}{6}\overline{U}_{i-1} + \frac{5}{6}\overline{U}_i + \frac{1}{3}\overline{U}_{i+1}, \tag{1.33b}$$

$$U^{(2)}_{i+\frac{1}{2}} = \frac{1}{3}\overline{U}_i + \frac{5}{6}\overline{U}_{i+1} - \frac{1}{6}\overline{U}_{i+2}, \tag{1.33c}$$

where $U^{(j)}_{i+\frac{1}{2}}$ is the abbreviation of $U^{(j)}\left(x_{i+\frac{1}{2}}\right)$. Similarly, we can construct a 4th degree polynomial using VIAs in large stencil $S_3$, which can achieve the possible largest order, by

$$U^{(3)}_{i+\frac{1}{2}} = \frac{1}{30}\overline{U}_{i-2} - \frac{13}{60}\overline{U}_{i-1} + \frac{47}{60}\overline{U}_i + \frac{9}{20}\overline{U}_{i+1} - \frac{1}{20}\overline{U}_{i+2}. \tag{1.34}$$

Furthermore, the fifth-order approximation can be written through a convex combination of the three third order approximation Eq,(1.33a,1.33b and 1.33c), namely

$$U^{(3)}_{i+\frac{1}{2}} = \gamma_0 U^{(0)}_{i+\frac{1}{2}} + \gamma_1 U^{(1)}_{i+\frac{1}{2}} + \gamma_2 U^{(2)}_{i+\frac{1}{2}}, \tag{1.35}$$

where $\{\gamma_0, \gamma_1, \gamma_2\} = \left\{\frac{1}{10}, \frac{3}{5}, \frac{3}{10}\right\}$. To eliminate the oscillation in the vicinity of discontinuities, the coefficients $\gamma_0, \gamma_1, \gamma_2$ should be replaced by the non-linear weights denoted as $\omega_1, \omega_2, \omega_3$ according to the smoothness of polynomials and respect the following conditions

1. $\omega_1 + \omega_2 + \omega_3 = 1$,

2. $\omega_j, j = 0, 1, 2$ should be close to zero for a non-smooth stencil and close to one for a smooth stencil.

The fifth-order WENO reconstructions for the left and right values at the cell boundaries [56] are given as

$$\begin{aligned}
U^L_{i+1/2} =& w_0 \left(\frac{1}{3}U_{i-2} - \frac{7}{6}U_{i-1} + \frac{11}{6}U_i\right) \\
&+ w_1 \left(-\frac{1}{6}U_{i-1} + \frac{5}{6}U_i + \frac{1}{3}U_{i+1}\right) \\
&+ w_2 \left(\frac{1}{3}U_i + \frac{5}{6}U_{i+1} - \frac{1}{6}U_{i+2}\right) \\
U^R_{i-1/2} =& w_0 \left(\frac{1}{3}U_i + \frac{5}{6}U_{i-1} - \frac{1}{6}U_{i-2}\right) \\
&+ w_1 \left(-\frac{1}{6}U_{i+1} + \frac{5}{6}U_i + \frac{1}{3}U_{i-1}\right) \\
&+ w_2 \left(\frac{1}{3}U_{i+2} - \frac{7}{6}U_{i+1} + \frac{11}{6}U_i\right)
\end{aligned} \tag{1.36}$$

where non-linear weights are given as

$$\omega_j = \frac{\alpha_j}{\alpha_0 + \alpha_1 + \alpha_2}, \quad \alpha_j = \frac{\gamma_j}{(\epsilon + \beta_j)^2}, \quad j = 0, 1, 2, \tag{1.37}$$

in which the smoothness indicators are defined as

$$\beta_j = \sum_{l=1}^{2} \int_{x_{i-\frac{1}{2}}}^{x_{i+\frac{1}{2}}} (\Delta x)^2 \left[\frac{\partial^l U^j(x)}{\partial x^l}\right]^2 dx, \quad j = 0, 1, 2. \tag{1.38}$$

or

$$\begin{aligned}\beta_0 &= \frac{13}{12}\left(U_{i-2} - 2U_{i-1} + U_i\right)^2 + \frac{1}{4}\left(U_{i-2} - 4U_{i-1} + 3U_i\right)^2, \\ \beta_1 &= \frac{13}{12}\left(U_{i-1} - 2U_i + U_{i+1}\right)^2 + \frac{1}{4}\left(U_{i-1} - U_{i+1}\right)^2, \\ \beta_2 &= \frac{13}{12}\left(U_i - 2U_{i+1} + U_{i+2}\right)^2 + \frac{1}{4}\left(3U_i - 4U_{i+1} + U_{i+2}\right)^2.\end{aligned} \tag{1.39}$$

where $\epsilon = 10^{-6}$ that is used to avoid the denominator equals to zero.

Even though the WENO reconstruction proposed by Jiang and Shu [56] has great success but still suffer from accuracy loss in some critical regions. Several efforts have been conducted to improve the accuracy of classical WENO scheme. For instance, WENO-Z scheme [3] can improve the accuracy by introducing new the smoothness indicators which are defined by

$$\beta_j = \left(\frac{\beta_j + \epsilon}{\beta_j + \epsilon + \tau_5}\right), \quad j = 0, 1, 2, \tag{1.40}$$

where $\epsilon$ equals to $10^{-40}$ and $\tau_5 = |\beta_2 - \beta_0|$. The new WENO weights $\omega_j$ can be then calculated by

$$\omega_j = \frac{\alpha_j}{\sum_{k=0}^{2} \alpha_k}, \quad \alpha_k = \frac{\gamma_j}{\beta_j}, \quad j = 0, 1, 2. \tag{1.41}$$

### 1.3.4 Riemann solvers

After determining the reconstructed left and right values at cell boundaries by using reconstruction scheme, Riemann solvers are adopted to calculate fluxes at the cell boundaries. We will focus on Riemann solvers which are employed in this work.

#### 1.3.4.1 Rusanov Riemann solver

Once left and right values at cell boundaries are reconstructed, the fluxes can be calculated based on the maximum local wave propagation speed by [87]

$$F_{i+1/2}^{Rusanov} = \frac{1}{2}\left(F(U_{i+1/2}^R) + F(U_{i+1/2}^L)\right) - \frac{a_{i+1/2}}{2}\left(U_{i+1/2}^R - U_{i+1/2}^L\right) \tag{1.42}$$

where $a_{i+1/2}$ is the local wave propagation speed which is given as

$$a_{i+1/2} = \max\left(|u|_i, |u-c|_i, |u+c|_i, |u|_{i+1}, |u-c|_{i+1}, |u+c|_{i+1}\right), \tag{1.43}$$

where $u$ is the velocity and $c$ is the local sound speed.

#### 1.3.4.2 HLLC Riemann solver

HLLC solver [108] is a modified version of HLL solver [49, 108], includes two averaged intermediate states, $U_L^*$ and $U_R^*$, separated by the contact wave of speed $S^*$. The HLLC solver is more accurate by assuming a three-wave model, which can resolve accurately contact and shear waves in the transverse directions. The three waves structure with wave speed estimates $S_L, S^*, S_R$, then flux is given as

$$\mathbf{F}^{\text{HLLC}} = \begin{cases} \mathbf{F}_L, & 0 \le S_L \\ \mathbf{F}_L^* = \mathbf{F}_L + S_L\left(\mathbf{U}_L^* - \mathbf{U}_L\right), & S_L \le 0 \le S^* \\ \mathbf{F}_R^* = \mathbf{F}_R + S_R\left(\mathbf{U}_R^* - \mathbf{U}_R\right), & S^* \le 0 \le S_R \\ \mathbf{F}_R \end{cases} \tag{1.44}$$

where $U_L^*$ and $U_R^*$ are the left and right values at the contact discontinuity between two linear waves, which can be calculated as following

$$\mathbf{U}_k^* = \rho_k \left(\frac{S_k - u_k}{S_k - S^*}\right) \begin{pmatrix} 1 \\ S^* \\ \dfrac{E_k}{\rho_k}\left(S^* - u_k\right)\left[S^* + \dfrac{p_k}{\rho_k\left(S_k - u_k\right)}\right] \end{pmatrix} \quad k = L, R. \tag{1.45}$$

In order to calculate completely the numerical fluxes, the three wave speed estimates $S_L, S_R, S^*$ are simply determined by

$$S_L = \min\left\{u_L - c_L, u_R - c_R\right\}, \quad S_R = \max\left\{u_L + c_L, u_R + c_R\right\}, \tag{1.46a}$$

$$S^* = \frac{p_R - p_L + \rho_L u_L\left(S_L - u_L\right) - \rho_R u_R\left(S_R - u_R\right)}{\rho_L\left(S_L - u_L\right) - \rho_R\left(S_R - u_R\right)}, \tag{1.46b}$$

where $c_L$ and $c_R$ are the sound speeds computed at the cell interface.

#### 1.3.4.3 HLLCM Riemann solver

Although HLLC solver is proven to be a great success in resolve exactly contact and shear waves, but it generates numerical shock instability or carbuncle phenomenon. HLLCM solver [92] is a modification of HLLC solver without shear wave in two-dimensional space version. The numerical flux is similar to HLLC flux computation as in Eq.(1.44).

The averaged intermediate states in the star region are defined as

$$\mathbf{U}_k^* = \rho_k \left( \frac{S_k - u_k}{S_k - S^*} \right) \begin{pmatrix} 1 \\ S^* \\ v_{HM}^* \\ E_{HM,k}^* \end{pmatrix} \quad k = L, R, \tag{1.47}$$

which imply that the solver has two states between the contact wave but has only a common tangent velocity. We require to determine the tangent velocity $v_{HM}^*$ and the specific total energy includes the normal and the tangent kinetic energy.

$$v_{HM}^* = \frac{\alpha_R v_R - \alpha_L v_L}{\alpha_R - \alpha_L}, \tag{1.48a}$$

$$E_{HM,k}^* = e_k^* - \mathbf{V} + \frac{1}{2} \frac{\alpha_R v_R^2 - \alpha_L v_L^2}{\alpha_R - \alpha_L}, \quad k = L, R, \tag{1.48b}$$

where $\alpha_L = \rho_L(S_L - u_L)$, $\alpha_R = \rho_R(S_R - u_R)$, and $\mathbf{V} = \frac{1}{2}\left(u_k^2 + v_k^2\right)$ which $u, v$ are the normal and tangent velocity, respectively. The specific total energy $e_k^*$ is defined as

$$e_k^* = \frac{E_k}{\rho_k} + \left(S^* - u_k\right)\left(S^* + p_k/\alpha_k\right). \tag{1.49}$$

The shear velocities on both sides of the contact wave are smeared for calculating the HLLCM flux and repalced by the average of the shear velocity $v_{HM}^*$. Thus, HLLCM solver can prevent the carbuncle phenomenon or shock instability when strong shocks

occur.

## 1.4 Issues of numerical methods for compressible flows

The numerical Godunov-type schemes under finite volume framework have been widely employed in compressible Euler equations. Since the strong shocks always occur in the simulation of compressible Euler equation, there are some issues have been noticed in the existing numerical methods.

1. Standard high-order shock-capturing schemes such as MUSCL, ENO, or WENO scheme can resolve discontinuous solutions without numerical oscillations by feeding extra dissipative errors or projecting to lower order. This implies that the excessive numerical dissipation is generated by the numerical schemes when the strong discontinuities occur, which noticed that still is a significant problem. For instance, the so-called WENO-JS is able to obtain the maximal fifth-order accuracy on smooth solution, nonetheless it may lose accuracy near the critical points. In consequence, several approaches have been proposed to improve the WENO scheme via the design of the smoothness indicators. Although these efforts are able to achieve greatly better results than WENO-JS scheme, but in some cases they still suffer from numerical dissipation in vicinity of strong discontinuities.

2. In recent years, high-order schemes were developed to handle both smooth and discontinuous solutions with less numerical dissipation. Nevertheless, one main issue of the original high-order schemes is that they may provide non-physical properties as negative density or pressure (positivity failure), which leads to a blow-up of the numerical computation and subsequent code crash. Most of classical high-order schemes fail to preserve positivity (or to maintain the physical validity of the solution) because of interpolation errors in the vicinity of very strong discontinuities or when vacuum or near vacuum states occur. On the other hand, the positivity failure is an extreme challenge for the compressible Euler equations supplemented with source terms (e.g. gravity, chemical reaction). Physically, both density $\rho$ and pressure $p$ should be positive. For instance, high-order schemes may provide negative physical properties when they are

applied for low density problems in computing blast waves, low pressure problems in computing high Mach numerical astrophysical jets and gaseous detonation propagation through different geometries.

3. In reactive Euler equations, the source term represents the chemical reactions which may be orders of magnitude faster than the gas flow. There are several difficulties in developing high-resolution and stable/robust numerical schemes to accurately solve a general hyperbolic system with source terms. For example, when the source term becomes stiff, shock capturing numerical methods may possibly predict wrong wave propagation speed of the detonation fronts or may generate spurious numerical propagation phenomenon of the shock waves in the flow structures. For instance, the numerical dissipation smears some discontinuities which, in return incorrectly trigger the reaction of the source term and then produce a wrong numerical solution. Furthermore, if the grid resolution is not sufficient enough, the enough temporal resolution cannot remove the incorrect propagation speed of the discontinuities and non-physical spurious waves cause by the discretization, especially in the flow with shock waves. Thus, the chemical reaction may be triggered at a wrong location. After the late or incorrectly located reaction, the new mass or energy in the vicinity of discontinuities is incorrectly captured (in space and time), and, all subsequent computed wave speeds and plateaus may be spoiled by excessive numerical dissipation. An other main issue in reaction flow simulations is positivity-preserving as mentioned previously. For instance, the occurrence of negative density or pressure is quite often encountered during the time evolution, which leads to a blow-up of the computation.

4. In compressible multi-phase flow, the development of numerical methods is more challenging than in compressible single phase flow. The flow structures become complex when involve material interfaces between two gases or two materials of different physical nature. Therefore, numerical algorithms have been proposed for identifying each fluid by coupling the Euler equations with other equation such as $\gamma$-model [1, 2], the volume fraction model [96], or a level-set function [79]. However, these models suffer from non-physical oscillations occurred at material interfaces. On the other hand, the numerical method for compressible multi-phase flow should obey three critical con-

ditions [28].

- Preserve the conservativeness of total mass, momentum and energy to correctly identify the location of material interfaces.

- Preserve numerical stability (no spurious oscillations at material interfaces)

- Maintain high-order accuracy in smooth regions of the flow

There are some difficulties in the one-fluid model when we apply solving compressible multiphase flows. The density and energy in compressible flow have to be solved simultaneously with the material indication function and couple with special formulations to maintain the physical and thermodynamical consistency as well as the pressure equilibrium across the interface. The high-resolution shock-capturing schemes for solving single phase compressible flow which generate numerical dissipation, then they tend to smear out discontinuities including the material interfaces.

In solving compressible multi-phase flows, standard shock-capturing numerical algorithm were also found in literature as TVD, MUSCL and WENO scheme [28, 59]. TVD and MUSCL scheme can solve discontinuities without spurious oscillations, however, they still suffer from excessive numerical dissipation. The excessive numerical dissipation smears out the flow fields as well as the discontinuities in mass or volume fraction which represents the material interfaces. Otherwise, WENO scheme can generously reduce numerical dissipation, capture well for the moving interfaces and provide high accuracy in smooth regions. However, it may generate numerical oscillations for compressible multi-phase flows with complex EOS as discussed in [28]. Commonly, the implementation of high order shock-capturing schemes to interfacial compressible multiphase flows requires further investigations.

5. Recently, new BVD schemes have been proposed by combining high-order linear-weight (constant-coefficient) polynomials and THINC function with multistage BVD algorithms. The resulting schemes, so-called $P_nT_m$-BVD (polynomial of n-degree and THINC function of m-level reconstruction based on BVD algorithm) schemes, are completely different from any existing high-resolution scheme that counts on nonlinear-weights polynomials to suppress spurious oscillations. However, these new BVD schemes fail to preserve the positivity of fluid properties such as density or pressure, and lead to

blow-ups of the computation (not robust when the solution involves near vacuum or vacuum states).

## 1.5 Objectives of research study

In the present work, novel high-resolution property-preserving numerical methods for complex compressible flows will be proposed and validated via numerical benchmark test cases involving vacuum or near vacuum states, strong discontinuities and also smooth flows. According to the existing issues mentioned in the previous section, our objectives of research study as following.

1. We propose a novel finite volume scheme to solve hyperbolic conservation laws under the multi-dimensional optimal order detection (MOOD) framework. The concept of this method is replacing the first-order finite volume method to the tangent of hyperbola interface capturing (THINC) scheme to capture sharply the discontinuities without spurious oscillations and obtain possible highest order of accuracy.

2. Furthermore, in order to achieve high fidelity, the numerical methods should preserve the solution properties such as: Accuracy on both smooth and discontinuous profile, non-oscillatory behavior and fail-safe behavior (positivity-preserving) we develop a general formulation of reconstruction in finite volume method by integrating the boundary variation diminishing (BVD) and multi-dimensional optimal order detection (MOOD) methodologies by blending of high-/low-order polynomials and hyperbolic tangent reconstructions. As a concrete example, we propose a high-resolution scheme under a three-stage cascade. For BVD reconstruction strategy, the linear fifth-order upwind or piecewise quartic method (PQM) on fourth-degree of polynomial (P4) [116] is implemented as one of the candidate reconstruction functions to capture smooth solutions. Other candidate reconstruction functions use tangent of hyperbola interface capturing (THINC) functions with different controlling the slope (jump thickness) to eliminate the numerical oscillation and to capture sharply all discontinuities. Furthermore, a MOOD algorithm performs and detects a candidate solution by PAD ensuring as such the positivity-preserving property.

3. We further extend our new approach (multi-stage BVD-MOOD) for the compressible Euler equations supplemented with source terms (e.g. gravity, chemical reaction). One of the main challenges when simulating these models is the occurrence of negative density or pressure during the time evolution, which leads to a blow-up of computation. Therefore, the new numerical scheme should be low dissipation to capture the propagation fronts as well as to preserve the positiveness of fluid properties even in low density or pressure test problems.

4. The newly proposed scheme is applied to solve the five-equation model for interface two-phase flows. This scheme is implemented under finite volume wave propagation method, which realizes the consistency among volume fraction and other physical variables. In addition, this approach is able to resolve discontinuous solutions which are sharper than other existing schemes as well as the material interfaces and provide high accuracy for smooth solution.

## 1.6 Outline of thesis

The remainder of this thesis is organized as follows. In Chapter 2, we introduce a novel finite volume scheme to solve hyperbolic conservation laws under the multi-dimensional optimal order detection (MOOD) technique. The main idea of this work is to replace the first-order finite volume method to the tangent of hyperbola interface capturing (THINC) scheme. We also introduce the local reconstruction schemes of PQM, PPM, Godunov and THINC. Furthermore, we describe about the MOOD algorithm with fully functions of detection criteria. MOOD algorithm consists of two criteria such as physical admissible detection (PAD) and numerical admissible detection (NAD). Finally, we demonstrate the numerical results for both scalar conservation laws and Euler equations comparing to original MOOD schemes as well as WENO-Z scheme.

In Chapter 3, we present a new high-resolution property-preserving scheme. It is called multi-stage BVD-MOOD scheme. In this work, we generally blend the high/low order polynomials reconstructions and hyperbolic tangent functions through integrating the boundary variation diminishing (BVD) and multi-dimensional optimal order detection

(MOOD) methodologies. In this chapter, the solution property preserving reconstruction is introduced including high/low order polynomial and THINC function. We also describe about the robustness and physical admissibility via an *a posteriori* MOOD procedure and illustrate the behavior of the reconstruction operators which employed in the propose scheme via examples of both smooth and discontinuous profile. In addition, we address the local section of reconstruction operator known as a three-stage BVD algorithm which is the main strategy and mandatory in this work. Accuracy and efficiency of the present scheme also discussed in this part. Verified through numerical benchmark tests involving very strong discontinuities and vacuum or near vacuum states, the present method is able to resolve smooth solution, capture sharply discontinuous solution and preserving positivity. Those results are comparable and competitive to existing high order positivity-preserving schemes.

In Chapter 4, we present the extension of multi-stage BVD-MOOD scheme for compressible Euler equations with source terms including gravity and chemical reaction. We briefly introduce the numerical methods to solve the Euler equations with source terms by operator splitting into convection operator and source term or reaction operator. In this work, since we operator splitting technique, then we employ the RK3 time integration for saving the computational cost, however, there is no significant difference from SSPRK time integration. Numerical results of benchmark tests show that the present method is able to resolve both smooth solution and discontinuous solution and is extremely robust for safe failure (positivity preserving) with excellent result quality competitive to other existing schemes. For instance, the reactive Euler flows with stiffness of C-J detonation, it shows that multi-stage BVD-MOOD scheme can correctly capture with sharp manner the reacting front of the gas detonation, while the WENO scheme provides unacceptable solution within the same grid resolution and even smaller time step. According to its algorithmic simplicity and robustness in simulations involving strong discontinuities, reacting front with stiff source terms and vacuum or near vacuum states, we believe the proposed scheme can become as a practical and stipulating numerical solver for complex compressible flows.

In Chapter 5, we apply the multi-stage BVD-MOOD scheme for compressible two-

phase flows by using five-equation model coupling with finite volume wave propagation method. Again, this scheme employs the high/low order polynomials reconstructions and hyperbolic tangent functions through integrating the boundary variation diminishing (BVD) and multi-dimensional optimal order detection (MOOD) methodologies. Due to the BVD principle that selects the appropriate reconstruction operator for the target cell, therefore effectively minimizes the dissipation error in numerical solution. All state variables including the volume fraction are reconstructed by multi-stage BVD-MOOD scheme and same finite volume wave propagation method. Numerical solutions demonstrate that the present scheme sharply captures the material interfaces and obtain numerical results of higher quality in comparison to other existing methods.

At last but not least, in Chapter 6, we will make a conclusion from this thesis. The major contributions of the current study and discussion about future work will also be given.

# Chapter 2

# Reconstruction approach by using MOOD and THINC method

## 2.1 Introduction

A novel limiting projection scheme, known as the Multi-dimensional Optimal Order Detection (MOOD) technique [15, 22, 34, 36], was recently proposed under the finite volume framework. The MOOD method is *a posteriori* limiting scheme since the limiting projection is performed after computing a candidate solution. In MOOD algorithm, some criterion were designed from constraints on computational stability and physics to detect the problematic cell which has to be recomputed by decrementing degree of local polynomial reconstruction. Firstly, we implement a local polynomial reconstruction of the highest-order ($d_{max}$) for the current time step and compute the candidate solution of highest order for the next time step without limiting. Then the detectors of MOOD check all cells with the prescribed criterion. For a cell where all criterion are satisfied, the candidate solution is accepted for next time step. Otherwise, a cell, where the candidate solution does not satisfy the criterion, is marked as a trouble cell within which the solution is recomputed by reducing the degree of local reconstruction polynomial. This process continues for the local reconstructions of the problematic cells with gradually degraded polynomials from high order to lower order. The piece-wise constant reconstruction is the final candidate which leads to the first-order finite volume

method that gives monotone and the most robust solution. In this chapter, we propose a novel high-resolution scheme under MOOD method by replacing the first-order finite volume method to the Tangent of Hyperbola INterface Capturing (THINC) method [32, 103, 118, 119]. THINC method mimics a jump-like solution and is employed to capture the discontinuous solutions. The first-order finite volume method generates excessive numerical dissipation and smears out the discontinuous solutions, while THINC method substantially improves the numerical solution to discontinuities.

## 2.2 Reconstruction schemes used in MOOD algorithm

In this section, we introduce the polynomial based interpolations (PPM and PQM) which are employed in mutli-dimensional optimal order detection algorithm as well as non-linear THINC function.

### 2.2.1 Piecewise parabolic reconstruction

The pieceiwse constant scheme results in a first-order accurate scheme which causes large numerical dissipation. Based on the linear reconstruction (P1), second-order scheme gains the improvement over the first-order scheme. The piecewise parabolic method (PPM) reconstruction scheme (P2) was proposed in [27, 54, 70] to get the third-order accuracy, where the reconstructed values at the left and right cell boundaries are denoted as $U^L_{i+1/2}$ and $U^R_{i-1/2}$, respectively, and are upwinded via the formula

$$\begin{aligned} U^L_{i+1/2} &= \frac{1}{6}\left(-U_{i-1} + 5U_i + 2U_{i+1}\right) \\ U^R_{i-1/2} &= \frac{1}{6}\left(2U_{i-1} + 5U_i - U_{i+1}\right) \end{aligned} \tag{2.1}$$

### 2.2.2 Piecewise quartic reconstruction

Similarly to PPM, the fifth-order accurate scheme based on piecewise polynomials of degree four (P4), known as piecewise quadtic method (PQM) was proposed in [116]. The reconstruction values at the left and right cell boundaries are denoted as $U^L_{i+1/2}$ and

$U^R_{i-1/2}$, respectively, and are upwinded via the formula

$$\begin{aligned} U^L_{i+1/2} &= \frac{1}{60}\left(2U_{i-2} - 13U_{i-1} + 47U_i + 27U_{i+1} - 3U_{i+2}\right) \\ U^R_{i-1/2} &= \frac{1}{60}\left(-3U_{i-2} + 27U_{i-1} + 47U_i - 13U_{i+1} + 2U_{i+2}\right) \end{aligned} \tag{2.2}$$

This reconstruction is high accurate (fifth order on smooth enough profiles in one dimension) and, unfortunately, oscillatory when steep gradients are encountered.

### 2.2.3 Tangent hyperbolic interface capturing function

Being proposed originally as a VOF (volume of fluid) scheme [118, 119] to capture moving interfaces in multiphase flows, the THINC (Tangent of Hyperbola for INterface Capturing) method uses the hyperbolic tangent function for spatial recon-struction. The hyperbolic tangent function is a sigmoid function and a differentiable and monotone function that mimics well a step-like discontinuity. It has been shown in successive researches that with a properly chosen steepness, THINC scheme works well as an advection scheme with accuracy competitive to the TVD schemes [32]. In this work, we employ the THINC scheme to replace the first-order finite volume method in the MOOD algorithm.

THINC reconstruction function is defined as

$$q_i(x) = U_{\min} + \frac{[\![U]\!]}{2}\left[1 + \theta \tanh\left(\beta\left(\frac{x - x_{i-1/2}}{x_{i+1/2} - x_{i-1/2}} - \widetilde{x}_i\right)\right)\right], \tag{2.3}$$

where $U_{\min} = \min(U_{i-1}, U_{i+1})$, $[\![U]\!] = \max(U_{i-1}, U_{i+1}) - U_{\min}$ and $\theta = \mathrm{sgn}(U_{i+1} - U_{i-1})$. The parameter $\beta$ is used for controlling the slope and the jump thickness, i.e. if $\beta$ has a value close to zero then the profile $q_i$ converges towards the average value of $\frac{U_{i-1}+U_{i+1}}{2}$ while, if $\beta$ is large, it tends to be a step-like function.

In Eq.(2.3), the only remaining unknown, $\widetilde{x}_i$, which presents the relative location of jump center in the cell, is calculated by solving the constraint condition $U_i = \frac{1}{\Delta x}\int_{I_i} q_i(x)\,dx$.

The reconstructed values at left and right ends of cell boundary are given by

$$\begin{aligned} U_i^L(x_{i+1/2}) &= q_i(x_{i+1/2}) = U_{min} + \frac{[\![U]\!]}{2}\left(1 + \theta\frac{\tanh(\beta) + A}{1 + A\tanh(\beta)}\right) \\ U_i^R(x_{i-1/2}) &= q_i(x_{i-1/2}) = U_{min} + \frac{[\![U]\!]}{2}(1 + \theta A) \end{aligned}$$

where $A = \frac{1}{\tanh(\beta)}\left(\frac{B}{\cosh(\beta)} - 1\right)$, $B = e^{\theta\beta(2C-1)}$ and $C = \dfrac{U_i - U_{min} + \epsilon}{[\![U]\!] + \epsilon}$ with $\epsilon = 10^{-20}$ to avoid division by zero.

## 2.3 Multi-dimensional optimal order detection algorithm

The basic idea of MOOD algorithm [22, 34] is based on an iteratively checking process by decrementing degree of local polynomial reconstruction from high-order ($d_{max}$) to lower-order if the reconstruction leads to a solution that does not meet the predetermined criterion. The lowest-order ($d_i = 0$) scheme is piecewise constant reconstruction used in the first-order accurate Godunov finite volume scheme, which is monotone, robust and positivity-preserving. A set of constraints is designed to reinforce numerical stability and desired physical properties. In MOOD algorithm, a candidate solution is firstly computed using a high-order polynomial reconstruction. Being an *a posteriori* limiting projection, the detectors of MOOD then check whether the candidate solution satisfies the criterion for each cell. The cell, where all the criterion are satisfied, is marked as "acceptable" cell and the corresponding solution with high-order polynomial reconstruction is updated as $U_i^{n+1}$ (the solution at time $t^{n+1}$) while the cells that do not pass the detection criterion are marked as "trouble" cells. The trouble cells are locally recomputed by a new reconstruction with a lower-degree polynomial. Analogously, the new candidate solution is again tested by the criterion of MOOD. The decrementing procedure is iterated if the new candidate solution is still not admissible regarding the MOOD criterion. This procedure continues until the decremented local polynomial reaches zero degree, i.e. the piecewise constant function in the first-order scheme. In Fig. 2.1 we show a sketch of MOOD scheme.

In this work, we replaced the piecewise constant interpolation by THINC scheme which

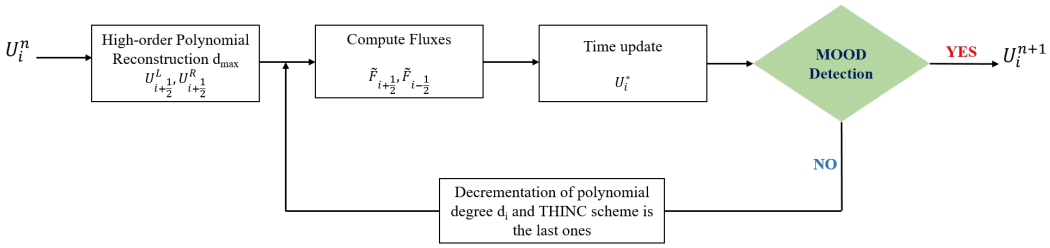


Figure 2.1: Sketch of multi-dimensional optimal order detection process

enables to provide sharp solution of discontinuities. The algorithm of MOOD method is as follows:

1. Given solution $U_i^n$ at time $t^n$ for all cells, compute high-order polynomial reconstruction ($d_{max}$)

2. Compute the numerical fluxes $\tilde{F}_{i+1/2}$ and $\tilde{F}_{i-1/2}$

3. Compute the candidate solution $U_i^*$ at time $t^{n+1}$ by finite volume scheme Eq.(1.16)

4. Check the candidate solution $U_i^*$ by the MOOD criterion. If solutions in cells are eligible for MOOD criterion, set $U_i^{n+1} = U_i^*$. Otherwise, for cells where the solutions are not admissible, decrement the degree of local polynomial and recompute the solution through steps 2-4.

**Remark 1.** The decrementing procedure is adjusted only for the trouble cells and their direct neighbors in the compact stencils need for reconstruction. For the next iterative step, only these re-updated cells have to be checked at current time $t^n$.
In this work, we use a cascade of scheme for the numerical experiments. For Example, $\mathbb{P}_{\mathbb{M}} \rightarrow \mathbb{P}_2 \rightarrow \mathbb{TH}$ with M = 4 and $\mathbb{TH}$ stands for THINC method.

### 2.3.1 Physical admissible detection (PAD)

PAD is the first criteria based on the physical properties for admissibility. This detector is used to ensure the positivity of fluid properties such as density and pressure values in Euler system. We set the following algorithm of PAD as

$$\rho^* > 0 \qquad \text{and} \qquad p^* > 0 \tag{2.4}$$

If solution in cell $I_i$ is not valid or satisfied for PAD criteria, the degree of local polynomial reconstruction is decremented, otherwise the candidate solution $U_i^*$ is admissible. This process is ensuring positivity-preserving for density and pressure.

### 2.3.2 Numerical admissible detection (NAD)

NAD is the second criteria designed to suppress spurious numerical oscillations associated with high order interpolation. NAD consists of two filters namely Discrete Maximum Principle (DMP) and $u2$ detection process.

#### 2.3.2.1 Discrete maximum principle (DMP)

The discrete maximum principle [17, 34] is firstly checked for the candidate solution $U_i^*$ for cell $I_i$, and DMP is defined as

$$\min_{j\in\bar{v}(i)}\left(U_i^n, U_j^n\right) \leq U_i^* \leq \max_{j\in\bar{v}(i)}\left(U_i^n, U_j^n\right), \tag{2.5}$$

where $j$ is index for neighbor cell $I_j$ of cell $I_i$ and $\bar{v}(i)$ is a set of compact stencils for cell $I_i$.

In practice, we used the relaxation discrete maximum principle (RDMP) to obtain high-order accuracy at smooth extrema

$$\min_{j\in\bar{v}(i)}\left(U_i^n, U_j^n\right) - \delta \leq U_i^* \leq \max_{j\in\bar{v}(i)}\left(U_i^n, U_j^n\right) + \delta, \tag{2.6}$$

The parameter $\delta$ implemented for relaxation the strict maximum principle to allow a very minimal undershoots and overshoots, we set as

$$\delta = \max\left(\delta_0, \epsilon.\left(\max_{j\in\bar{v}(i)}\left(U_j^n\right) - \min_{j\in\bar{v}(i)}\left(U_j^n\right)\right)\right), \tag{2.7}$$

with $\delta_0 = 10^{-4}$ and $\epsilon = 10^{-3}$. This relaxation does not affect to positivity of physical properties because PAD performed separately.

#### 2.3.2.2 *u*2 detection process

If the candidate solution does not satisfy DMP, then we check the *u*2 detection process [34]. A candidate solution $U_i^*$ in the cell $I_i$ violating the DMP is nonetheless eligible if

$$\chi_i^{max}\chi_i^{min} > 0, \tag{2.8}$$

$$\frac{\left|\chi_i^{max}\right|}{\left|\chi_i^{min}\right|} \geq 1 - \varepsilon, \tag{2.9}$$

where $\varepsilon = 1/2$ is a smoothness parameter and $\chi_i^{max}$ and $\chi_i^{min}$ are the maximal and minimal local curvatures. We calculate curvatures as $\chi_i = \partial_{xx}\widetilde{U}_i \in \mathbb{R}$ which is the second derivative of second order polynomial reconstruction, $\widetilde{U}_i = \widetilde{U}_i(x, 2)$. Then we set

$$\chi_i^{min} = \min_{j\in\bar{v}(i)}(\chi_i, \chi_j) \quad \text{and} \quad \chi_i^{max} = \max_{j\in\bar{v}(i)}(\chi_i, \chi_j) \tag{2.10}$$

The algorithm of numerical admissible is following

1. A candidate solution $U_i^*$ of cell $I_i$ was first checked by DMP detector Eq.(2.5) and in practice Eq.(2.6)

2. If $U_i^*$ is not eligible DMP then perform the *u*2 criterion

   (a) Compute $\chi_i$ and $\chi_j$ for $i, j \in \bar{v}(i)$

   (b) Check detector Eq.(2.8). If $U_i^*$ is satisfied, set $U_i^{n+1} = U_i^*$ as a solution for next time step, else $U_i^*$ recomputed by decrementing degree of local polynomial reconstruction

   (c) Check detector Eq.(2.9). If $U_i^*$ is not smooth extrema then $\mathrm{d_i}$ of polynomial is decremented, otherwise $U_i^*$ is valid and set $U_i^{n+1} = U_i^*$.

**Remark 2.** The degree of local polynomial reconstruction is decremented until zero, but in this work the last scheme is THINC method.

## 2.4 Numerical experiments

In this section, we show the performance of proposed scheme via the numerical results of some benchmark tests for scalar and Euler conservation laws. The numerical in-house FV code is built on the following key tools: the reconstruction procedure is conducted in terms of primitive variables, the Rusanov Riemann solver [87] is used for flux computation, a third-order TVD Runge-Kutta (RK3) in time discretisation is employed, the MOOD algorithm for the space reconstruction is used, and at last the THINC function is implemented to capture sharply the discontinuities.

### 2.4.1 Scalar conservation laws

#### 2.4.1.1 Linear advection equation

The linear advection equation is expressed as

$$\frac{\partial U}{\partial t} + \frac{\partial U}{\partial x} = 0 \tag{2.11}$$

**Convergence test:** The initial condition for smooth profile expressed by $U(x,0) = sin(\pi x), x \in [-1,1]$ is advected. The $L_1$ and $L_\infty$ errors and convergence rates shown in table 2.1 after one period by MOOD algorithms (MOOD_P4-P2-P0 and MOOD_P4-P2-TH) under gradually refined mesh resolutions. By observing the results, the numerical errors and convergence rates of two schemes are identical for all mesh resolution. It proves that the proposed scheme MOOD_P4-P2-TH can achieve 5th-order as MOOD_P4-P2-P0 for smooth solution.

Table 2.1: Numerical errors and convergence rates for 1D advection at $t = 2.0$

| N | MOOD (P4-P2-P0) | | | | MOOD (P4-P2-TH) | | | |
|---|---|---|---|---|---|---|---|---|
| | $L_1$ | order | $L_\infty$ | order | $L_1$ | order | $L_\infty$ | order |
| 20 | 1.99e-04 | - | 3.15e-04 | - | 1.99e-04 | - | 3.15e-04 | - |
| 40 | 6.34e-06 | 4.97 | 9.98e-06 | 4.98 | 6.34e-06 | 4.97 | 9.98e-06 | 4.98 |
| 80 | 1.99e-07 | 4.98 | 3.13e-07 | 4.98 | 1.99e-07 | 4.98 | 3.13e-07 | 4.98 |
| 160 | 6.3e-09 | 4.98 | 9.9e-09 | 4.98 | 6.3e-09 | 4.98 | 9.9e-09 | 4.98 |
| 320 | 2.04e-10 | 4.97 | 3.12e-10 | 4.98 | 2.04e-10 | 4.97 | 3.12e-10 | 4.98 |

**Advection of square waves:** In this test, the initial condition is given by

$$U(x,0) = \begin{cases} 1, & 0.3 \leq x \leq 0.7, \\ 0, & \text{otherwise.} \end{cases} \tag{2.12}$$

The numerical simulations are calculated with 100 cells with time $t = 1.0$ using WENO-Z scheme, MOOD (P4-P2-P0), MOOD (P4-P2-TH, $\beta = 1.6$), and MOOD (P4-P2-TH, $\beta = 2.4$) in Fig. 2.2. We observe that MOOD schemes produce no oscillation near discontinuities, which are equivalent WENO-Z scheme. However, for MOOD (P4-P2-P0) is more diffusive by nearly 9 cells than MOOD (P4-P2-TH) by nearly 8 cells for $\beta = 1.6$ and 7 cells for $\beta = 2.4$.

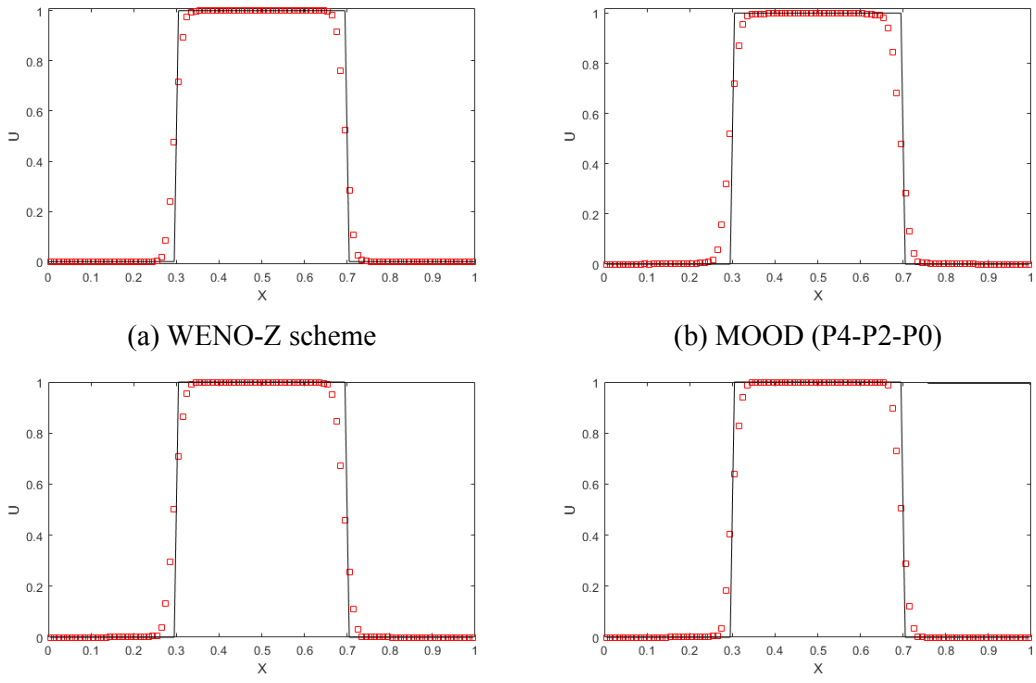


(a) WENO-Z scheme

(b) MOOD (P4-P2-P0)

(c) MOOD (P4-P2-TH, $\beta = 1.6$)

(d) MOOD (P4-P2-TH, $\beta = 2.4$)

Figure 2.2: Advection of square waves with 100 uniform mesh at $t = 1.0$ – solid line: Exact solution, symbol: Numerical solution.

**Jaing and Shu's test:** The test is proposed in [56], the initial condition consists of both discontinuities and smooth profiles known as propagation of complex wave. The

initial condition with computational domain $\Omega = [-1, 1]$ is defined as

$$U(x,0) = \begin{cases} \frac{1}{6}\left(G(x,\beta,z-\delta) + G(x,\beta,z+\delta) + 4G(x,\beta,z)\right), & -0.8 \leq x \leq -0.6, \\ 1, & -0.4 \leq x \leq -0.2, \\ 1 - |10(x-0.1)|, & 0.0 \leq x \leq 0.2, \\ \frac{1}{6}\left(F(x,\alpha,a-\delta) + G(x,\alpha,a+\delta) + 4G(x,\alpha,z)\right) & 0.4 \leq x \leq 0.6, \\ 0, & \text{otherwise.} \end{cases} \tag{2.13}$$

The functions $F$ and $G$ are defined by

$$G(x,\beta,z) = \exp\left(-\beta(x-z)^2\right), \qquad F(x,\alpha,a) = \sqrt{\max(1-\alpha^2(x-a)^2, 0)}, \tag{2.14}$$

and the coefficients are given by

$$a = 0.5,\ z = -0.7,\ \delta = 0.005,\ \alpha = 10,\ \beta = \log 2/36(\delta^2). \tag{2.15}$$

The results of Jiang and Shu's test are shown in Fig. 2.3 comparing to WENO-Z scheme, MOOD (P4-P2-P0), MOOD (P4-P2-TH, $\beta = 1.6$) and MOOD (P4-P2-TH, $\beta = 2.4$). MOOD (P4-P2-TH) for both beta values can capture the sharp discontinuity without oscillation and retain the smooth profile with high resolution as WENO-Z scheme while MOOD (P4-P2-P0) is diffusive in both discontinuity and smooth profile.

#### 2.4.1.2 Inviscid Burger's Equation

Considering the 1D Burger's equation is

$$\frac{\partial U}{\partial t} + \frac{\partial U^2}{\partial x} = 0 \tag{2.16}$$

**Burgers equation with smooth initial profile of sine wave:** A sine wave in this test has an initial profile [103] defined as $U(x,0) = 0.5 + sin(\pi), x \in [0,2]$. Due to convexity of Burgers flux, the sine wave will develop a shock wave after the time $= 1.5/\pi$. The numerical results are computed on a 100-cell grids at $= 1.5/\pi$ in Fig. 2.4. In this case,

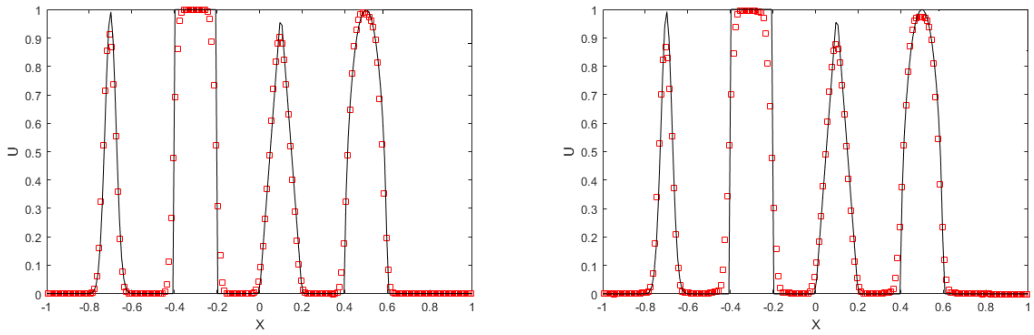


(a) WENO-Z scheme




(b) MOOD (P4-P2-P0)

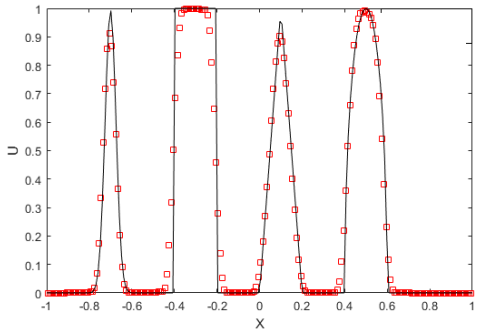


(c) MOOD (P4-P2-TH, $\beta = 1.6$)

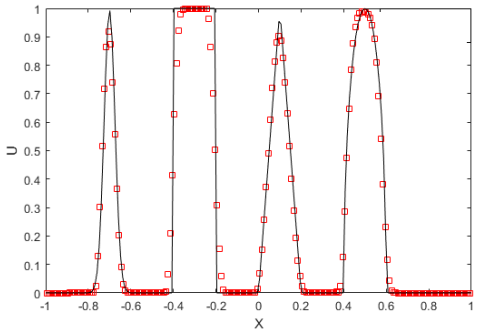


(d) MOOD (P4-P2-TH, $\beta = 2.4$)

Figure 2.3: Numerical results for advection of complex waves with 200-cell mesh after one period ($t = 2.0$) – solid line: Exact solution, symbol: Numerical solution.

we see that the shock wave can be captured within 2 grid cells for WENO-Z scheme and MOOD (P4-P2-P0) while MOOD (P4-P2-TH) with both beta values resolved just only one cell.

**Burger's equation with square wave as initial profile:** The initial condition is given by

$$U(x,0) = \begin{cases} 1, & 0.3 \leq x \leq 0.75, \\ 0, & \text{otherwise.} \end{cases} \tag{2.17}$$

The numerical results are computed for time $t = 0.2$, see in Fig. 2.5. For this case, both shock and rarefaction wave are existed. We observe that the WENO-Z scheme and MOOD (P4-P2-TH) schemes provide high accuracy for both the shock and expansion fan while MOOD (P4-P2-P0) gives numerical diffusion at expansion fan.

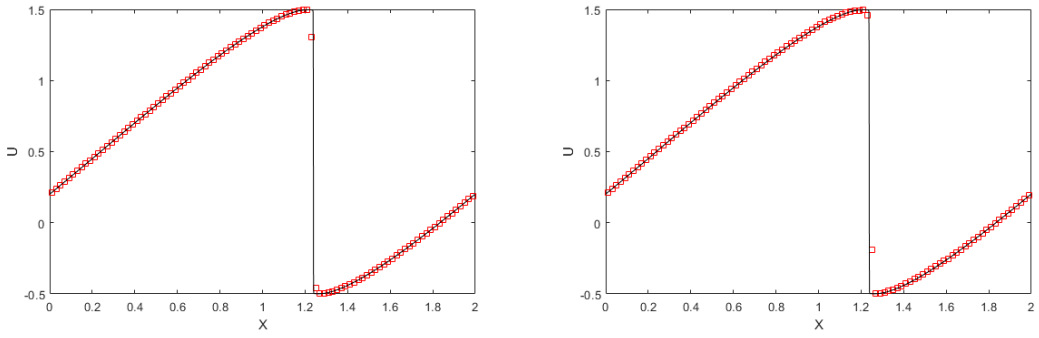


(a) WENO-Z scheme




(b) MOOD (P4-P2-P0)

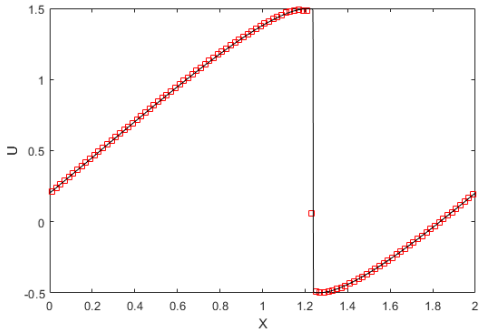


(c) MOOD (P4-P2-TH, $\beta = 1.6$)

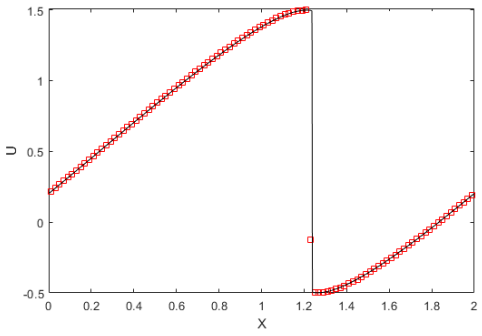


(d) MOOD (P4-P2-TH, $\beta = 2.4$)

Figure 2.4: Numerical solutions for Burger's equation with sine wave initial condition on a 100-grid cells until $t = 1.5/\pi$. – solid line: Exact solution, symbol: Numerical solution.

#### 2.4.1.3 Buckley Leverett equation

one-dimensional of Buckley Leverett equation is defined as

$$\frac{\partial U}{\partial t} + \frac{\partial F(U)}{\partial x} = 0, \tag{2.18}$$

where

$$F(U) = \frac{4U^2}{4U^2 + (1-U)^2}. \tag{2.19}$$

The initial condition is set as

$$U(x,0) = \begin{cases} 1 - 3x, & 0 \leq x \leq 1/3, \\ 0, & \text{otherwise.} \end{cases} \tag{2.20}$$

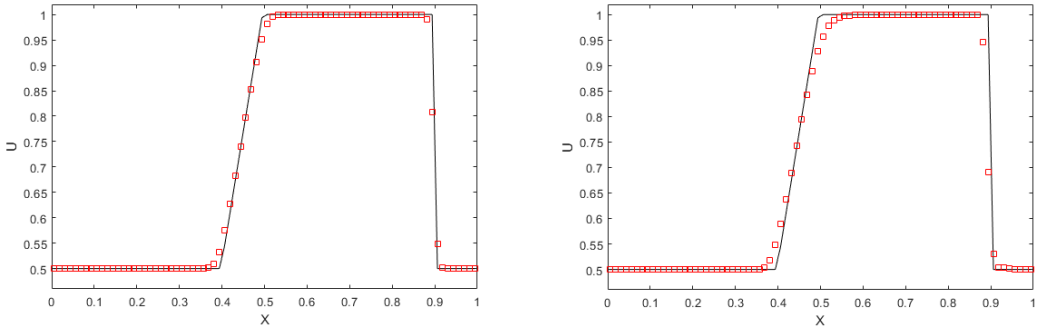


(a) WENO-Z scheme




(b) MOOD (P4-P2-P0)

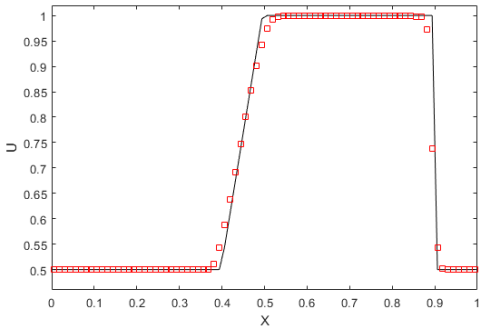


(c) MOOD (P4-P2-TH, $\beta = 1.6$)

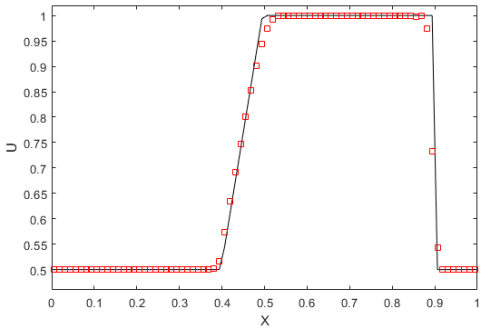


(d) MOOD (P4-P2-TH, $\beta = 2.4$)

Figure 2.5: Numerical solutions for Burger's equation with square-pulse initial condition on a 80-cell grid at $t = 0.2$. – solid line: Exact solution, symbol: Numerical solution.

The numerical results are shown in Fig. 2.6 executed the computation up to time $t = 0.2$ on a 80-cell grid. We can observe that all schemes provide a high resolution with such a low grid number. Furthermore, WENO-Z scheme and MOOD (P4-P2-P0) scheme capture the shock by nearly 2 cells while MOOD (P4-P2-TH) scheme can produce nearly 1 cells. However, for MOOD schemes still produce a little oscillation at first start of contact discontinuity and near the shock.

### 2.4.2 Euler equations

The Euler equations of compressible gas dynamics consist of conservation laws of mass, momentum and total energy.

The Euler equations in one-dimensional are expressed as following

$$\frac{\partial U}{\partial t} + \frac{\partial F(U)}{\partial x} = 0, \quad t \geq 0, \quad x \in \mathbb{R} \tag{2.21}$$

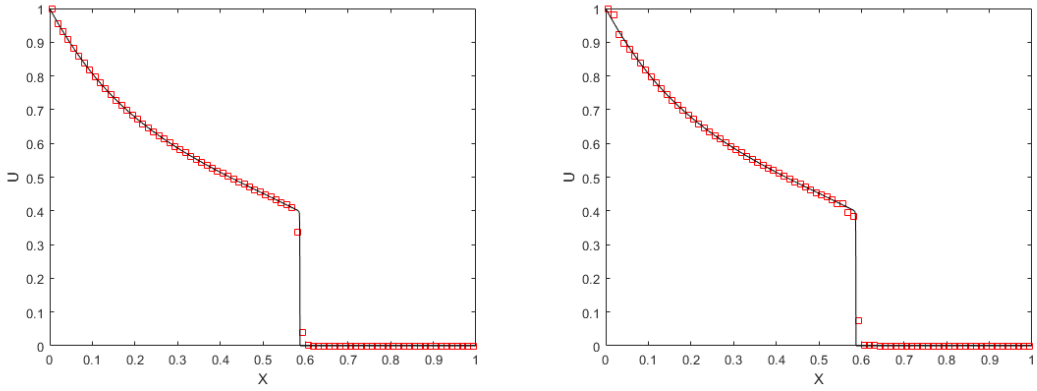


(a) WENO-Z scheme




(b) MOOD (P4-P2-P0)

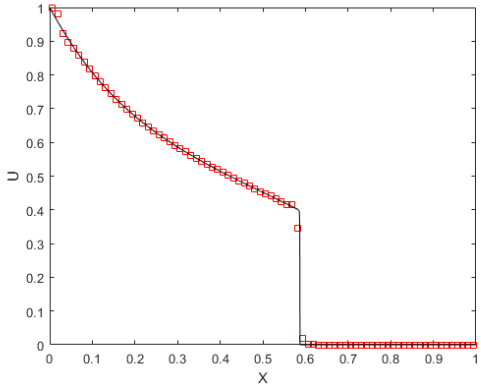


(c) MOOD (P4-P2-TH, $\beta = 1.6$)

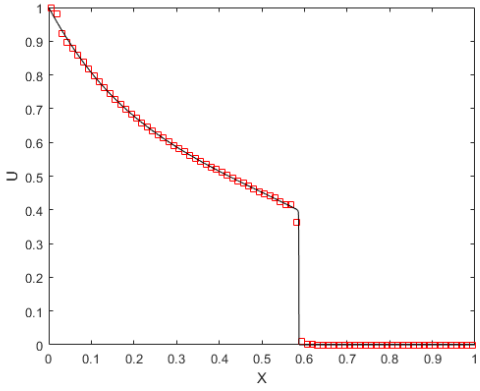


(d) MOOD (P4-P2-TH, $\beta = 2.4$)

Figure 2.6: Numerical solutions for Burger's equation with square-pulse initial condition on a 80-cell grid at $t = 0.2$. – solid line: Exact solution, symbol: Numerical solution.

where

$$\mathbf{U}(x,t) = \begin{pmatrix} \rho \\ \rho u \\ E \end{pmatrix}, \quad \mathbf{F}(\mathbf{U}) = \begin{pmatrix} \rho u \\ \rho u^2 + p \\ u(E+p) \end{pmatrix} \tag{2.22}$$

Here $\rho$, $u$, $p$ are the density, velocity, and pressure, respectively. $E$ is the total energy expressed as $E = e + \frac{1}{2}\rho u^2$ and $e$ is the specific internal energy. For ideal gas, the pressure can be computed by the equation of state (EOS) is defined as $p = (\gamma - 1)\rho e$ where $\gamma$ is the ratio of specific heats, and set $\gamma = 1.4$ for numerical tests in this work. The total enthalpy is computed by $H = (E + p)/\rho$.

For Euler equations, the MOOD algorithm is described as follows.

1. Firstly, check each cell for primitive variables (fluid properties) such as density $\rho$

and pressure $p$ with the physical admissible detection (PAD) criterion.

$$\rho_i^* > 0 \quad \text{and} \quad p_i^* > 0 \tag{2.23}$$

If $\rho_i^*$ and/or $p_i^*$ are not satisfied Eq.(2.23) then the degree of polynomial is decremented and recomputed simultaneously its neighbor cells. Otherwise, the valid cell continues for checking the numerical admissible detection (NAD) criterion.

2. At this stage, the candidate numerical solution is checked by the numerical admissible detection (NAD). The first criterion of NAD is discrete maximum principle (DMP) for the density of each solution cell $I_i$ as

$$\min_{j\in\bar{v}(i)} \left(\rho_i^n, \rho_j^n\right) \leq \rho_i^* \leq \max_{j\in\bar{v}(i)} \left(\rho_i^n, \rho_j^n\right) \tag{2.24}$$

3. If $\rho_i^*$ does not satisfy the DMP Eq.(2.24), then check with the $u2$ process criterion

   (a) Compute $\chi_i$ and $\chi_j$ for $i, j \in \bar{v}(i)$, where $\chi_i = \partial_{xx}\widetilde{\rho}_i$ and $\widetilde{\rho}_i = \widetilde{\rho}_i(x; 2)$

   (b) Now, $\rho_i^*$ is checked by detector Eq.(2.8). If $\rho_i^*$ is satisfied, set $U_i^{n+1} = U_i^*$ as a solution for next time step, otherwise $U_i^*$ is recomputed by decrementing degree of local polynomial reconstruction, where $U = (\rho, \rho u, E)$.

   (c) Check detector Eq.(2.9). If $\rho_i^*$ is not smooth extrema then $\mathrm{d_i}$ of the polynomial is decremented, otherwise $U_i^*$ is valid and set $U_i^{n+1} = U_i^*$ as a solution for next time step.

We perform the numerical results of two benchmark tests for 1D Euler equations to verify our proposed scheme with Rusanov Riemann solver in [87]. For MOOD algorithm, we implement the primitive variable reconstruction.

For instance, we simulate the 1D planar Sod shock tube problem and the classical Lax shock tube problem to assess the ability of the schemes to capture simple waves and suppress numerical oscillations.

**SOD's problem:** The initial condition is given by

$$(\rho_0, u_0, p_0) = \begin{cases} (1, 0, 1), & 0 \leq x \leq 0.5, \\ (0.125, 0, 0.1), & \text{otherwise.} \end{cases} \tag{2.25}$$

The Fig. 2.7 shows the results computed by WENO-Z, MOOD (P4-P2-P0) and MOOD (P4-P2-TH, $\beta = 1.6$) schemes at time $t = 0.25$ with 100-cell mesh for comparison. We observe that WENO-Z scheme with primitive variables reconstruction produces an overshoot and an undershoot in the vicinity of contact discontinuity and overshoot in the front of expansion fan while WENO-Z scheme with characteristic variable reconstruction gives a smooth solution for whole computational domain. For MOOD (P4-P2-P0) also gives the smooth solution but it produces numerical diffusion for the contact discontinuity region by nearly 6 cells. Furthermore, MOOD (P4-P2-TH, $\beta = 1.6$) can resolve better the con-tact discontinuity with only 4 cells while other schemes have nearly 6 cells but it produces an undershoot at the tail of expansion fan.

**Lax's prolem:** The initial condition is given by

$$(\rho_0, u_0, p_0) = \begin{cases} (0.445, 0.698, 3.528), & -1 \leq x \leq 0, \\ (0.5, 0, 0.571), & \text{otherwise.} \end{cases} \tag{2.26}$$

We demonstrate the numerical results at time $t = 0.16$ over computational domain $\Omega = [-1, 1]$ computed by WENO-Z scheme, MOOD (P4-P2-P0) and MOOD (P4-P2-TH, $\beta = 1.6$) in Fig. 2.8 for comparison. It is observed that both WENO-Z scheme on primitive variables and WENO-Z scheme on characteristic variables can capture sharply the contact discontinuity and high accuracy for smooth profile of the rarefaction wave but an oscillation produced by WENO-Z scheme on primitive variables. MOOD (P4-P2-P0) can resolve with non-oscillation behavior that is equivalent to WENO-Z scheme on characteristic variables but it cannot achieve high accuracy for smooth profile and gives numerical dissipation for the contact discontinuity by nearly 7 cells and 3 cells for the shock. MOOD (P4-P2-TH, $\beta = 1.6$)) can resolve sharply the contact discontinuity

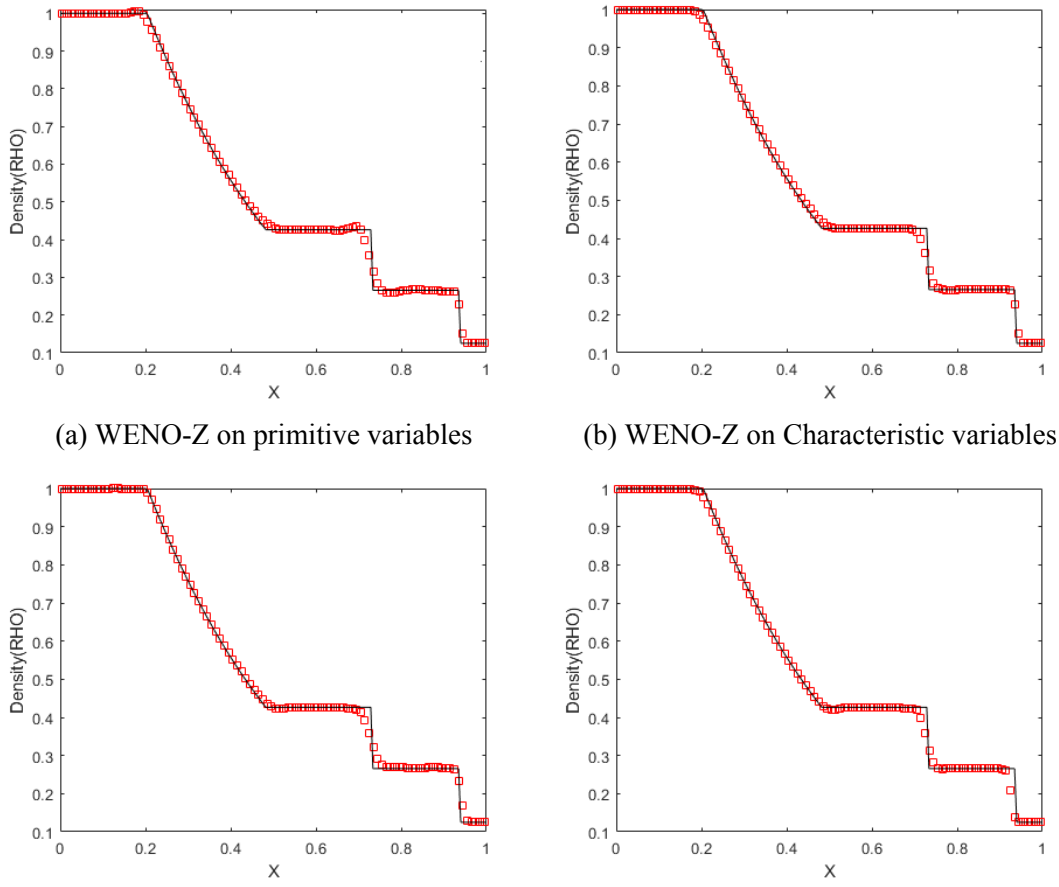


(a) WENO-Z on primitive variables

(b) WENO-Z on Characteristic variables

(c) MOOD (P4-P2-P0)

(d) MOOD (MOOD (P4-P2-TH, $\beta = 1.6$)

Figure 2.7: Numerical results of SOD's problem at time $t = 0.25$ with 100 cells. – solid line: Exact solution, symbol: Numerical solution.

equivalent to WENO-Z scheme on characteristic variables and can better capture the shock only 2 cells but produces an undershoot at the tail of rarefaction wave.

## 2.5 Summary

We have proposed a novel scheme in MOOD algorithm under finite volume framework to solve hyperbolic conservation laws including both smooth and discontinuous solution profiles. Being *a posteriori* MOOD-THINC approach, the proposed scheme is essentially non-oscillatory and of high accuracy. Following the MOOD algorithm, the solution is detected with prescribed MOOD criterion. If the cell is detected as problematic cell, we re-compute the solution by decrementing the degree of polynomial reconstructions. In proposed approach, the first order scheme is replaced by monotonic THINC

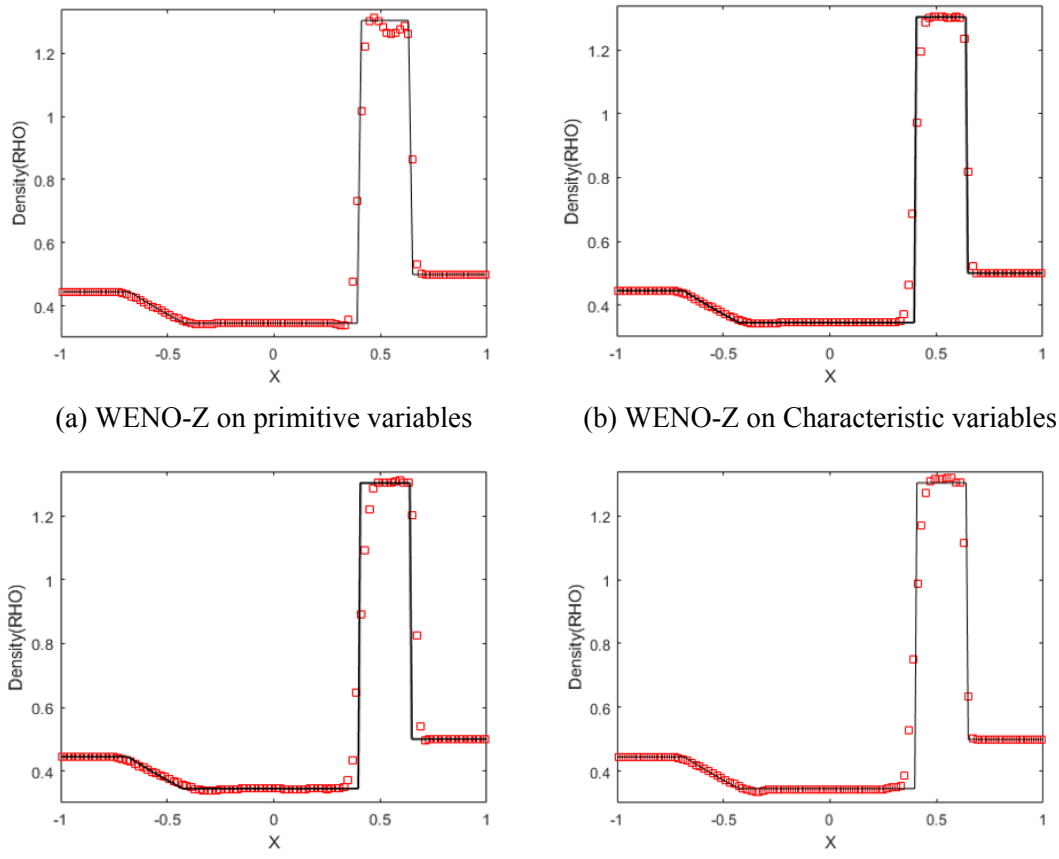


(a) WENO-Z on primitive variables

(b) WENO-Z on Characteristic variables

(c) MOOD (P4-P2-P0)

(d) MOOD (MOOD (P4-P2-TH, $\beta = 1.6$)

Figure 2.8: Numerical results of Lax's problem at time $t = 0.16$ with 100 cells. – solid line: Exact solution, symbol: Numerical solution.

function to increase the accuracy at discontinuities.

The numerical simulations show that the proposed scheme can maintain high-order accuracy gained by polynomial-based reconstruction in smooth profile and capture discontinuous solution without spurious oscillation and with less numerical dissipation.

# Chapter 3

# Solution property preserving reconstruction: BVD+MOOD scheme

## 3.1 Introduction

In finite volume framework, several issues are appeared in high-order shock-capturing methods such as numerical oscillations, excessive numerical dissipation when dealing with problems involving strong discontinuities, and, safe-failure of positivity-preserving when solving problems involving vacuum or near vacuum states.

For instace, some classical high-order schemes [3, 56, 86, 93, 94] fail to preserve the positivity (or to maintain the physical validity of the solution) because of interpolation errors in the vicinity of very strong discontinuities or when vacuum or near vacuum states occur. On the other hand, the first-order finite volume so-called Godunov scheme [42, 108] has an excessive numerical dissipation and tends to smear out flow structures. Nonetheless, the Godunov scheme is monotone, robust, and preserves the positivity. Recently, Zhang and Shu developed some positivity-preserving strategy to be supplemented with discontinuous Galerkin (DG) [127, 129], finite volume/difference WENO scheme [128]/[130] by employing a flux limiter with a restriction on the CFL number. Other approaches based on Flux Corrected Transport (FCT) [74], cut-off limiters, bound-preserving strategy [121] or alternative techniques are also available.

Following a different path, the Multi-dimensional Optimal Order Detection (MOOD)

approach is an *a posteriori* limiting scheme which was proposed in [22, 34, 36], and further used for different families of schemes: DG context [35, 112], Lagrangian and Arbitrary-Lagrangian-Eulerian schemes [14, 15], or for other physical contexts apart from pure Euler equations, such as Shallow-water equation [23], compressible turbulence models [58], hyperbolic systems with stiff source terms [12], Navier-Stokes equations [110], etc.

The main idea in a MOOD-like algorithm consists in computing a candidate numerical solution at the next time level. The MOOD algorithm picks out the bad cells from the good ones, and re-compute the bad ones using a more dissipative scheme. A cell for which the criterion of physical admissible detection (PAD) and numerical admissible detection (NAD) are satisfied, then it is accepted for the next time step. Otherwise, if a cell does not satisfy the criteria, it is marked as problematic and re-computed by 'decrementing' the degree of the local reconstruction polynomials, expecting that a lower order scheme will deposit more dissipation in the troubled cells. This process of decrementing the local polynomial degree continues up to the cell becomes valid, or, when the lowest order possible reconstruction is attained (piece-wise constant is usually the last possibility).

Using polynomial reconstructions in an FV context is the ultra classical path followed by the majority of researchers to reach high accurate FV schemes. However, when discontinuous or step-like solutions are encountered, such polynomial reconstructions become inefficient, or, worse, counterproductive. For several years, in order to capture such discontinuous solutions, some researchers rely on the Tangent of Hyperbola INterface Capturing (THINC) method which mimics a step-like function, see for instance [99, 118, 119]. Later on THINC has been used in a so-called Boundary Variation Diminishing (BVD) algorithm proposed in [103]. The purpose is to hybridize a WENO polynomial reconstruction with THINC functions. The BVD principle consists in appropriately selecting between these reconstructions. The diagnostics used by the BVD algorithm to select the appropriate reconstructions rely on minimizing the jump between the reconstructed values at the cell boundary. The BVD schemes are then capable to resolve both discontinuous and smooth solutions with high fidelity, see for instance

[29, 32, 103]. In more recent works [30, 31], new BVD schemes have been proposed by combining high-order linear-weight (constant-coefficient) polynomials and THINC function with multi-stage BVD algorithms. The resulting schemes, so-called $P_nT_m$-BVD (polynomial of n-degree and THINC function of m-level reconstruction based on BVD algorithm) schemes, are completely different from any existing high-resolution scheme that counts on nonlinear-weights polynomials to suppress spurious oscillations. Numerical verification shows that the $P_nT_m$-BVD schemes are able to achieve very high order accuracy for smooth solution, and effectively remove numerical oscillation in presence of discontinuity. As shown in [30], for example, a 11th order scheme can be devised by using the 10th order polynomial as one of the candidate for reconstruction.

In this chapter, we present a general formulation of reconstruction in finite volume method by integrating the BVD and MOOD methodologies. As a concrete example, we propose a high-resolution scheme under a three-stage cascade BVD algorithm and MOOD method to fulfill the shock capturing and positivity-preserving properties. For BVD reconstruction algorithm, the linear 5th order upwind or piece-wise quartic method based on 4th-degree of polynomial (P4) is implemented as one of the candidate reconstruction functions to capture smooth solutions. Other candidate reconstruction functions use THINC function to eliminate the numerical oscillation and to capture sharply all discontinuities. Furthermore, a MOOD algorithm performs and detects a candidate solution by physical admissible detection (PAD) ensuring as such the positivity-preserving property. In this work, we demonstrate the effectiveness of P4-THINC-BVD-MOOD scheme, or $P_4T_3$-BVD-MOOD scheme, in resolving smooth solution, capturing sharp discontinuous solution and preserving positivity via some benchmark tests. The numerical results of present scheme show superior solution quality competitive to other existing high-order shock-capturing schemes as well as high-order positivity-preserving schemes.

## 3.2 Numerical algorithm

For the sake of simplicity, we introduce the numerical method thoroughly in $d = 1$ dimension. Its extension to multi-dimensions, here $d = 2$, carried on by dimension splitting, is presented in a next section. Let us describe the finite volume method, the reconstruction schemes and the positivity-preserving process in the following sections.

### 3.2.1 Finite Volume semi-discretization

Let us consider a scalar hyperbolic conservation law under the form

$$\frac{\partial U}{\partial t} + \frac{\partial F(U)}{\partial x} = 0, \tag{3.1}$$

where $U(x,t)$ is the solution variable and $F(U)$ is the flux function. Because Eq.(3.1) is hyperbolic, the characteristic speed $\alpha = F'(U)$ is a real number in 1D.

The computational domain in space is defined as $\Omega = [x^L, x^R]$ and divided into $N$ cells, $I_i = [x_{i-1/2}, x_{i+1/2}]$, for $i = 1, 2, ..., N$. The grid size is uniform over the computational domain and denoted by $\Delta x = x_{i+1/2} - x_{i-1/2}$. The time coordinate is $t$ and $0 \leq t \leq T$, where $T > 0$ is the final time. The time interval $[0, T]$ is split into $N_t$ time steps $[t^n, t^{n+1}]$, the time-step is non-uniform and denoted by $\Delta t = t^{n+1} - t^n > 0$, with $t^0 = 0$ and $t^{N_t} = T$.

For the standard finite volume semi-discretization, we employ the approximated volume integrated-average (VIA) of the solution $U(x,t)$ over a mesh cell $I_i$ at time $t$ as

$$U_i(t) = \frac{1}{\Delta x} \int_{x_{i-1/2}}^{x_{i+1/2}} U(x,t)\, dx \qquad \text{where} \qquad i = 1, 2, \ldots, N. \tag{3.2}$$

Let us denote by $\mathsf{U} = (U_i)_{i=1,2,...,N}$ the vector of discrete FV data in the mesh.

The VIA $U_i(t)$ for each cell $I_i$ is updated by

$$\frac{dU_i}{dt} = -\frac{1}{\Delta x}\left(\widetilde{F}_{i+1/2}(t) - \widetilde{F}_{i-1/2}(t)\right), \tag{3.3}$$

where $\widetilde{F}_{i+1/2}(t)$ and $\widetilde{F}_{i-1/2}(t)$ are the numerical fluxes at cell boundaries, calculated by a Riemann Solver

$$\widetilde{F}_{i+1/2}(t) = F^{\text{Riemann}}_{i+1/2}(U^L_{i+1/2}, U^R_{i+1/2}, t), \tag{3.4}$$

where $U^L_{i+1/2}$ and $U^R_{i+1/2}$ are the left-side and right-side values at cell boundaries respectively, given by reconstructions over left and right support stencils. Particularly, the Riemann flux can be written into a canonical form as

$$F^{\text{Riemann}}_{i+1/2}(U^L_{i+1/2}, U^R_{i+1/2}, t) = \underbrace{\frac{1}{2}\left(F(U^L_{i+1/2}) + F(U^R_{i+1/2})\right)}_{\text{Central flux}} - \underbrace{\frac{|a_{i+1/2}|}{2}(U^R_{i+1/2} - U^L_{i+1/2})}_{\text{Dissipation}}, \tag{3.5}$$

where $a_{i+1/2}$ is a characteristic speed linked to the maximal eigenvalue of the hyperbolic conservation law. In this work a classical HLLC flux is employed [108] but any approximate Riemann solver could be employed.

A reconstruction procedure is used to calculate $U^L_{i+1/2}$ and $U^R_{i+1/2}$ at given time $t$, we denote by $\mathcal{R}_i \equiv \mathcal{R}(\mathsf{U}, S_i)$ the reconstruction operator in cell $I_i$ which, given the discrete solution $\mathsf{U}$ and a stencil $S_i$ of neighbor cells provides a function in $I_i$. This reconstructed function is further evaluated at boundary points $x_{i\pm1/2}$ to get $U^L_{i+1/2} = \mathcal{R}_i(x_{i+1/2})$ and $U^R_{i-1/2} = \mathcal{R}_i(x_{i-1/2})$ at time $t$.

### 3.2.2 Time integration

In order to improve the temporal accuracy for Eq.(3.3), the full discretization is obtained by employing a fourth-order strong stability preserving Runge-Kutta (SSPRK) developed by Ruuth and Speteri [43, 88, 101]. Defining

$$L(U) = -\frac{1}{\Delta x}\left(\widetilde{F}_{i+1/2}(t) - \widetilde{F}_{i-1/2}(t)\right), \tag{3.6}$$

then the time integration is given by

$$
\begin{aligned}
U^{(1)} &= U^n + 0.391752226571890\Delta t L(U^n),\\
U^{(2)} &= 0.444370493651235U^n + 0.555629506348765U^{(1)} + 0.368410593050371\Delta t L(U^{(1)}),\\
U^{(3)} &= 0.620101851488403U^n + 0.379898148511597U^{(2)} + 0.251891774271694\Delta t L(U^{(2)}),\\
U^{(4)} &= 0.178079954393132U^n + 0.821920045606868U^{(3)} + 0.544974750228521\Delta t L(U^{(3)}),\\
U^{n+1} &= 0.517231671970585U^{(2)} + 0.096059710526147U^{(3)} + 0.063692468666290\Delta t L(U^{(3)})\\
&+ 0.386708617503269U^{(4)} + 0.226007483236906\Delta t L(U^{(4)}).
\end{aligned}
\tag{3.7}
$$

In this work we design a Solution Property Preserving Reconstruction operator by introducing a blending of high/low order polynomials and hyperbolic tangent reconstructions.

In figure 3.1 we sketch the principal steps of such an FV scheme, that is the Reconstruction operator, the flux computation and the Runge-Kutta iterative method. In this

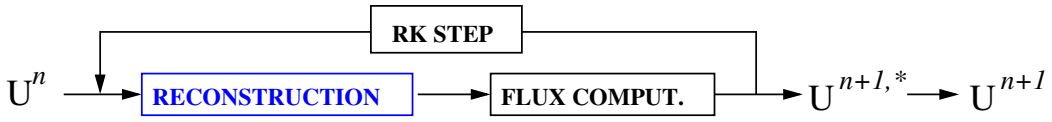


Figure 3.1: Sketch of the finite volume scheme with the reconstruction operator, the flux computation and the Runge-Kutta iterative method.

chapter, when Euler system of partial differential equations are considered, then the reconstructions are performed on the characteristics variables called $W_1, W_2, W_3$ linked to the three real eigenvalues $\lambda_1 = u - c$, $\lambda_2 = u$ and $\lambda_3 = u + c$, respectively.

## 3.3 Solution property preserving reconstruction

During the simulation of a hyperbolic system of partial differential equations, one generally observes large zones where the solution is regular, some discontinuities, usually of dimension $d - 1$, possibly in interaction, and, few and small but extremely demanding regions for which the correct physics is difficult to capture. These regions are the places where we have to resort numerical simulation to get an idea of the true physical solution, usually too complex to be derived as an analytical solution. Ideally, the regular zones should be resolved with an unlimited high accurate scheme, for instance, using

a piece-wise high order polynomial reconstruction. The discontinuous zones demand the use of a numerical method that can capture the discontinuity in a sharp manner and at the same time is free from spurious oscillations like a TVD 2nd order FV scheme. At last, the demanding regions of the flow can usually be dealt only with a genuinely dissipative scheme, the first order Godunov scheme being one of such representatives.

All of those regions are intimately related to some properties of the numerical solution which should be preserved by the numerical scheme:

- High accuracy in regular zones $\longrightarrow$ Accuracy on smooth profile.
- Free from spurious oscillation close to steep gradient $\longrightarrow$ Non oscillatory behavior.
- Sharp capture of discontinuity $\longrightarrow$ Accuracy on discontinuous profile.
- Robustness for extreme situations $\longrightarrow$ Fail-safe behavior

Therefore given the data $\mathsf{U}^n$, the reconstruction operator should provide a reconstructed function in each cell which does generate (after the flux evaluation and the solution update) a numerical solution $\mathsf{U}^{n+1}$ fulfilling with the previously list of properties. We can see this problem of reconstruction as a chained cascade of different reconstruction operators. We call them $\mathcal{R}_{\text{HO}}$ for high order reconstruction, $\mathcal{R}_{\text{ENO}}$ for essentially non-oscillatory reconstruction, $\mathcal{R}_{\text{SHARP}}$ for sharp reconstruction, see figure 3.2. A key tool is the so-called 'selector'. The selector chooses which reconstruction is the most appropriate one in a given cell. For instance, if the solution is smooth, the selector should select $\mathcal{R}_{\text{HO}}$ reconstruction, while, in the case of a step function/shock or steep gradient, then $\mathcal{R}_{\text{SHARP}}$ must be selected. Such a selector is a key point because it drives the reconstructions and, as a consequence, the numerical dissipation of the numerical method, then its accuracy. In this work the selector is acting given two candidate reconstructions in a cell, and chooses only one. Because we consider three different reconstructions, then two selectors are operating in cascade, see figure 3.2. Let us first present the reconstruction operators $\mathcal{R}_{\text{HO}}$, $\mathcal{R}_{\text{ENO}}$, $\mathcal{R}_{\text{SHARP}}$. Then the selector will be described.

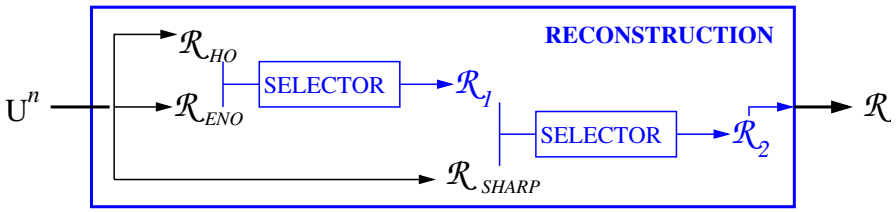


Figure 3.2: Illustration of the Solution Property Preserving Reconstruction. $\mathcal{R}_{\text{HO}}$ is high order reconstruction operator, $\mathcal{R}_{\text{ENO}}$ is an essentially non-oscillatory one, $\mathcal{R}_{\text{SHARP}}$ is a sharp one. First the selector chooses between HO and ENO to get reconstruction number 1. Then the selector picks either reconstruction 1 or SHARP to get reconstruction number 2.

### 3.3.1 $\mathcal{R}_{\text{HO}}$: $\mathbb{P}_4$ unlimited polynomial reconstruction

To achieve higher accuracy in space, piece-wise polynomial reconstructions were developed within FV schemes. For instance, the piece-wise parabolic method (PPM) developed in [27, 54, 70] achieves the third-order accuracy. Similarly to PPM, the fifth-order accuracy scheme based on piece-wise polynomial of degree four (P4), known as piece-wise quartic method (PQM) was proposed for instance in [116]. In this work we adopt the PQM reconstruction by selecting one central stencil made of five cells surrounding the current one, see figure 3.3, the stencil $S_i$ is therefore constituted of cell indexes $i+k$ with $k = -2, \ldots, 2$. The reconstruction values at the left and right cell boundary are denoted as $U^{L,P4}_{i+1/2}$ and $U^{R,P4}_{i-1/2}$ respectively and are up-winded via the formula

$$\begin{aligned} U^{L,P4}_{i+1/2} &= \frac{1}{60}\left(2\,U_{i-2} - 13\,U_{i-1} + 47\,U_i + 27\,U_{i+1} - 3\,U_{i+2}\right) \\ U^{R,P4}_{i-1/2} &= \frac{1}{60}\left(-3\,U_{i-2} + 27\,U_{i-1} + 47\,U_i - 13\,U_{i+1} + 2\,U_{i+2}\right) \end{aligned} \tag{3.8}$$

This reconstruction is high accurate (5th order on smooth enough profiles in 1D) and, unfortunately, oscillatory when steep gradients are encountered.

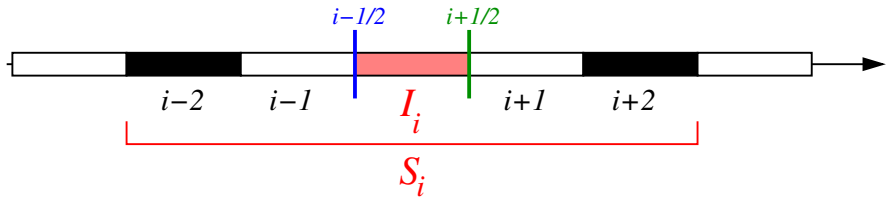


Figure 3.3: Stencil selection for the right/left interface $i \pm 1/2$

### 3.3.2 $\mathcal{R}_{\mathbf{LO}}$: no reconstruction/$\mathbb{P}_0$ polynomial

When considering no reconstruction, i.e. $\mathbb{P}_0$ 'reconstruction', we set $U_{i+1/2}^{L,P0} = U_{i-1/2}^{R,P0} = U_i$. Such values lead to a first order FV scheme. Although it is a low accurate scheme, it presents nonetheless an extremely robust behavior. We are using this scheme as the last resort when extreme situations are encountered, such as a lack of positivity for Euler equations, occurrence of NaN, etc. see Section 3.3.4. Obviously in this case the stencil $S_i$ is made by only cell $I_i$.

### 3.3.3 $\mathcal{R}_{\mathbf{ENO}}$, $\mathcal{R}_{\mathbf{SHARP}}$: THINC reconstruction with $\beta \leq 1.2$ or $\beta \geq 1.6$

THINC stands for Tangent Hyperbola for INterface Capturing method, which is originally a volume of fluid (VOF) scheme employing the hyperbolic tangent function for spatial reconstruction. Being a sigmoid, differentiable and monotone function, hyperbolic tangent function mimics a step-like discontinuity. In the case of strictly increasing or decreasing set of values $(U_{i-1}, U_i, U_{i+1})$ then the THINC function can be expressed as [103, 118] in $I_i$ as

$$q_i(x) = U_{\min} + \frac{[\![U]\!]}{2}\left[1 + \theta \tanh\left(\beta\left(\frac{x - x_{i-1/2}}{x_{i+1/2} - x_{i-1/2}} - \widetilde{x}_i\right)\right)\right], \tag{3.9}$$

where $U_{\min} = \min(U_{i-1}, U_{i+1})$, $[\![U]\!] = \max(U_{i-1}, U_{i+1}) - U_{\min}$ and $\theta = \mathrm{sgn}(U_{i+1} - U_{i-1})$. The parameter $\beta$ is used for controlling the slope and the jump thickness, i.e. if $\beta$ has a value close to zero then the profile $q_i$ converges towards the average value of $\frac{U_{i-1}+U_{i+1}}{2}$ while, if $\beta$ is large, it tends to be a step-like function, see figure 3.4. In Eq.(3.9), the only remaining unknown, $\widetilde{x}_i$, which presents the relative location of jump center in the cell, is calculated by solving the constraint condition $U_i = \frac{1}{\Delta x}\int_{I_i} q_i(x)\,dx$. The reconstructed values at left and right ends of cell boundary are given by

$$\begin{aligned} U_i^L(x_{i+1/2}) &= q_i(x_{i+1/2}) = U_{min} + \frac{[\![U]\!]}{2}\left(1 + \theta\frac{\tanh(\beta) + A}{1 + A\tanh(\beta)}\right) \\ U_i^R(x_{i-1/2}) &= q_i(x_{i-1/2}) = U_{min} + \frac{[\![U]\!]}{2}(1 + \theta A) \end{aligned}$$

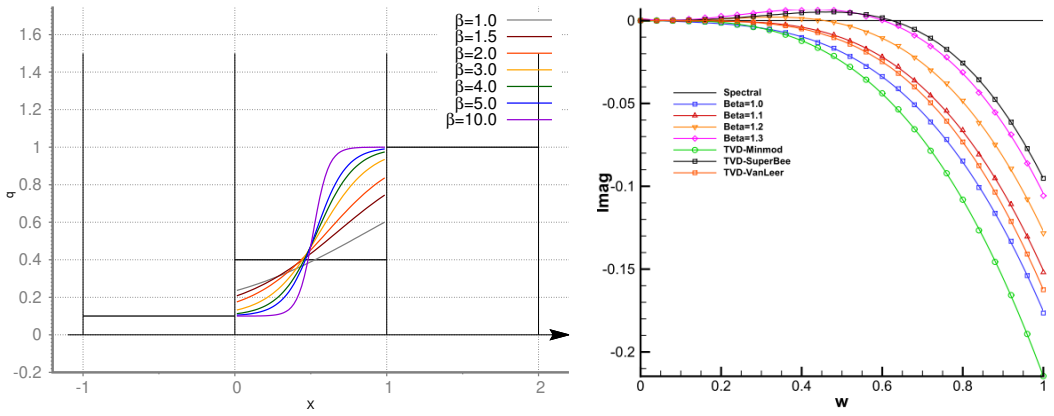


Figure 3.4: Left panel: Examples of THINC reconstruction $q_i(x)$ as a function of $\beta$ for $\bar{q}_i = 0.4$ case over unit-length cell — Right panel: Imaginary parts of modified wave-number from THINC schemes with $\beta = 1, 1.1, 1.2$, and $1.3$. The results for some TVD schemes limited with minmod, van Leer or superbee slope limiter are also displayed. (The picture focuses on small wave-numbers.)

where $A = \frac{1}{\tanh(\beta)}\left(\frac{B}{\cosh(\beta)} - 1\right)$, $B = e^{\theta\beta(2C-1)}$ and $C = \dfrac{U_i - U_{min} + \epsilon}{[\![U]\!] + \epsilon}$ with $\epsilon = 10^{-20}$ to avoid division by zero. We denote by $U^{L,Th\beta}_{i+1/2} = U^L_i(x_{i+1/2})$ and $U^{R,Th\beta}_{i-1/2} = U^R_i(x_{i-1/2})$ the reconstruction values for THINC's candidate interpolation function with $\beta$ parameter.

**Remark 1.** The THINC reconstruction stencil $S_i$ is constituted by the direct neighbors, i.e. $I_{i-1}$ and $I_{i+1}$, which are only used for the computation of min and max bounds.

**Remark 2.**: In the case of $U_i$ is out of the bound of $\min(U_{i-1}, U_{i+1})$ and $\max(U_{i-1}, U_{i+1})$, which means that $U_i$ is a local extremum and $U_i = \frac{1}{\Delta x}\int_I q_i(x)dx$ does not hold, we simply set $q_i(x) = U_i$ for all $x \in I_i$. This could be improved even further by employing a parabolic reconstruction for instance.

**Remark 3.** Notice that an alternative form of Eq.(3.9) is

$$q_i(x) = \overline{U}_i + \frac{U_{\max} - U_{\min}}{2}\tanh\left(\beta\left(\frac{x - x_{i-1/2}}{x_{i+1/2} - x_{i-1/2}} - \widetilde{x}_i\right)\right), \tag{3.10}$$

from which the convergence toward $\overline{U}_i$ when $\beta$ tends to 0 is evident.

**$\mathcal{R}_{\text{ENO}}$: THINC reconstruction with $\beta \leq 1.2$:** In order to avoid oscillatory behavior we employ THINC reconstructions with small values of parameter $\beta$. More precisely we use $\beta = 1.2$ or $\beta = 1.1$ which are small enough values corresponding, more or less,

to the same dissipation as a 2nd order TVD FV scheme with either the van Leer slope limiter or the Minmod one respectively. The operator are respectively denoted by $\mathcal{R}^2_{\text{ENO}}$ and $\mathcal{R}^1_{\text{ENO}}$. The FV schemes associated to these operators $\mathcal{R}_{\text{ENO}}$ are therefore close to classical 2nd order TVD numerical schemes. In other words, the FV schemes generated by $\mathcal{R}_{\text{ENO}}$ reconstructions are relatively low accurate but (essentially) non-oscillatory.

In order to justify this statement, we apply the approximate dispersion relation (ADR) analysis described in [82] to the THINC scheme with different wave numbers $w$. The numerical dissipation is quantified through the imaginary parts of the modified wave number and the results are shown on the right-panel of figure 3.4. Beyond $\beta \simeq 1.1$ the numerical scheme presents an anti-dissipative behavior. In order to compare with other popularly TVD schemes, we also show the numerical dissipation of the 2nd order FV scheme with Minmod, Van Leer and Superbee limiters [66]. THINC scheme with $\beta = 1.1$ has a much smaller numerical dissipation than the TVD scheme employing the Minmod limiter. It presents a similar or slightly better performance than the scheme with Van Leer limiter. THINC schemes with larger parameters $\beta = 1.2$ (or $1.3$) have a similar spectral property compared to the TVD method with the Superbee limiter. They both show a positive imaginary part at low wave number band leading to the well-known staircase/squaring effect [82] on the solution profile. For the purpose of designing an essentially non-oscillatory scheme it is reasonable to choose THINC reconstructions with $\beta = 1.2$ and possibly $\beta = 1.1$ for a more important dissipation.

**$\mathcal{R}_{\text{SHARP}}$: THINC reconstruction with $\beta \geq 1.6$:** The last THINC reconstruction operator in this paper uses $\beta = 1.6$ to capture sharper discontinuous profiles by employing the staircase/squaring behavior. The associated scheme to the reconstruction operator $\mathcal{R}_{\text{SHARP}}$ is therefore anti-dissipative, leading to staircase shapes even for smooth profiles.

### 3.3.4 Robustness and physical admissibility via an *a posteriori* MOOD procedure

The last property corresponds to the ability of the numerical method to handle extreme physical and numerical situations, for instance the lack of positivity for density or en-

ergy for Euler equations or the occurrence of Not-A-Number (NaN) value, etc. None of the previous reconstruction procedures can ensure neither the positivity nor a fail-safe behavior. For this matter we employ the so-called *a posteriori* Multi-dimensional Optimal Order Detection (MOOD) procedure. In a MOOD algorithm, a candidate solution at time $t^{n+1}$ is tested against several goodness criteria (physical or numerical). This detection procedure separates the cells into 'valid' ones for which the numerical solution is accepted, and, 'troubled' ones. The troubled cells are locally recomputed with a first-order Godunov scheme, that is employing no reconstruction (i.e. a $\mathbb{P}_0$ polynomial). This first-order finite volume method has an excessive numerical dissipation and tends to smear out cell flow structures. However, it is known to be monotone, robust and positivity-preserving. Therefore, this scheme should be used only as a last resort. The detection criteria are split into a Physical Admissible Detection (PAD) and a Numerical Admissible Detection (NAD)

$$\text{Detect:} \qquad \text{PAD}(U_i^{n+1,*}), \qquad \text{and} \qquad \text{NAD}(U_i^{n+1,*}), \tag{3.11}$$

where $*$ denotes the fact that the solution is not the final one, but only a candidate solution. A cell is marked as NAD troubled if, for instance, $U_i^{n+1,*} = \texttt{NaN}$, otherwise the cell is valid. In the case of Euler equations, a cell is PAD troubled if $U_i^{n+1,*} \leq 0$ with $U = \rho$, the density or $\varepsilon$ the specific internal energy. This corresponds to ensuring the physical admissibility of the solution for Euler equations. In the case of a linear advection equation a cell is PAD troubled if $U_i^{n+1,*} < \min_j(U_j^0)$ or $U_i^{n+1,*} > \max_j(U_j^0)$.

If the cell $I_i$ is troubled, then it is locally recomputed by the first-order Godunov scheme. For safety reason, its direct neighbors may also be marked as troubled cells. In figure 3.5, we complete the sketch of a the Finite Volume scheme with an *a posteriori* MOOD procedure. Remark that only troubled cells are re-computed, which is expected to occur only in rare events. The direct neighbors of a troubled cell (i.e. sharing a flux with $I_i$) must also be re-updated for conservation purposes.

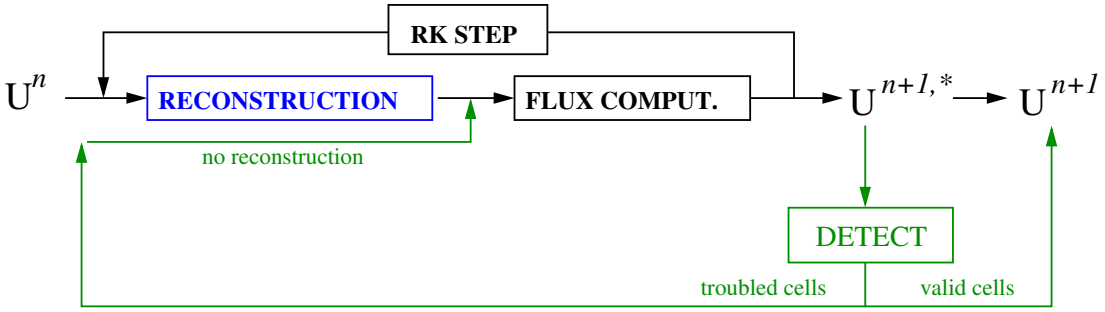


Figure 3.5: Sketch of the Finite Volume scheme with *a posteriori* MOOD procedure which detects troubled cells (the ones where positivity is violated, or where NaN is occurring), then recomputes the solution by a first order Godunov scheme (no reconstruction). The neighbor cells of a troubled cell must also be re-updated. Contrarily valid cells are accepted without any modification.

### 3.3.5 Illustration of the behavior of the reconstructions $\mathcal{R}$

In this section, we illustrate the behavior of the FV schemes with different reconstructions, namely using $\mathcal{R}_{\text{HO}}$ with the unlimited 5th order polynomial ($\mathbb{P}_4$), $\mathcal{R}_{\text{ENO}_2}$ with $\text{THINC}_{\beta=1.2}$, $\mathcal{R}_{\text{ENO}_1}$ with $\text{THINC}_{\beta=1.1}$, $\mathcal{R}_{\text{SHARP}}$ with $\text{THINC}_{\beta=1.6}$ and $\mathcal{R}_{\text{LO}}$ with piecewise constant data ($\mathbb{P}_0$). Recall that the FV scheme is 1D, using a 4th order SSPRK time discretization, a HLLC flux function and one of the reconstruction operator listed above.

**Smooth sine profile:** Let us consider in 1D on $\Omega = [0, 1]$ the smooth function $U(x) = \sin(2\pi x)$ subjects to a scalar advection equation with constant velocity $a = 1$. The domain is meshed with $20$ uniform cells and $40$ time iterations with $\Delta t = 0.025$ are performed. Periodic boundary conditions are considered. The exact solution consists of the same profile after one revolution. In figure 3.6 (left panel), we present the numerical solution obtained by each of the FV scheme using one of the $5$ reconstruction operators. As expected for a smooth profile the reconstruction $\mathcal{R}_{\text{HO}}$ (unlimited $\mathbb{P}_4$ FV scheme) provides the most accurate results. $\mathcal{R}_{\text{ENO}_2}$ and $\mathcal{R}_{\text{ENO}_1}$ produce monotone but diffuse results, with $\mathcal{R}_{\text{ENO}_2}$ results being more accurate. They match approximately TVD-van Leer and TVD-superbee results. $\mathcal{R}_{\text{SHARP}}$ results present the staircase behavior and $\mathcal{R}_{\text{LO}}$ ones are extremely diffused.

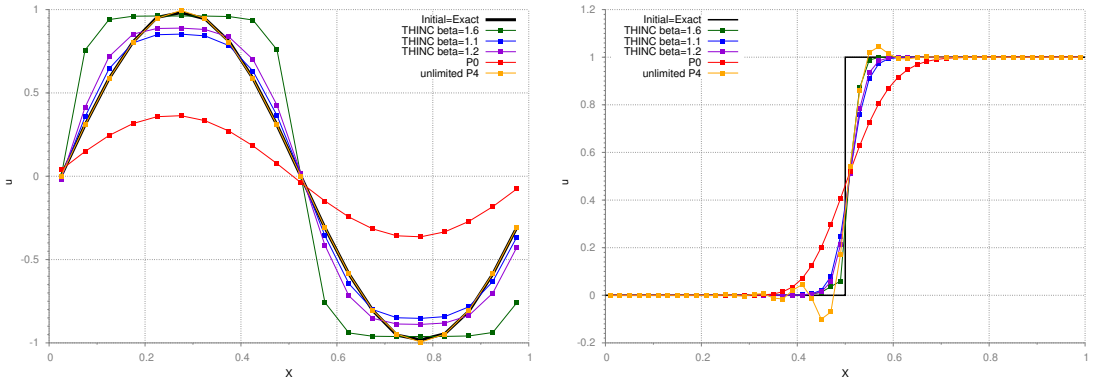


Figure 3.6: Advection of a sine profile (left panel) and a step profile (right panel) by the FV schemes using different reconstruction operators $\mathcal{R}$. Displays are the results of $\mathcal{R}_{\text{HO}}$, $\mathcal{R}_{\text{LO}}$, $\mathcal{R}_{\text{ENO}_2}$, $\mathcal{R}_{\text{ENO}_1}$ and $\mathcal{R}_{\text{SHARP}}$ reconstructions against the exact solution.

**Discontinuous step profile:** Next we consider in 1D the step like function $U(x) = 1/2(1 + (x - 1/4)/|x - 1/4|)$, discontinuous at $x = 1/4$. $10$ time steps and $50$ uniform cells are considered. The exact solution corresponds to the initial one shifted by distance $D = 0.25$. In figure 3.6 (right panel), we present the results of the FV scheme with different reconstructions. As expected for a discontinuous profile, the reconstruction $\mathcal{R}_{\text{HO}}$ (unlimited $\mathbb{P}_4$ FV scheme) generates spurious oscillations but with the discontinuity maintained over $3 - 4$ cells. Accordingly $\mathcal{R}_{\text{LO}}$ results are monotone but truly diffusive ($\sim 15$ cells). Contrarily the reconstructions $\mathcal{R}_{\text{ENO}_{1,2}}$ produce monotone but a somewhat diffuse discontinuity ($5-6$ cells). $\mathcal{R}_{\text{SHARP}}$ results presents a sharper discontinuity spread over the same number of cells than the one obtained with $\mathcal{R}_{\text{HO}}$ reconstruction.

The five reconstructions listed in table 3.1 are appropriately behaving for different situations; on regular solution, on discontinuous profile, to suppress spurious oscillations and to handle extreme situations. As a consequence it is important to correctly choose which reconstruction is the most appropriate one at a given time and location. This is the goal of the 'selector' introduced in Section 3.3 which is designed in the following section.

Table 3.1: Table of reconstructions used in this work and their associated target property.

| Acronym | Reconstruction | Parameter | Solution property |
|---|---|---|---|
| HO | $\mathbb{P}_k$ unlimited polynomial | $k = 4$ | smooth profiles |
| $ENO_2$ | THINC | $\beta = 1.2$ | (damp) spurious oscillations |
| $ENO_1$ | THINC | $\beta = 1.1$ | (kill) spurious oscillations |
| SHARP | THINC | $\beta = 1.6$ | discontinuities |
| LO | $\mathbb{P}_0$, no reconstruction | — | positivity issue |

### 3.3.6 Local selection of reconstruction operator: a 3-stage BVD algorithm

In this work, the selector relies on a 3-stage Boundary Variation Diminishing (BVD) algorithm [30, 31, 103]. The total boundary variation (TBV) in a 1D cell $I_i$ is defined by the sum of the jumps generated by the reconstructed values (using reconstruction operator $\mathcal{R}$) at the cell interfaces:

$$\mathrm{TBV}_i^{\mathcal{R}}(U) = \left|U_{i-1/2}^{L,\mathcal{R}} - U_{i-1/2}^{R,\mathcal{R}}\right| + \left|U_{i+1/2}^{L,\mathcal{R}} - U_{i+1/2}^{R,\mathcal{R}}\right| \geq 0 \tag{3.12}$$

Each term represents the amount of dissipation introduced in the numerical flux in Eq.(3.5) for one edge of cell $I_i$, therefore $\mathrm{TBV}_i$ scales like the numerical dissipation in the cell. When two reconstructions $\mathcal{R}_1$ and $\mathcal{R}_2$ of the same data U are available then the comparison of $\mathrm{TBV}_i^{\mathcal{R}_1}$ and $\mathrm{TBV}_i^{\mathcal{R}_2}$ allows to choose the least dissipative one in cell $I_i$. BVD algorithm exploits this fact.

More precisely, in this work, the following 3-stage procedure is employed in spirit of [30, 31]. Let us call the actual reconstruction used in cell $i$ by $r_i$ where $r_i$ can be HO, $ENO_1$, $ENO_2$, SHARP or LO.

Stage 1. Selection between $\mathcal{R}_{\mathrm{HO}}$ and $\mathcal{R}_{\mathrm{ENO_2}} \rightarrow \mathcal{R}_{\mathrm{ST_1}}$

For all cell $i$, if $\mathrm{TBV}_i^{\mathcal{R}_{\mathrm{HO}}} > \mathrm{TBV}_i^{\mathcal{R}_{\mathrm{ENO_2}}}$ then $(r_{i-1}, r_i, r_{i+1}) = \mathrm{ENO_2}$, else $r_i = \mathrm{HO}$.

$\mathcal{R}_{\mathrm{ST_1}} = \{r_i,\, i = 1, \ldots, N\}$

Stage 2. Selection between $\mathcal{R}_{\mathrm{ST_1}}$ and $\mathcal{R}_{\mathrm{ENO_1}} \rightarrow \mathcal{R}_{\mathrm{ST_2}}$

For all cell $i$, if $\mathrm{TBV}_i^{\mathcal{R}_{\mathrm{ST_1}}} > \mathrm{TBV}_i^{\mathcal{R}_{\mathrm{ENO_1}}}$ then $(r_{i-1}, r_i, r_{i+1}) = \mathrm{ENO_1}$, else $r_i =$

$\mathrm{ST}_1$.

$\mathcal{R}_{\mathrm{ST}_2} = \{r_i,\, i = 1, \ldots, N\}$

Stage 3. Selection between $\mathcal{R}_{\mathrm{ST}_2}$ and $\mathcal{R}_{\mathrm{SHARP}} \rightarrow \mathcal{R}_{\mathrm{ST}_3}$

For all cell $i$, if $\mathrm{TBV}_i^{\mathcal{R}_{\mathrm{ST}_2}} > \mathrm{TBV}_i^{\mathcal{R}_{\mathrm{SHARP}}}$ then $r_i = \mathrm{SHARP}$, else $r_i = \mathrm{ST}_2$.

$\mathcal{R}_{\mathrm{ST}_3} = \{r_i,\, i = 1, \ldots, N\}$

In the case of a scalar equation the selector Eq.(3.12) acts on the only variable $u$, while in the case of systems of three variables, say $W_1$, $W_2$, $W_3$ being the characteristic variables corresponding to $u - c$, $u$ and $u + c$, respectively, we may have several options, for instance:

- $W_1, W_2, W_3$ may be considered as variables independent from each other, and, consequently each of them goes through the selector Eq.(3.12) and the selection of reconstruction. Numerical tests have shown that this option is too diffusive and the solution may even get noisy.

- $W_1, W_2, W_3$ are considered as variables connected each other. Extensive numerical tests have shown that an acceptable strategy then consists in

  Stage 1: the selector Eq.(3.12) is computed for $W_1, W_2$ and $W_3$, their neighbor cells will reconstructed based on the selection of $W_3$ use as $\mathcal{R}_{\mathrm{ST}_1}$

  Stage 2: the selector Eq.(3.12) is computed for $W_1, W_2$ and $W_3$, their neighbor cells will reconstructed based on the selection of $W_1$ use as $\mathcal{R}_{\mathrm{ST}_2}$

  Stage 3: each variable is independently sharpened use as $\mathcal{R}_{\mathrm{ST}_3}$.

**Remark 4.** In stage 1, if the THINC reconstruction is selected by $W_3$ for cell $I_i$ then its two direct neighbors $I_{i-1}, I_{i+1}$ are reconstructed with the same THINC function and also for the neighbor cells of other variables $W_1$ and $W_2$.

**Remark 5.** In stage 2, similar to stage 1 if the THINC reconstruction is selected by $W_1$ for cell $I_i$ then its two direct neighbors $I_{i-1}, I_{i+1}$ are reconstructed with the same THINC function and also for the neighbor cells of other variables $W_2$ and $W_3$. Indeed this cell has been selected due to a smaller $\mathrm{TBV}_i$ which is computed with genuinely

THINC fluxes on both sides and this implies that the neighbor cells use the same reconstruction operator as $I_i$. The neighbor cells $I_{i-1}$ and $I_{i+1}$ may be mixed cells with one flux calculated by THINC reconstruction on one side and a polynomial calculated flux on the other.

The role of $W_3$ in stage 1 and $W_1$ in stage 2 could be reversed without much changes in the results. The reason why stage 3 is treated differently relies on the fact that if sharpening should be conducted (because the TBV selector says so) then it must be constructed in order to steepen any interface present for any variable. This ends the description of the 3-stage BVD algorithm.

**Remark 6.** The oscillation-free solution is obtained after stage 1 and stage 2 occurring. The numerical dissipation at discontinuous/steep gradients is reduced after stage 3 if needed. It means that the desired numerical solution properties are attained respectively at different stages by this multi-stage BVD approach.

**Remark 7.** In the multi-stage of reconstruction operators HO $\rightarrow$ ENO $\rightarrow$ SHARP $\rightarrow$ LO other TVD numerical methods could be used in replacement of THINC function with $\beta = 1.1$ or $\beta = 1.2$ (ENO). On the contrary the unlimited high order polynomial reconstruction (HO) as well as THINC with $\beta = 1.6$ used to sharpen discontinuities (SHARP) are mandatory. The first one ensures the highest possible accuracy (because no dissipative mechanism is employed), while the second one allows to maintain extremely sharp discontinuities. Up to our knowledge, we are not aware of better reconstruction operators for these situations. For the same reason, the low order (LO) scheme must be carefully chosen to ensure positivity and valid representation of numbers. In this work, the first order accurate Godunov scheme is employed as being one of the simplest and more robust positivity-preserving schemes.

**Remark 8.** We have experimented using the BVD algorithm to the primitive variables as well. Similar to the results shown in [103], implementing BVD algorithm to primitive variables results in more oscillatory numerical solution in comparison with the characteristic variables. We use the characteristic variables in this work, which lead to more stable solutions.

## 3.4 Extension to 2D

The extension of the 2D structured grid is carried on by dimensional splitting in a straightforward manner. Our goal with this extension is to maintain the simplicity and efficiency of the method. Recall that our goal is to design a genuinely efficient and accurate limiter-free scheme, to sharply capture shocks and steep gradients, and at the same time to deal robustly with near-vacuum states. For this reason, some approximations are produced from the classical high-accurate polynomial-based FV scheme. However, it will be evident in the numerical tests, and those approximations do not deteriorate the efficiency of our non-linear numerical method. Let us directly focus on some essential points for this 2D extension.

### 3.4.1 Two dimensional finite volume framework

The computational domain is assumed to be a rectangular box $\Omega = [x^L, x^R] \times [y^L, y^R]$ divided into rectangular uniform cells $I_{i,j} = [x_{i-1/2}, x_{i+1/2}] \times [y_{j-1/2}, y_{j+1/2}]$. A point vector is denoted by a capital letter $X = (x, y)^t$. The cell center is denoted by $X_{i,j} = (x_i, y_j)^t$ and the cell sizes are $\Delta x$ and $\Delta y$ with $z_k = \frac{z_{k-1/2}+z_{k+1/2}}{2}$, and $\Delta z = z_{k+1/2} - z_{k-1/2}$ where $z$ is standing for $x$ and $y$, and, $k$ for $i$ and $j$ respectively. We write the 2D equation of hyperbolic conservation law into

$$\frac{\partial U}{\partial t} + \frac{\partial F(U)}{\partial x} + \frac{\partial G(U)}{\partial y} = 0, \tag{3.13}$$

where $F(U)$ and $G(U)$ stand for the flux functions in $x$ and $y$ directions respectively. The numerical solution of $U(X, t)$ over a mesh cell $I_{i,j}$ at time $t$ is approximated by a piecewise constant value

$$U_{i,j}(t) = \frac{1}{\Delta x\, \Delta y} \int_{I_{i,j}} U(X, t)\, dx\, dy \qquad \text{where} \qquad i = 1, 2, \ldots, M, j = 1, 2, \ldots, N. \tag{3.14}$$

Let us denote by $\mathsf{U}(t) = (U_{i,j}(t))_{i,j=1,2,\ldots,N}$ the vector of discrete FV data in the mesh. The semi-discretization of Eq.(3.13) over cell $I_{i,j}$ after the application of Green theorem

yields

$$\frac{dU_{i,j}(t)}{dt} + \frac{1}{\Delta x\,\Delta y}\int\limits_{\partial I_{i,j}} \mathbf{F}(U(t))\cdot\mathbf{n}_{i,j}\,ds = 0, \tag{3.15}$$

where $\mathbf{n}_{i,j}$ is the outward pointing unit normal of the cell boundary $\partial I_{i,j}$, and $\mathbf{F}(U) = (F(U(t)), G(U(t)))$. Let us call the four edges forming $\partial I_{i,j}$ by $e_{i\pm1/2,j}$ and $e_{i,j\pm1/2}$ and rewrite the previous equation into

$$\frac{dU_{i,j}(t)}{dt} + \frac{1}{\Delta x}\left(F_{i+1/2,j}(t) - F_{i-1/2,j}(t)\right) + \frac{1}{\Delta y}\left(G_{i,j+1/2}(t) - G_{i,j-1/2}(t)\right) = 0, \tag{3.16}$$

which is then updated in time using the aforementioned Runge-Kutta scheme. The fluxes $F_{i\pm1/2,j}(t)$ and $G_{i,j\pm1/2}(t)$ are computed likewise their 1D counterparts. For instance to compute $F_{i+1/2,j}(t)$ along the vertical edge $e_{i+1/2,j}$, the left and right states, $U^L_{i+1/2,j}$ and $U^R_{i+1/2,j}$, are first computed by the use of left/right 1D reconstructions in cells $I_{i,j}$ and $I_{i+1,j}$. These reconstructions are both evaluated at the center point of edge denoted by $x_{i+1/2,j}$ at instant $t$ for each time level as well as Runge-Kutta sub-step. Then, a Riemann solver is further employed to get the final value of the flux

$$F_{i+1/2,j}(t) = F^{\text{Riemann}}_{i+1/2,j}\left(U^L_{i+1/2,j}, U^R_{i+1/2,j}, t\right). \tag{3.17}$$

The same procedure is employed in $y$-direction to compute the fluxes $G_{i,j+1/2}(t)$. In this work a HLLC Riemann solver is used [108]. Following the 1D section, a fourth-order accurate SSPRK scheme [43, 88, 101] is employed for a high accurate time discretization.

### 3.4.2 Reconstruction operators

As previously mentioned, the reconstructions are performed direction by direction. In other words, the same $\mathbb{P}_4$ reconstructions as described in Eq.(3.8) are first made for data aligned in $x$ direction: $U_{i-2,j}, U_{i-1,j}, U_{i,j}, U_{i+1,j}, U_{i+2,j}$, to get the edge centered values $U^L_{i+1/2,j}$ and $U^R_{i-1/2,j}$ for cell $I_{i,j}$. Then, the 1D reconstructions in $y$ direction consider $y$-aligned data $U_{i,j-2}, U_{i,j-1}, U_{i,j}, U_{i,j+1}, U_{i,j+2}$ to get values $U^L_{i,j+1/2}$ and $U^R_{i,j-1/2}$ in cell $I_{i,j}$. The THINC reconstructions are exactly the same as in 1D, their stencils are thus

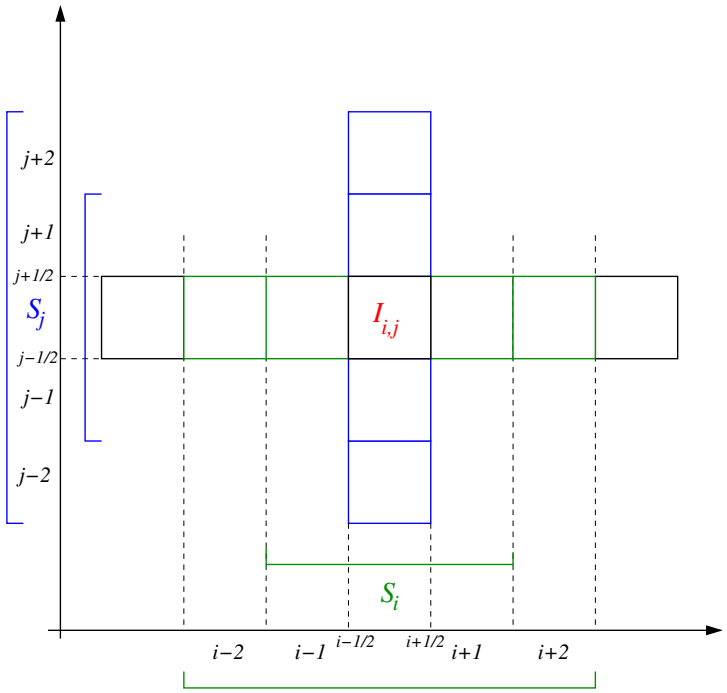


Figure 3.7: Stencil in 2D.

restricted to two aligned neighbor cells only. The *a posteriori* MOOD loop operates also alike. The local selection of reconstruction operator follows the same algorithm depicted in Section 3.3.6 and the selection of reconstruction operator is independent in $x$ and $y$ directions. Consequently we do not repeat those descriptions.

### 3.4.3 Discussion on accuracy and efficiency

The 1D formulation and time discretization lead to a 5th order of accuracy for smooth solution of linear advection equation as in [30]. However, it is noted that our scheme is formally only second-order accurate for 1D Euler equations and in 2D due to variable dependent selection of BVD algorithm and a simple multi-dimensional implementation. Indeed the flux integration along the edges is calculated using only one integration point at the edge center. This choice has been made for three reasons. First, in order to maintain the scheme as efficient as possible, we have not multiplied the number of function evaluations ($\mathbb{P}_4$, THINC) by using Gauss quadrature points per edge, which would led to a formal 5th order accuracy for the integration, matching the target order of accuracy of the scheme. Unfortunately, this would also lead to a cost of $8$ Riemann solvers, one for each of the $8$ integration points, and, consequently, $16$ function evaluations. This is

usually one of the costly part of a FV scheme. Contrarily, in our scheme, the number of function evaluations is reduced to $8$ for $4$ Riemann solvers.

Second, in our work the $\mathbb{P}_4$ reconstructions are not multi-dimensional ones. Hence, the expected 5th order of accuracy is somewhat spoiled by the dimensional splitting during the reconstruction step. If one decides to reconstruct a true 2D $\mathbb{P}_4$ polynomial, then about $25$ neighbor cell values must be used for $15$ polynomial coefficients, leading to a $15 \times 25$ linear system to invert per cell.

Third, our scheme is intrinsically non-linear due to the presence of THINC reconstructions. Therefore, the formal notion of 'order of accuracy on smooth flow' is more complicated to handle than for linear schemes. Only the accuracy at given mesh remains a valid and comprehensive notion, and, our 2D numerical results show that the scheme is accurate and efficient with this choice of one only integration point per edge.

Recall that the goal in this work is not to build a genuine 5th order accurate numerical method which would certainly demand true 2D polynomial reconstructions and accurate enough quadrature rule. On the contrary, this work is intended to build a genuine simple, efficient, robust and accurate enough scheme emphasizing that an appropriate mixing of linear and non-linear reconstruction operators may replace classical limiting techniques (slope/flux limiters, artificial viscosity, WENO, etc.). The following numerical section is intended to provide some numerical evidences.

## 3.5 Numerical results

In this section, we validate the numerical scheme for some benchmark tests for a linear advection equation and the Euler equations involving strong interacting discontinuities. In addition, we also show some typical test cases involving near vacuum states to test the positivity-preserving property of the scheme. The numerical in-house FV code is built on the following key tools: the reconstruction procedure is conducted in terms of characteristic decomposition, the HLLC Riemann solver [108] is used for flux computation, a SPPRK of fourth order in time discretisation is employed, the BVD algorithm

for the space reconstruction is used, and, at last an *a posteriori* MOOD loop is implemented for the positivity-preservation. In order to demonstrate the performance of the present scheme, some numerical results are compared to 5th order WENO-Z scheme with the same reconstruction procedure and time discretization. The WENO-Z scheme generally presents good accuracy on smooth flows and a non-oscillatory behavior near discontinuity, see [3, 39]. The numerical results produced by the current scheme in this work will be compared to this reference scheme. The CFL number is set to $0.4$.

### 3.5.1 One-dimensional linear advection equation

The scalar advection equation consists in considering $U$ as a scalar field, and $F(U) = a\,U$ with $a$ the convective velocity. We set $a = 1$ in this work. As such, any profile $U(x, t = 0)$ is convected so that the exact solution at $t \geq 0$ is given by $U(x, t) = U(x - a\,t, 0)$. For this equation the physical admissibility (PAD criteria) is set to $\min_i(U_i^0) \leq U_i^{n+1} \leq \max_i(U_i^0)$. In order to evaluate if the present scheme can resolve different smooth profiles and discontinuity of different kinds, one simulates the test which was proposed in [56]. The initial condition on the computation domain $[-1, 1]$ is defined as

$$U(x,0) = \begin{cases} \dfrac{1}{6}\left(G(x,\beta,z-\delta) + G(x,\beta,z+\delta) + 4G(x,\beta,z)\right), & -0.8 \leq x \leq -0.6, \\ 1, & -0.4 \leq x \leq -0.2, \\ 1 - |10(x-0.1)|, & 0.0 \leq x \leq 0.2, \\ \dfrac{1}{6}\left(F(x,\alpha,a-\delta) + G(x,\alpha,a+\delta) + 4G(x,\alpha,z)\right) & 0.4 \leq x \leq 0.6, \\ 0, & \text{otherwise.} \end{cases} \tag{3.18}$$

The functions $F$ and $G$ are defined by

$$G(x,\beta,z) = \exp\left(-\beta(x-z)^2\right), \qquad F(x,\alpha,a) = \sqrt{\max(1-\alpha^2(x-a)^2, 0)}, \tag{3.19}$$

and the coefficients are given by

$$a = 0.5,\ z = -0.7,\ \delta = 0.005,\ \alpha = 10,\ \beta = \log 2/36(\delta^2). \tag{3.20}$$

The numerical results of the test at final time $t = 2.0$ and for 200 uniform grid cells are shown in figure 3.8. This test is used to evaluate the occurrence of spurious numerical oscillations, the preservation of smooth and discontinuous extremes and smooth profiles. Compared to WENO-Z scheme [3][1] (figure 3.8-(left)), the proposed scheme (figure 3.8-(right)) can better resolve the sharp discontinuous profiles, the step-like profile. It also effectively eliminates the numerical oscillations generated by the Gibbs phenomenon.

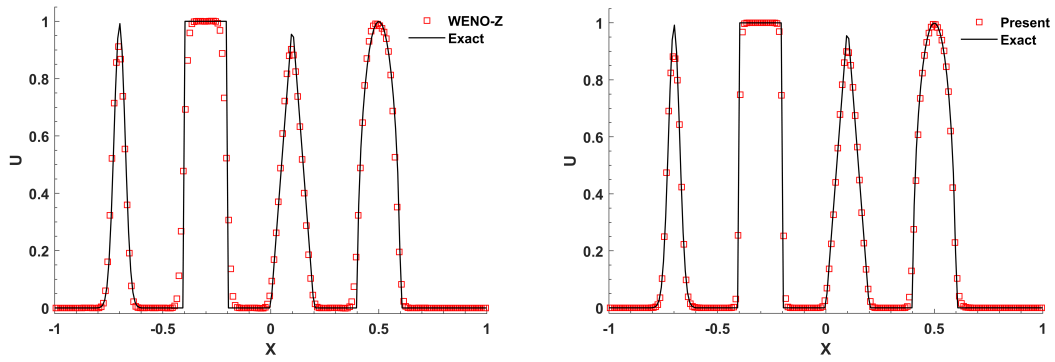


Figure 3.8: Numerical results for the advection of complex waves with 200 grid cells after one period ($t = 2.0$) computed by WENO-Z scheme and the proposed one.

## 3.5.2 One-dimensional Euler equations

The Euler equations of compressible gas dynamics consist of conservation laws of mass, momentum and total energy with $U = (\rho, \rho u, E)^T$ and $F(U) = [\rho u, \rho u^2 + p, (E + p)u]^T$ and $\rho$, $u$, $p$ are the density, velocity and pressure, respectively. $E$ is the total energy expressed as $E = e + \frac{1}{2}\rho u^2$ and $e$ is the specific internal energy. For ideal gas, the equation of state (EOS) is defined as $p = (\gamma - 1)\rho e$ where $\gamma$ is the ratio of specific heats. We set $\gamma = 1.4$ for the numerical tests if not otherwise mentioned. For the Euler equations with an ideal EOS, a candidate solution is physically admissible if $\rho_i^n > 0$ and $p_i^n > 0$ and these are the PAD criterion checked by the MOOD loop.

### 3.5.2.1 Problems involving simple waves

**Double rarefaction or 123 problem:** The 123 problem is one of benchmark tests presenting near vacuum state as it involves two rarefaction fans moving in opposite direc-

[1]Recall that WENO-Z has been designed in particular to avoid loss of accuracy at critical points. Hence, for this test it can be considered as a truly appropriate and adapted numerical method.

tion, therefore emptying a central zone. The initial condition on computational domain $\Omega = [-1, 1]$ is given in table 3.2 [70] $400$ cells are considered and the final time is set to $t_{\text{final}} = 0.6$. Outflow boundary conditions are implemented. The numerical results of the current scheme are compared to the exact solution (straight line) and represented in figure 3.9 with symbols. The numerical solution is in good agreement with the exact solution and the quality is comparable to positivity-preserving fifth-order finite difference WENO scheme [130] and positivity-preserving DG method [127]. The spurious peak in the internal energy profile is a classical flaw of many numerical methods when dealing with near vacuum state [72].

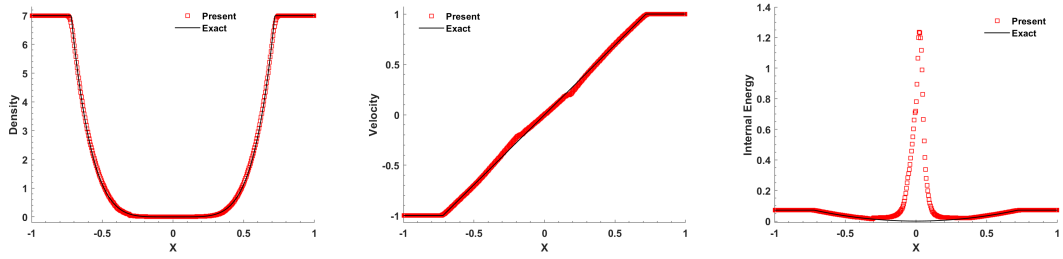


Figure 3.9: Numerical results for Euler equations – 123 problem – $400$ cells – From left to right: density, velocity and internal energy.

**Sedov blast-waves:** We also evaluate the scheme on the Sedov blast-wave involving low density and low pressure [91]. The initial condition is such that the density is $1$, the fluid is at rest and the total energy is $10^{-12}$ everywhere except for the center cell where $\frac{E_0}{\Delta x}$ with $E_0 = 3.2 \times 10^6$ emulating a $\delta$-function at the origin. The exact solution at $t > 0$ is constituted by two shock waves emanating from the origin and traveling in opposite directions and an exponentially rarefaction after the shocks leading to near-vacuum states. The computational domain is set to $\Omega = [-2, 2]$ and outflow boundary conditions are considered. The mesh size is $\Delta x = \frac{1}{200}$ and final time is $t_{\text{final}} = 0.001$. The computational results in figure 3.10 show that the proposed scheme provides sharp solutions for the shocks and maintains an admissible solution throughout the simulation. Notice that the original high-order reconstruction schemes like PQM [116] or WENO sometimes fail due to the generation of non-admissible numerical states, which leads to code termination. In this work such a situation is avoided by the *a posteriori* MOOD

Table 3.2: Initial left and right states for the density $\rho$, velocity $u$ and the pressure $p$ for the shock tube problems. The final simulation times $t_{\text{final}}$, domain size and the position of the initial discontinuity $x_d$ are also given.

| **Problems** | $\rho_L^0$ | $u_L^0$ | $p_L^0$ | $\rho_R^0$ | $u_R^0$ | $p_R^0$ | $t_{\text{final}}$ | $\Omega$ | $x_d$ |
|---|---|---|---|---|---|---|---|---|---|
| **123** | 1.0 | -1.0 | 0.2 | 1.0 | 1.0 | 0.2 | 0.6 | [-2,2] | 0 |
| **Sod** | 1.0 | 0.0 | 1.0 | 0.125 | 0.0 | 0.1 | 0.25 | [0,1] | 0.5 |
| **Lax** | 0.445 | 0.698 | 3.528 | 0.5 | 0.0 | 0.571 | 0.16 | [0,1] | 0.5 |
| **Le Blanc** | 1 | 0.0 | $\frac{2}{3} \times 10^{-1}$ | $10^{-3}$ | 0.0 | $\frac{2}{3} \times 10^{-10}$ | 6 | [0,9] | 3 |

loop which locally uses a first-order but extremely robust scheme to cure such situations when they are observed by the detection criteria.

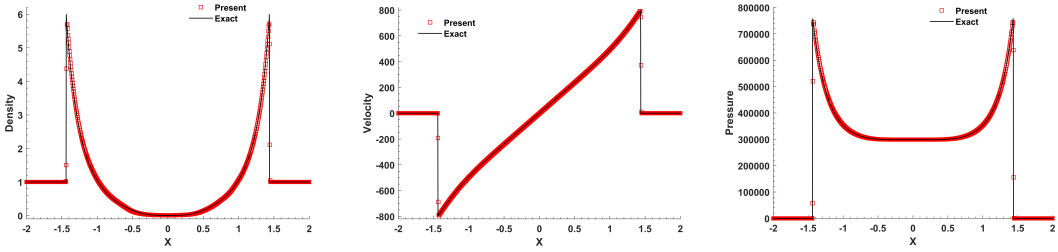


Figure 3.10: Numerical results for Euler equations – Sedov problem – 800 cells – From left to right: density, velocity and pressure.

**Sod and Lax shock tube problems:** We simulate the 1D planar Sod shock tube problem and the classical Lax shock tube problem to assess the ability of the schemes to capture simple waves. The initial conditions for density, velocity and pressure are listed in table 3.2. An exact solution for both problems can be derived from the one-dimensional Riemann problem, see [108]. The computational domain $\Omega = [0, 1]$ is covered by 200 cells and Dirichlet boundary conditions are imposed on both ends of the domain. The numerical solution depicted in figure 3.11 is good agreement with the exact solutions. The shock waves are sharply captured essentially on one or two cells. More notably is the ability of the scheme to capture the contact discontinuity over two cells only which is a rare ability for Eulerian schemes, even for high accurate ones.

**Le Blanc shock tube problem:** In this test, we consider the so-called Le Blanc shock tube problem with specific heat ratio $\gamma = 5/3$, with the initial condition given in table 3.2. The domain is $\Omega = [0, 9]$ and the discontinuity is initially at location $x_d = 3$. This

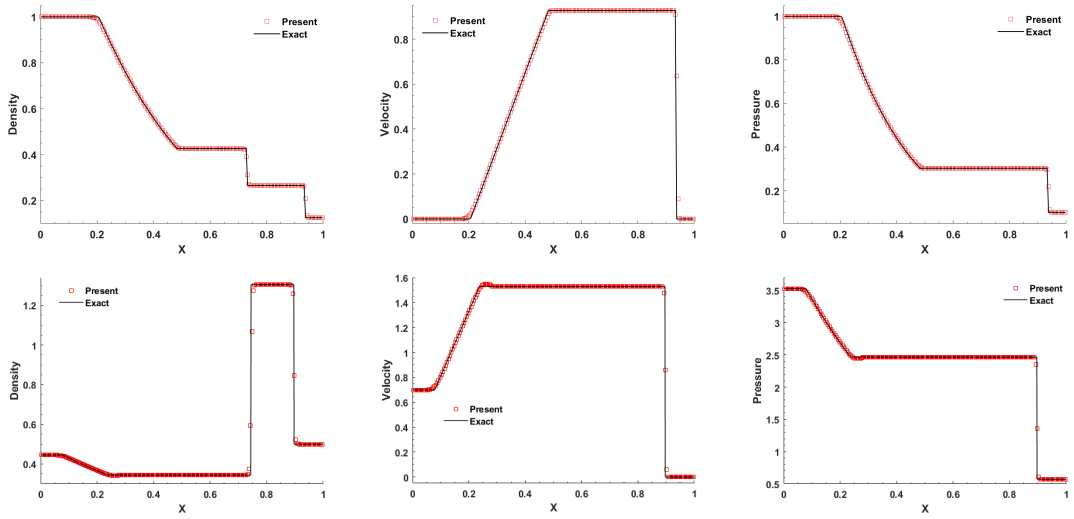


Figure 3.11: Numerical results for Euler equations – Sod (top) and Lax (bottom) shock tube problems – 200 cells – From left to right: density, velocity and pressure.

test is an extreme version of a shock tube for which the jump in density is $10^3$ while the jump in pressure is $10^9$ leading to violent waves, which, however are still simple waves that can be exactly computed [108]. The numerical results at final time $t_{\text{final}} = 6$ are presented in figure 3.12 when 800 cells are used. The computed density and internal energy are plotted using a log scale to enhance the structure of the solution while we use a linear scale for the velocity. We observe that the present scheme provides a high resolution solution with sharp discontinuities without any lack of positivity. The shock wave is not at the exact location due to the fact that, for this extreme shock tube, 800 cells are not sufficient to reach the mesh convergence. Therefore, even if the numerical method is conservative and converges towards a weak solution of the Euler equations, for a coarse resolution, any numerical solution may present such misbehavior due to inaccuracy. This is classically observed for other high resolution schemes in the literature, see [75, 76, 73, 85] for a non-exhaustive variety of numerical results on this problem.

#### 3.5.2.2 Problems involving interacting waves

**Collela-Woodward blast-wave:** This test was first introduced by Collela and Woodward [27] and it involves interactions of simple waves. The initial condition is given

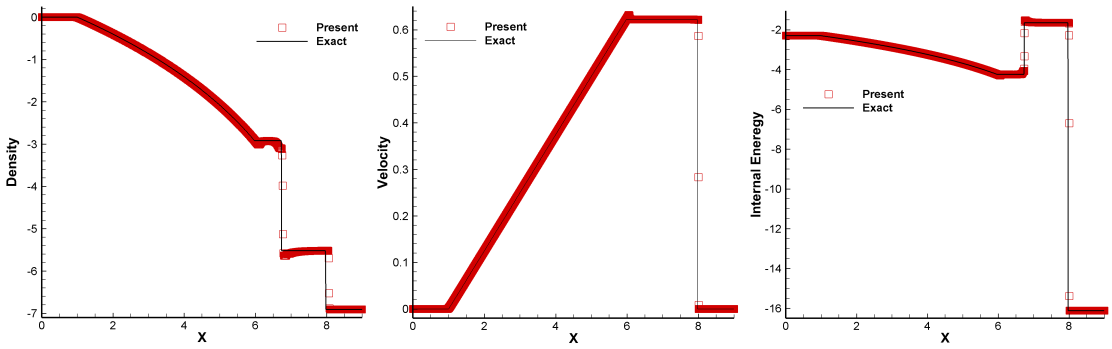


Figure 3.12: Numerical results for Euler equations – Le Blanc problem – 800 cells – From left to right: density, velocity and specific internal energy.

by

$$(\rho_0, u_0, p_0) = \begin{cases} (1,\ 0,\ 1000) & \text{if } 0 < x < 0.1, \\ (1,\ 0,\ 0.01) & \text{if } 0.1 < x < 0.9, \\ (1,\ 0,\ 100) & \text{otherwise.} \end{cases} \tag{3.21}$$

and the final time is set to $t_{\text{final}} = 0.38$. Reflective boundary conditions are set on the left and right ends of the computational domain. We compute the numerical results with $400$ mesh cells. In figure 3.13 we observe that the proposed scheme can capture sharply the shock waves and, more notably, the contact discontinuities on very few cells (1 or 2). Recall that contrarily to classical Eulerian FV schemes based on polynomial reconstructions (with embedded limiter), our approach considers non-polynomial reconstructions (THINC) in conjunction with high accurate polynomial ones. This combination shows its importance on such test case on the left-most contact discontinuity. Obviously our approach is not exempt from drawbacks for instance the smooth region between $x = 0$ and $x = 0.5$ seems to reveal some oscillations in the velocity field. Nevertheless, our numerical experiments show that using a smaller $\beta$ in the first two stages effectively reduces such oscillations in velocity field.

**Shu-Osher oscillatory problem:** This test problem [94, 103] is a particular shock tube where the downstream flow has a sinusoidal density fluctuation $\rho = 1 - \varepsilon \sin(\lambda x - A)$ with a wave length of $\lambda = 50$, an amplitude of $\varepsilon = 0.2$ and the constant value $A = 25$. A Mach 3 shock front is initially located at $x = 0.1$ on domain $\Omega = [0, 1]$. The left and the right states are given by $\rho_L^0 = 3.857143$, $u_L^0 = 2.629369$, $p_L^0 = 10.33333$ and

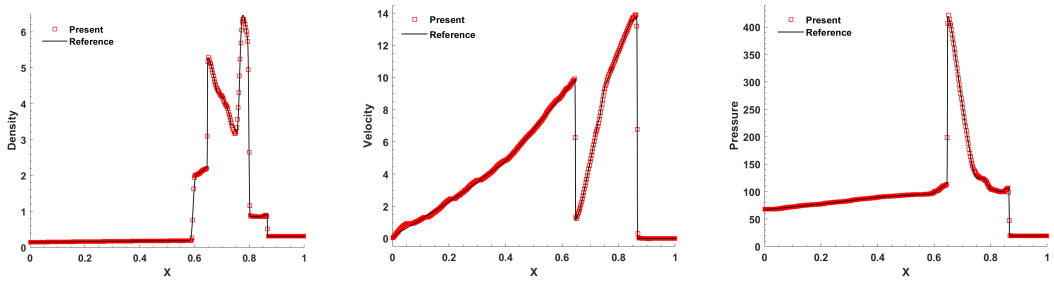


Figure 3.13: Numerical results for Euler equations – Collela-Woodward blast-wave problem – 400 cells – From left to right: density, velocity and pressure.

$\rho_R^0 = 1 + 0.2\sin(50x - 25)$, $u_R^0 = 0$ and $p_R^0 = 1$. The final time is $t_{\text{final}} = 0.18$. This problem involves small scale oscillating structures after the shock has interacted with the initial sine wave. We present the results for 300, 600 and 1000 uniform cells against a reference solution computed with WENO-Z scheme with 1000 cells. In figure 3.14 are presented the density variable (top panels) and a zoom on the oscillatory section (bottom panels) for the three mesh resolutions. We can observe that, as expected when the number of cells increases then the scheme captures more accurately the physical oscillations. While our scheme does not outperform WENO-Z scheme on this test case, its performance is acceptable for 1000 cells. Notice that the shock wave on the left-most part of the domain presents a tiny oscillation. Also our approach can not produce accurate results for 200 cells, the selector being less performing on coarse meshes.

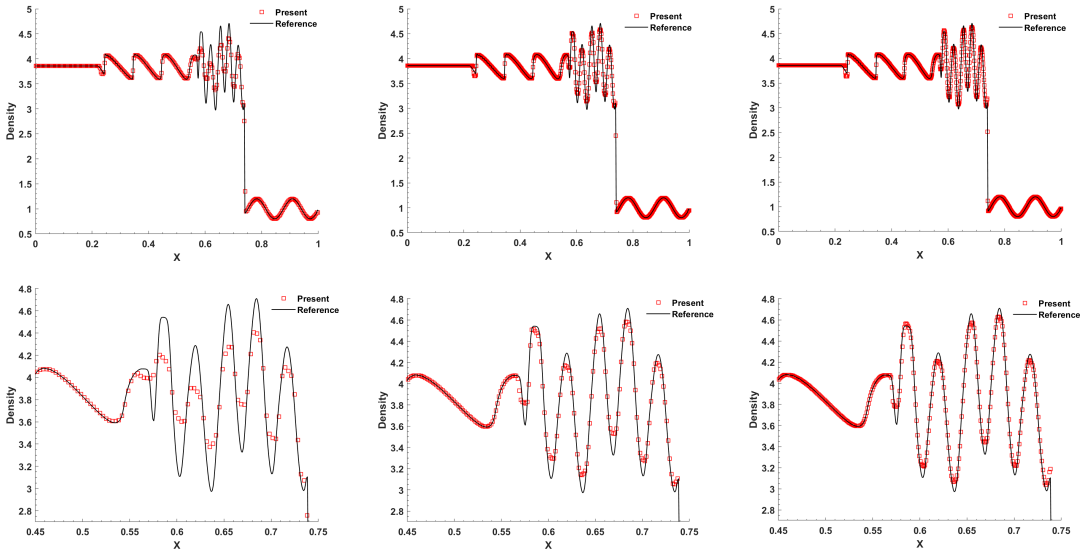


Figure 3.14: Numerical results for Euler equations – Shu-Osher problem – Density for 300, 600, 1000 cells from left to right – Top panels: full view – Bottom panels: zoom.

#### 3.5.2.3 Diagnostics on reconstruction selection

In this section, we provide some figures related to the selectors. In figure 3.15, for the Collela-Woodward blast-wave we color the cells according to the type of reconstruction selected (red for HO, blue for SHARP and green for $\text{ENO}_1$ or $\text{ENO}_2$) for each of the $N_t = 1605$ time-steps needed to complete the simulation in $y$-direction . The three characteristic variables $W_1, W_2, W_3$ are displayed on left, middle and right panels respectively. From this figure, it is interesting to notice that the main waves and their interactions are somewhat captured. Moreover, a majority of cells are dealt with the HO reconstruction (red cells), a relative important number of cells are sharpened (blue cells), and, only few need some numerical dissipation (green cells). In table 3.3

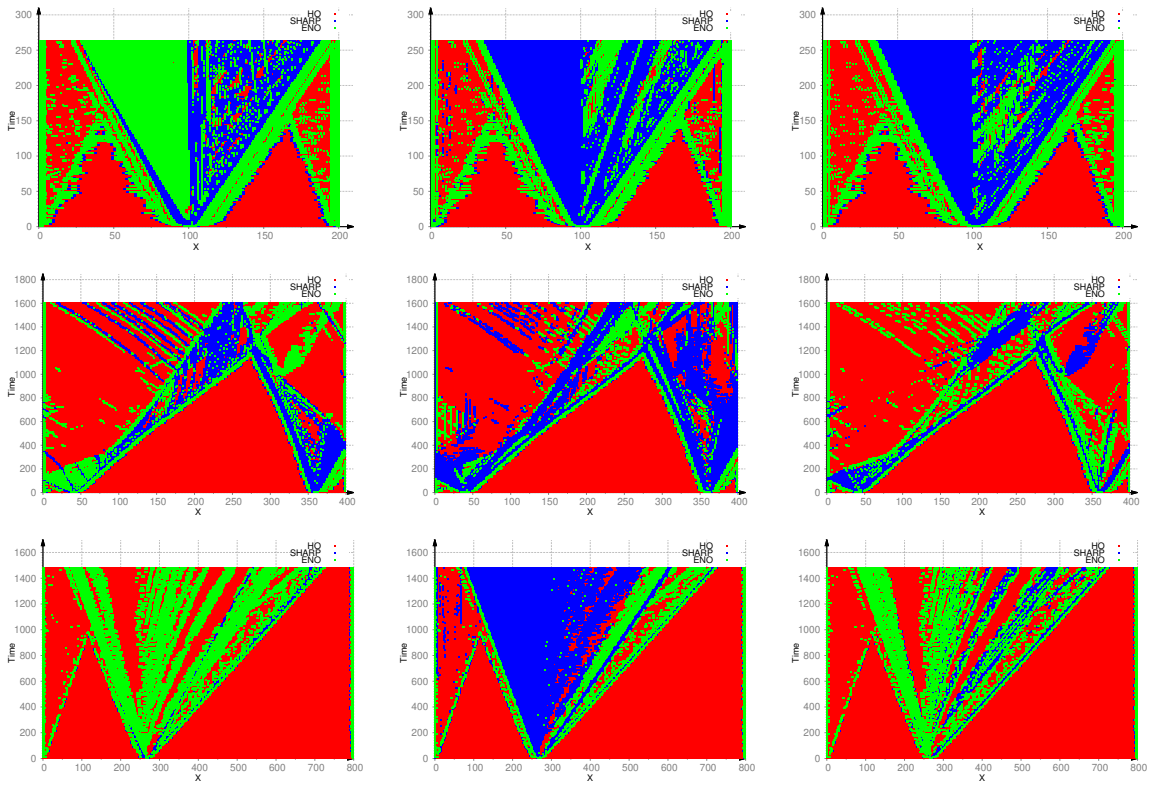


Figure 3.15: Numerical results for Sod (top panels), Collela-Woodward blast-wave (middle panels) and Le Blanc (bottom panels) problems – Cell number in $x$ axis, time iteration in $y$ axis – Each cell ($x$-direction) is colored according to the selector as a function of time-steps, red for HO, blue for SHARP and green for $\text{ENO}_1$ or $\text{ENO}_2$ reconstruction – From left to right: characteristic variables $W_1, W_2, W_3$.

we present the percentage of cells dealt with the HO, SHARP, or ENO reconstructions for Sod, Collela-Woodward and Le Blanc test cases. More precisely, one sums up for

all time steps the number of cells using the same reconstruction and take the percentage with respect to the total number $N_t \times N_c$. As expected the percentages in table 3.3 do not allow to extract a general behavior because each test case presents different flow characteristics which demand the adaptation of the scheme and its reconstructions. However, it seems that the optimally accurate HO reconstruction is chosen for $40\%$ up to $75\%$ of cells. In other words those cells are updated with the 5th order of accuracy without any dissipation mechanism. The dissipative ENO reconstructions are chosen for $10\%$ up to $38\%$ of cells to avoid spurious oscillations. At last, the sharp reconstruction is selected for $2\%$ up to $36\%$ of cells.

Table 3.3: Percentage of cells dealt with the SHARP, HO, ENO reconstructions for the three characteristic variables $W_1, W_2, W_3$ and three 1D test cases.

| **Test** | $N_t, N_c$ | $W_1$ | | | $W_2$ | | | $W_3$ | | |
|---|---|---|---|---|---|---|---|---|---|---|
| | | SH | HO | ENO | SH | HO | ENO | SH | HO | ENO |
| **Sod** | 263, 200 | 18.9% | 43.1% | 38.0% | 35.8% | 42.1% | 22.0% | 36.2% | 43.8% | 20.0% |
| **Blast-w** | 1605, 400 | 15.1% | 70.7% | 14.3% | 25.8% | 64.0% | 10.2% | 11.0% | 74.7% | 14.4% |
| **Le Blanc** | 1488, 800 | 2.2% | 75.4% | 22.4% | 28.4% | 63.4% | 8.2% | 8.5% | 75.6% | 15.8% |

### 3.5.3 Two-dimensional Euler equations

#### 3.5.3.1 Riemann problems

In order to verify that the multi-stage BVD-MOOD scheme is accurate, robust, and produces non-oscillatory solutions, we test a set of two-dimensional Riemann problems which have been introduced and widely studied in [63, 90]. Recently, Balsara $et\ al$, [5, 6, 7] have employed the 2D Riemann problems to build a genuinely multi-dimensional HLL type Riemann Solvers. The computational domain is $\Omega = [-0.5, 0.5] \times [-0.5, 0.5]$ and the initial conditions are given by

$$\mathbf{U}(x, y, t = 0) = \begin{cases} \mathbf{U}_1 & \text{if} \quad x > 0 \wedge y > 0, \\ \mathbf{U}_2 & \text{if} \quad x \leq 0 \wedge y > 0, \\ \mathbf{U}_3 & \text{if} \quad x \leq 0 \wedge y \leq 0, \\ \mathbf{U}_4 & \text{if} \quad x > 0 \wedge y \leq 0. \end{cases} \tag{3.22}$$

Table 3.4: Initial conditions for the 2D Riemann problems numbered from 1 to 5. These further correspond to Configurations 3, 4, 6, 8 and 12 in [63]

| # | | $\rho$ | $u$ | $v$ | $p$ | $\rho$ | $u$ | $v$ | $p$ | $t_{\text{final}}$ |
|---|---|---|---|---|---|---|---|---|---|---|
| | | $x \leq 0$ | | | | $x > 0$ | | | | |
| **RP1** | $y > 0$ | 0.5323 | 1.206 | 0.0 | 0.3 | 1.5 | 0.0 | 0.0 | 1.5 | 0.3 |
| | $y \leq 0$ | 0.138 | 1.206 | 1.206 | 0.029 | 0.5323 | 0.0 | 1.206 | 0.3 | |
| **RP2** | $y > 0$ | 0.5065 | 0.8939 | 0.0 | 0.35 | 1.1 | 0.0 | 0.0 | 1.1 | 0.25 |
| | $y \leq 0$ | 1.1 | 0.8939 | 0.8939 | 1.1 | 0.5065 | 0.0 | 0.8939 | 0.35 | |
| **RP3** | $y > 0$ | 2.0 | 0.75 | 0.5 | 1.0 | 1.0 | 0.75 | -0.5 | 1.0 | 0.30 |
| | $y \leq 0$ | 1.0 | -0.75 | 0.5 | 1.0 | 3.0 | -0.75 | -0.5 | 1.0 | |
| **RP4** | $y > 0$ | 1.0 | -0.6259 | 0.1 | 1.0 | 0.5197 | 0.1 | 0.1 | 0.4 | 0.25 |
| | $y \leq 0$ | 0.8 | 0.1 | 0.1 | 1.0 | 1.0 | 0.1 | -0.6259 | 1.0 | |
| **RP5** | $y > 0$ | 1.0 | 0.7276 | 0.0 | 1.0 | 0.5313 | 0.0 | 0.0 | 0.4 | 0.25 |
| | $y \leq 0$ | 0.8 | 0.0 | 0.0 | 1.0 | 1.0 | 0.0 | 0.7276 | 1.0 | |

The initial conditions and the final solution time, $t_{\text{final}}$, for the five configurations tested in this chapter are listed in table 3.4. For more information about the other configurations the reader is referred to [63, 90]. For the computation we have employed a uniform grid of $400 \times 400$ mesh cells for both schemes (WENO-Z and multi-stage BVD-MOOD). The numerical solutions are illustrated for the first two and the last three configurations in figure 3.16 and 3.17, respectively. In the left panels and the right panels we respectively show the density profile at the final time computed by WENO-Z and present scheme, with 30 equidistant iso-lines between the minimum and maximum values. We observe that the computational results of two schemes equivalently produce numerical solutions for the main flow structures of all 2D Riemann problems with this mesh.

Therefore, the multi-stage BVD-MOOD scheme performs well in capturing the discontinuities without spurious oscillations and also without excessive numerical dissipation for the smooth part of the flow structures. Furthermore, we also show the results of RP3 for both schemes with $600 \times 600$ mesh cells in figure 3.18. We can observe that the present scheme has better performance than WENO-Z scheme by showing the birth of the Kelvin-Helmholtz instability on the shear waves as an evidence of a lower dissipation scheme.

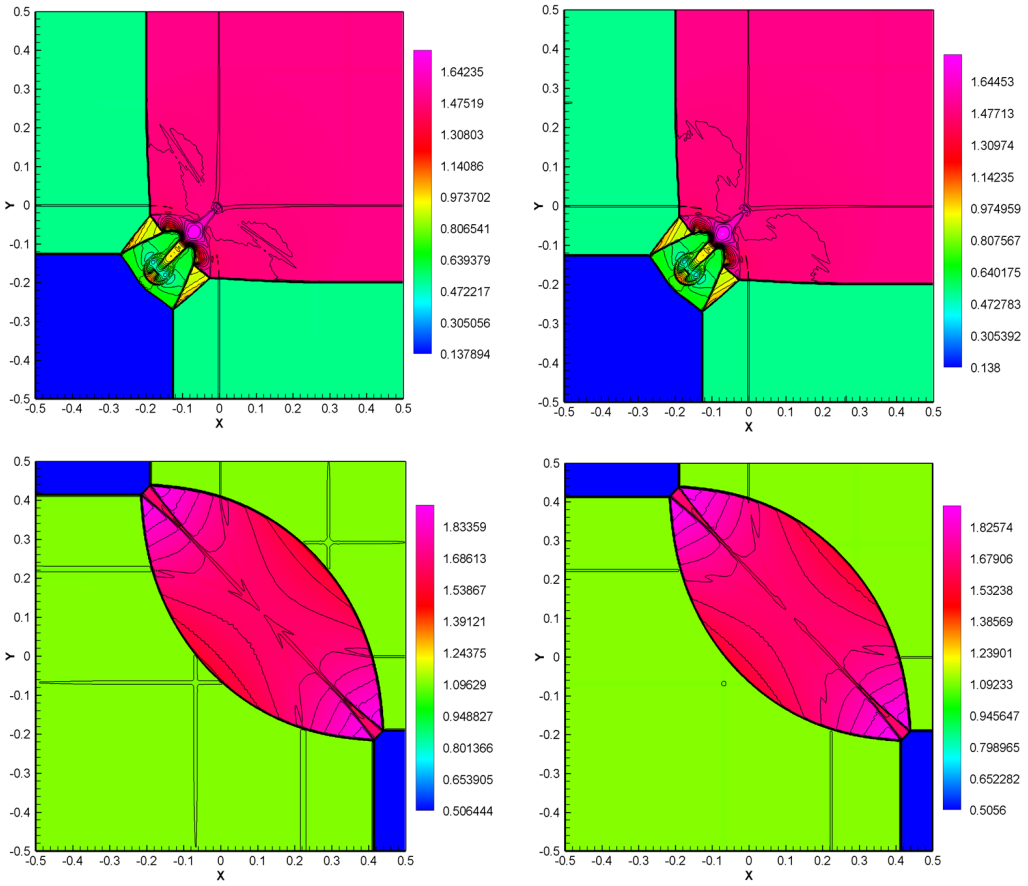


Figure 3.16: Numerical results for Riemann problems computed by WENO-Z and the present scheme with $400 \times 400$ mesh cells – 30 contours from min to max values for density – Left: WENO-Z scheme; Right: Present scheme.

#### 3.5.3.2 Double Mach reflection

Next, we have run the 2D double Mach reflection problem of a strong shock that was proposed by Woodward and Colella [117]. This test problem involves a Mach 10 shock in a perfect gas with $\gamma = 1.4$ which hits a $30^\circ$ ramp with the $x$-axis. Using Rankine-Hugoniot conditions we can deduce the initial conditions ($t = 0$) in front of and after the shock wave

$$(\rho, u, v, p)(x, y, 0) = \begin{cases} (8.0, 8.25\cos(\pi/6), -8.25\sin(\pi/6), 116.5), & \text{if} \quad x < x_0 = \frac{1}{6} + \frac{y}{\sqrt{3}}, \\ (1.4, 0.0, 0.0, 1.0), & \text{if} \quad x \geq x_0 = \frac{1}{6} + \frac{y}{\sqrt{3}}, \end{cases} \tag{3.23}$$

on the domain $\Omega = [0, 3.2] \times [0, 1]$. Reflecting wall boundary conditions are prescribed on the bottom and inflow and outflow boundary conditions on the left side and the right side, respectively. The exact solution of an isolated moving oblique shock wave with

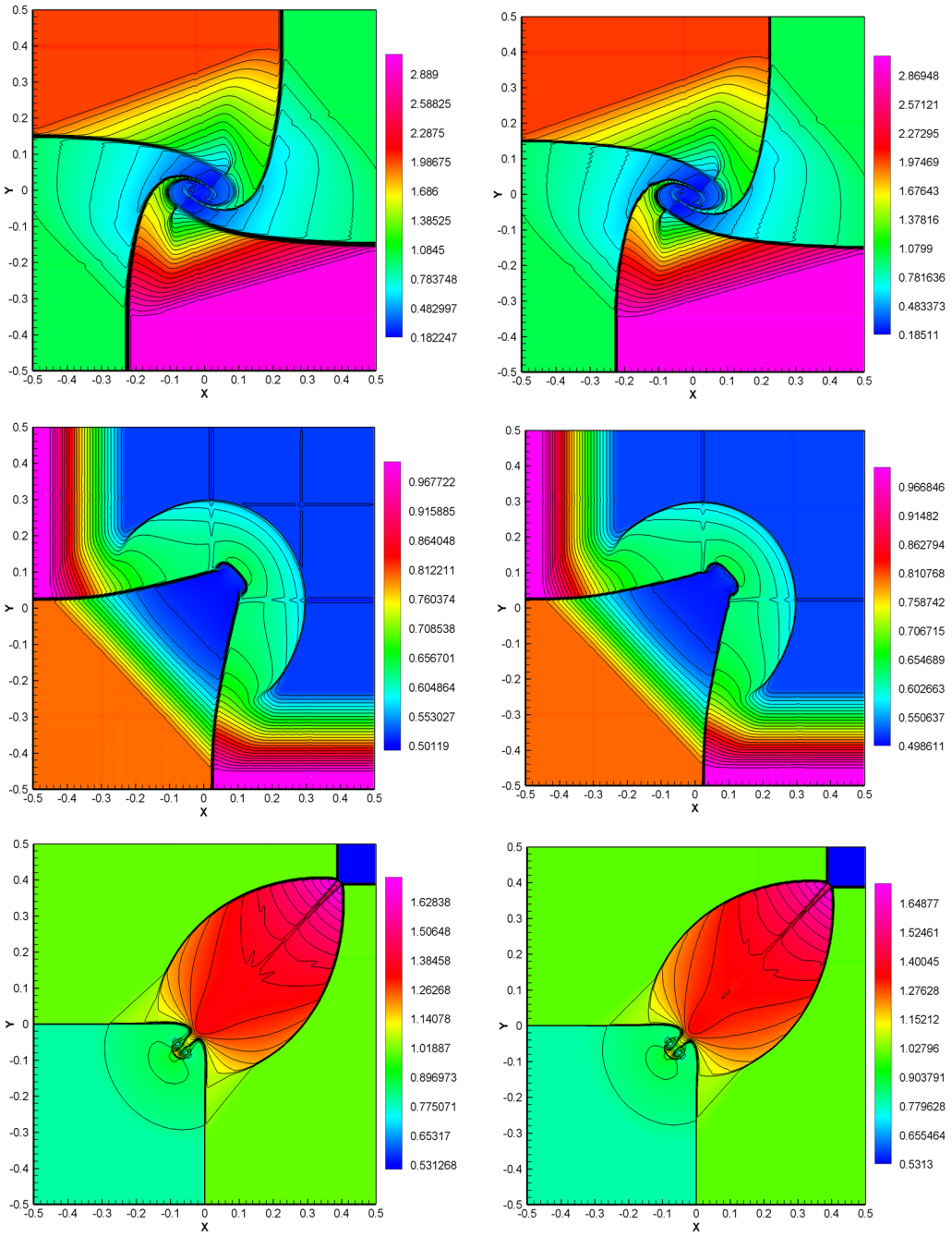


Figure 3.17: Numerical results for Riemann problems computed by WENO-Z and the present scheme with $400 \times 400$ mesh cells – 30 contours from min to max values for density – Left: WENO-Z scheme; Right: Present scheme.

Mach number $M_s = 10$ is imposed on the upper boundary. The location of shock-wave at any time $t$ on top boundary $y = 1$ is $s(t) = x_0 + \frac{1+20t}{\sqrt{3}}$. The boundary conditions on

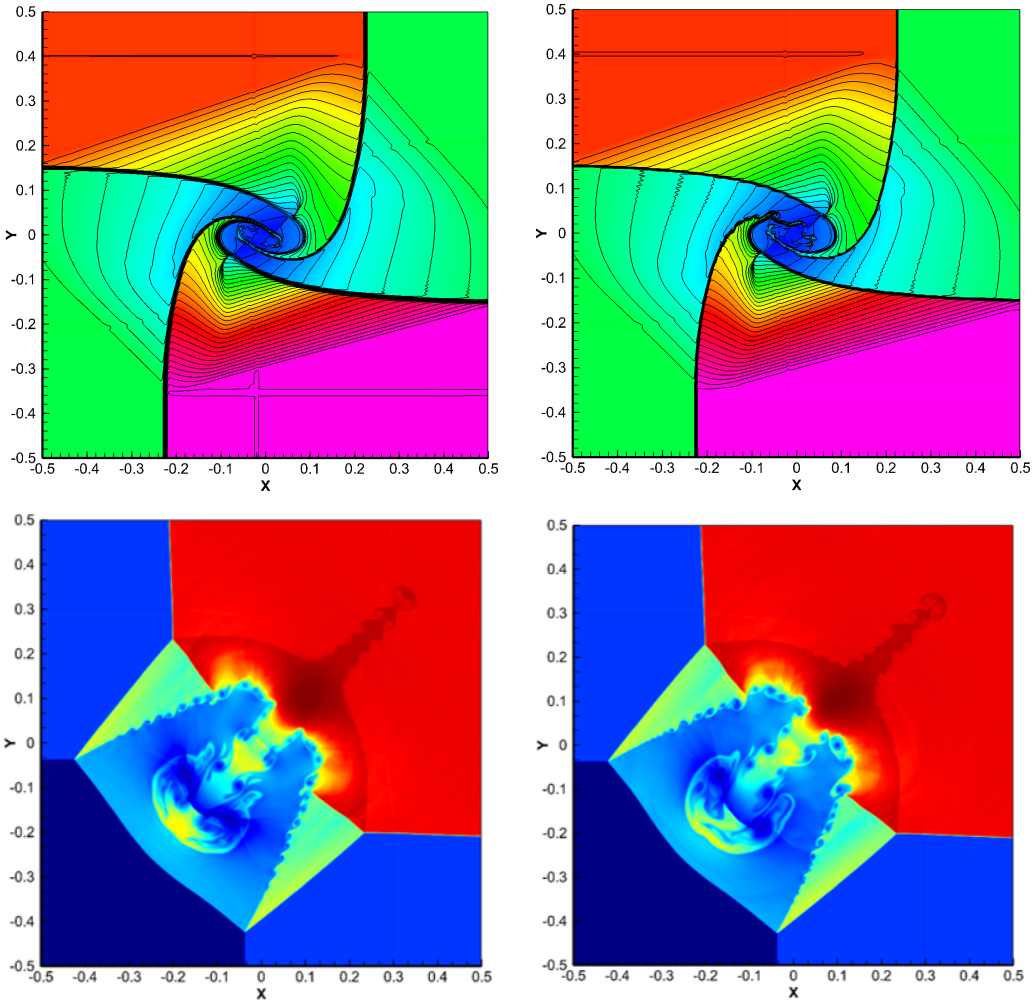


Figure 3.18: Numerical results for Riemann problems computed by WENO-Z and the present scheme with $600 \times 600$ mesh cells – 40 contours from min to max values for density – Left: WENO-Z scheme; Right: Present scheme, showing the Kelvin-Helmholtz instability on the shear waves.

the top boundary are therefore given by

$$(\rho, u, v, p)(x, y = 1, t) = \begin{cases} (8.0, 8.25\cos(\pi/6), -8.25\sin(\pi/6), 116.5), & \text{if} \quad 0 \leq x < s(t), \\ (1.4, 0.0, 0.0, 1.0), & \text{if} \quad s(t) \leq x \leq 4, \end{cases} \tag{3.24}$$

and the final time is set to $t_{\text{final}} = 0.2$. The mesh is made of $N_x \times N_y$ cells with $N_x = 320, 640, 960$ and $N_y = 100, 200, 300$, respectively. Although there exists no exact solution for this problem, it has become a classical bench-marking test in the literature because it involves shock waves and smooth recirculating flow zones.

In figure 3.19 we present the density variable in color with 30 contour iso-lines spanning

the interval $[1.4, 22.5]$ computed by three different grid resolutions, $\Delta x = \Delta y = \dfrac{1}{100}$ for the top panels, $\Delta x = \Delta y = \dfrac{1}{200}$ for the middle panels and $\Delta x = \Delta y = \dfrac{1}{300}$ for the bottom panels of figure 3.19. The zoomed-in part of the numerical results are presented in figure 3.20. The results obtained by the present scheme and those simulated by high order schemes in [39] (page 352 and figure 17) are in good agreement. Moreover, the present scheme has properly detected the shock waves without spurious oscillations and the vortexes along the slip line are more visible as shown by the fine grid computation.

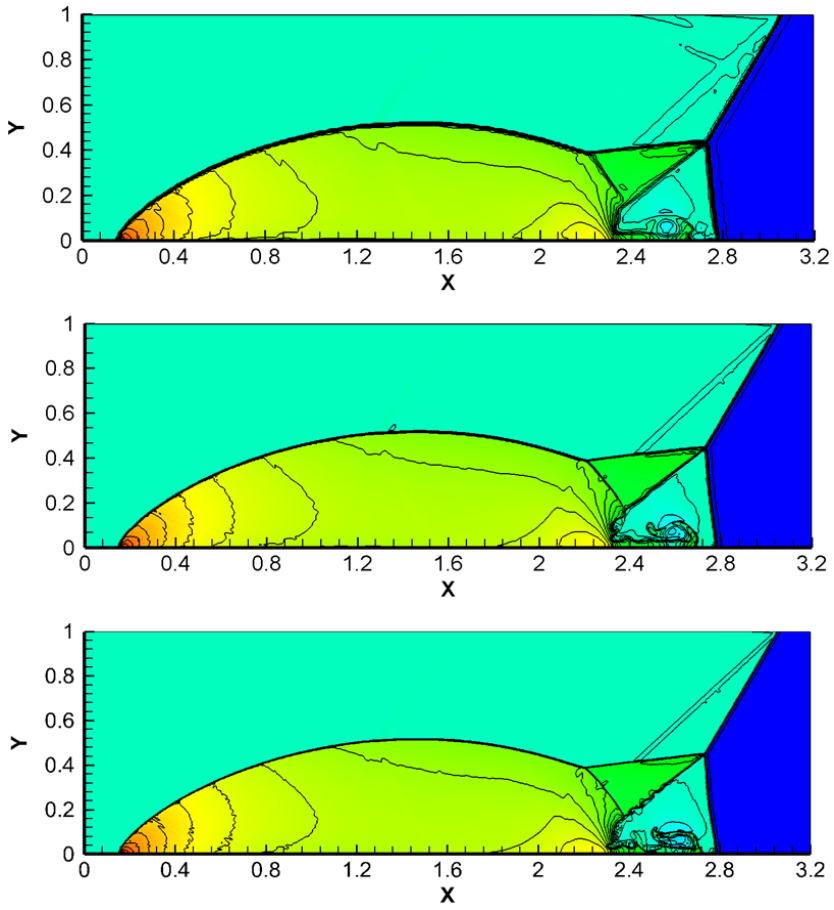


Figure 3.19: Numerical results for the 2D Euler equations – Double Mach reflection problem at time $t = 0.2$ simulated by the present scheme with different mesh numbers – Density variable in color and with 30 contour iso-lines spanning the interval $[1.4, 22.5]$ – Top panels: $320 \times 100$ mesh cells; Middle panels: $640 \times 200$ mesh cells; Bottom panels: $960 \times 300$ mesh cells.

#### 3.5.3.3 Shock-vortex interaction

Another classical test in two space dimensions is the interaction of a vortex with a steady shock wave. Originally proposed by [84], this test involves complex flow patterns with

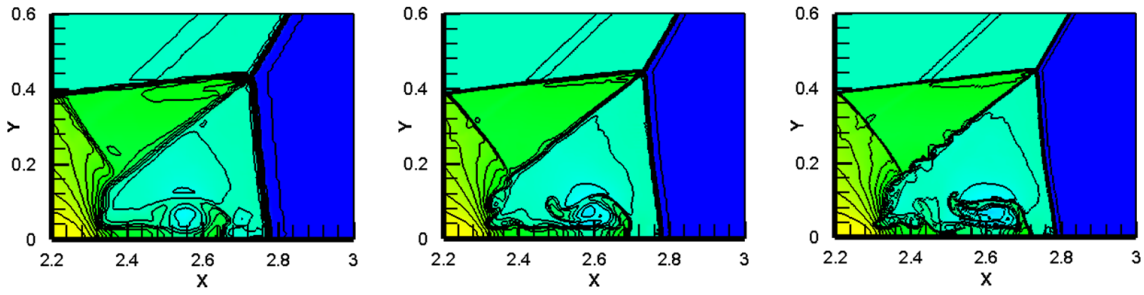


Figure 3.20: Numerical results for the 2D Euler equations – Double Mach reflection problem at time $t = 0.2$ simulated by the present scheme with different mesh numbers – Density variable in color and with 30 contour iso-lines spanning the interval $[1.4, 22.5]$ – Left panels: $320 \times 100$ mesh cells; Middle panels: $640 \times 200$ mesh cells; Right panels: $960 \times 300$ mesh cells.

smooth features and discontinuous waves. The initial conditions, defined over the computational domain $\Omega = [0,1] \times [0,1]$, are given by a stationary normal shock wave placed at $x = 0.5$ and by a vortex, which is centered at $(x_c, y_c) = (0.25, 0.5)$. The left and right states separated by the shock wave are given by

$$(\rho, u, v, p)(x, y, 0) = \begin{cases} (1, \sqrt{\gamma}, 0, 1), & \text{if} \quad x < \frac{1}{2}, \\ \left(\dfrac{\gamma - 1 + 1.3(\gamma+1)}{\gamma + 1 + 1.3(\gamma-1)}, \sqrt{\gamma} - \sqrt{2}\left(\dfrac{0.3}{\sqrt{\gamma - 1 + 1.3(\gamma+1)}}\right), 0, 1.3\right), & \text{if} \quad x \geq \frac{1}{2}, \end{cases} \tag{3.25}$$

The left state is supplemented by an isentropic vortex of the form

$$(\delta u, \delta v) = \left(\varepsilon \frac{y - y_c}{r_c} e^{\alpha(1-r^2)}, -\varepsilon \frac{x - x_c}{r_c} e^{\alpha(1-r^2)}\right), \quad \delta T = -\varepsilon^2 \frac{\gamma - 1}{4\alpha\gamma} e^{2\alpha(1-r^2)}, \tag{3.26}$$

with $r^2 = \dfrac{\|X - X_c\|^2}{r_c^2}$. The numerical simulations are performed over a uniformly mesh using 200 grid points per direction. Transmitive boundary conditions are imposed on the boundary and the final time is taken to be $t_{\text{final}} = 0.5$. The remaining parameters are set to $\varepsilon = 0.3$, $\alpha = 0.204$ and $r_c = 0.05$.

In figure 3.21 we present the 30 contours of density profile spanning $[0.998296, 1.30234]$ at final time for the WENO-Z (left panel) and $[0.997274, 1.29747]$ for the present scheme (right panel). We observe that both of the schemes have captured appropriately the shock waves without spurious oscillations as well as the smooth solution region. The CPU times observed for both schemes are 1953 seconds for WENO and 6% more expensive for the present scheme (2070 seconds) both ran on DEV-C++ Integrated Development

Environment. Hence, the present scheme can reproduce the quality of WENO-Z results for a comparable CPU time.

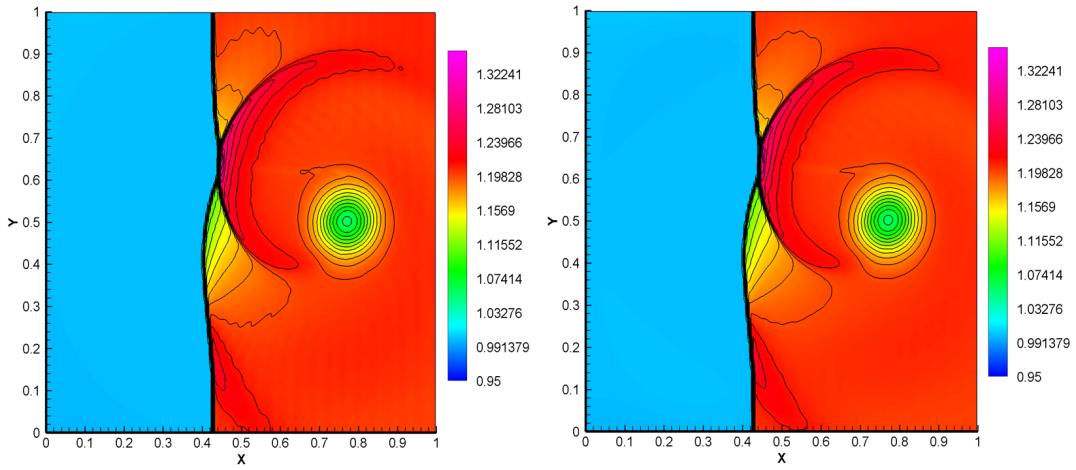


Figure 3.21: Numerical results for the 2D Euler equations – Shock-vortex interaction problem at final time – 30 contours from 0.95 to 1.35 for density – Left: WENO-Z scheme; Right: Present scheme.

#### 3.5.3.4 The 2D Sedov blast waves

For this cylindrical Sedov test [91], the computational domain is reduced to $[0, 1.2] \times [0, 1.2]$ where only the lower left corner cell contains the high energy of a perfect gas at rest ($\gamma = 1.4$). The initial condition is given by

$$(\rho_0, u_0, v_0, p_0) = \begin{cases} (1,\ 0,\ 0,\ \dfrac{0.244816}{\Delta x \Delta y}), & \text{if } x < \Delta x \quad \text{and} \quad y < \Delta y, \\ (1,\ 0,\ 0,\ 4 \times 10^{-13}), & \text{otherwise,} \end{cases} \tag{3.27}$$

where $\Delta x = \Delta y = \dfrac{1.2}{120}$ ($120 \times 120$ square cells) and the final time is $t_{\text{final}} = 1$. For the boundary conditions, an outflow boundary is applied to the right and upper boundaries while a reflective boundary is considered on the left and bottom boundaries. Figure 3.22 shows the density profiles computed by the present scheme at final time. We can observe that the results are in good agreement with the exact solution as a function of cell radius on the first panel. The cylindrical waves (shock and rarefaction) is well captured and preserved and the shock is maintained on few cells. Even though the value of density is very low towards the origin, the present scheme can simulate the test without any

blow-up or code crash.

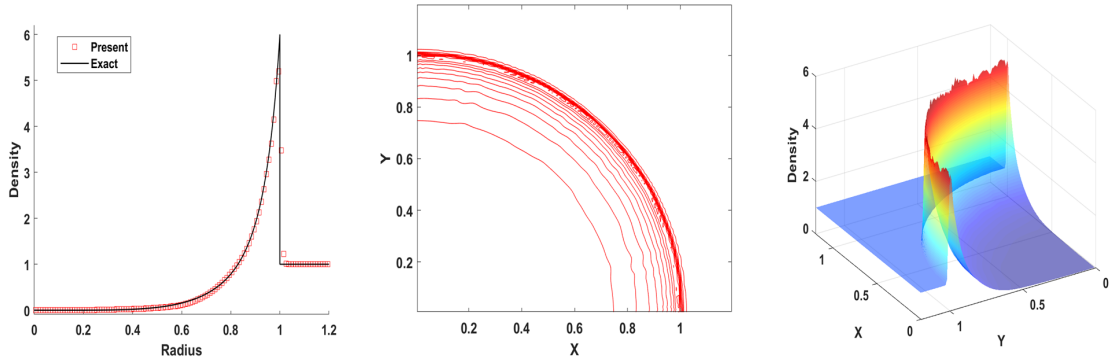


Figure 3.22: The numerical results for 2D Sedov blast waves problem at time $t_{\text{final}} = 1$ with $120$ mesh cells — Left: Density profile along $y = 0$ line vs the exact solution; Middle: $10$ density contours from $0$ to $6$; Right: Surface of density profile.

#### 3.5.3.5 High Mach number astrophysical jets

For this case we simulate some high speed of gas flows without radiative cooling, see [44, 45, 127, 128]. Notice that negative density and pressure could occur for such flows. We simulate two jets, a Mach 80 and a Mach 2000, described in [127] with $\gamma = 5/3$ on a computational domain $\Omega$. The initial condition is defined by

$$(\rho, u, v, p) = \begin{cases} (5,\ u_{\text{in}},\ 0,\ 0.4127), & \text{if } y \in [-0.05, 0.05], \\ (0.5,\ 0,\ 0,\ 0.4127), & \text{otherwise}, \end{cases} \tag{3.28}$$

where $u_{\text{in}} > 0$ is the inflow jet set on a portion of the left boundary. The boundary conditions are set to outflow for the right, top and bottom boundaries. The left boundary is an inflow boundary condition.

First, we simulate a Mach 80 on $\Omega = [0, 2] \times [-0.5, 0.5]$ with $u_{\text{in}} = 30$. The numerical solutions is computed up to time $t_{\text{final}} = 0.07$ with $448 \times 224$ mesh cells.

Figure 3.23 presents the numerical results for the density, pressure and temperature profiles in logarithmic scale. Even though very low density and pressure value occur in this test, the present scheme still performs well. The numerical results are comparable to those in [127]. Moreover the present scheme captures more complex small scale structures of the flow. Second, we simulate a Mach 2000 jet on $\Omega = [0, 1] \times [-0.25, 0.25]$

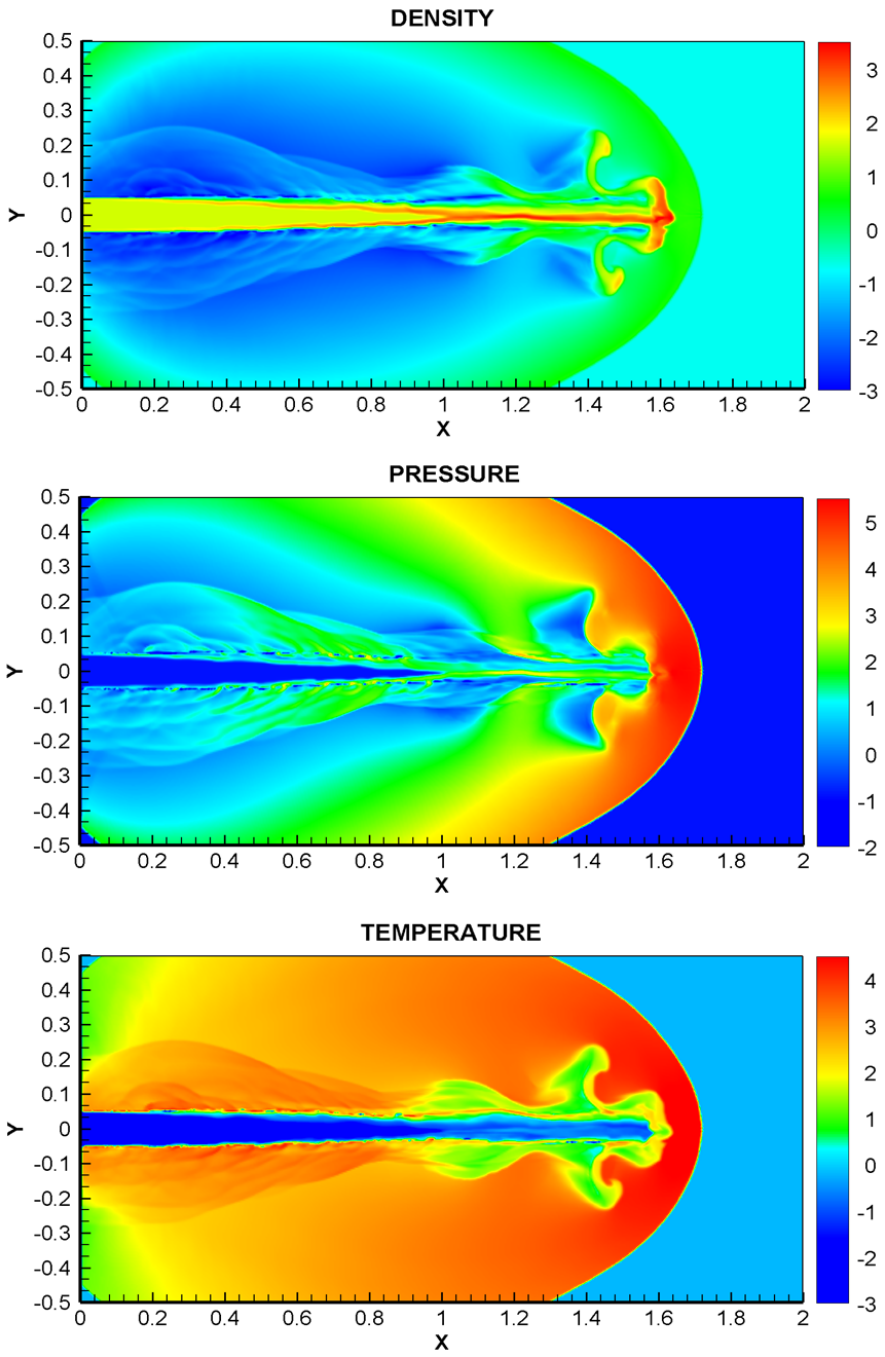


Figure 3.23: Numerical results for the 2D Euler equations – Mach jet 80 problem at time $t$final $= 0.07$ with $448 \times 224$ mesh cells simulated by the present scheme. Density, pressure and temperature maps in logarithmic scales.

by considering an inflow velocity magnitude $u_{\text{in}} = 800$. The numerical solution is computed up to time $t_{\text{final}} = 0.001$ with $640 \times 320$ mesh cells. Figure 3.24 presents the numerical results for density, pressure and temperature profiles in logarithmic scale.

The numerical results are comparable to those in [127, 130]. Again, the current method seems to capture more flow structures. This flow is obviously more violent than the pre-

vious one, emphasizing that the proposed numerical method is genuinely robust thanks to the MOOD loop and the first-order FV scheme used as a last resort.

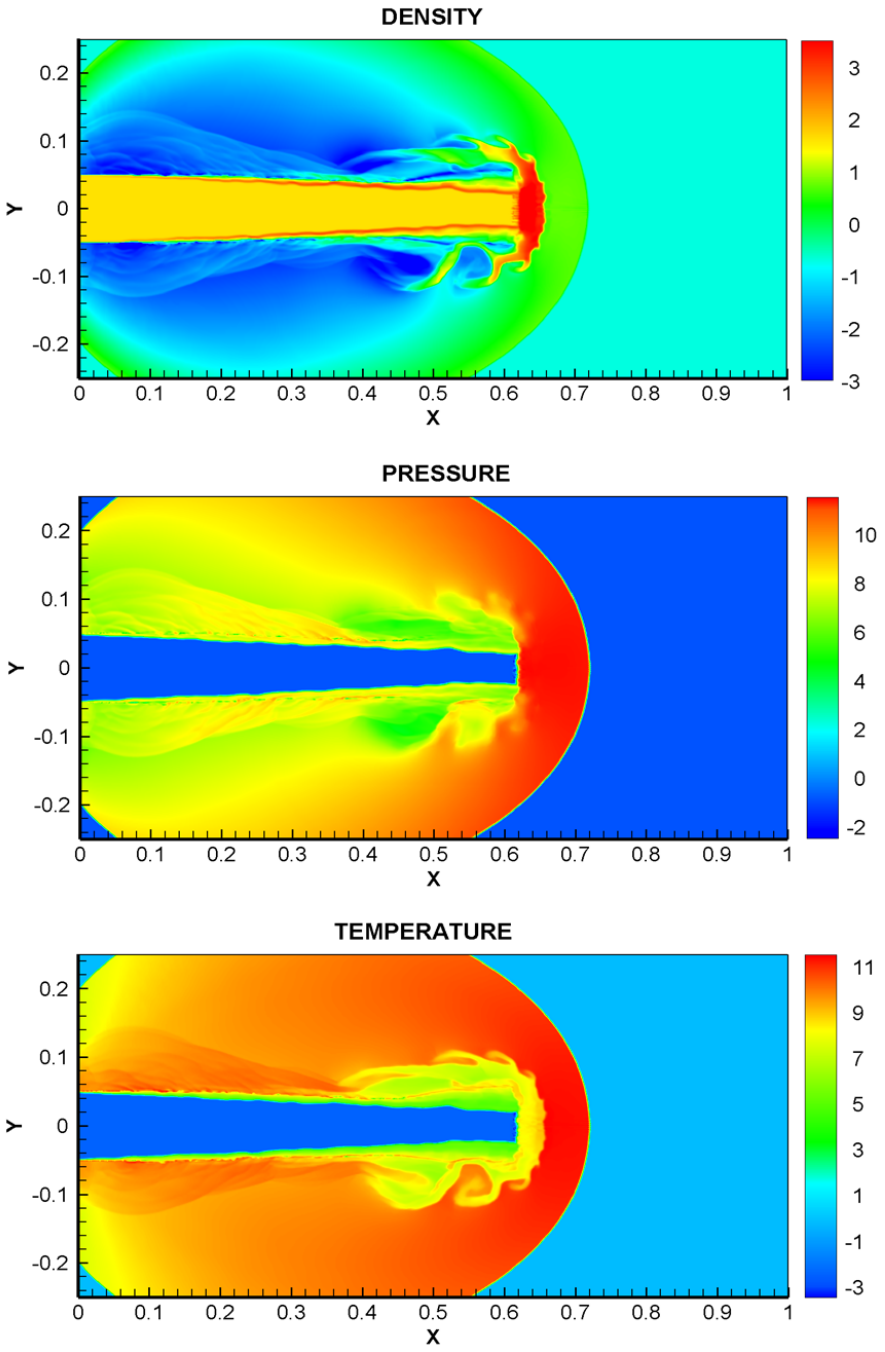


Figure 3.24: Numerical results for the 2D Euler equations – Mach jet 2000 problem at time $t\text{final} = 0.001$ with $640 \times 320$ mesh cells simulated by the present scheme. Density, pressure and temperature maps in logarithmic scales.

#### 3.5.3.6 Shock diffraction problem

As a last test case, the shock diffraction problem has been simulated. We can find this test in the literature for the DG method [25, 127] as well as finite difference WENO schemes [130]. Physically it consists of the diffraction of a shock wave at a sharp convex corner. Yet, no general theory exists which may describe this problem completely. Numerical simulations have been widely employed to understand the flow features generated by the shock diffraction, and, this problem has become popular to challenge new numerical methods. The main reason is that spurious negative density and/or pressure may be generated below and on the right of the corner.

The computational domain is the union of $\Omega_1 = [0,1]\times[6,11]$ and $\Omega_2 = [1,13]\times[0,11]$. The initial condition is a pure right-moving shock of mach $5.09$, initially located at $x = 0.5$ and $6 \leq y \leq 11$, and moving into the undisturbed air ahead of the shock characterized by a density of $1.4$ and a pressure of $1$. The boundary conditions are set to inflow at the left-most boundary $x = 0$ (for $6 \leq y \leq 11$), outflow at the right, top and bottom ones, $0 \leq y \leq 11$, $1 \leq x \leq 13$, $y = 0$, and $0 \leq x \leq 13$, $y = 11$, and reflective walls are considered on boundary $\Gamma_1 = \{(x,y),\ \text{s.t. } 0 \leq x \leq 1,\ y = 6\}$ and $\Gamma_2 = \{(x,y),\ \text{s.t. } 0 \leq y \leq 6,\ x = 1\}$. The specific heat ratio $\gamma = 1.4$ and final time of the computation is $t_{\text{final}} = 2.3$.

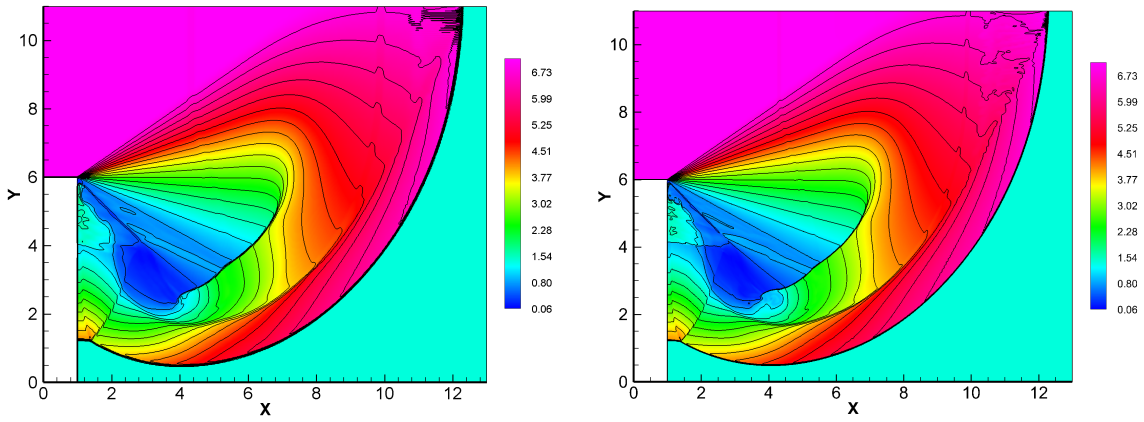


Figure 3.25: Numerical results for the 2D Euler equations – Shock Diffraction Problem 20 contours from $0.06$ to $7.1$ for density variable – Left: $\Delta x = \Delta y = \frac{1}{32}$; Right: $\Delta x = \Delta y = \frac{1}{64}$.

In figure 3.25 and figure 3.26 we present respectively the density variable in color with

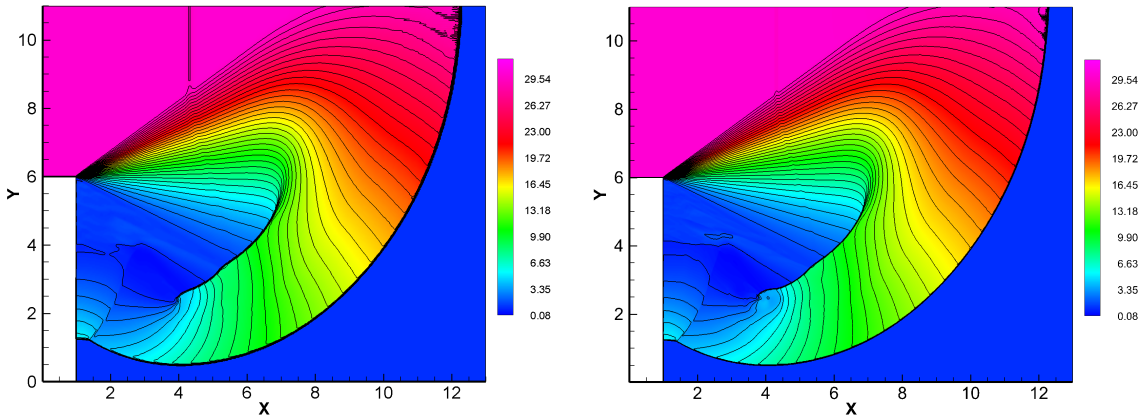


Figure 3.26: Numerical results for the 2D Euler equations – Shock Diffraction Problem $40$ contours from $0.08$ to $32$ for pressure variable – Left: $\Delta x = \Delta y = \frac{1}{32}$; Right: $\Delta x = \Delta y = \frac{1}{64}$.

$20$ contour iso-lines spanning the interval $[0.06, 7.1]$ and the pressure variable with $40$ contour iso-lines spanning the interval $[0.08, 32]$. Two different grid resolutions are considered, $\Delta x = \Delta y = \dfrac{1}{32}$ for the left panels and $\Delta x = \Delta y = \dfrac{1}{64}$ for the right panels. We observe that the results are comparable to those in [25, 127, 130] for the main flow structures. In our simulations, the MOOD loop allows to handle appropriately the occurrence of negative density or pressure which are cured by the use of the first-order FV scheme when needed. This allows the present scheme to become "fail-safe" to non-admissible physical Moreover the finer grid resolution allows to observe sharper discontinuities without the creation of spurious oscillations.

#### 3.5.3.7 Diagnostics on reconstruction selection for 2D Euler equations

Likewise for the 1D tests, in table 3.5 we present the percentage of cells for the four characteristic variables $W_1, W_2, W_3, W_4$ which are dealt with the HO, SHARP, ENO and piece-wise constant (P0) reconstructions. The tests are the 2D Sedov Blast waves, Mach 80 jet, Mach 2000 jet, shock-vortex interaction and shock diffraction problem with $\Delta x = \Delta y = \dfrac{1}{32}$. One sums up for every 10 time steps and final time step the number of cells using the same reconstruction and further takes the percentage with respect to the total number: $\dfrac{N_t}{10} \times (N_x \times N_y) + N_x \times N_y$. Each test case produces different flow patterns and the scheme does adapt. Consequently, for the reconstructions, we can not identify a general behavior which was expected. However, it seems that the HO reconstruction

Table 3.5: Percentage of cells dealt with the SHARP, HO, ENO, P0 reconstructions for the four characteristic variables $W_1, W_2, W_3, W_4$ and five test cases.

| **Test** | $N_t, N_x \times N_y$ | $W_1/W_3$ | | | | $W_2/W_4$ | | | |
|---|---|---|---|---|---|---|---|---|---|
| | | SH | HO | ENO | P0 | SH | HO | ENO | P0 |
| **Shock-V** | 657, 200x200 | 6.56% | 65.32% | 28.12% | 0% | 58.72% | 31.63% | 9.64% | 0% |
| | | 10.38% | 65.49% | 25.06% | 0% | 7.94% | 64.24% | 27.82% | 0% |
| **Sedov** | 3441, 120x120 | 7.22% | 81.41% | 11.37% | 0% | 6.51% | 81.1% | 12.39% | 0% |
| | | 5.99% | 81.79% | 12.22% | 0% | 9.75% | 80.57% | 9.68% | 0% |
| **M-80** | 1613, 448x224 | 9.25% | 77.9% | 12.8% | 0.05% | 9.85% | 76.49% | 13.61% | 0.05% |
| | | 9.64% | 78.09% | 12.22% | 0.05% | 9.77% | 77.28% | 12.9% | 0.05% |
| **M-2000** | 1904, 640x320 | 6.95% | 83.20% | 9.81% | 0.04% | 7.58% | 82.25% | 10.13% | 0.04% |
| | | 7.27% | 83.33% | 9.36% | 0.04% | 8.00% | 82.44% | 9.51% | 0.04% |
| **Shock-D** | 1708, 416x352 | 8.28% | 77.74% | 13.98% | 1E-4% | 7.97% | 78.14% | 13.89% | 1E-4% |
| | | 17.06% | 71.89% | 11.05% | 1E-4% | 10.43% | 76.8% | 12.77% | 1E-4% |

(target 5th order accuracy without dissipation) is selected for about $30\%$ up to $83\%$ of cells. The dissipative ENO reconstructions are selected between $9\%$ to $28\%$ of cells while the sharp reconstruction is chosen for $6\%$ up to $58\%$ of cells. At last the piecewise constant reconstruction is almost never selected (maximal $0.05\%$). But, recall that each time it is selected then it means that the code has created a non-physical state. In other words the code has been simply saved from code-crashing[2].

## 3.6 Summary

In this paper we have presented a reconstruction strategy to be employed in Finite Volume (FV) scheme which differs from classical polynomial-based with *a priori* limiting strategy. Most of classical schemes are based on a (linear) polynomial reconstruction, which is further supplemented with a non-linear limiter: classical slope limiter for piecewise linear reconstruction, (C)WENO blending, hierarchical moment limiter, artificial viscosity, etc. As such the accuracy in space of such FV schemes, measured for smooth solutions, is obtained by the accuracy with which the polynomials are reconstructed. In other words the polynomial degree drives the scheme accuracy. Meanwhile, the robustness and non-oscillatory behavior are obtained by the non-linear limiter which is often

[2]Note that $0.05\%$ of the cells for the Mach 80 jet problem may seem rather small. However it corresponds to about $81000$ cells among the $162$ millions of cell updates computed during the whole simulation.

computed just after the reconstructions.

Our approach differs because our cell-based reconstruction procedure relies on several types of reconstructions: (1) 5th order accurate polynomials for smooth solutions, (2) viscous non-linear THINC functions to add dissipation and (3) sharp non-linear ones to handle discontinuity and steep gradients, and, at last, (4) no reconstruction at all for extreme situations.

The fundamental mechanism in our approach to choose between these reconstructions relies on the BVD (Bounded Variation Diminishing) strategy. The reconstruction in one cell is chosen to be the one producing the smallest jumps at the cell interfaces. With BVD the reconstruction is polynomial $\mathbb{P}_4$ for smooth solutions, viscous on non-smooth solution (like a limited $\mathbb{P}_1$ reconstruction) and adopts a step-like shape for genuine discontinuous solution. Moreover, an *a posteriori* loop is added to the scheme to ensure that in the case the obtained numerical solution at time $t^{n+1}$ does not ensure fundamental properties like the positivity, computer representation, then, locally, the solution is recomputed with a first-order accurate FV scheme, *i.e.* without any reconstruction. As such a solution property preserving non-linear reconstruction procedure for Finite Volume scheme is designed. The rest of the FV scheme employs a HLLC flux, a Runge-Kutta time discretisation and dimension splitting to avoid costly multidimensional polynomial reconstructions. The goal is not to develop a provable optimal high accurate numerical method for smooth flows. Rather, the purpose of this work is to provide an efficient replacement for the pair (polynomial reconstruction, limiter) used in classical FV scheme (TVD, WENO, etc.). Indeed in our approach the scheme must select among several reconstructions, the most appropriate one according to goodness criteria. Some criteria are set *a priori* with BVD, some are verified *a posteriori* with MOOD. Being fundamentally 1D, the FV scheme proposed in this work is genuinely inexpensive. The numerical results prove that the scheme can capture both contact discontinuities and shocks on only two cells in 1D. Remarkably, such sharp interfaces can not generally be obtained with the state of the art FV schemes of high accuracy. This behavior is confirmed on 2D test problems for which the numerical method present genuinely sharp discontinuity for a second-order accurate scheme according to classical numerical analysis. The scheme

is extremely robust to positivity issues due to the *a posteriori* treatment and, at last, the directional splitting yields a very reasonable cost for such apparent accuracy.

# Chapter 4

# BVD+MOOD scheme for compressible Euler equations with source terms

In this chapter, the multi-stage BVD+MOOD scheme proposed in previous chapter is extended for applying the simulation of Euler equations with source terms (e.g. gravity and chemical reaction). The source terms of gravity and reaction are added to the Euler equations in this chapter. The Euler equations with gravitational source terms are implemented to model in several interesting physical phenomena. In the combustion process [41], the detonation is high speed combustion waves with strong leading shocks. The chemical reactions take place very fast and time scale of the chemical reaction is very small compared to the time scale of the fluid flow. According to its practical importance, the detonation is still and active area of research in both theoretical studies and numerical methods for aeronautics and astronautics engineering applications.

## 4.1 Issues of existing high-order finite volume methods

Existing high-order shock-capturing schemes are facing with several issues such as numerical oscillations, excessive numerical dissipation and failure in positivity-preserving when solving problems involving strong discontinuities and vacuum or near vacuum states occur.

As mentioned above, in reactive Euler equations, the source term represents the chem-

ical reactions which may move with a speed fasten than gas flow. For the problems involving reacting fronts that become stiff (strong mass transfer and heat release), to obtain reliable numerical results is resolving accurately and capturing sharply discontinuity of reacting fronts. The spurious phenomena in simulating stiff reacting flow is reported in [26, 115, 122, 126]. The detonation fronts may be predicted incorrectly by standard shock-capturing methods due to numerical dissipation. For example, the numerical dissipation smears some discontinuities which, in return incorrectly trigger the reaction of the source term and then produce a wrong numerical solution. Furthermore, if the grid is not sufficient enough, the enough temporal resolution cannot remove the incorrect propagation speed of the discontinuities and non-physical spurious waves cause by the discretization, especially in the shock with shock waves. Thus, the chemical reaction may be triggered at a wrong location. After the late or incorrectly located reaction, the new mass or energy in the vicinity of discontinuities is incorrectly captured (in space and time), and, all subsequent computed wave speeds and plateaus may be spoiled by excessive numerical dissipation.

For the last two decades, various strategies and numerical methods have been proposed to deal with this problem in order to obtain the correct wave propagation speed. A main strategy is to minimize the numerical diffusion in numerical scheme. A front tracking techniques, like ghost fluid/level set method [16, 80] or locally refined grid/time step [11, 55] and random choice scheme [20, 21] have been successfully resolved the problems of the under-resolved detonation waves. Another strategy, a simple temperature extrapolation method [37] was proposed and as well as ignition temperature random during reaction step [10]. Later, the random projection method [8, 9] was proposed by replacing the ignition temperature with uniformly distributed random variable. Recently, subcell-resolution [115] and fractional-step [126] methods were proposed which solves the convection step and reaction step separately.

Although the above mentioned numerical methods have successfully resolved the correct propagation wave speed, there is a main issue that quite often encounter situations is safe-failure in positivity-preserving. Physically, both density $\rho$ and pressure $p$ should be positive. For instance, high-order schemes may provide negative physical properties

when they are applied for low density problems in computing blast waves, low pressure problems in computing gaseous detonation propagation through different geometries. The occurrence of negative density or pressure is quite often encountered during the time evolution, which leads to a blow-up of the computation.

## 4.2 Solution procedure for compressible Euler equations with source terms

In this section, we introduce the solution procedure for compressible Euler equations with source term. General compressible Euler equations with different type of source terms are considered as models for physical situations such as gravitational source terms and detonation waves.

### 4.2.1 Governing equations

We consider the general form of one dimensional Euler equations with source terms, which is defined as

$$\frac{\partial U}{\partial t} + \frac{\partial F(U)}{\partial x} = S(U); \quad t \geq 0, \quad x \in \mathbb{R} \tag{4.1}$$

where where

$$\mathbf{U}(x,t) = \begin{pmatrix} \rho \\ \rho u \\ E \end{pmatrix}, \quad \mathbf{F}(\mathbf{U}) = \begin{pmatrix} \rho u \\ \rho u^2 + p \\ u(E+p) \end{pmatrix} \tag{4.2}$$

Here $\rho$, $u$, $p$ are the density, velocity, and pressure, respectively. $E$ is the total energy expressed as $E = e + \frac{1}{2}\rho u^2$ and $e$ is the specific internal energy. For ideal gas, the pressure can be computed by the equation of state (EOS) is defined as $p = (\gamma - 1)\rho e$ where $\gamma$ is the ratio of specific heats. The total enthalpy is computed by $H = (E+p)/\rho$. $S(U)$ is the source terms, i.e. gravity acceleration and detonation models of premixed reactive gases. The source terms are possibly becoming stiff compared to the local time

and space scales, and usually their main effect is to drastically modify the behavior of the solution.

### 4.2.2 Operator splitting

To solve the above model system, the numerical solution at each time step interval $[t, t+\Delta t]$ is computed in a split way: First the homogeneous conservation law (convection step) and, second the ODE system (source term step or reaction step). We describe in the following the fractional step approach [108] for gravitational source terms, and, the second order Strang-splitting method [102] for the more complex chemical reaction source terms.

**The Euler equations with gravity-like source terms:** The numerical solution at time level $t + \Delta t$ is approximated by

$$U(t + \Delta t) = C(\Delta t)\, R(\Delta t)\, U(t). \tag{4.3}$$

The convection operator $C(\Delta t)$ approximates the solution on the time interval $U(t+\Delta t)$ from the approximate solution $U(t)$, solving

$$\frac{\partial U}{\partial t} + \frac{\partial F(U)}{\partial x} = 0, \quad t \leq t' \leq t + \Delta t. \tag{4.4}$$

Different numerical schemes for hyperbolic conservation laws can be used at this stage. In this work, we use the third-order TVD Runge-Kutta method [43] for time integration and the multi-stage BVD-MOOD scheme for spatial discretization supplemented with HLLCM Riemann solver [92] to prevent the carbuncle phenomenon or shock instability. Other approximate Riemann solvers could be also employed for most cases.

The source term operator $R(\Delta t)$ approximates the solution on a time step of the ODE system

$$\frac{dU}{dt} = S(U), \quad t \leq t' \leq t + \Delta t. \tag{4.5}$$

Then, the explicit forward Euler method is used as follows

$$\overline{U}_R^{n+1} = \overline{U}^n + \Delta t S(\overline{U}^n), \tag{4.6}$$

in which the $\overline{U}_R^{n+1}$ is the updated value at source term step and $S(\overline{U}^n)$ is the source term. Any ODE solver can be used to deal with such source terms.

**The reactive Euler equations:** The numerical solution at time level $t + \Delta t$ is approximated generically by

$$U(t + \Delta t) = C\left(\frac{\Delta t}{2}\right) R\left(\Delta t\right) C\left(\frac{\Delta t}{2}\right) U(t). \tag{4.7}$$

In our numerical examples, $N_r$ su-steps may be employed in one reaction step. Therefore, the above equation is become as

$$U(t + \Delta t) = C\left(\frac{\Delta t}{2}\right) R\left(\frac{\Delta t}{N_r}\right) \cdots R\left(\frac{\Delta t}{N_r}\right) C\left(\frac{\Delta t}{2}\right) U(t). \tag{4.8}$$

Similarly, $C$ is the convection operator acting over time $\Delta t/2$ and $R$ is the reaction operator. We use $N_r = 2$ sub-steps in this work. Any ODE solver can be used for the reaction operator providing that the discontinuities are sharply dealt with during the convective step.

### 4.2.3 Finite volume method

In this section, we briefly describe the fundamental algorithm under the finite volume context for the convection step. Let us consider the computational domain in space as $\Omega = [x^L, x^R]$ divided into $N$ non-overlapping cells with $I_i = [x_{i-1/2}, x_{i+1/2}]$, for $i = 1, 2, ..., N$. The cell size is denoted by $\Delta x = x_{i+1/2} - x_{i-1/2}$ and is uniform over the computation domain. Furthermore, the time variable is denoted by $t$ and $0 < t < t_{\text{final}}$, where $t_{\text{final}} > 0$ is the terminal time for the computation. The time is split into $N_t$ non-uniform time steps paving the interval $[0, t_{\text{final}}]$. The time step is denoted as $\Delta t = t^{n+1} - t^n > 0$, where $t^n$ is the time at $n^{th}$ step, likewise for $t^{n+1}$. The time-step

will be restricted by a CFL condition later.

We employ the volume integrated-average (VIA) of the solution $U(x,t)$ using a standard finite volume semi-discretization, over a mesh cell $I_i$ at time $t$ as

$$U_i(t) = \frac{1}{\Delta x} \int_{x_{i-1/2}}^{x_{i+1/2}} U(x,t)\, dx \qquad \text{where} \qquad i = 1, 2, \ldots, N. \tag{4.9}$$

The VIA $U_i(t)$ for each cell $I_i$ is updated by

$$\frac{dU_i(t)}{dt} = -\frac{1}{\Delta x} \left( F_{i+1/2}(t) - F_{i-1/2}(t) \right), \tag{4.10}$$

where $F_{i+1/2}(t)$ and $F_{i-1/2}(t)$ are the numerical fluxes at cell boundaries, calculated by a (approximated) Riemann solver

$$F_{i+1/2}(t) = F^{\text{Riemann}}_{i+1/2}(U^L_{i+1/2}, U^R_{i+1/2}, t), \tag{4.11}$$

where $U^L_{i+1/2}$ and $U^R_{i+1/2}$ are the left-side and right-side values of $U$ at $x_{i+1/2}$ respectively. They are computed by a so-called reconstruction procedure over left and right potential stencils. The approximate flux in Eq.(4.11) can be written for a wide range of Riemann solvers into the general form

$$F^{\text{Riemann}}_{i+1/2}(U^L_{i+1/2}, U^R_{i+1/2}, t) = \frac{1}{2} \left( F(U^L_{i+1/2}) + F(U^R_{i+1/2}) \right) - \frac{|a_{i+1/2}|}{2} (U^R_{i+1/2} - U^L_{i+1/2}), \tag{4.12}$$

where $a_{i+1/2}$ varies among different Riemann solvers. As already mentioned we use the HLLCM approximate Riemann solver, the details of which can be found in [92].

### 4.2.4 Time Integration

In order to achieve high-order numerical accuracy in time, the discretization in time is made by the third-order TVD Runge-Kutta method (RK3, see [93, 43]). More precisely, defining

$$L(U) = -\frac{1}{\Delta x} \left( F_{i+1/2}(t) - F_{i-1/2}(t) \right), \tag{4.13}$$

as the spatial operator, then the time integration corresponds to a convex combination of three explicit steps as

$$\begin{aligned} U^{(1)} &= U^n + \Delta t L(U^n), \\ U^{(2)} &= \frac{3}{4}U^n + \frac{1}{4}U^{(1)} + \frac{1}{4}\Delta t L(U^{(1)}), \\ U^{n+1} &= \frac{1}{3}U^n + \frac{2}{3}U^{(2)} + \frac{2}{3}\Delta t L(U^{(2)}). \end{aligned} \tag{4.14}$$

This time integration scheme is restricted by the CFL condition

$$\Delta t \leq \text{CFL}\frac{\Delta x}{\max_i(|u_i|, |u_i \pm a_i|)}, \tag{4.15}$$

where CFL $< 1$ is a safety constant.

The remaining main task (detailed in the previous chapter) is the calculation of states $U^L_{i+1/2}$ and $U^R_{i+1/2}$ at given time $t$ through a reconstruction procedure.

In this work, we introduce a blending of high/low order polynomial and hyperbolic tangent reconstructions. The blending serves the purpose of preserving some of the properties of the solution. Moreover, the reconstructions are performed on the characteristics variables and each variable of the same cell employs the same reconstruction type. Because we employ high order polynomials and non-linear hyperbolic tangent as reconstruction types, the limiting procedure, mandatory to avoid Gibbs phenomenon and damp spurious oscillations, is handled in a non-classical way. Indeed following previous chapter we split the numerical solution into three parts: a large part of the domain welcomes a smooth solution, relatively small area suffer from the presence of discontinuous solutions, and, extremely small area present extreme physical situations (close to vacuum states for instance).

## 4.3 Review of reconstruction schemes for solution property preserving

The numerical solution for the hyperbolic system of partial differential equations (PDEs) is split into three regions: 'smooth' (large), 'discontinuous' (few) and 'demanding' enduring physics violation (almost zero). An unlimited piece-wise high order polynomial reconstruction is employed for the smooth profile, while a shock-capturing THINC reconstruction deals with discontinuous profiles in a sharp and essentially non-oscillatory manner. At last, the demanding regions in the flow where non-admissible physical state may be computed which are dealt with the monotonic, dissipative and robust first order Godunov scheme.

The numerical scheme should preserve some properties of the numerical solution related to those regions, for instance, a high accurate description of smooth profiles, an essentially non-oscillatory behavior in the vicinity of steep gradients, a sharp capture of discontinuity (contact, material interface), and, robustness for extreme situations.

### 4.3.1 Candidate reconstruction schemes

In order to fulfill these properties, we design a chain of different reconstruction operators via a multi-stage BVD-MOOD algorithm [106]. We denote them as $\mathcal{R}_{HO}$, $\mathcal{R}_{ENO}$, $\mathcal{R}_{SHARP}$ and $\mathcal{R}_{LO}$ standing for High Order polynomial, Essentially Non-Oscillatory, Sharp and Low Order polynomial reconstructions, respectively. The main tool is the so-called BVD which acts as a selector which chooses the most suitable reconstruction. For instance, for a smooth profile, the selector should choose the high-order reconstruction $\mathcal{R}_{HO}$, while the sharp one $\mathcal{R}_{SHARP}$ should be selected for the steep gradient or step-like profile/shock. In table 4.1, the five candidate reconstructions are listed with their different behaviors; on smooth solutions, to suppress spurious oscillations, on discontinuous solutions, and to handle extreme demanding situations.

In this work, the BVD 'selector' is operating on two reconstructed candidates in the same cell, and, chooses the most suitable one. Since we consider of three possible re-

Table 4.1: Table of reconstructions and their associated target property.

| Acronym | Reconstruction | Parameter | Solution property |
|---|---|---|---|
| $\mathcal{R}_{\text{HO}}$ | $\mathbb{P}_k \Rightarrow$ unlimited polynomial | $k = 4$ | smooth profile |
| $\mathcal{R}_{\text{ENO}_2}$ | THINC | $\beta = 1.2$ | (damp) spurious oscillations |
| $\mathcal{R}_{\text{ENO}_1}$ | THINC | $\beta = 1.1$ | (kill) spurious oscillations |
| $\mathcal{R}_{\text{SHARP}}$ | THINC | $\beta = 1.6$ | steep profile |
| $\mathcal{R}_{\text{LO}}$ | $\mathbb{P}_k \Rightarrow$ no reconstruction | $k = 0$ | ensure admissible solution (i.e positivity issue, `NaN`) |

constructions, $\mathcal{R}_{HO}$, $\mathcal{R}_{ENO}$ or $\mathcal{R}_{SHARP}$, then the BVD algorithm acts in 2 stages leading to a so-called multi-stage BVD, see figure 3.2. This BVD algorithm is exhaustively described in Section 4.3.2.

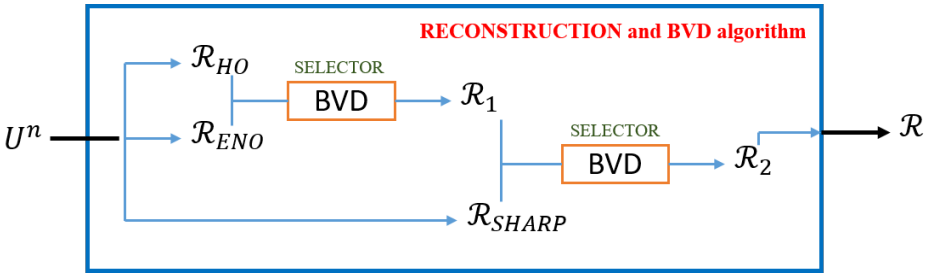


Figure 4.1: Sketch of Reconstruction schemes for Solution Property Preserving and BVD algorithm for a given cell. At stage 1, the BVD algorithm selects between $\mathcal{R}_{\text{HO}}$ and $\mathcal{R}_{\text{ENO}}$ reconstructions to get the most suitable of the two, say $\mathcal{R}_1$. Then, At stage 2, BVD chooses either reconstruction $\mathcal{R}_1$ or $\mathcal{R}_{\text{SHARP}}$ to get $\mathcal{R}_2$ as the final reconstruction to be used to update the current cell.

### 4.3.2 A 3-stage BVD algorithm: local reconstruction selector

The fifth-order upwind scheme or PQM is used to achieve optimal order for smooth solution. However, the numerical oscillations will appear in the vicinity of discontinuity. In order to suppress the numerical oscillations and to resolve the discontinuous solutions, the THINC reconstruction functions are employed and relied on Boundary Variation Diminishing (BVD) algorithm [30, 31, 32, 103]. In this work, the selection algorithm in the P4-THINC-BVD-MOOD scheme designed in [106] is re-used. It determines the candidate interpolant with three-stages cascade BVD process which minimizes the total boundary variation (TBV) in the desired cell. More precisely, the TBV of cell $I_i$ is defined by the sum of the jumps generated by the reconstructed values using reconstruction

operator $\mathcal{R}$ at cell interfaces, that is

$$\mathrm{TBV}_i^{\mathcal{R}}(U) = \left|U_{i-1/2}^{L,\mathcal{R}} - U_{i-1/2}^{R,\mathcal{R}}\right| + \left|U_{i+1/2}^{L,\mathcal{R}} - U_{i+1/2}^{R,\mathcal{R}}\right| \geq 0. \tag{4.16}$$

Each term of the right hand side represents the amount of dissipation introduced by the numerical flux (4.12) for one edge of cell $I_i$. Thus, $\mathrm{TBV}_i^{\mathcal{R}}$ scales like the numerical dissipation in the cell. For simplicity of exposition, we denote by $\mathcal{R}_{\mathrm{ST}_1}$, $\mathcal{R}_{\mathrm{ST}_2}$, and $\mathcal{R}_{\mathrm{ST}_3}$ the reconstruction operators in cell $I_i$ after the first, second and third stage, respectively. For instance, when two reconstructions $\mathcal{R}_1$ and $\mathcal{R}_2$ of the same data $\mathsf{U}$ are available then we compute, compare $\mathrm{TBV}_i^{\mathcal{R}_1}$ and $\mathrm{TBV}_i^{\mathcal{R}_2}$, and choose the least dissipative one. The BVD algorithm automatically exploits this matter.

The 3-stage BVD algorithm is implemented in the spirit of [30, 31, 106]. Let us denote by $\mathrm{r}_i$ the actual reconstruction employed in cell $I_i$ which can be HO, $\mathrm{ENO}_1$, $\mathrm{ENO}_2$, or SHARP.

**Stage 1.** Selection between $\mathcal{R}_{\mathrm{HO}}$ and $\mathcal{R}_{\mathrm{ENO}_2} \to \mathcal{R}_{\mathrm{ST}_1}$

Compute the $\mathrm{TBV}_i$ values for the cell $I_i$ by $\mathcal{R}_{\mathrm{HO}}$ and $\mathcal{R}_{\mathrm{ENO}_2}$ as

$$\begin{aligned}
\mathrm{TBV}_i^{\mathcal{R}_{\mathrm{HO}}} &= \left|U_{i-1/2}^{L,\mathcal{R}_{\mathrm{HO}}} - U_{i-1/2}^{R,\mathcal{R}_{\mathrm{HO}}}\right| + \left|U_{i+1/2}^{L,\mathcal{R}_{\mathrm{HO}}} - U_{i+1/2}^{R,\mathcal{R}_{\mathrm{HO}}}\right| \\
\mathrm{TBV}_i^{\mathcal{R}_{\mathrm{ENO}_2}} &= \left|U_{i-1/2}^{L,\mathcal{R}_{\mathrm{ENO}_2}} - U_{i-1/2}^{R,\mathcal{R}_{\mathrm{ENO}_2}}\right| + \left|U_{i+1/2}^{L,\mathcal{R}_{\mathrm{ENO}_2}} - U_{i+1/2}^{R,\mathcal{R}_{\mathrm{ENO}_2}}\right|
\end{aligned} \tag{4.17}$$

For cell $i$, if $\mathrm{TBV}_i^{\mathcal{R}_{\mathrm{HO}}} > \mathrm{TBV}_i^{\mathcal{R}_{\mathrm{ENO}_2}}$ then $(\mathrm{r}_{i-1}, \mathrm{r}_i, \mathrm{r}_{i+1}) = \mathrm{ENO}_2$, else $\mathrm{r}_i = \mathrm{HO}$.

$\mathcal{R}_{\mathrm{ST}_1} = \{\mathrm{r}_i,\ i = 1, \ldots, N\}$

**Stage 2.** Selection between $\mathcal{R}_{\mathrm{ST}_1}$ and $\mathcal{R}_{\mathrm{ENO}_1} \to \mathcal{R}_{\mathrm{ST}_2}$

Compute the $\mathrm{TBV}_i$ values for the cell $I_i$ by $\mathcal{R}_{\mathrm{ST}_1}$ and $\mathcal{R}_{\mathrm{ENO}_1}$ as

$$\begin{aligned}
\mathrm{TBV}_i^{\mathcal{R}_{\mathrm{ST}_1}} &= \left|U_{i-1/2}^{L,\mathcal{R}_{\mathrm{ST}_1}} - U_{i-1/2}^{R,\mathcal{R}_{\mathrm{ST}_1}}\right| + \left|U_{i+1/2}^{L,\mathcal{R}_{\mathrm{ST}_1}} - U_{i+1/2}^{R,\mathcal{R}_{\mathrm{ST}_1}}\right| \\
\mathrm{TBV}_i^{\mathcal{R}_{\mathrm{ENO}_1}} &= \left|U_{i-1/2}^{L,\mathcal{R}_{\mathrm{ENO}_1}} - U_{i-1/2}^{R,\mathcal{R}_{\mathrm{ENO}_1}}\right| + \left|U_{i+1/2}^{L,\mathcal{R}_{\mathrm{ENO}_1}} - U_{i+1/2}^{R,\mathcal{R}_{\mathrm{ENO}_1}}\right|
\end{aligned} \tag{4.18}$$

Similar to stage 1, for cell $i$, if $\mathrm{TBV}_i^{\mathcal{R}_{\mathrm{ST}_1}} > \mathrm{TBV}_i^{\mathcal{R}_{\mathrm{ENO}_1}}$ then $(\mathrm{r}_{i-1}, \mathrm{r}_i, \mathrm{r}_{i+1}) = \mathrm{ENO}_1$.

$\mathcal{R}_{\mathrm{ST}_2} = \{\mathrm{r}_i,\ i = 1, \ldots, N\}$

**Stage 3.** Selection between $\mathcal{R}_{\text{ST}_2}$ and $\mathcal{R}_{\text{SHARP}} \rightarrow \mathcal{R}_{\text{ST}_3}$

Compute the $\text{TBV}_i$ values for the cell $I_i$ by $\mathcal{R}_{\text{ST}_2}$ and $\mathcal{R}_{\text{SHARP}}$ as

$$\begin{aligned} \text{TBV}_i^{\mathcal{R}_{\text{ST}_2}} &= \left| U_{i-1/2}^{L,\mathcal{R}_{\text{ST}_2}} - U_{i-1/2}^{R,\mathcal{R}_{\text{ST}_2}} \right| + \left| U_{i+1/2}^{L,\mathcal{R}_{\text{ST}_2}} - U_{i+1/2}^{R,\mathcal{R}_{\text{ST}_2}} \right| \\ \text{TBV}_i^{\mathcal{R}_{\text{SHARP}}} &= \left| U_{i-1/2}^{L,\mathcal{R}_{\text{SHARP}}} - U_{i-1/2}^{R,\mathcal{R}_{\text{SHARP}}} \right| + \left| U_{i+1/2}^{L,\mathcal{R}_{\text{SHARP}}} - U_{i+1/2}^{R,\mathcal{R}_{\text{SHARP}}} \right| \end{aligned} \tag{4.19}$$

For cell $i$, if $\text{TBV}_i^{\mathcal{R}_{\text{ST}_2}} > \text{TBV}_i^{\mathcal{R}_{\text{SHARP}}}$ then $\text{r}_i = \text{SHARP}$.

$\mathcal{R}_{\text{ST}_3} = \{\text{r}_i,\ i = 1, \ldots, N\}$

**Remark 1.** According to the formulation of this method, the essentially oscillation-free solution is obtained after stage 1 and 2. In addition, the numerical dissipation at discontinuous/steep gradients is reduced after stage 3, if needed. It means that the desired properties are reinforced respectively at different stages by the multi-stage BVD algorithm.

**Remark 2.** In this chapter, we employ the BVD algorithm independently for each characteristic variables [30, 31], however, one could also consider the implementation of BVD algorithm with a dependency among the reconstructed variables such as in [106]. Otherwise, for the reactive Euler equations, the BVD algorithm with a dependency among the reconstructed variables is not suitable to employ since it may generate spurious oscillations due to stiffness of source terms and volume fraction variables. Our numerical experiments reveal that our approach can achieve optimal high order, however, it may produce slightly noisy and diffusive results in some cases.

**Remark 3.** In the multi-stage BVD the THINC reconstruction with small $\beta$ values (ENO) as $\beta = 1.1$ or $\beta = 1.2$ could be replaced by another TVD scheme. Contrarily, the unlimited high order polynomial reconstruction (HO) and THINC with high $\beta$ value (SHARP) as $\beta = 1.6$ are mandatory operators. The HO one ensures the highest possible accuracy for smooth profiles, while the SHARP one is efficient, robust scheme and steepens discontinuous profiles. As well as other reconstruction scheme, the low order (LO) must be carefully detected by MOOD algorithm in order to preserve the positivity and valid representation of numbers. In this work, we employ the first order accurate

Godunov scheme which is simplest, monotonic and most robust positivity-preserving scheme.

### 4.3.3 Positivity-preserving and physical admissibility via an *a posteriori* MOOD algorithm

The last property of paramount importance is the ability to handle or deal with extreme physical and numerical situations such as the lack of positivity for density or pressure for gas flows or the occurrence of un-representable digit values (`NaN`, `Inf`). The positivity-preserving or a fail-safe behavior is usually difficult to ensure *a priori* by the reconstruction operators which are employed in the multi-stage BVD algorithm. Here we use the so-called *a posteriori* Multi-dimensional Optimal Order Detection (MOOD) algorithm [22, 34, 36]. In a MOOD procedure, the non-oscillatory behavior and physics admissibility are ensured via a list of criteria detecting the problematic or troubled cells. Being an *a posteriori* limiting procedure, it is performed after the computation of a candidate solution at $t^{n+1}$. The detection procedure checks whether the candidate solution $U_i^{n+1,*}$ satisfies the criteria for each cell. The cells where they are satisfied, are marked as 'valid' cells, and, the numerical solution is accepted: $U_i^{n+1} = U_i^{n+1,*}$. Contrarily the cells which do not pass the criteria are marked as 'troubled'. A troubled cell is locally recomputed starting again at time $t^n$ but using the first-order Godunov scheme (piecewise constant reconstruction), see in figure 4.2. This first-order finite volume scheme produces an excessive numerical viscosity and tends to smear out the flow structures. However, it is conservative, monotone, robust and positivity-preserving.

In addition, the detection is split into a Physical Admissible Detection (PAD) and Numerical Admissible Detection (NAD). The PAD is based on the physical properties to ensure that a solution is admissible. For Euler system of equations the physical admissibility is related to the positivity of density $\rho$ and pressure $p$. More precisely, a cell is PAD troubled if $\rho_i^{n+1,*} \leq 0$ or $p_i^{n+1,*} \leq 0$. In addition, for the reacting Euler equations, a cell may be PAD troubled if $\alpha_i^{n+1,*} < 0$, where $\alpha$ is the mass fraction, otherwise the cell is eligible. The NAD checks if a cell is such that $U_i^{n+1,*} = \texttt{NaN}$ then it is flagged as NAD troubled, otherwise the cell is valid.

Once a cell $I_i$ is troubled, then, as already mentioned, it is locally recomputed by the first-order Godunov scheme. Its direct neighbors are also marked as troubled cells for safety reason.

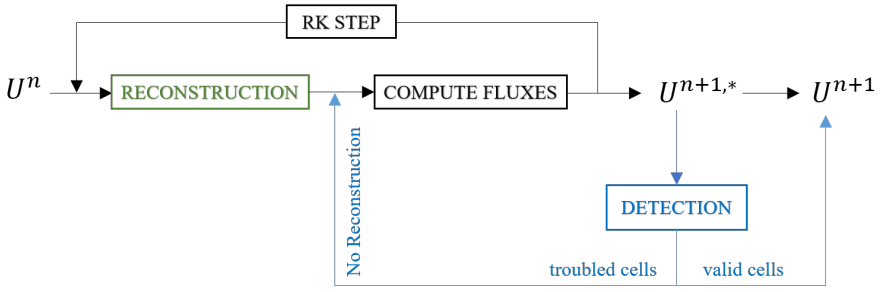


Figure 4.2: Sketch of FV method with an *a posteriori* MOOD algorithm. If the positivity is violated or a `NaN` is occurring, the Detection procedure (PAD or NAD) marks the troubled cells. Then, those troubled cells and their direct neighbors are sent back to $t^n$ for a re-computation by the first order Godunov scheme (using $\mathbb{P}_0$ reconstruction). Otherwise, the valid cells are accepted as the final solution.

## 4.4 Extensions to multi-space dimensions

We have implemented and extended the previous numerical scheme in two-dimensions on structured grids. The scheme in 1D has been designed to be genuinely efficient, accurate and limiter-free, to sharply capture the shocks and steep gradients, and, to be robust when extreme events occur (near-vacuum states for instance). Our aim is to maintain these properties for the two-dimensional extension.

The two dimensional Euler equations with source terms are given by

$$\frac{\partial U}{\partial t} + \frac{\partial F(U)}{\partial x} + \frac{\partial G(U)}{\partial y} = S(U); \qquad t \geq 0, \qquad x, y \in \mathbb{R} \tag{4.20}$$

where

$$\mathbf{U}(x,t) = \begin{pmatrix} \rho \\ \rho u \\ \rho v \\ E \end{pmatrix}, \quad \mathbf{F}(\mathbf{U}) = \begin{pmatrix} \rho u \\ \rho u^2 + p \\ \rho uv \\ u(E+p) \end{pmatrix} \quad \mathbf{G}(\mathbf{U}) = \begin{pmatrix} \rho u \\ \rho uv \\ \rho v^2 + p \\ v(E+p) \end{pmatrix} \tag{4.21}$$

where $\rho$, $u$,$v$, $p$ are the density, velocity in $x$ and $y$ directions and pressure, respectively. $E$ is the total energy and $e$ is the internal energy. The pressure is linked to two thermodynamic variables via the perfect gas equation of state with adiabatic gas constant $\gamma$. Also, $S(U)$ are the source terms which are detailed in the next section: gravity, or two chemical state reaction.

Similar to 1D case, we employ the fractional step approach for gravity and second order Strang-splitting method [102] for chemical reaction source terms. For instance, the numerical solution at each time step level is computed in two steps: The homogeneous conservation law (convection step) and ODE system (source term or reaction step), successively. The two dimensional convection operator $C$ approximates the solution of the homogeneous system on the time interval $[t^n, t^{n+1}]$.

$$\frac{\partial U}{\partial t} + \frac{\partial F(U)}{\partial x} + \frac{\partial G(U)}{\partial y} = 0, \quad t^n \leq t \leq t^{n+1}. \tag{4.22}$$

For the convection step, we consider the computational domain in space as a rectangular box $\Omega = [x^L, x^R] \times [y^L, y^R]$ divided into rectangular uniform cells $I_{i,j} = [x_{i-1/2}, x_{i+1/2}] \times [y_{j-1/2}, y_{j+1/2}]$. We denote the cell center by $(x_i, y_j)$ and the cell sizes $\Delta x = x_{i+1/2} - x_{i-1/2}$ and $\Delta y = y_{j+1/2} - y_{j-1/2}$. For standard finite volume semi-discretization, we employ the volume integrated-average (VIA) of the numerical solution $U(x, y, t)$ over a mesh cell $I_{i,j}$ at time $t$ by a piece-wise constant value

$$U_{i,j}(t) = \frac{1}{\Delta x\, \Delta y} \int\limits_{I_{i,j}} U(x, y, t)\, dx\, dy \qquad \text{where} \qquad i = 1, 2, \ldots, M, \quad j = 1, 2, \ldots, N. \tag{4.23}$$

Similar to 1D, the VIA $U_{i,j}(t)$ for each mesh cell $I_{i,j}$ is updated by

$$\frac{dU_{i,j}(t)}{dt} = -\frac{1}{\Delta x} \left(F_{i+1/2,j}(t) - F_{i-1/2,j}(t)\right) - \frac{1}{\Delta y} \left(G_{i,j+1/2}(t) - G_{i,j-1/2}(t)\right), \tag{4.24}$$

where $F_{i\pm1/2,j}(t)$ and $G_{i,j\pm1/2}(t)$ are the two-point fluxes in $x$ and $y$ direction, respectively.

They are computed like their 1D counterparts, that is a Riemann solver is further used

to get

$$F_{i+1/2,j}(t) = F^{\text{Riemann}}_{i+1/2,j}\left(U^L_{i+1/2,j}, U^R_{i+1/2,j}, t\right), \tag{4.25}$$

where $U^L_{i+1/2,j}$ and $U^R_{i+1/2,j}$ are the left-side and right-side values of $U_{i,j}(x,y,t)$ at cell boundary in $x$ direction respectively. The same procedure is employed in $y$-direction to compute the fluxes $G_{i,j+1/2}(t)$. In this work, the HLLCM Riemann solver [92] is employed. Similar to 1D section, the third-order TVD Runge-Kutta method (RK3, see [93, 43]) is used for high accurate time integration.

In 2D the reconstructions are performed direction by direction. In other words, the same $\mathbb{P}_4$ reconstructions as described in Eq.(3.8) are first made for data aligned in $x$ direction: $U_{i-2,j}$, $U_{i-1,j}$, $U_{i,j}$, $U_{i+1,j}$, $U_{i+2,j}$, to get the edge centered values $U^L_{i+1/2,j}$ and $U^R_{i-1/2,j}$ for cell $I_{i,j}$. Then, the 1D reconstructions in $y$ direction consider $y$-aligned data $U_{i,j-2}$, $U_{i,j-1}$, $U_{i,j}$, $U_{i,j+1}$, $U_{i,j+2}$ to get values $U^L_{i,j+1/2}$ and $U^R_{i,j-1/2}$ in cell $I_{i,j}$.

The THINC reconstructions are exactly the same as in 1D, their stencils are thus restricted to two aligned neighbor cells only. The *a posteriori* MOOD loop operates also alike. The local selection of reconstruction operator follows the same algorithm as in 1D and the selection of reconstruction operator is independent in $x$ and $y$ directions.

In the present work, the 2D scheme is constructed via a simple but efficient direction-by-direction extension. Indeed the flux integration along the edges is calculated using only one integration point at the edge center. So, the 2D scheme is formally of maximal second order accuracy.

Recall that the goal in this work is not to build a genuine 5th order accurate numerical method. On the contrary, we aim at building a genuine simple, efficient, robust and accurate enough scheme emphasizing that an appropriate mixing of linear and non-linear reconstruction operators may replace classical limiting techniques (such as slope/flux limiters, artificial viscosity, WENO, etc.). In previous works [31, 57], it has been observed that the present BVD scheme can maintain a high order of accuracy on smooth profiles of the advection equation in 1D and 2D. Moreover, the comparison of dispersion and dissipation relations with respect to other schemes (TVD, WENO, WENO-Z) have been conducted and it was shown that the current scheme has comparable behaviors. Extensive numerical tests have been conducted in previous works such as [31, 32, 57, 106]

to assess the appropriate behavior of this BVD scheme on classical 1D and 2D test cases. One can find the tables of convergence rate for the present scheme as well as the simulation of the standard 2D isentropic vortex problem and simpler advection tests in 2D in references [31, 57].

The following numerical section provides some numerical evidences mainly in the non homogeneous case.

## 4.5 Numerical experiments

In this section, we test the performance of the numerical scheme on some benchmark test problems of Euler system of PDEs ($\gamma = 7/5$ or $5/3$) without or with various source terms. The finite volume numerical scheme is built under the following key tools: the reconstruction process is conducted in terms of characteristic decomposition, the HLLCM Riemann solver [92] is employed for the flux computation, a TVD-RK3 of third order for time integration, the BVD algorithm is used for the selector of space reconstructions, and, at last, an *a posteriori* MOOD loop is implemented for physical admissibility. For homogeneous Euler equations it consists of a the PAD criterion, that is the positivity preservation, while for the reactive Euler equations we must add the positivity of the mass fraction $\alpha_i^n \geq 0$.

### 4.5.1 Homogeneous Euler equations

#### 4.5.1.1 2D explosion test

An axi-symmetric two dimensional explosion problem described in [107, 125] is first simulated. The computational domain is $\Omega = [-1, 1] \times [-1, 1]$ and the initial condition is given by

$$(\rho_0, u_0, v_0, p_0) = \begin{cases} (1,\ 0,\ 0,\ 1) & \text{if } r \leq R, \\ (0.125,\ 0,\ 0,\ 0.1) & \text{otherwise,} \end{cases} \tag{4.26}$$

where $r = \sqrt{x^2 + y^2}$ is the distance to the center of computational domain and $R = 0.5$. The fluid with high density and pressure inside the circle $R = 0.5$ spreads out into three

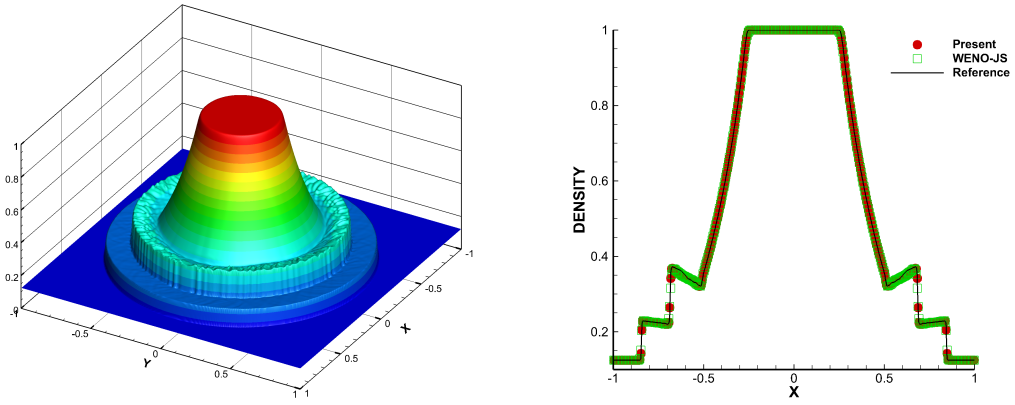


Figure 4.3: Numerical results for 2D explosion test – Density variable — Left: bird's eye view of density distribution computed by present scheme; Right: Cut-off profile along the radial direction.

circular waves: a diverging shock, followed by a diverging contact discontinuity and a converging rarefaction wave. The simulation runs up to $t_{\text{final}} = 0.2$ with a uniform grid made of $400 \times 400$ cells. In figure 4.3, we show the bird's eye view of density distribution and the cross-section profile along the radial direction. From the results, we observe that the present scheme captures the contact discontinuity and the shock wave without spurious oscillations and maintain the cylindrical symmetry.

Moreover, compared to the reference WENO-JS scheme [56] (right panel), the present scheme captures a slightly sharper contact discontinuity.

#### 4.5.1.2 2D Riemann problems

In order to test the multi-stage BVD-MOOD scheme (accuracy, oscillatory-free and robustness), we simulate a set of two-dimensional Riemann problems (RP) which have been introduced and extensively studied in [63, 64, 90]. The computational domain is $\Omega = [-0.5, 0.5] \times [-0.5, 0.5]$ and the initial conditions made of $2 \times 2$ constant states are given by

$$\mathbf{U}(x, y, t = 0) = \begin{cases} \mathbf{U}_1 & \text{if} \quad x > 0 \wedge y > 0, \\ \mathbf{U}_2 & \text{if} \quad x \leq 0 \wedge y > 0, \\ \mathbf{U}_3 & \text{if} \quad x \leq 0 \wedge y \leq 0, \\ \mathbf{U}_4 & \text{if} \quad x > 0 \wedge y \leq 0. \end{cases} \tag{4.27}$$

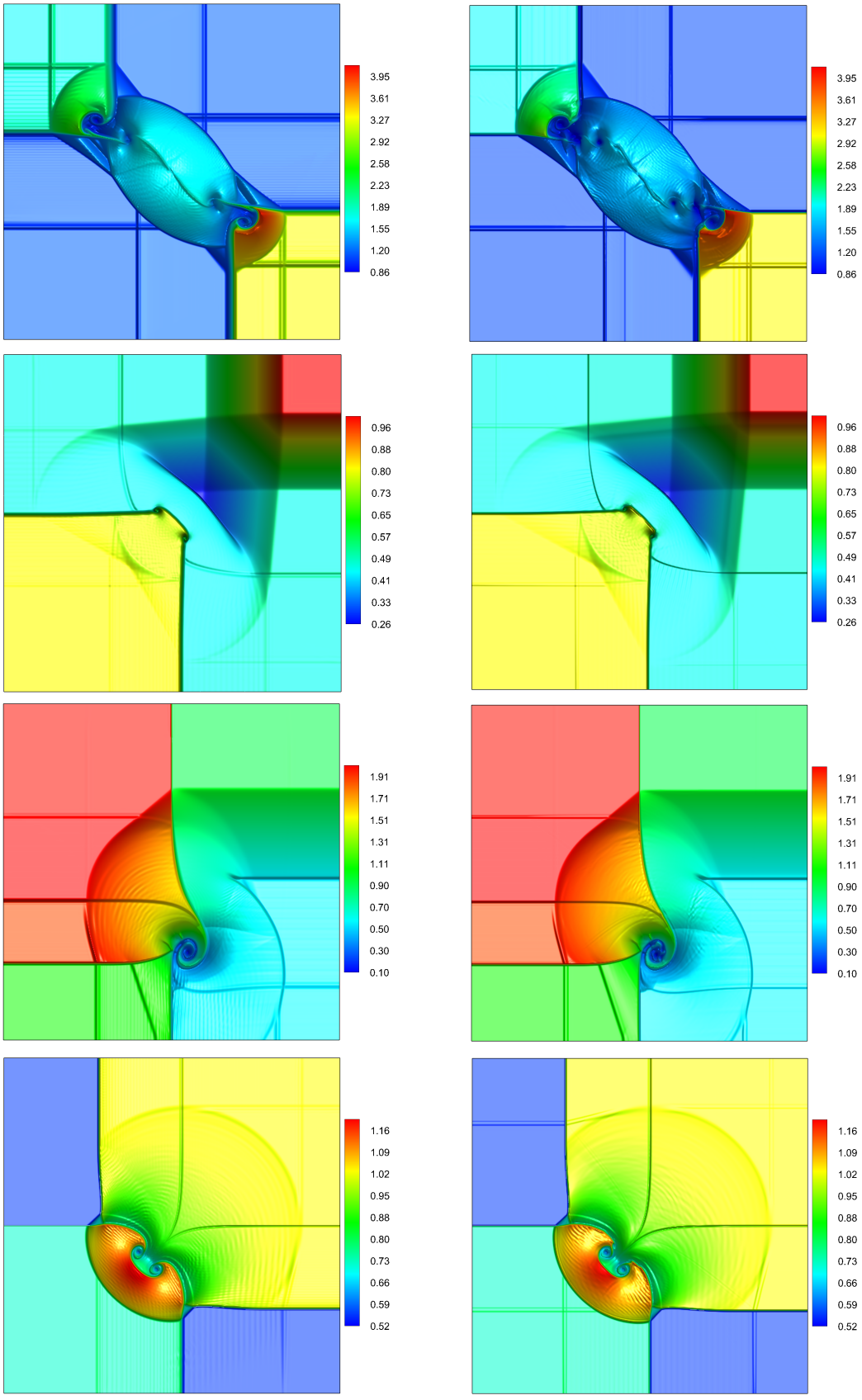


Figure 4.4: Numerical results for Riemann problems 1, 2, 3, 4 – Density variable — Left: WENO-JS scheme; Right: Present scheme.

Table 4.2: Initial conditions for the 2D Riemann problems (RP) numbered from 1 to 4. These data correspond to Configurations 5, 7, 11 and 17 in [63].

| # | | $\rho$ | $u$ | $v$ | $p$ | $\rho$ | $u$ | $v$ | $p$ | $t_{\text{final}}$ |
|---|---|---|---|---|---|---|---|---|---|---|
| | | $x \leq 0$ | | | | $x > 0$ | | | | |
| **RP1** | $y > 0$ | 2.0 | -0.75 | 0.5 | 1.0 | 1.0 | -0.75 | -0.5 | 1.0 | 0.23 |
| | $y \leq 0$ | 1.0 | 0.75 | 0 .5 | 1.0 | 3.0 | 0.75 | -0.5 | 0.3 | |
| **RP2** | $y > 0$ | 0.5197 | -0.6259 | 0.1 | 0.4 | 1.0 | 0.1 | 0.1 | 1.0 | 0.25 |
| | $y \leq 0$ | 0.8 | 0.1 | 0.1 | 0.4 | 0.5197 | 0.1 | -0.6259 | 0.4 | |
| **RP3** | $y > 0$ | 0.5313 | 0.8276 | 0.0 | 0.4 | 1.0 | 0.1 | 0.0 | 1.0 | 0.30 |
| | $y \leq 0$ | 0.8 | 0.1 | 0.0 | 0.4 | 0.5313 | 0.1 | 0.7276 | 0.4 | |
| **RP4** | $y > 0$ | 2.0 | 0.0 | -0.3 | 1.0 | 1.0 | 0.0 | -0.4 | 1.0 | 0.30 |
| | $y \leq 0$ | 1.0625 | 0.0 | 0.2145 | 0.4 | 0.5197 | 0.0 | -1.1259 | 0.4 | |

The initial conditions and the final solution time $t_{\text{final}}$ for the four configurations are listed in table 4.2. The ratio of specific heats is set to $\gamma = 1.4$. The simulations are run with a uniform grid made of $600 \times 600$ mesh cells with the CFL number $0.4$ in all calculations. We compare our numerical solution against the reference scheme WENO-JS from [56]. The numerical results for the density variable are shown in figure 4.4. In the left and right panels, we display the numerical density at the final time with the same scale and color for the WENO-JS and BVD-MOOD schemes respectively. A reference solution can be found for instance in [60]. In figure 4.4, we can observe on the computational results of two schemes that they comparably capture the main flow structures of all 2D Riemann Problems. Therefore, the multi-stage BVD-MOOD scheme seems to perform well in shock capturing situation without spurious oscillations, and, in the smooth parts of flow without excessive numerical dissipation. Furthermore, the present scheme does capture sharper discontinuities, more pronounced small-scale structures, and, present the birth of the Kelvin-Helmholtz instability on the shear waves compared to WENO-JS scheme. This is an evidence of a lower dissipation.

#### 4.5.1.3 Forward facing step (Mach 3 step tunnel)

We simulate the so-called forward facing step (FFS) benchmark test which was proposed by Woodward and Collela in [117]. In this test a right-moving Mach 3 shock in a tunnel impacts a forward step. The initial condition contains a uniform gas with density $\rho =$

$1.4$, pressure $p = 1$, velocity components $u = 3$, $v = 0$ and specific heat ratio $\gamma = 1.4$. The computational domain is a wind tunnel $\Omega = [0, 3] \times [0, 1]$ with a step of $0.2$ units high located at $0.6$ units away from the entrance of the tunnel. The inflow and outflow boundary conditions are applied at the entrance and the exit while reflective wall boundary conditions are imposed at the remaining boundaries. The solution of this test involves complex flow structures, density disturbances and shear flows due to the interactions among shocks with the boundaries. The simulation is run up to $t_{\text{final}} = 4$ as a final time with CFL number is $0.4$. For this test, the mesh is made of uniform cells with mesh size $\Delta x = 1/160$ and $1/240$. In figure 4.5, we display the density variable at the final time calculated by the proposed scheme. On the top panel, we plot the 3D bird's eye view of density field on $1/240$ mesh size, which shows the adequately resolved shock waves, and the vortices of the Kelvin-Helmholtz instabilities developing along the top shear wave. On the same figure, the middle panels show the numerical results of $1/160$ and $1/240$ mesh size respectively. Furthermore, the numerical results converge rapidly on the finer mesh and the vortexes along the shear wave are more visible as shown in finer grid computation. The small scale flow structures are better captured with the finer grid results as expected, moreover the discontinuities (shocks, contact) seem to be sharply captured by our approach. Notice that there is no issue with positivity in this numerical simulation test.

### 4.5.2 Euler equations with gravitational source terms

Let us consider Euler equations supplemented with standard gravitational source terms in vertical $y$-direction for the thermally ideal gas, which is expressed as

$$\begin{pmatrix} \rho \\ \rho u \\ \rho v \\ E \end{pmatrix}_t + \begin{pmatrix} \rho u \\ \rho u^2 + p \\ \rho uv \\ (E+p)u \end{pmatrix}_x + \begin{pmatrix} \rho v \\ \rho uv \\ \rho v^2 + p \\ (E+p)v \end{pmatrix}_y = \begin{pmatrix} 0 \\ 0 \\ -\rho g \\ -\rho vg \end{pmatrix} \tag{4.28}$$

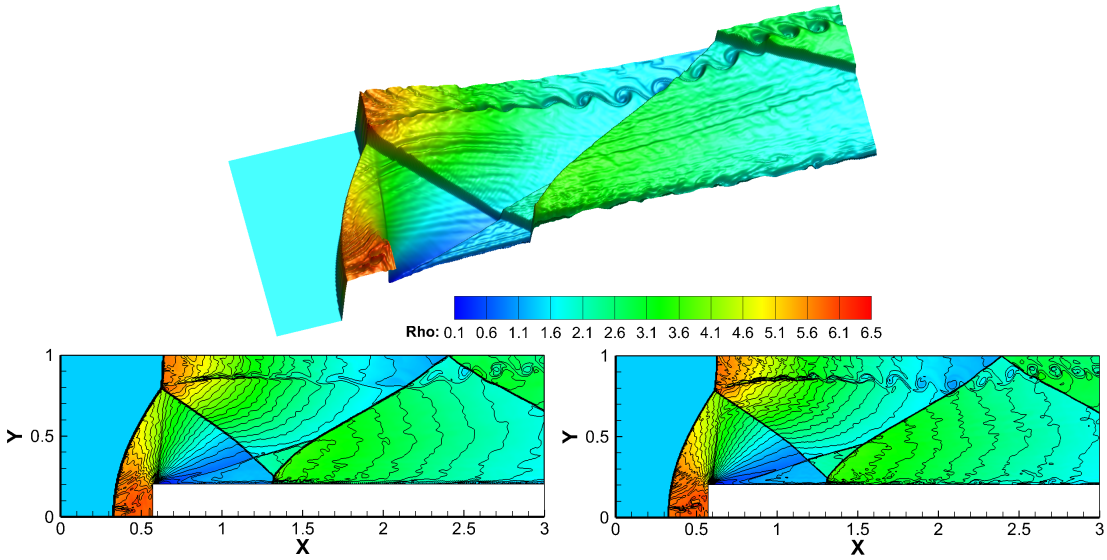


Figure 4.5: Numerical results for forward facing step problem at $t_{\text{final}} = 4$ simulated by the present scheme – Top-panel: Bird's eye view of density (color and elevation) with mesh size $1/240$; Left-panel: 2D view, mesh size $1/160$; Right-panel: 2D view, mesh size $1/240$.

where $\rho$, $u$,$v$, $p$ are the density, velocity in x direction, velocity in y direction and pressure, respectively. $E$ is the total energy expressed as $E = e + \frac{1}{2}\rho(u^2 + v^2)$ with $e$ is the internal energy and $g$ is gravity source. We set $g = 1$ for 2D Rayleigh-Taylor instability and $g = -1$ for 2D double rarefaction waves with gravity.

#### 4.5.2.1 Two-dimensional Rayleigh-Taylor instability

The Rayleigh-Taylor instability contains both discontinuities and complex flow structures, see [39, 40, 120, 123]. In this test, the instability occurs on an interface between two fluids of different densities when an acceleration is directed from the heavier towards the lighter fluid. The computational domain is $\Omega = [0, 0.25] \times [0, 1]$ and the initial condition is given by

$$(\rho_0, u_0, v_0, p_0) = \begin{cases} (2,\ 0,\ -0.025\, a\, \cos(8\pi x),\ 1 + 2y) & \text{if } 0 \le y \le 1/2, \\ (1,\ 0,\ -0.025\, a\, \cos(8\pi x),\ y + 3/2) & \text{if } 1/2 \le y < 1, \end{cases} \tag{4.29}$$

where $a = \sqrt{\gamma p/\rho}$ is the sound speed and the ratio of specific heat is set to $\gamma = 5/3$. Reflective boundary conditions are imposed for the left and right ends of the domain. On

the upper boundary, we assign the primitive variables $(\rho, u, v, p) = (1, 0, 0, 2.5)$ and for the bottom boundary, we assign $(\rho, u, v, p) = (2, 0, 0, 1)$. The computational domain is discretized into a uniform $200 \times 800$ mesh. The fluid flow is simulated up to the final time $t_{\text{final}} = 1.95$ with CFL number $0.4$. In figure 4.6, we display $15$ uniform density contour lines spanning $[0.8, 2.3]$ for the WENO-JS (left panel) and the present scheme (right panel). We observe that the present scheme has resolved much richer vorticity structures than WENO-JS scheme. While the present scheme has a clear ability to resolve complex and small flow structures, however it induces some symmetry breaking probably due to the order dependency of the BVD algorithm, see [39].

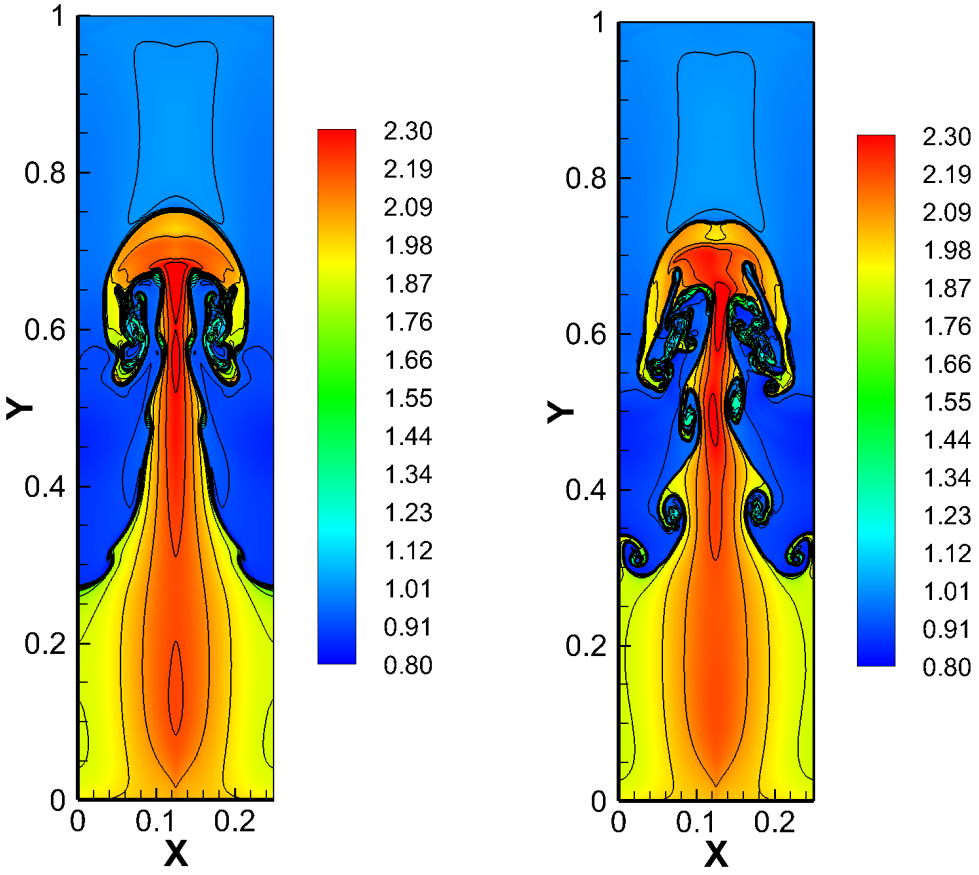


Figure 4.6: Density profile with $15$ iso-contour lines for the Rayleigh-Taylor instability problem at $t_{\text{final}} = 1.95$. Left panel: WENO-JS scheme; Right panel: Present scheme.

#### 4.5.2.2 Two-dimensional double rarefaction waves with gravity

The double rarefaction waves problem is a 2D Riemann problem which presents near vacuum state at the central zone as it involves two rarefaction fans moving in opposite

directions [71, 127]. The initial condition on computational domain $\Omega = [0, 2] \times [0, 2]$ is given by [129]

$$(\rho_0, u_0, v_0, p_0) = \begin{cases} (7,\ -1,\ 0,\ 2) & \text{if } x \leq 1, \\ (7,\ 1,\ 0,\ 2) & \text{otherwise,} \end{cases} \tag{4.30}$$

and the final time is set to $t_{\text{final}} = 0.6$ with CFL number set to $0.4$ and $\gamma = 7/5$. The reflective boundary conditions are set on the top and bottom ends and outflow boundary conditions are set to the left and right ends of the computational domain. A mesh made of $80 \times 80$ cells is considered and a reference solution is obtained with $400 \times 400$ mesh cells. The numerical results are shown in figure 4.7. Due to the gravity source term pointing in the negative $y$ direction, the numerical solution presents some expansion on the top part ($y \geq 1.6$) and compression on the bottom one ($y \leq 0.05$). The numerical solution is genuinely smooth and has a good agreement with the reference one. Moreover the obtained solution is comparable to the one in [129] without presenting any spurious effects in the central near vacuum state for which the density drops down to $\rho \simeq 5.72E-06$.

### 4.5.3 The reactive Euler equations – Detonation waves

In this section, we show the numerical benchmark tests suite used in 1D and 2D for the reactive Euler equations. We set the CFL to $0.05$ for WENO-JS scheme and to $0.1$ for the present BVD+MOOD scheme for the following test cases.

#### 4.5.3.1 1D reactive Euler equations

We consider the time-dependent inviscid compressible flow with reaction between two chemical states in one-dimensional space. The homogeneous Euler system (4.1) (i.e. with $S(U) = 0$) is supplemented with an equation on the mass fraction of the unburnt

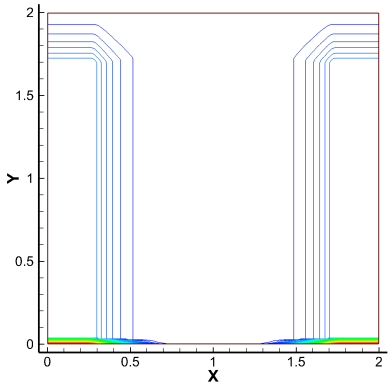


(a) 60 contour lines of density from 0 to 60.

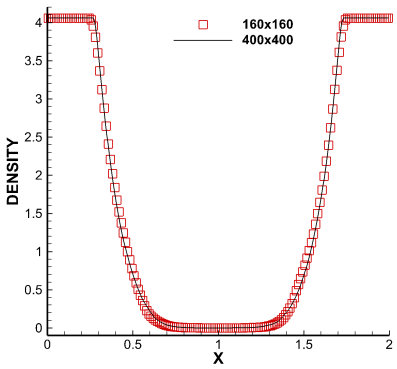


(b) Cut along the line $y = 1.7875$.

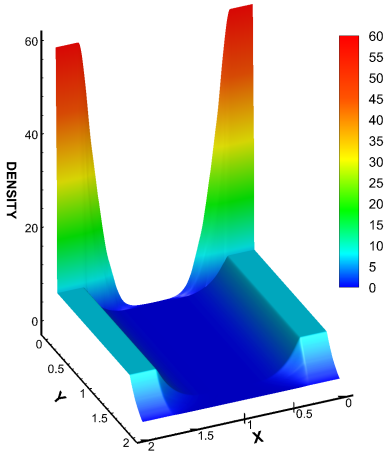


(c) Extruded 3D density.

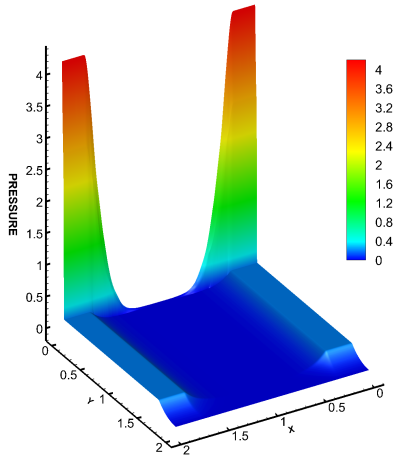


(d) Extruded 3D pressure.

Figure 4.7: Numerical results for two-dimensional double rarefaction waves under gravity – (a) 60 equally spaced contour lines of density from 0 to 60; (b) the cutting lines along y-direction which is $y = 1.7875$, the solid line is the numerical solution fo $400 \times 400$ mesh cells and the symbol is the numerical solution of $80 \times 80$ mesh; (c) Bird's eye view for 3D density. (color and elevation). ; (d) Extruded 3D pressure (color and elevation).

gas $\alpha$ as

$$\begin{pmatrix} \rho \\ \rho u \\ E \\ \rho\alpha \end{pmatrix}_t + \begin{pmatrix} \rho u \\ \rho u^2 + p \\ (E+p)u \\ \rho u \alpha \end{pmatrix}_x = \begin{pmatrix} 0 \\ 0 \\ 0 \\ \dot{\omega} \end{pmatrix} \tag{4.31}$$

where $\rho, u, E, \alpha$ are density, velocity, total energy and mass fraction of unrated gas, respectively and $\dot{\omega} = K(T)\rho\alpha$, $T$ is the temperature and $K(T)$ is the chemical reaction

rate. The pressure is obtained from an equation of state like

$$p = (\gamma - 1)\left(E - \frac{1}{2}\rho u^2 + \mathsf{R}\right), \tag{4.32}$$

where $\mathsf{R} = -q_0(\rho\alpha)$ models the heat released from the chemical reaction processes, and $q_0$ denotes the chemical heat release. The temperature is computed by $T = \dfrac{p}{\rho}$ and we set the $\gamma$ to $1.4$. The reaction rate $K(T)$ can be modeled with the so-called Arrhenius kinetics [109] as

$$K(T) = K_0 \exp\left(\frac{-T_{ign}}{T}\right), \tag{4.33}$$

where $K_0$ the pre-exponential coefficient and $T_{ign}$ the ignition (or activation) temperature are model parameters. When the source term becomes stiff, the reaction rate may be modeled by a Heaviside kinetics as

$$K(T) = \begin{cases} \frac{1}{\xi} & \text{if} \quad T \geq T_{ign}, \\ 0 & \text{if} \quad T < T_{ign}. \end{cases} \tag{4.34}$$

where $\xi$ represents the reaction time.

**Chapman-Jouguet (C-J) detonation wave with Arrhenius Law:** In this test, the Arrhenius source term Eq.(4.33) is employed, see [33, 51, 109, 115]. The initial condition consists of a completely burnt gas ($\alpha = 0$) on the left-hand side facing an un-burnt counterpart ($\alpha = 1$) on the right. The density, velocity and pressure of the un-burnt state are given by $(\rho_u = 1, u_u = 0, p_u = 1, \alpha_u = 1)$. The heat release is set to $q_0 = 25$, the ignition temperature to $T_{ign} = 25$ and $K_0 = 16.418 \times 10^3$.

We obtain the C-J initial state for the burnt state $(\rho_{CJ}, u_{CJ}, p_{CJ}, \alpha_{CJ} = 0)$ following [21, 115]. For instance, for any given initial state of un-burnt gas ($\rho_u = \rho_0, u_u =$

$u_0, p_u = p_0, \alpha_u = 1$) on the right, one can obtain the C-J initial state on the left by

$$p_{\text{CJ}} = -b + \left(b^2 - c\right)^{1/2} \tag{4.35}$$

$$\rho_{\text{CJ}} = \frac{\rho_0 \left[p_{\text{CJ}}(\gamma + 1) - p_0\right]}{\gamma p_{\text{CJ}}} \tag{4.36}$$

$$D_{\text{CJ}} = \left[\rho_0 u_0 + \left(\gamma p_{\text{CJ}} \rho_{\text{CJ}}\right)^{1/2}\right] / \rho_0 \tag{4.37}$$

$$u_{\text{CJ}} = D_{\text{CJ}} - \left(\gamma p_{\text{CJ}} / \rho_{\text{CJ}}\right)^{1/2} \tag{4.38}$$

where $b = -p_0 - \rho_0 q_0(\gamma - 1), c = p_0^2 + 2(\gamma - 1)p_0\rho_0 q_0/(\gamma + 1)$, and $D_{\text{CJ}}$ is the speed of the sharp front (in a C-J detonation). Observe that the values $p_{\text{CJ}}$, $\rho_{\text{CJ}}$, and $u_{\text{CJ}}$ depend only on $p_0, u_0, \rho_0$, and $q_0$( and not on $K$, i.e., $\varepsilon$ or $T_0$ ).

The 1D computational domain is $\Omega = [0, 30]$ and the initial discontinuity is located at $x_d = 10$. The final time is $t_{\text{final}} = 1.8$ for which the detonation wave has reached location $x_d = 22.8$. The simulation was performed by the standard $5^{th}$ order WENO-JS scheme and the present multi-stage BVD-MOOD scheme both using $N = 300$ cells. The reference solution is calculated by WENO-JS scheme with $10000$ cells and displayed in solid line in figure 4.8. In this figure we show the numerical results for the density, mass fraction, pressure and temperature for both schemes. We observe that the present scheme is able to capture the correct propagation speed of the C-J detonation wave with a larger CFL number whereas WENO-JS scheme produces spurious oscillations and errors linked to an extra dissipation (extra plateaus or wrong shock speed) in the vicinity of the discontinuity. Moreover, the WENO-JS numerical scheme inaccurately locates the discontinuity, and, as a consequence, produces a wrong physical solution. Contrarily, the BVD-MOOD scheme, being less diffusive is able to capture the correct chronometry of the wave along with the expected numerical solution.

**Chapman-Jouguet detonation wave with the Heaviside Model:** In this example we consider the C-J detonation model for which the chemical reaction is in its Heaviside form. The parameter values of the model are taken from [26, 32, 78, 115] as $\frac{1}{\xi} = 0.5825 \times 10^{10}$, $q_0 = 0.5196 \times 10^{10}$, $T_{ign} = 0.1155 \times 10^{10}$ and $\gamma = 1.4$. The 1D computational domain is $\Omega = [0, 0.05]$ and the initial discontinuity is set at $x_d = 0.005$.

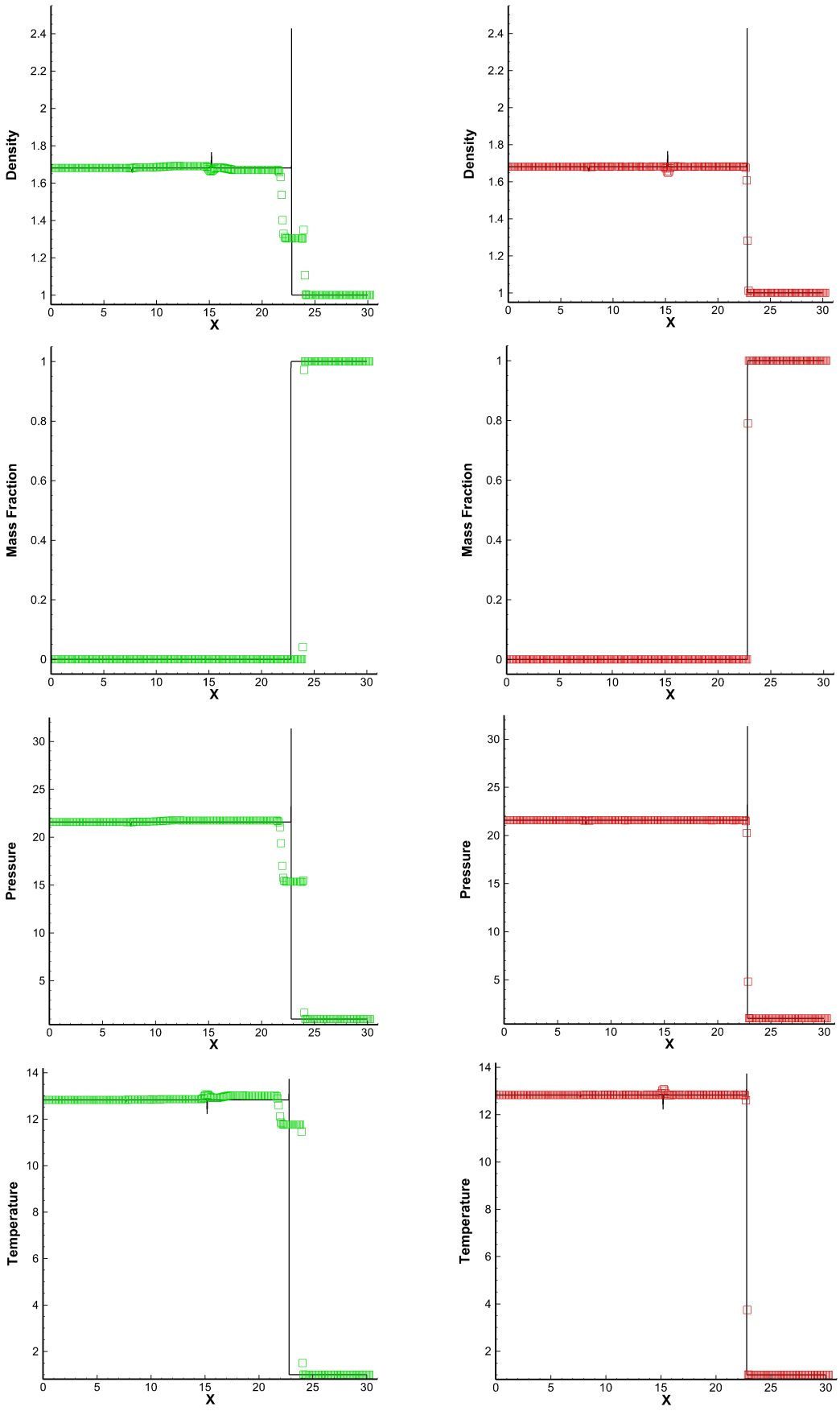


Figure 4.8: Numerical results for density, mass fraction, pressure and temperature of Arrhenius case at time $t_{\text{final}} = 1.8$ – Left: WENO-JS scheme; Right: Present scheme.

The density, velocity and pressure of the un-burnt state are given by $(\rho_u = 1.201 \times 10^{-3}, u_u = 0, p_u = 8.321 \times 10^5, \alpha_u = 1)$.

The totally burned gas is located on the left side of the tube, where $(\rho_{CJ}, u_{CJ}, p_{CJ}, \alpha_{CJ} = 0)$ are determined by the C-J detonation model. The computation is run up to final time $t_{\text{final}} = 3 \times 10^{-7}$ with a uniform mesh made of $N = 300$ cells. The exact position of the detonation wave is at $x_d = 0.03764$ at final time.

We plot the results of the density, mass fraction, pressure and temperature variables for both schemes in figure 4.9 where the reference solution is computed by WENO-JS scheme with $10000$ mesh cells. We observe that the detonation wave is correctly and sharply captured by the proposed scheme, whereas WENO-JS scheme produces a wrong numerical solution (even if smaller time steps are used because the stiffness of detonation wave is emphasized by the spatial errors rather than the temporal ones), as already reported in [115].

**Interaction between a detonation wave and an oscillatory profile (Heaviside model):** In this section we consider the interaction between a detonation wave and an oscillatory profile which is taken from [9, 32, 115]. The parameter of this test are $\gamma = 1.2$, $q_0 = 50$, $\frac{1}{\xi} = 1000$, and $T_{ign} = 3$. The computational domain is $\Omega = [0, 2\pi]$ with a uniform mesh made of $N = 200$ cells. The initial condition is given by

$$(\rho_0, u_0, p_0, \alpha_0) = \begin{cases} (1.79463,\ 3.0151,\ 21.53134,\ 0) & \text{if } x \leq \frac{\pi}{2}, \\ (1 + 0.5\sin(2x),\ 0,\ 1,\ 1) & \text{otherwise.} \end{cases} \tag{4.39}$$

The numerical solution is calculated up to time $t_{\text{final}} = \frac{\pi}{5}$ and the reference solution is computed by WENO-JS scheme with $10000$ mesh cells. In figure 4.10 we observe the occurrence of spurious waves produced by WENO-JS scheme. On the contrary the present BVD-MOOD scheme prevents their appearance. Furthermore, the present scheme is able to resolve the flow field produced after the interaction between the detonation wave and the oscillatory profile. At last the shock is again sharply captured.

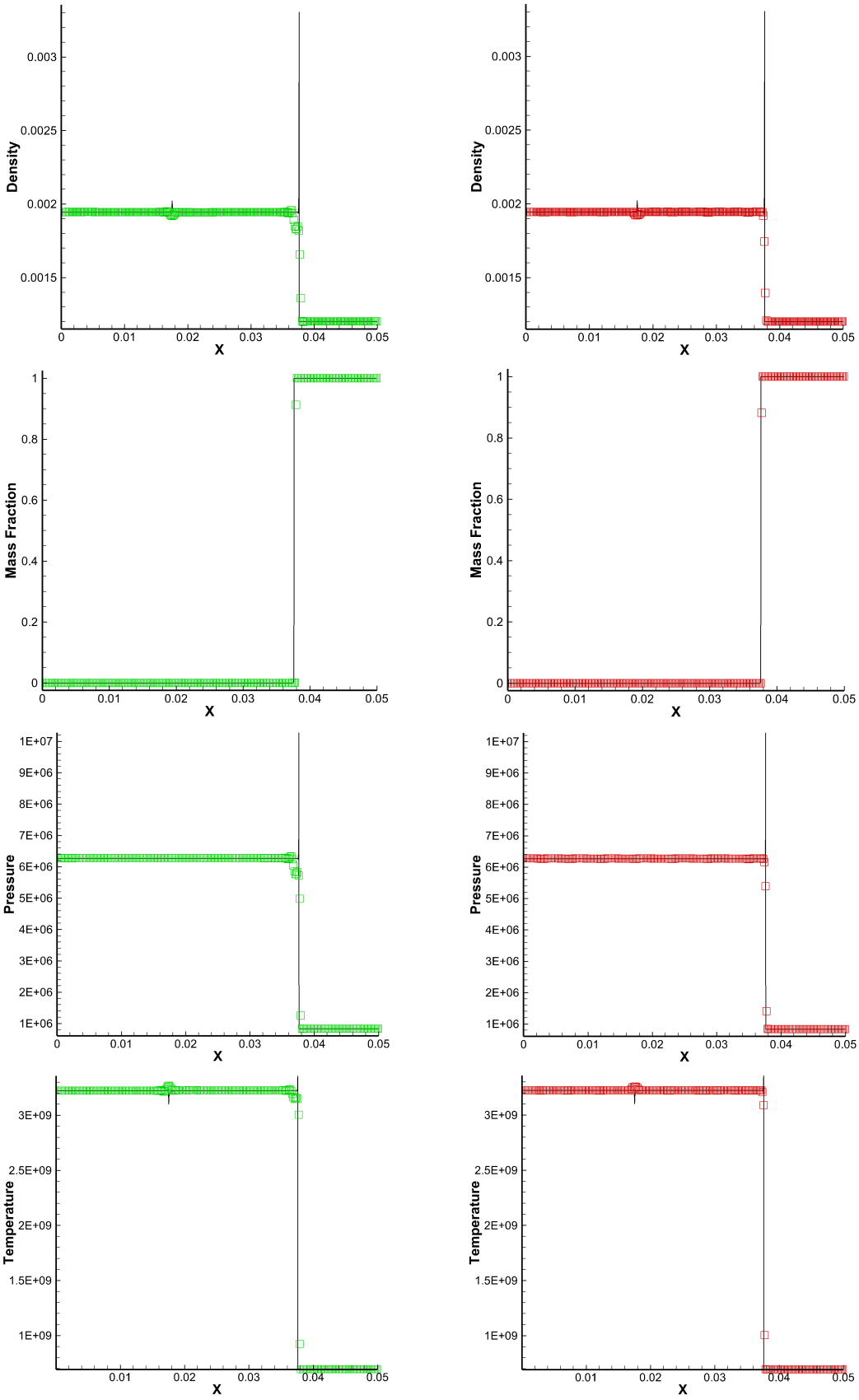


Figure 4.9: Numerical results for density, mass fraction, pressure and temperature of Heaviside model at time $t_{\text{final}} = 3 \times 10^{-7}$ – Left: WENO-JS scheme; Right: Present scheme.

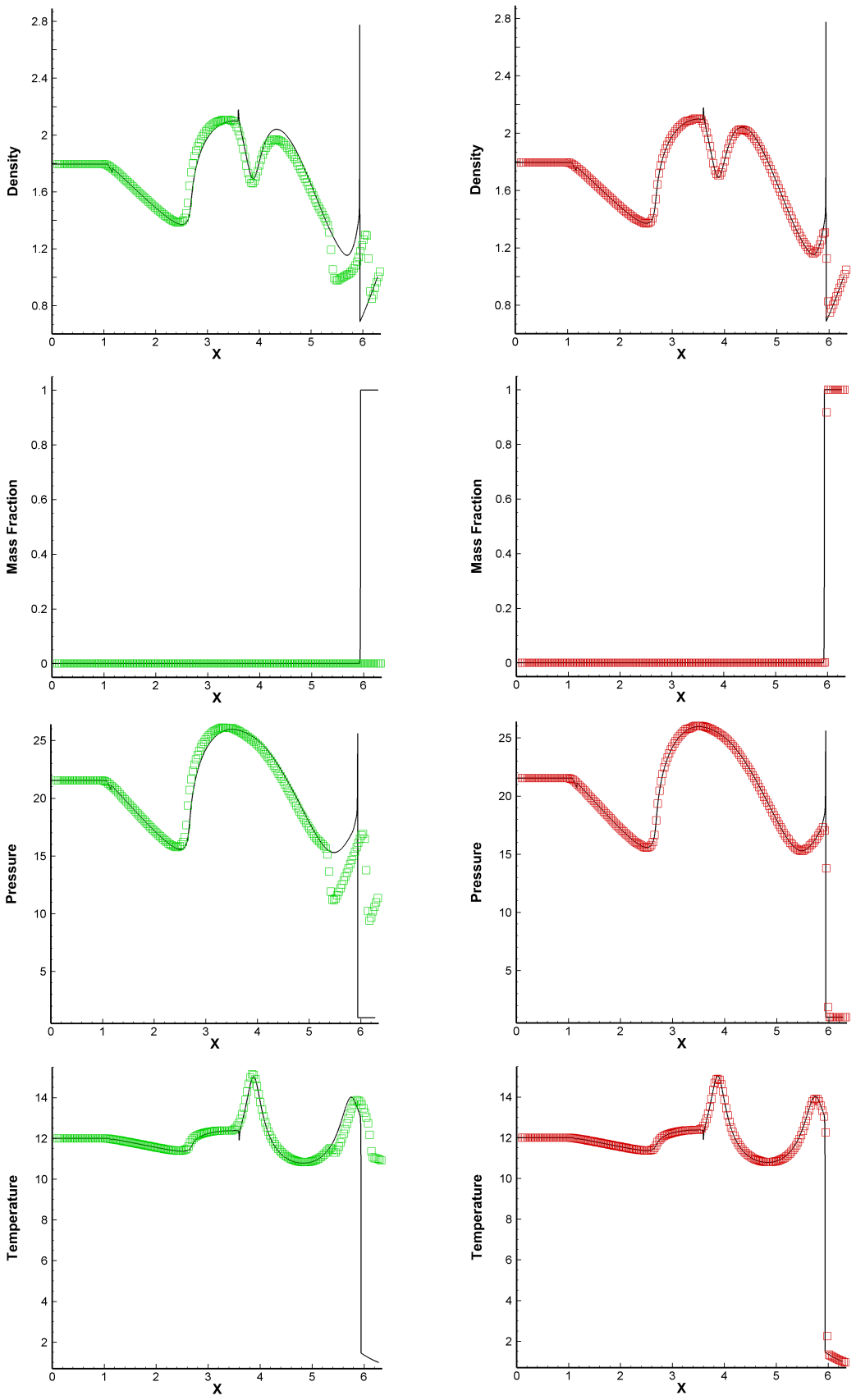


Figure 4.10: Numerical results for density, mass fraction, pressure and temperature of interaction between a detonation wave and an oscillatory profile at time $t_{\text{final}} = \frac{\pi}{5}$ – Left: WENO-JS scheme; Right: Present scheme.

**Collision of two detonation waves:** The last 1D reactive Euler model test case consists in a collision of detonation waves. It resembles the Woodward-Collela blastwave benchmark test used for the homogeneous Euler equations [26]. This test presents three constant states. The middle state is the un-burnt gas while the left and right high-density, high-pressure burnt gases moves towards the fresh middle state. At $t > 0$ it generates left and right moving detonation waves along with rarefaction fans and contacts after impinging on the burning fronts. After some time we observe the collision between two detonation waves. The parameter of the model are taken following [9], i.e $\gamma = 1.2$, $q_0 = 50$, $\frac{1}{\xi} = 230.75$, and $T_{ign} = 3$. The computational domain is $\Omega = [0, 100]$ meshed with uniform cells ($N = 200$). The initial condition is given by

$$(\rho_0, u_0, p_0, \alpha_0) = \begin{cases} (1.79463,\ 3.0151,\ 30,\ 0) & \text{if } x \leq 10, \\ (1,\ 0,\ 1,\ 1) & \text{if } 10 < x < 90, \\ (1.79463,\ -8,\ 21.53134,\ 0) & \text{if } 90 \leq x. \end{cases} \tag{4.40}$$

The numerical solution is calculated up to time $t_1 = 4$ (before collision) in figure 4.11, and, time $t_2 = 6$ (after collision) in figure 4.12, respectively. The reference solution is computed by WENO-JS scheme with $N = 10000$ mesh cells. Density, mass fraction, pressure and temperature are displayed in the figures.

Before and after the collisions, the BVD-MOOD scheme correctly and sharply captures the shocks, contacts and rarefaction waves in excellent agreement with the reference solution. On the contrary the WENO-JS scheme produces spurious supernumerary numerical waves which are unrelated to the model of PDEs. The embedded numerical diffusion of WENO-JS scheme incorrectly triggers the reaction which then produces a wrong numerical solution as can be seen: indeed, it can not capture the correct location of shock speed for instance. Notice that the left-most contact discontinuity is captured on less than two cells with BVD-MOOD scheme while WENO-JS demands about five cells. This extra numerical dissipation is responsible for the observed inappropriate behaviors.

From these 1D numerical tests for reactive Euler equations, we can see that the BVD-

MOOD scheme can accurately reproduce the complex wave structure of this model, moreover it captures sharply the contact and material interfaces (on one or two cells), and can handle the interactions between simple waves: detonation waves, oscillatory smooth profiles, rarefactions and contacts.

#### 4.5.3.2 2D reactive Euler equations

The two-dimensional version of the previous 1D system considers Eq.(4.20) with $S(U) = 0$ supplemented with the 2D version of Eq.(1.4), i.e

$$\begin{pmatrix} \rho \\ \rho u \\ \rho v \\ \rho E \\ \rho\alpha \end{pmatrix}_t + \begin{pmatrix} \rho u \\ \rho u^2 + p \\ \rho uv \\ (E+p)u \\ \rho u\alpha \end{pmatrix}_x + \begin{pmatrix} \rho v \\ \rho uv \\ \rho v^2 + p \\ (E+p)v \\ \rho v\alpha \end{pmatrix}_y = \begin{pmatrix} 0 \\ 0 \\ 0 \\ 0 \\ \dot{\omega} \end{pmatrix} \tag{4.41}$$

where $\rho, u, v, E, \alpha$ are density, velocity in $x$ direction,velocity in $y$ direction, total energy and mass fraction of unrated gas, respectively and $\dot{\omega} = K(T)\rho\alpha$, $T$ is the temperature and $K$ is the chemical reaction rate. The pressure is obtained from an equation of state as the following form

$$p = (\gamma - 1)\left(E - \frac{1}{2}(\rho u^2 + \rho v^2) + \mathsf{R}\right), \tag{4.42}$$

where $\mathsf{R} = -q_0\rho Y$ is the heat release from chemical reaction processes, where $q_0$ denotes chemical heat release. The temperature is computed by $T = p/\rho$. The source term is modeled as described in the one-dimensional case in Section 4.5.3.1.

**Numerical convergence study of discontinuous solutions** Here, we test the grid convergence study of the proposed scheme [114, 131]. The computational domain is

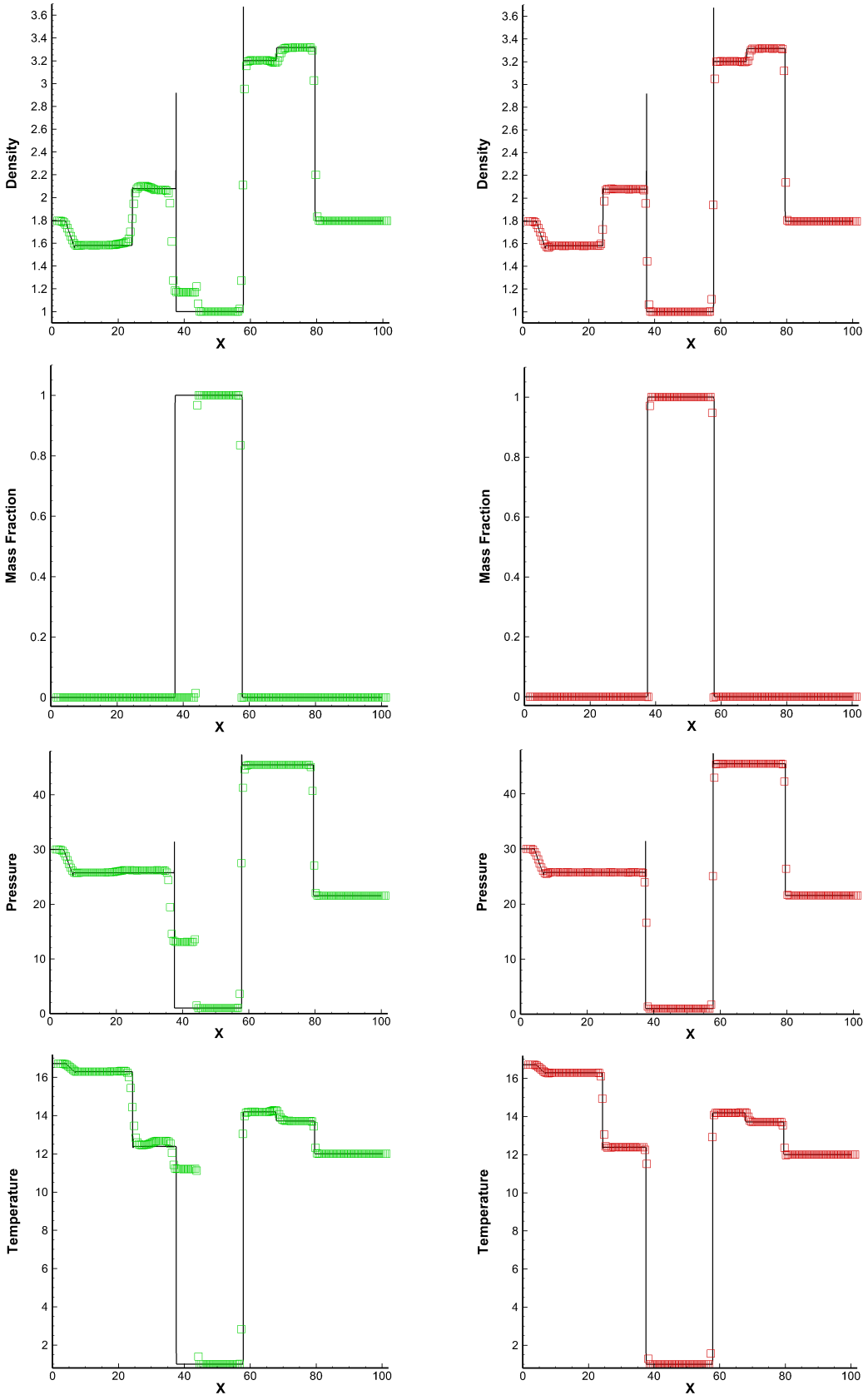


Figure 4.11: Numerical results for density, mass fraction, pressure and temperature of collision of two detonations at time $t_{\text{final}} = 4$ – Left: WENO-JS scheme; Right: Present scheme.

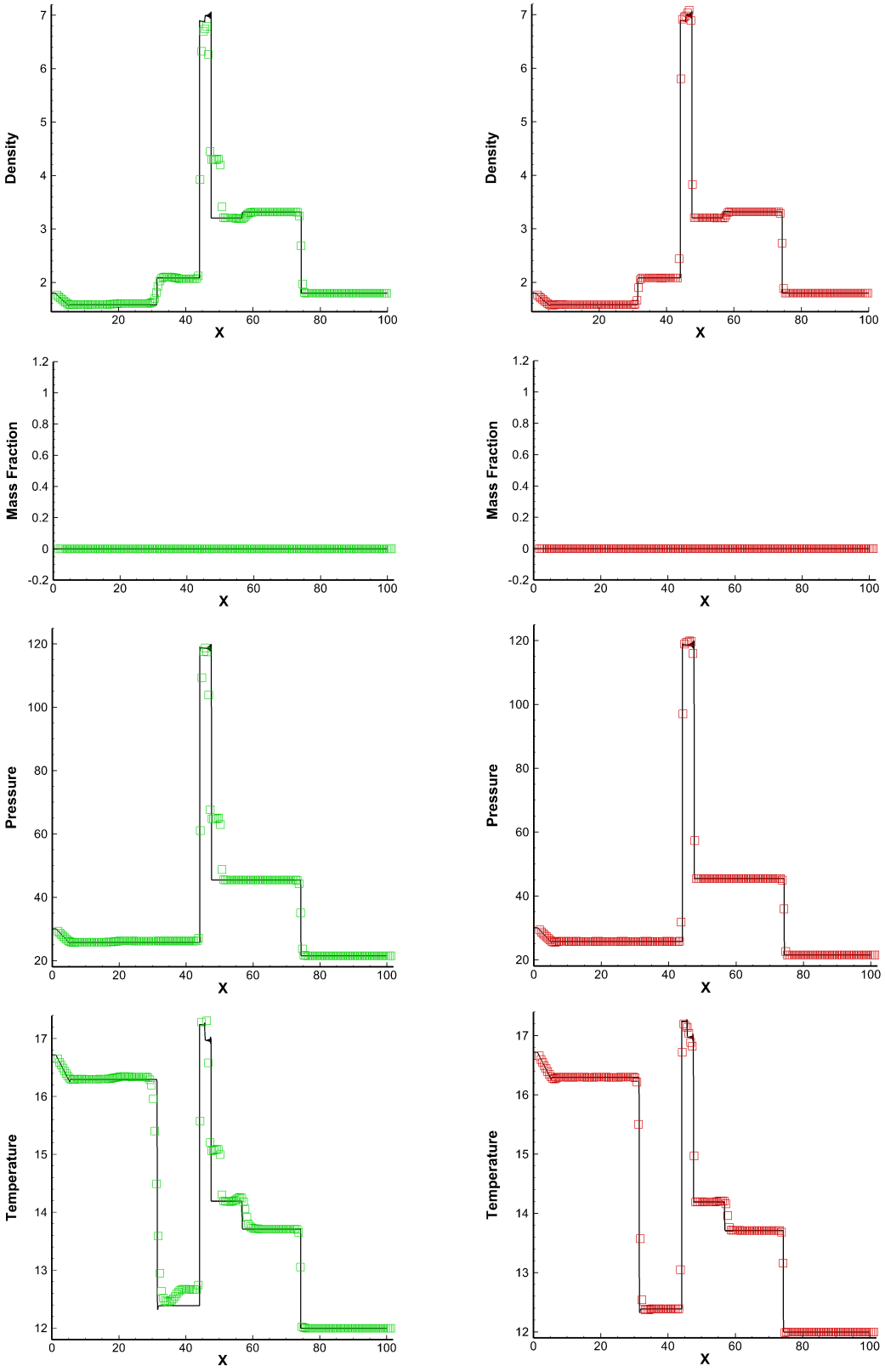


Figure 4.12: Numerical results for density, mass fraction, pressure and temperature of collision of two detonations at time $t_{\text{final}} = 6$ – Left: WENO-JS scheme; Right: Present scheme.

$\Omega = [0,2] \times [0,2]$ and the initial conditions consist of a circular burnt region as

$$(\rho_0, u_0, v_0, p_0, \alpha_0) = \begin{cases} (1,\ 0,\ 0,\ 80,\ 0) & \text{if } x^2 + y^2 \leq 0.36, \\ (1,\ 0,\ 0,\ 10^{-9},\ 1) & \text{otherwise,} \end{cases} \tag{4.43}$$

with reflective boundary conditions on the left and on the bottom and outflow on top and right ones. The final time is $t_{\text{final}} = 0.2$ and the parameters are $\gamma = 1.2$, $q = 50$, $T_{ign} = 50$, $K_0 = 2566.4$. The numerical simulations are performed over a uniform mesh made of $N_x \times N_y$ cells with $N_x = N_y = 160$ and $N_x = N_y = 320$ respectively. In figure 4.13 we illustrate the density and pressure in color maps for the finer mesh. Furthermore, we observe that the results obtained by the present scheme for the two meshes show a good convergence in this grid-refinement test, and the results are comparable to those in [114, 131]. Even though the value of density is low, the present scheme can simulate the test without any blow-up or code crash.

**Detonation-diffraction problems:** In this subsection, some detonation-diffraction problems are simulated, see [69, 114, 130]. Physically, the test consists of the detonation-diffraction of a shock wave emerging at a sharp convex corner with $90^o$ angle or passing around an obstacle with $180^o$ angle. There exists no general theory to completely analyze this situation. However, this problem has been extensively numerically studied to understand the flow features produced by detonation-diffraction of a shock wave. It became a popular challenging test case for numerical methods because the density and pressure drop drastically towards zero, and positivity issues are often encountered. The initial condition is given as

$$(\rho_0, u_0, v_0, E_0, \alpha_0) = \begin{cases} (11,\ 6.18,\ 0,\ 970,\ 1) & \text{if } x < L_s, \\ (1,\ 0,\ 0,\ 55,\ 1) & \text{otherwise,} \end{cases} \tag{4.44}$$

where $L_s$ is the initial shock location. The parameters of the model are $\gamma = 1.2, q = 50, T_{ign} = 50, K_0 = 2566.4$.

$90^o$ **corner test problem.** The computational domain is the union of $\Omega_1 = [0,1] \times [2,5]$

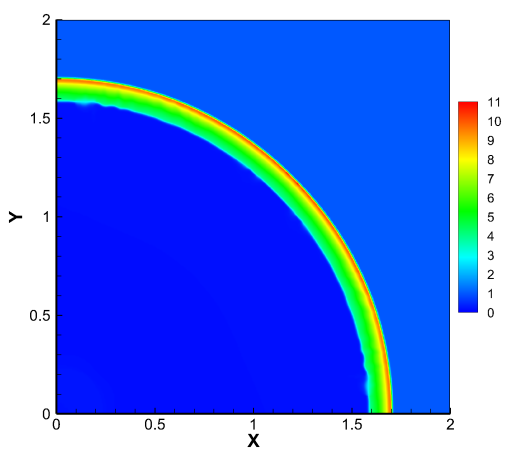


(a) Contour lines of density.

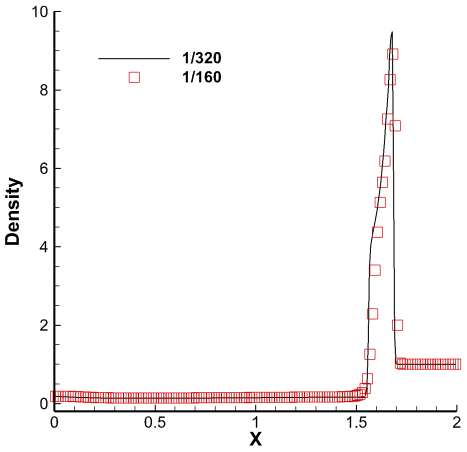


(b) Cut along the line y=0.25.

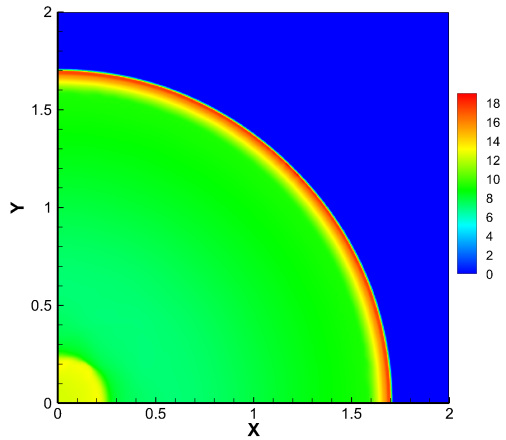


(c) Color map of pressure.

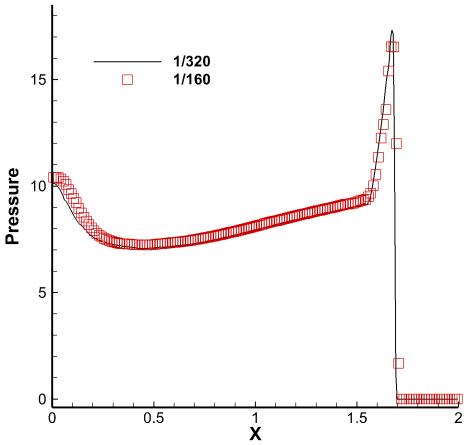


(d) Cut along the line y=0.25.

Figure 4.13: Numerical results for numerical convergence study – (a) Color map of density; (b) Cut along the line $y = 0.25$ for density; (c) Color map of pressure; (d) Cut along the line $y = 0.25$ for pressure.

and $\Omega_2 = [1, 5] \times [0, 5]$. A vertical shock is initially located at $L_s = 0.5$. The boundary conditions are reflective everywhere, except that at the left-most boundary $x = 0$ where $(\rho_{\text{in}}, u_{\text{in}}, v_{\text{in}}, E_{\text{in}}, \alpha_{\text{in}}) = (11,\ 6.18,\ 0,\ 970,\ 1)$ is imposed as inflow boundary condition. The final time of the computation is $t_{\text{final}} = 0.6$. The color maps and iso-line contours of density and pressure computed by the present BVD-MOOD scheme with $N_x \times N_y = 400 \times 400$ cells are plotted in figure 4.14. The complex flow structures generated from the diffraction of the detonation wave at the corner is in adequation with the results from [69, 114, 130]. Moreover, we can observe that the density and pressure drop down to values 0.0077 and 0.00023, respectively, for our simulation.

$180^o$ **corner test problem.** The computational domain is $\Omega = [0, 6] \times [0, 5]$ with a wall

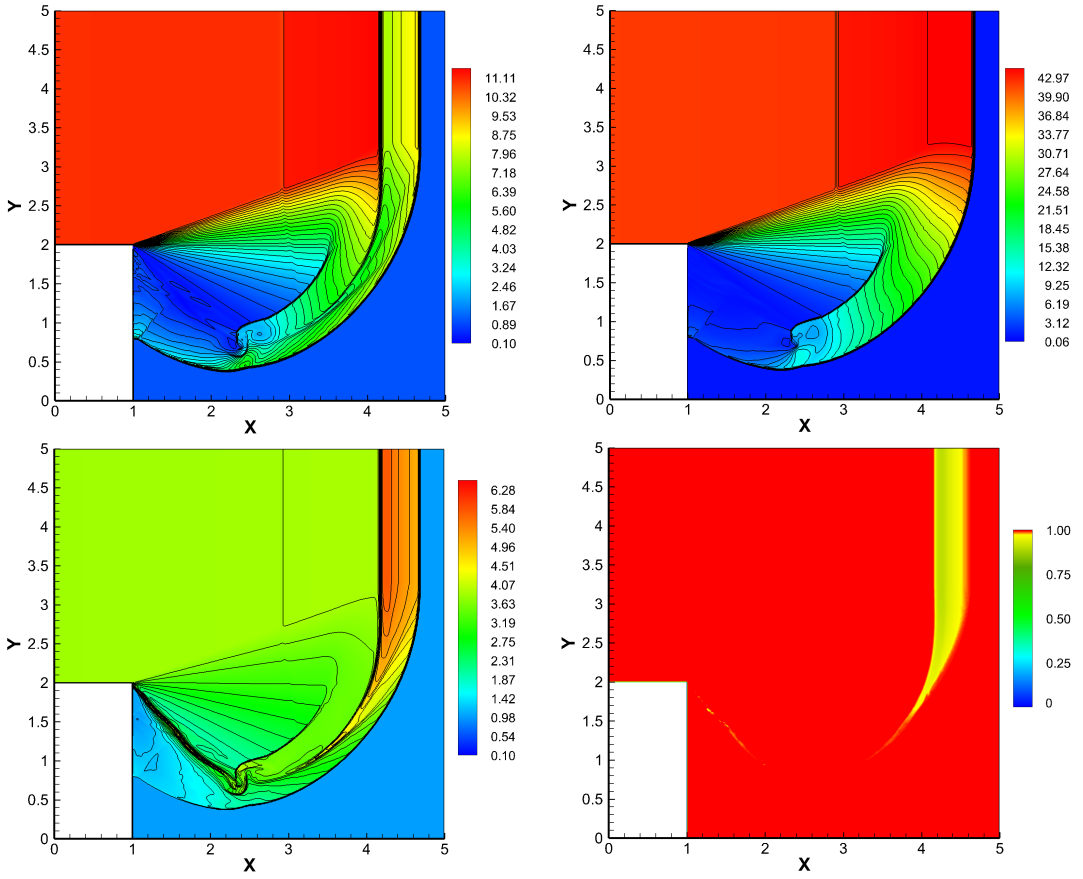


Figure 4.14: 2D Reactive Euler equations — Diffraction of detonation waves — Numerical results of a $90^o$ corner test case at time $t_{\text{final}} = 0.6$ with $400 \times 400$ mesh cells simulated by the BVD-MOOD scheme – Top-left panel: Density variable; Top-right panel: Pressure variable; Bottom-left panel: Temperature variable; Bottom-right panel: Mass fraction variable.

type obstacle $A = [0, 1.5] \times [2, 2]$. The initial vertical shock is located at $L_s = 1$. The boundary conditions are reflective ones everywhere, except for the left-most boundary $x = 0$ and $y > 2$ where inflow is imposed like previously. The final time of the computation is $t_{\text{final}} = 0.68$. The color maps and iso-line contours for the density and pressure computed by the BVD-MOOD scheme with $N_x \times N_y = 480 \times 400$ cells are plotted in figure 4.15. Again the main flow structures are well resolved and in good agreement with the ones in [69] without any trouble concerning the positivity preservation or the out-of-bound mass fraction, or, any robustness problem in general.

In our simulations for these two demanding test cases, the MOOD loop appropriately handles the occurrence of negative density/pressure as well as out-of-bound mass fraction, which are cured by the ultimate use of first-order Godunov scheme when and where

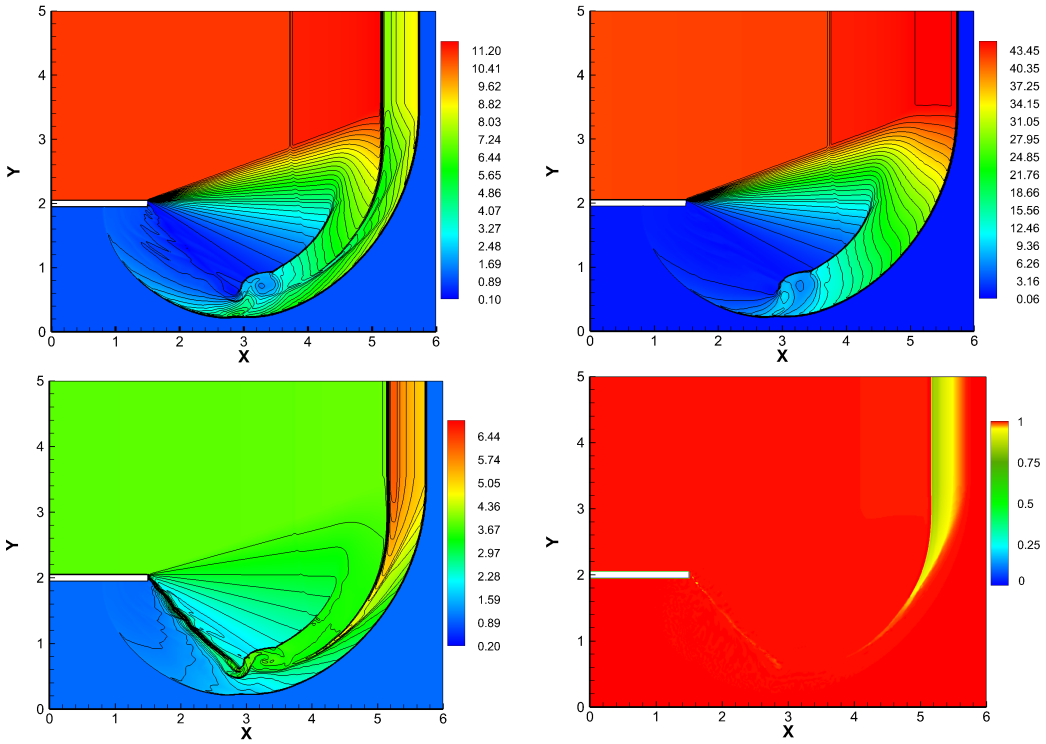


Figure 4.15: 2D Reactive Euler equations — Diffraction of detonation waves — Numerical results of $180^o$ corner test case at time $t_{\text{final}} = 0.68$ with $480 \times 400$ mesh cells simulated by the BVD-MOOD scheme – Top-left panel: Density variable; Top-right panel: Pressure variable; Bottom-left panel: Temperature variable; Bottom-right panel: Mass fraction variable.

required.

**Multiple obstacles problem:** As the last test case, we simulate the detonation wave passing multiple rectangular obstacles [69, 114] which is a even more challenging test case for the positivity preservation property. The main reason is that spurious negative density and/or pressure may occur below and on any of the sharp corners. The computational domain is $\Omega = [0, 8.3] \times [0, 10]$ with the first and second obstacle located at $A_1 = [1.3, 3.3] \times [0, 2.6]$ and $A_2 = [5.1, 8.3] \times [0, 4.3]$, respectively. The boundary conditions are reflective everywhere including the surface of obstacles. The related model parameters are set $\gamma = 1.2$, $q_0 = 50$, $T_{ign} = 20$, $K_0 = 2410.2$. The initial condition is

$$(\rho_0, u_0, v_0, E_0, \alpha_0) = \begin{cases} (7,\ 0,\ 0,\ 200,\ 0) & \text{if } x^2 + y^2 \leq 0.36, \\ (1,\ 0,\ 0,\ 55,\ 1) & \text{otherwise,} \end{cases} \tag{4.45}$$

which corresponds to a cylindrical detonation wave separating the burnt from the unburnt gas. The final time is set to $t_{\text{final}} = 1.4$. The numerical results are performed over the uniform mesh made of $N_x \times N_y = 332 \times 400$ cells. The 30 colored contours of density and pressure are presented in figure 4.16, which fit well with those in [69, 114]. Again, the BVD-MOOD scheme maintains the positivity of the physical variables (density, pressure) and the in-bound property of the mass fraction $\alpha$.

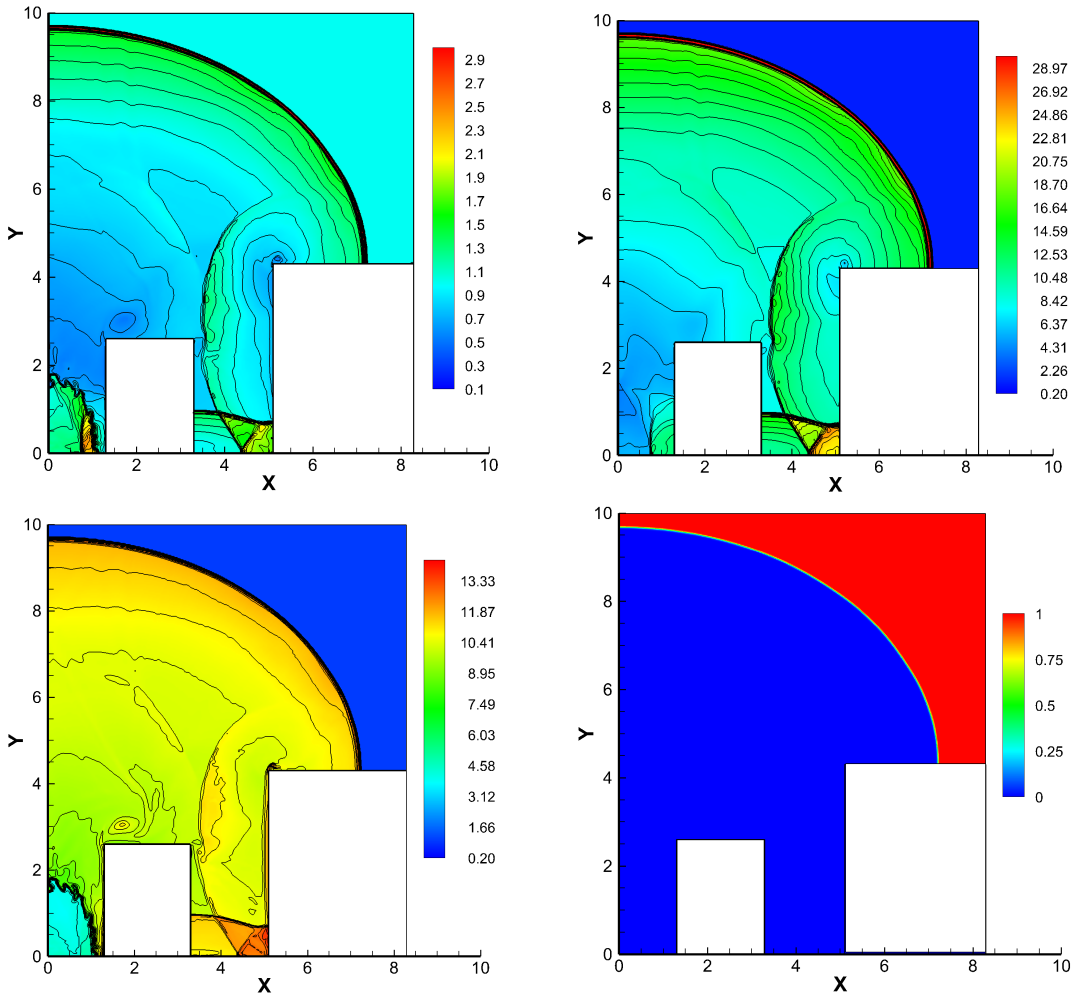


Figure 4.16: 2D Reactive Euler equations — Diffraction of detonation waves — Numerical results of multiple obstacles problem at time $t_{\text{final}} = 1.4$ with $332 \times 400$ mesh cells simulated by the BVD-MOOD scheme – Top-left panel: Density; Top-right panel: Pressure; Bottom-left panel: Temperature; Bottom-right panel: Mass fraction.

## 4.6 Summary

In this chapter we have presented a solution properties preserving reconstruction method called multi-stage BVD-MOOD scheme which solves the compressible Euler equations supplemented with three types of source terms. Different from the classical high order schemes based on a *a priori* limited polynomial reconstructions, the present scheme employs limiter-free mixed reconstructions. More precisely the algorithm relies on the Boundary Variation Diminishing (BVD) algorithm to choose between (1) a $4^{th}$ order unlimited polynomial interpolation for smooth profiles, (2) non-linear monotone THINC (hyperbolic tangent) functions of different smoothness to add dissipation and suppress spurious oscillations, (3) a sharp non-linear THINC function to deal with discontinuity and steep gradients, and (4) no reconstruction (i.e piecewise-constant leading to the $1^{st}$ order Godunov FV scheme) for extreme situations as the last resort.

The BVD strategy consists in selecting the reconstruction in one cell which is producing the smallest jumps at the cell boundaries because the numerical dissipation scales with those jumps. The BVD algorithm automatically selects the highest possible polynomial interpolation $\mathbb{P}_4$ for smooth solutions, the THINC reconstruction with a mild steepness on non-smooth area, which provides an oscillation-free solution (similar to TVD-MUSCL), and the step-like THINC shape to capture sharply the genuine discontinuous solution (contact, material interface, shock). Furthermore, the scheme is supplemented with an *a posteriori* MOOD loop to ensure that the numerical solution remains in its admissible set. If the candidate solution at time $t^{n+1}$ does not satisfy the Physical Admissible Detection (PAD) criterion, then the solution is locally recomputed with a $1^{st}$ order FV scheme. The *a posteriori* MOOD loop cures for instance the lack of positivity for density or internal energy, the in-bound property of mass fraction and the computer un-representable floating points `Nan, Inf`.

In our approach, among several reconstructions, the scheme is able to choose the most appropriate one according to some goodness criteria; the *a priori* BVD (least dissipative reconstruction), and, an *a posteriori* MOOD (robustness and fail-safe).

Based on the numerical experiments of benchmark test problems, it is demonstrated that

the present scheme can sharply capture the discontinuity, material interfaces, contacts, shocks and detonation fronts in both 1D and 2D. Moreover, due to the small but sufficient numerical dissipation, the small-scale structures are well represented, simultaneously with the prevention of the occurrence of spurious oscillations. The *a posteriori* detection loop renders the scheme extremely robust to positivity issues.

The comparison with the state of the art of high accurate numerical schemes such as WENO-JS is generally in favor of our approach. Recall that our approach is 'limiter-free' in the sense that the mechanism of dissipation is brought by the appropriate choice of the type of reconstruction (polynomial, smooth THINC, sharp THINC, piecewise constant).

# Chapter 5

# Implementation of BVD+MOOD scheme for compressible multi-phase flows

## 5.1 Introduction

In compressible multi-phase flow, the development of numerical methods is more challenging than in compressible single phase flow. The flow structures become complex when involving material interfaces between two gases or two materials of different physical nature. Therefore, numerical algorithms have been proposed for identifying each fluid by coupling the Euler equations with other equation such as $\gamma$-model [1, 2], the volume fraction model [96], or a level-set function [79]. However, these models suffer from non-physical oscillations occurred at material interfaces. On the other hand, the numerical method for compressible multi-phase flow should obey three critical conditions [28].

- Preserve the conservativeness of total mass, momentum and energy to correctly identify the location of material interfaces.

- Preserve numerical stability (no spurious oscillations at material interfaces)

- Maintain high-order accuracy in smooth regions of the flow

There are some difficulties in the one-fluid model when we apply solving compressible

multiphase flows. The density and energy in compressible flow have to be solved simultaneously with the material indicating function and couple with special formulations to maintain the physical and thermodynamical consistency as well as the pressure equilibrium across the interface. The high-resolution shock-capturing schemes for solving single-phase compressible flow, which generating numerical dissipation, then they tend to smear out discontinuities including the material interfaces.

In solving compressible multi-phase flows, standard shock-capturing numerical algorithms were also found in literature as TVD, MUSCL and WENO scheme [28, 59]. TVD and MUSCL scheme can solve discontinuities without spurious oscillations, however, they still suffer from excessive numerical dissipation. The excessive numerical dissipation smears out the flow fields as well as the discontinuities in mass or volume fraction which represents the material interfaces. Otherwise, WENO scheme can generously reduce numerical dissipation, capture well for the moving interfaces and provide high accuracy in smooth regions. However, it may generate numerical oscillations for compressible multi-phase flows with complex EOS as discussed in [28]. Commonly, the implementation of high order shock-capturing schemes to interfacial compressible multiphase flows requires further investigations.

This work presents a novel strategy to resolve the problems addressed above. We apply the multi-stage BVD-MOOD scheme [105, 106] which introduced in the previous chapters to solve five-equation model. More precisely, multi-stage BVD-MOOD scheme is applied to all state variables including volume fraction under finite volume wave propagation framework, so that the consistency can be realized among the physical variables and volume fraction throughout the solution procedure. There is no additional treatment or special techniques to adjust the consistency of physical variables and volume fraction. The numerical model is formulated under a standard finite volume method with a HLLC Riemann solver in the wave propagation form [61].

Verifying the numerical tests show that the present method is capable in capturing the material interfaces as a well-resolved sharp jump in volume fraction. Furthermore, there is no visible spurious oscillations at material interfaces and the numerical results show superior solution quality competitive to other existing methods.

## 5.2 Solution procedures for compressible two-phase flows by using five-equation model

### 5.2.1 Governing equations

The five-equation model [4] is employed in this present work for simulating the inviscid compressible two-phase flows. In this five-equation model, the velocity and pressure of the mixture are assumed to be equilibrium for material interface. The five-equation model consists of two continuity equations for phasic mass, a momentum equation, an energy equation, and an advection equation of volume fraction as follows

$$\begin{aligned}
&\frac{\partial}{\partial t}\left(\alpha_1\rho_1\right) + \nabla\cdot\left(\alpha_1\rho_1\mathbf{u}\right) = 0,\\
&\frac{\partial}{\partial t}\left(\alpha_2\rho_2\right) + \nabla\cdot\left(\alpha_2\rho_2\mathbf{u}\right) = 0,\\
&\frac{\partial}{\partial t}(\rho\mathbf{u}) + \nabla\cdot\left(\rho\mathbf{u}\otimes\mathbf{u}\right) + \nabla p = 0,\\
&\frac{\partial E}{\partial t} + \nabla\cdot\left(E\mathbf{u} + p\mathbf{u}\right) = 0,\\
&\frac{\partial \alpha_1}{\partial t} + \mathbf{u}\cdot\nabla\alpha_1 = 0,
\end{aligned} \tag{5.1}$$

where $\rho_k$ and $\alpha_k$ are the $k$th phasic density and volume fraction, respectively, for $k = 1, 2$ which $\alpha_k \in [0, 1]$, $\mathbf{u}$ is the vector of mixture velocity, $p$ is the mixture pressure, and $E$ is the total energy.

This five-equation model is not closed. To close the system, a mixture of two Mie-Grüneisen fluids for equation of state [98] are considered where $\Gamma_k = \left(1/\rho_k\right)\left(\partial p_k/\partial e_k\right)\big|_{\rho_k}$ is the Grüneisen coefficient, and $p_{\infty,k}, e_{\infty,k}$ are the properly chosen states of the pressure the internal energy along some reference curves (e.g., along an isentrope, a single shock Hugoniot, or the other empirically fitting curves) in order to match the experimental data of the examined material [77]. The parameters $\Gamma_k, p_{\infty,k}$ and $e_{\infty,k}$ can be simplified as functions of density only. This Mie-Grüneisen equation of state can be approximated a wide variety of materials including some gaseous or solid explosives and solid metals under high pressure. For conservativeness constraints, the global quantities

and thermodynamical parameters for the mixture can be defined as follows

$$\begin{aligned} &\alpha_1 + \alpha_2 = 1, \\ &\alpha_1\rho_1 + \alpha_2\rho_2 = \rho, \\ &\alpha_1\rho_1 e_1 + \alpha_2\rho_2 e_2 = \rho e. \end{aligned} \tag{5.2}$$

From [98] under the isobaric assumption, the Grüneisen coefficient, reference pressure $p_\infty$ and reference internal energy $e_\infty$ can be expressed as

$$\begin{aligned} &\frac{\alpha_1}{\Gamma_1(\rho_1)} + \frac{\alpha_2}{\Gamma_2(\rho_2)} = \frac{1}{\Gamma}, \\ &\alpha_1\rho_1 e_{\infty,1}(\rho_1) + \alpha_2\rho_2 e_{\infty,2}(\rho_2) = \rho e_\infty, \\ &\alpha_1\frac{p_{\infty,1}(\rho_1)}{\Gamma_1(\rho_1)} + \alpha_2\frac{p_{\infty,2}(\rho_2)}{\Gamma_2(\rho_2)} = \frac{p_\infty(\rho)}{\Gamma(\rho)}, \end{aligned} \tag{5.3}$$

then, the mixture pressure is calculated by

$$p = \left(\rho e - \sum_{k=1}^{2}\alpha_k\rho_k e_{\infty,k}(\rho_k) + \sum_{k=1}^{2}\alpha_k\frac{p_{\infty,k}(\rho_k)}{\Gamma_k(\rho_k)}\right) \Big/ \sum_{k=1}^{2}\frac{\alpha_k}{\Gamma_k(\rho_k)}. \tag{5.4}$$

These mixing rules of Eq.(5.3) and Eq.(5.4) are ensuring that the mixture pressure is free of spurious oscillations across the material interfaces[1, 2, 96, 97, 98]. Under isobaric assumption [4], the sound speed of mixture could be calculated as the volumetric average of the phasic sound speeds as

$$c^2 = \alpha_1 c_1^2 + \alpha_2 c_2^2 \tag{5.5}$$

**Note:** The time step is restricted with the local wave speed and local sound speed since sound speed is totally different from different materials.

### 5.2.2 Solution procedures with finite volume wave propagation method

We can rewrite the Eq.(5.1) into the form of quasi-conservative five-equation model as

$$\frac{\partial \mathbf{U}}{\partial t} + \frac{\partial \mathbf{F(U)}}{\partial x} + \mathbf{B(U)}\frac{\partial \mathbf{U}}{\partial x} = 0, \tag{5.6}$$

where the vectors of physical variables **U** and flux function **F(U)** are

$$\begin{aligned} \mathbf{U} &= (\alpha_1\rho_1, \alpha_2\rho_2, \rho u, E, \alpha_1)^T, \\ \mathbf{F(U)} &= (\alpha_1\rho_1 u, \alpha_2\rho_2 u, \rho u u + p, Eu + pu, 0)^T, \end{aligned} \tag{5.7}$$

respectively. The matrix **B(U)** is expressed as

$$\mathbf{B(U)} = \text{diag}(0, 0, 0, 0, u), \tag{5.8}$$

where $u$ denotes the velocity component is $x$ direction.

The space computational domain is defined as $\Omega = [x^L, x^R]$ and divided into $N$ cells, $I_i = [x_{i-1/2}, x_{i+1/2}]$, for $i = 1, 2, ..., N$. The grid size is uniform over the computational domain and denoted by $\Delta x = x_{i+1/2} - x_{i-1/2}$. The time coordinate is $t$ and $t \leq T$, where $T > 0$ is the final time. The time interval $[0, T]$ is split into time steps $[t^n, t^{n+1}]$, the size of the time-step is non-uniform and denoted by $\Delta t = t^{n+1} - t^n > 0$. For the standard finite volume semi-discretization, we employ the approximated volume-integrated average (VIA) of the solution $U(x, t)$ over a mesh cell $I_i$ at time $t$ as

$$\overline{U}_i(t) = \frac{1}{\Delta x} \int_{x_{i-1/2}}^{x_{i+1/2}} U(x, t)\, dx, \qquad \text{where} \qquad i = 1, 2, \ldots, N. \tag{5.9}$$

From Eq.(5.6), denote $\mathcal{L}(\overline{U}(t))$ as all the spatial discretization terms, then the semi-discrete version of the finite volume method can be expressed as system of ODEs (Ordinary Differential Equations)

$$\frac{\partial \overline{U}(t)}{\partial t} = \mathcal{L}(\overline{U}(t)), \tag{5.10}$$

where the spatial discretization terms in a cell $C_i$ is calculated by

$$\mathcal{L}\left(\overline{U}_i(t)\right) = -\frac{1}{\Delta x}\left(\mathcal{A}^+\Delta U_{i-1/2} + \mathcal{A}^-\Delta U_{i+1/2} + \mathcal{A}\Delta U_i\right), \tag{5.11}$$

where $\mathcal{A}^+\Delta U_{i-1/2}$ and $\mathcal{A}^-\Delta U_{i+1/2}$, are the right- and left-moving fluctuations, respec-

tively, which enter into the grid cell, and $\mathcal{A}\Delta U_i$ is the total fluctuation within $C_i$. We need to solve Riemann problems to determine these fluctuations. The right- and left-moving fluctuations can be calculated using

$$\mathcal{A}^{\pm}\Delta U_{i-1/2} = \sum_{k=1}^{3} \left[s^k\left(U^L_{i-1/2}, U^R_{i-1/2}\right)\right]^{\pm} \mathcal{W}^k\left(U^L_{i-1/2}, U^R_{i-1/2}\right), \tag{5.12}$$

where moving speeds $s^k$ and jumps $\mathcal{W}^k$ of the $k$ propagating discontinuities can be solved by Riemann solvers [108] given the reconstructed values $U^L_{i-1/2}$ and $U^R_{i-1/2}$, which are computed from the reconstruction functions $\widetilde{U}_{i-1}(x)$ and $\widetilde{U}_i(x)$ to the left and right of the cell edge $x_{i-1/2}$, respectively. Normally, the notations for the quantities $s^{\pm}$ are set by $s^+ = \max(s, 0)$ and $s^- = \min(s, 0)$. In similar manner, the total fluctuation can be defined by

$$\mathcal{A}\Delta U_i = \sum_{k=1}^{3} \left[s^k\left(U^R_{i-1/2}, U^L_{i+1/2}\right)\right] \mathcal{W}^k\left(U^R_{i-1/2}, U^L_{i+1/2}\right). \tag{5.13}$$

Similarly, the remain task (detailed in the chapter 3 as well as previous chapter) is the calculation of states $U^L_{i-1/2}$ and $U^R_{i-1/2}$ of cell boundaries at given time $t$ through a reconstruction procedure.

In practice, given the reconstructed values $U^L_{i-1/2}$ and $U^R_{i-1/2}$ at cell boundaries, the minimum and maximum moving speeds (wave speed estimates) $s^1(U^L_{i-1/2}, U^R_{i-1/2})$ and $s^3(U^L_{i-1/2}, U^R_{i-1/2})$ can be simply determined and used in HLLC Riemann solver as

$$\begin{aligned} s^1 &= \min\left\{u^L_{i-1/2} - c^L_{i-1/2}, u^R_{i-1} - c^R_{i-1}\right\}, \\ s^3 &= \max\left\{u^L_{i-1/2} + c^L_{i-1/2}, u^R_{i-1} + c^R_{i-1}\right\}, \end{aligned} \tag{5.14}$$

where $c^L_{i-1/2}$ and $c^R_{i-1/2}$ are sound speeds calculated by using reconstructed values $U^L_{i-1/2}$ and $U^R_{i-1/2}$, respectively. Then the speed of the middle wave is estimated by

$$s^2 = \frac{p^R_{i-1/2} - p^L_{i-1/2} + \rho^L_{i-1/2}u^L_{i-1/2}\left(s^1 - u^L_{i-1/2}\right) - \rho^R_{i-1/2}u^R_{i-1/2}\left(s^3 - u^R_{i-1/2}\right)}{\rho^L_{i-1/2}\left(s^1 - u^L_{i-1/2}\right) - \rho^R_{i-1/2}\left(s^3 - u^R_{i-1/2}\right)}. \tag{5.15}$$

The left-side and right-side intermediate state variables $\mathbf{U}^{*L}_{i-1/2}$ and $\mathbf{U}^{*R}_{i-1/2}$ is computed by

$$\mathbf{U}^{*L}_{i-1/2} = \frac{\left(\mathbf{u}^{L}_{i-1/2} - s^1\right)\mathbf{U}^{L}_{i-1/2} + \left(p^{L}_{i-1/2}\mathbf{n}^{L}_{i-1/2} - p^{*}_{i-1/2}\mathbf{n}^{*}_{i-1/2}\right)}{s^2 - s^1} \tag{5.16a}$$

$$\mathbf{U}^{*R}_{i-1/2} = \frac{\left(\mathbf{u}^{R}_{i-1/2} - s^3\right)\mathbf{U}^{R}_{i-1/2} + \left(p^{R}_{i-1/2}\mathbf{n}^{R}_{i-1/2} - p^{*}_{i-1/2}\mathbf{n}^{*}_{i-1/2}\right)}{s^2 - s^3} \tag{5.16b}$$

where the vector $\mathbf{n}^{L}_{i-1/2} = (0, 0, 1, u^{L}_{i-1/2}, 0)$, $\mathbf{n}^{R}_{i-1/2} = (0, 0, 1, u^{L}_{i-1/2}, 0)$, and $\mathbf{n}^{*}_{i-1/2} = (0, 0, 1, s^2, 0)$.

Also, the vector $\mathbf{u}^{L}_{i-1/2}$ and $\mathbf{u}^{R}_{i-1/2}$ are

$$\mathbf{u}^{L}_{i-1/2} = (u^{L}_{i-1/2}, u^{L}_{i-1/2}, u^{L}_{i-1/2}, u^{L}_{i-1/2}, u^{L}_{i-1/2}, s^2), \tag{5.17a}$$

$$\mathbf{u}^{R}_{i-1/2} = (u^{R}_{i-1/2}, u^{R}_{i-1/2}, u^{R}_{i-1/2}, u^{R}_{i-1/2}, u^{R}_{i-1/2}, s^2). \tag{5.17b}$$

The intermediate pressure also may be estimated as

$$p^{*}_{i-1/2} = \rho^{L}_{i-1/2}\left(u^{L}_{i-1/2} - s^1\right)\left(u^{L}_{i-1/2} - s^2\right) + p^{L}_{i-1/2} = \rho^{R}_{i-1/2}\left(u^{R}_{i-1/2} - s^1\right)\left(u^{R}_{i-1/2} - s^2\right) + p^{R}_{i-1/2}. \tag{5.18}$$

Then we can calculate the jumps $\mathcal{W}^k(U^{R}_{i-1/2}, U^{L}_{i-1/2})$ as

$$\begin{aligned} \mathcal{W}^1 &= \mathbf{U}^{*L}_{i-1/2} - \mathbf{U}^{L}_{i-1/2}, \\ \mathcal{W}^2 &= \mathbf{U}^{*R}_{i-1/2} - \mathbf{U}^{*L}_{i-1/2}, \\ \mathcal{W}^3 &= \mathbf{U}^{R}_{i-1/2} - \mathbf{U}^{*R}_{i-1/2}. \end{aligned} \tag{5.19}$$

### 5.2.3 Time integration

Given the spatial discretization, time integration scheme can be used to solve ODEs. In order to achieve high-order numerical accuracy in time, the discretization in time are made by the third-order TVD Runge-Kutta (RK3) method [43, 93]. More precisely, the

third-order TVD Runge-Kutta (RK3) is given by

$$\begin{aligned} U^{(1)} &= U^n + \Delta t L\left(U^n\right), \\ U^{(2)} &= \frac{3}{4}U^n + \frac{1}{4}U^{(1)} + \frac{1}{4}\Delta t L\left(U^{(1)}\right), \\ U^{n+1} &= \frac{1}{3}U^n + \frac{2}{3}U^{(2)} + \frac{2}{3}\Delta t L\left(U^{(2)}\right). \end{aligned} \tag{5.20}$$

## 5.3 Numerical experiments

In this section, we present some sample numerical results simulated by the multi-stage BVD-MOOD scheme for tracking material interfaces arising from compressible two-phase flows. For verifying our algorithm, we also compare the results of present scheme to the results of WENO-Z [3] scheme which is one of representative high order shock capturing schemes. The reconstruction process is conducted in terms of primitive variables reconstruction for both schemes, HLLC Riemann solver is employed for the flux computation and a TVD-RK3 for time integration.

### 5.3.1 Passive advection of a square liquid column

Firstly, we simulate a simple interface-only problem in order to evaluate the ability of the present scheme to correctly capture material interfaces as well as to maintain the equilibrium of velocity and pressure fields. The problem consists of a square liquid column in gas transported with a uniform velocity $u = u_0 = 10^2$ m/s under equilibrium pressure which is $p = p_0 = 10^5$ Pa in a shock tube of one meter ($\Omega = [0, 1]$). The initial condition is given as

$$(\rho_1\alpha_1, \rho_2\alpha_2, u_0, p_0, \alpha_1) = \begin{cases} (1000, 0, 100, 10^5, 1-\epsilon) & \text{if} \quad 0.4 \leq x \leq 0.6, \\ (0, 1, 0, 10^5, \epsilon) & \text{otherwise.} \end{cases} \tag{5.21}$$

where $\epsilon$ is set to $10^{-8}$ in numerical tests in this section. To model the thermodynamic behavior of liquid and gas, we use the stiffened gas equation of state where the parameter

material-dependent parameters appeared in Eq.(5.3) are

$$\Gamma_k = \gamma_k - 1, \quad p_{\infty,k} = \gamma_k \mathcal{B}_k, \quad e_{\infty,k} = 0.$$

with the parameter values taken in turn to be $\gamma_1 = 4.4, \mathcal{B}_1 = 6 \times 10^8$ Pa and $\gamma_2 = 1.4, \mathcal{B}_2 = 0$ for the liquid and gas phases respectively. The simulation was performed by the standard $5^{th}$ order WENO-Z scheme and the present multi-stage BVD-MOOD scheme both using a uniform mesh made of $N = 200$ cells with CFL = 0.5 and the computation run up to final time $t_{\text{final}} = 10$ ms (one revolution). In this test case, periodic boundary condition is used on the left and right boundaries during the computation. We plot the results of density of fluid 1, volume fraction of fluid 1, pressure, and velocity variables for both schemes in figure 5.1. We observe that the multi-sage BVD-MOOD scheme can solve the sharp interfaces within only few cells whereas WENO-Z scheme generates excessive numerical dissipation for the interfaces as other convectional shock capturing schemes. In addition, the present scheme can retain the correct pressure equilibrium and particle velocity without introducing spurious oscillations across the interfaces.

### 5.3.2 Two-material impact problem

An other benchmark test is two-phase impact problem which is in [89, 98]. This test consists of copper plate which impacts on an inert explosive. Initially, the a right moving copper plate with velocity $u_1 = 1500$ m/s interacting with explosive is at rest on the right of the plate. The two materials are under atmospheric conditions which have pressure $p_0 = 10^5$ Pa and temperature $T_0 = 300$ K throughout the domain. The material properties of copper and (solid) explosive are governed by Cochran-Chan of state where written in the Mie-Grüneisen as in Eq.(5.3) and we set the same $\Gamma_k$ as in the EOS

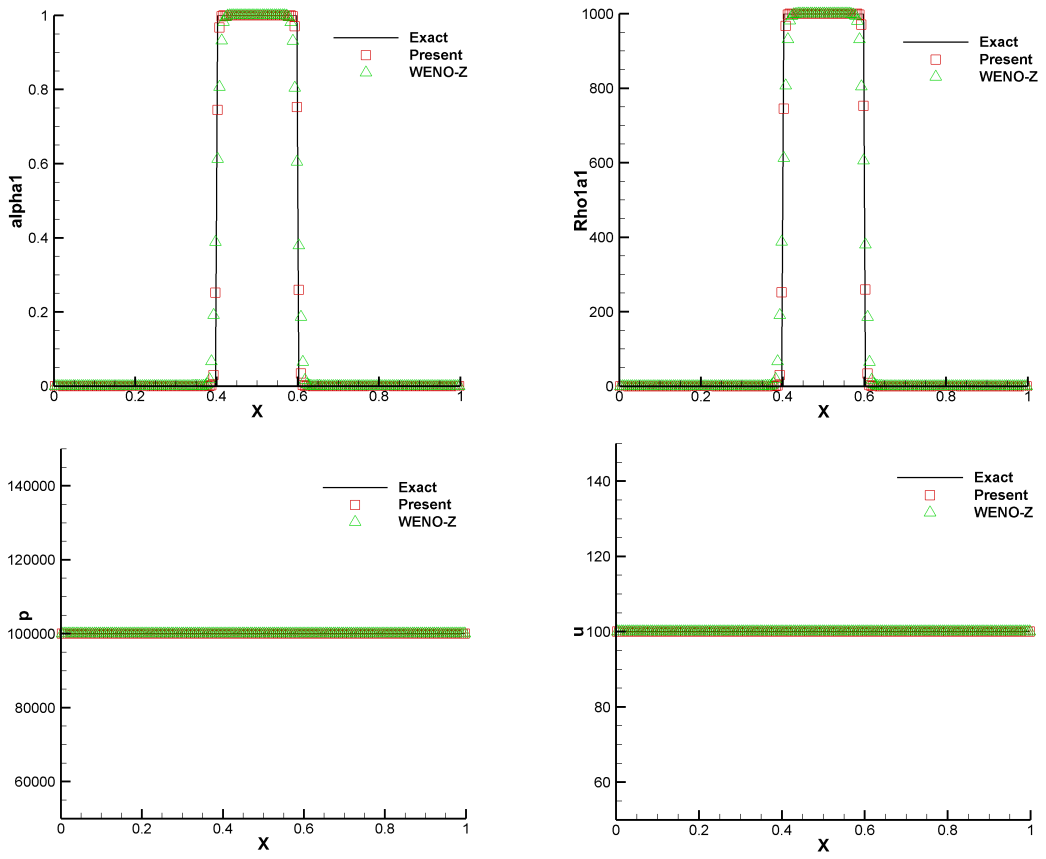


Figure 5.1: Numerical results computed by WENO-Z scheme and present scheme for volume fraction, density of fluid 1, pressure and velocity of passive advection of a square liquid column at time $t_{\text{final}} = 10$ ms.

of stiffened gas case, but $p_{\infty,k}, e_{\infty,k}$ are expressed as follows

$$
\begin{aligned}
p_{\infty,k}\left(\rho_k\right) &= \mathcal{B}_{1k}\left(\frac{\rho_{0k}}{\rho_k}\right)^{-\mathcal{E}_{1k}} - \mathcal{B}_{2k}\left(\frac{\rho_{0k}}{\rho_k}\right)^{-\mathcal{E}_{2k}}, \\
e_{\infty,k}\left(\rho_k\right) &= \frac{-\mathcal{B}_{1k}}{\rho_{0k}\left(1-\mathcal{E}_{1k}\right)}\left[\left(\frac{\rho_{0k}}{\rho_k}\right)^{1-\mathcal{E}_{1k}}\right] + \frac{\mathcal{B}_{2k}}{\rho_{0k}\left(1-\mathcal{E}_{2k}\right)}\left[\left(\frac{\rho_{0k}}{\rho_k}\right)^{1-\mathcal{E}_{2k}}\right] - C_{vk}T_0.
\end{aligned}
\tag{5.22}
$$

where $\rho_{0k}$, $\mathcal{B}_{1k}$, $\mathcal{B}_{2k}$, $\mathcal{E}_{1k}$ $\mathcal{E}_{2k}$, $\gamma_k$ and $C_{vk}$ are the material-dependent quantities which are listed in table 5.1 for a typical set of numerical values for copper and (solid) explosive.

Table 5.1: Material quantities for copper ($k = 1$) and explosive ($k = 2$) in Cochran-Chan equation of state Eq.(5.22).

| **k** | $\rho_{0k}$ (kg/m$^3$) | $\mathcal{B}_{1k}$ (GPa) | $\mathcal{B}_{2k}$ (GPa) | $\mathcal{E}_{1k}$ | $\mathcal{E}_{2k}$ | $\gamma_k$ | $C_{vk}$ (J/kg.K) |
|---|---|---|---|---|---|---|---|
| **1** | 8900 | 145.67 | 147.75 | 2.99 | 1.99 | 3 | 393 |
| **2** | 1840 | 12.87 | 13.42 | 4.1 | 3.1 | 1.93 | 1087 |

The solution of this test consists of two shock waves. One is facing to right and propagating in the inert explosive while another is facing to the left and propagating in the copper. A material interface is lying in between the shock waves and separating these two different materials. We simulate this problem up to time $t_{\text{final}} = 85\mu s$ with a 200-cell grid and CFL set to 0.5. The reference solution is computed by MUSCL scheme with 8000-cell grid. In figure 5.2 we demonstrate the results for the copper volume frac-

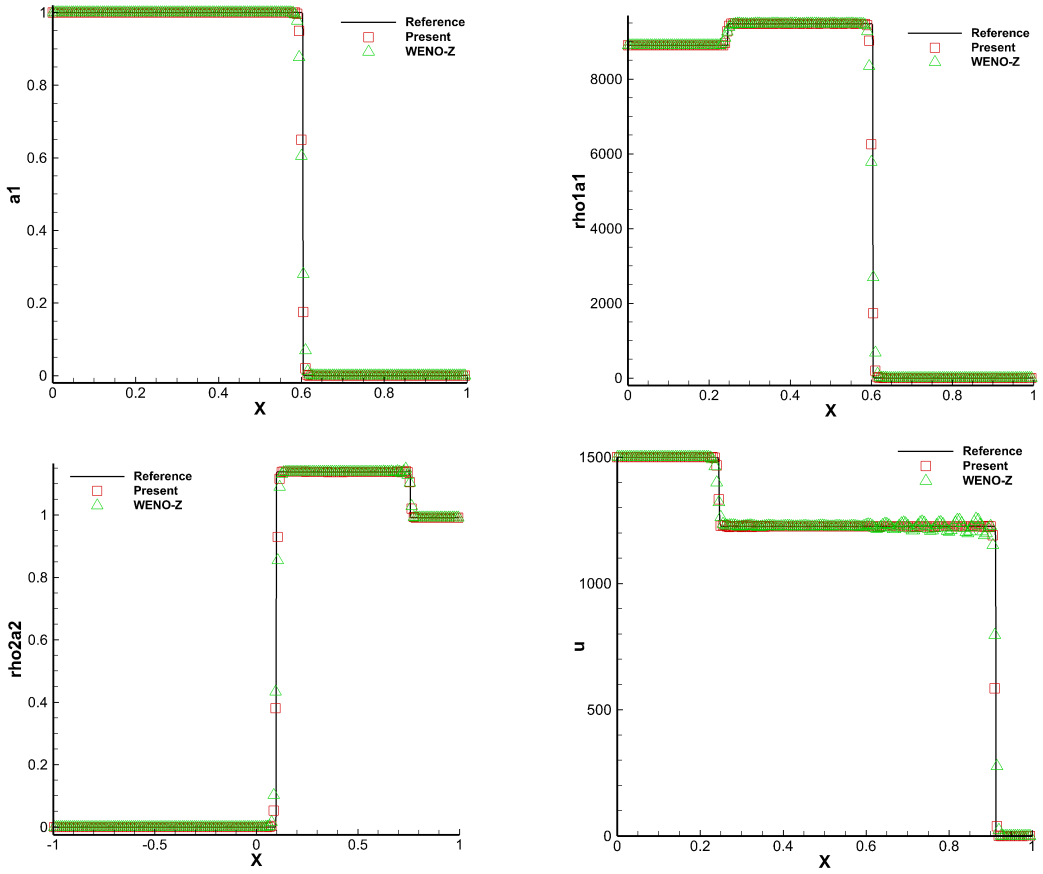


Figure 5.2: Numerical results computed by WENO-Z scheme and present scheme for volume fraction, partial densities and velocity of copper and inert explosive impact problem at $t_{\text{final}} = 85\mu s$.

tion, the partial densities, and velocity of both WENO-Z and multi-stage BVD-MOOD scheme for comparison. We observe that multi-stage BVD-MOOD scheme is able to keep sharp interface without spurious numerical oscillations in velocity fields while WENO-Z scheme generates spurious numerical oscillations.

### 5.3.3 Shock interface interaction problem

In this test, the interaction between a shock wave and a material interface is considered. Commonly, this problem is a challenging problem for numerical shock-capturing schemes. For instance, the schemes which have lost the conservation on discrete level at material interface may miscalculate the position and speed of waves resulted from the interaction[28]. Here, the interaction between a strong shock wave in helium and an air/helium interface is studied.

The initial condition of the problem is set the same as [28, 29]. As given, the problem consists of a Mach 8.96 shock wave is traveling in helium with $\gamma_1 = 1.67$, toward a material interface with air $\gamma_2 = 1.4$ which is simultaneously moving toward the shock wave. The initial condition of this problem is given as

$$(\alpha_1\rho_1, \alpha_2\rho_2, u_0, p_0, \alpha_1) = \begin{cases} (0.386, 0, 26.59, 100, 1-\epsilon) & \text{for } -1 \leq x < -0.8, \\ (0.1, 0, -0.5, 1, 1-\epsilon) & \text{for } -0.8 \leq x < -0.2, \\ (0, 1, -0.5, 1, \epsilon) & \text{for } -0.2 \leq x < 1. \end{cases} \tag{5.23}$$

The computational domain is $\Omega = [-1, 1]$ with a uniform mesh made of $N = 200$ cells. The solution is calculated up to time $t_{\text{final}} = 0.07$ and the CFL number is set to 0.1. In figure 5.3 we plot the results of both schemes for the helium volume fraction, total density, pressure and velocity for comparisons. The numerical solution of both schemes has good agreement with the reference or exact one, correctly capture the location and speed of all the waves in the shock interface interaction. Moreover, there is no spurious oscillations at the material interface are observed and the multi-stage BVD-MOOD scheme can capture the interface sharper than WENO-Z scheme. Eventually, for both schemes some oscillations are appeared in the wake of the reflected shock wave. As in [28], it is an evidence of high-order accuracy of the spatial reconstruction scheme, and spurious oscillations is latter reduced and disappeared.

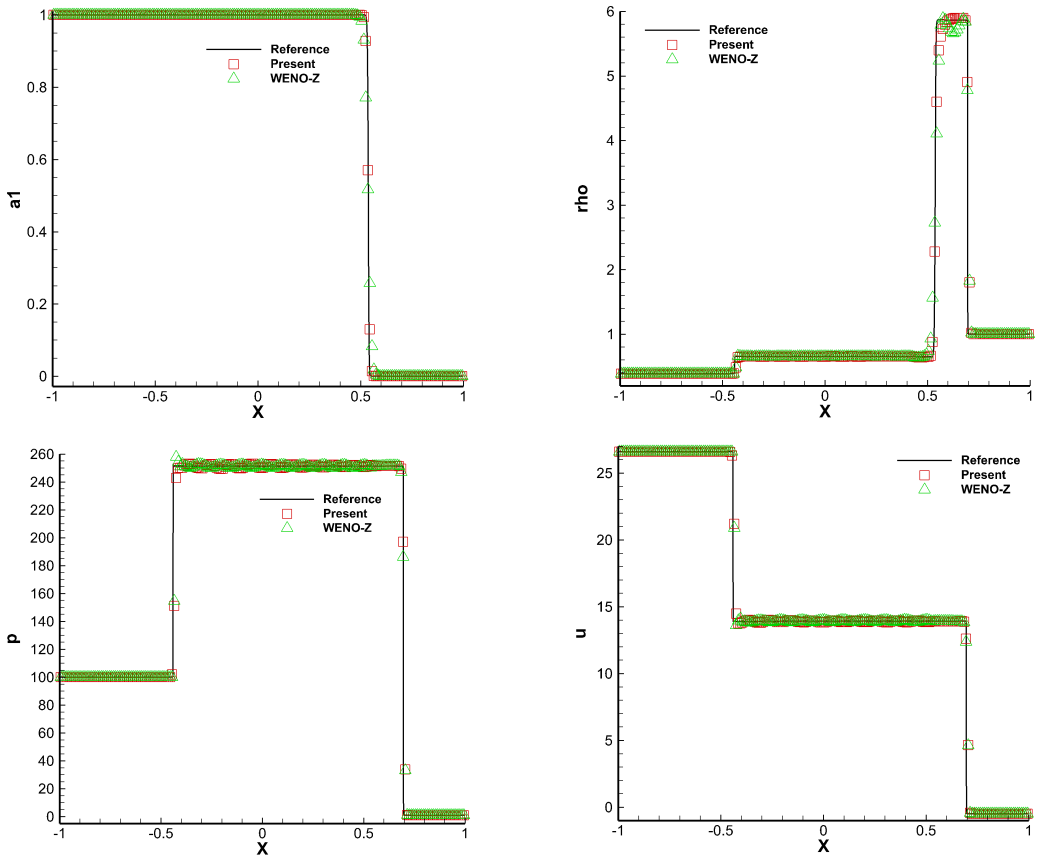


Figure 5.3: Numerical results computed by WENO-Z scheme and present scheme for helium volume fraction, total density, pressure and velocity of shock/interface interaction problem at $t_{\text{final}} = 0.07$.

### 5.3.4 Gas/gas shock tube problem

Chen and Liang [19] first proposed the test problem. Within a shock tube of unit length as $\Omega = [0, 1]$, the interface initially locates at $x = 0.5$. The high pressure gas with $\gamma_1 = 1.6$ is on the left side while the low pressure gas with $\gamma_2 = 1.4$ is on the right side. More precisely, the initial condition is given as

$$(\alpha_1\rho_1, \alpha_2\rho_2, u, p, \alpha_1) = \begin{cases} (1, 0, 0, 500, 1 - \epsilon), & 0 \leq x \leq 0.5, \\ (0, 1, 0, 0.2, \epsilon), & 0.5 \leq x \leq 1. \end{cases} \tag{5.24}$$

The solution is run up to time $t_{\text{final}} = 0.01$ with a uniform mesh made of $N = 200$ cells and CFL $= 0.5$. The results of the volume fraction, partial density (fluid 1), pressure and velocity computed by WENO-Z and multi-stage BVD-MOOD scheme are shown in figure 5.4. It is observed that the results obtained by both schemes are in quite good agree-

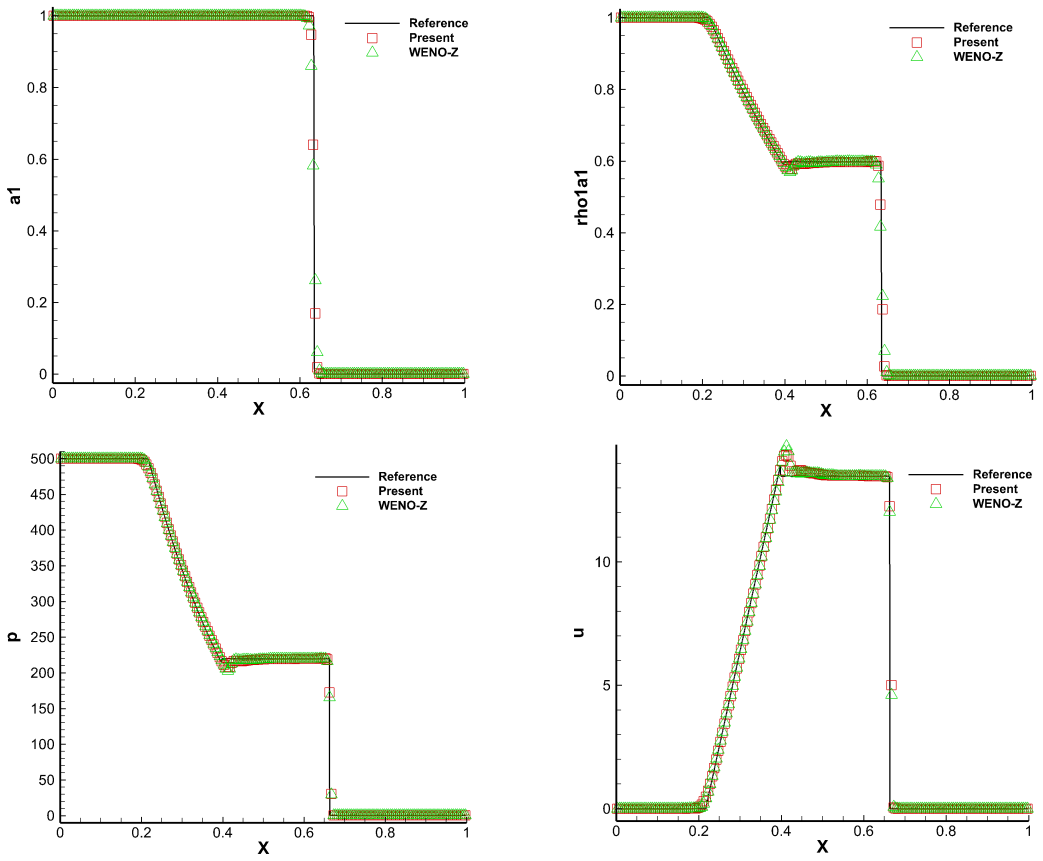


Figure 5.4: Numerical results computed by WENO-Z scheme and present scheme for the volume fraction, partial density (density of fluid 1), pressure and velocity of gas/gas shock tube problem at $t_{\text{final}} = 0.01$.

ment. However, the present scheme can keep sharper interface compares to WENO-Z scheme.

### 5.3.5 Gas-liquid Riemann problem

The test problem is firstly proposed as a model for under water explosions by Cocchi et *al*[24], and subsequently by Shyue [98]. In this test, the stiffened gas EOS is considered. Initially, the left state of the problem consists of high pressure air, while the right state is low pressure water at atmospheric pressure. The solution consists of a left-moving rarefaction wave, a right-moving shock wave and material interface. The initial condition

is the same as in [113] and is given in non-dimensionalization as

$$(\alpha_1\rho_1, \alpha_2\rho_2, u, p, \alpha_1) = \begin{cases} (1.241, 0, 0, 2.753, 1-\epsilon) & \text{for} \quad -1 \leq x < 0, \\ (0, 0.991, 0, 3.059 \times 10^{-4}, \epsilon) & \text{for} \quad 0 \leq x \leq 1. \end{cases} \tag{5.25}$$

To model the thermodynamic behavior of liquid and gas, we use the stiffened gas equation of state where the parameter material-dependent parameters appeared in Eq.(5.3) are

$$\Gamma_k = \gamma_k - 1, \quad p_{\infty,k} = \gamma_k \mathcal{B}_k, \quad e_{\infty,k} = 0$$

with the parameter values taken in turn to be $\gamma_1 = 1.4, \mathcal{B}_1 = 0$ Pa and $\gamma_2 = 5.5, \mathcal{B}_2 = 1.505$ for the gas and liquid phases respectively. The computational domain is $\Omega = [-1, 1]$, which divided into uniform grid composed of $200$ cells. The simulation is run up to time $t_{\text{final}} = 0.2$ with CFL $= 0.5$. In figure 5.5 the numerical solutions of WENO-Z and present scheme for volume fraction, density, pressure and velocity are given. Once again, the numerical solution of both schemes have good agreement with the reference or exact one and identifies correctly the location and speed of all waves in the problem as well as no visible oscillations at the material interface. However, there are overshoots in vicinity of the shock wave for both schemes due to using the primitive variables reconstruction.

### 5.3.6 Air-water shock problem

The problem is a general two-phase liquid-gas Riemann problem [89, 97]. A unit length of tube which contains two chamber separated by an interface at $x = 0.7$ m. Its left chamber is filled in by a liquid at high pressure and its right chamber is filled in by a gas at low pressure. The initial condition is given as

$$(\alpha_1\rho_1, \alpha_2\rho_2, u, p, \alpha_1) = \begin{cases} = (1000\text{kg/m}^3, 0, 0, 10^9\text{Pa}, \epsilon), & 0 \leq x < 0.7, \\ (0, 50\text{kg/m}^3, 0, 10^5\text{Pa}, 1-\epsilon), & 0.7 \leq x \leq 1, \end{cases} \tag{5.26}$$

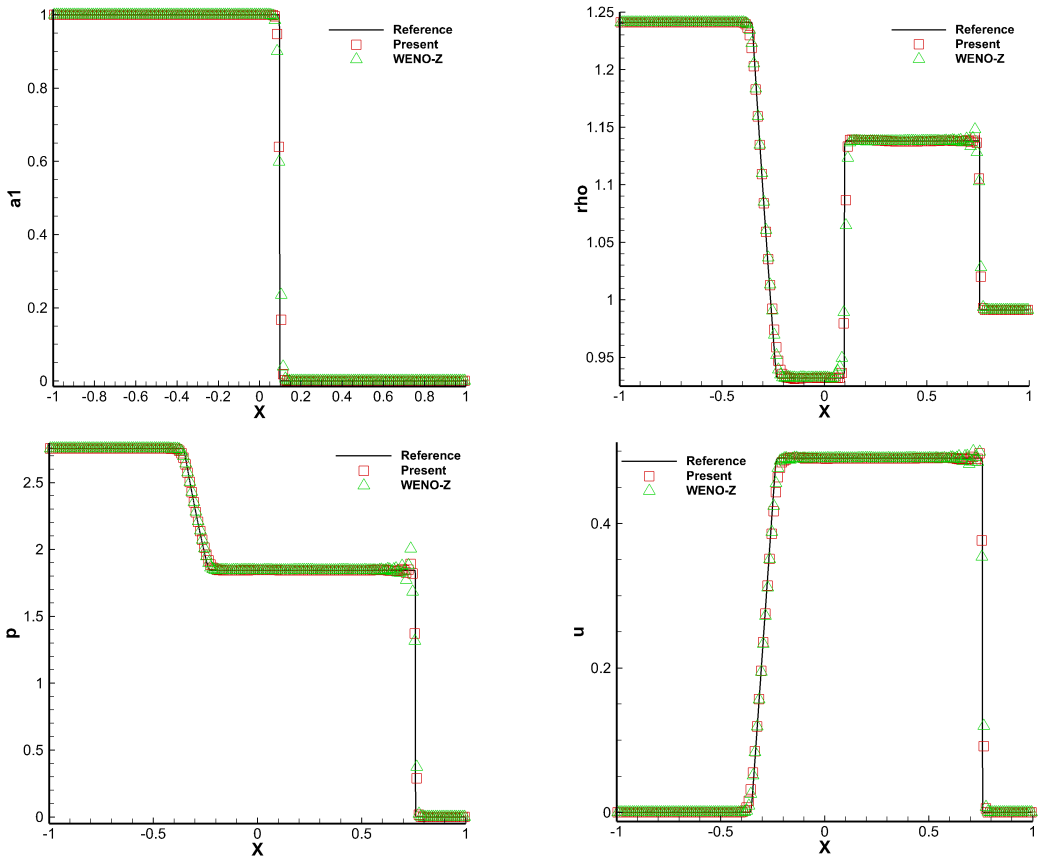


Figure 5.5: Numerical results computed by WENO-Z scheme and present scheme for the volume fraction, partial density (density of fluid 1), pressure and velocity of gas/gas shock tube problem at $t_{\text{final}} = 0.2$.

where $\gamma_l = 4.4$ and $\mathcal{B}_l = 6 \times 10^8$ Pa are the material-dependent quantities of liquid and $\gamma_g = 1.4$ and $\mathcal{B}_g = 0$ are the material-dependent quantities of gas. The computational domain is $\Omega = [0, 1]$ with a uniform mesh made of $N = 200$ cells. The solution is calculated up to time $t_{\text{final}} = 237.44\mu$s and the CFL number is set to 0.5. In figure 5.6 we plot the volume fraction, partial density (liquid), pressure and velocity computed by WENO-Z and multi-stage BVD-MOOD scheme. We observe that the solutions of both schemes have good agreement with reference or exact solution by capture sharply the interface. However, there is visible overshoot generated by WENO-Z scheme.

### 5.3.7 Two dimensional shock-bubble interactions

Here, we consider the shock-bubble interactions tests of Air-R22 and Air-Helium cases (gas cylinders), respectively. These tests were first experimentally studied in [46] and

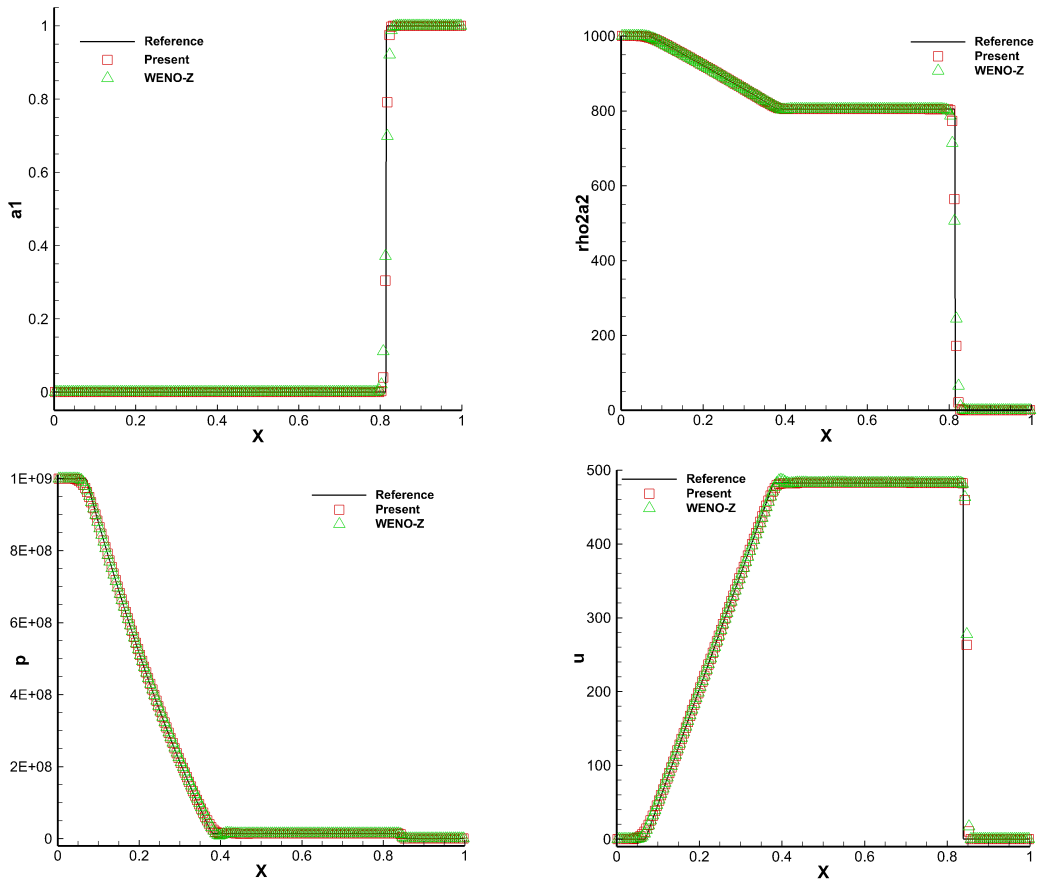


Figure 5.6: Numerical results computed by WENO-Z scheme and present scheme for the volume fraction, partial density (density of fluid 1), pressure and velocity of gas/gas shock tube problem at $t_{\text{final}} = 0.2$.

later numerically studied in [28, 29, 59, 83, 99, 100]. The R22 (refrigerant-22) gas has greater density than the air while the Helium gas has lower density than the air. Initially, a planar rightward-moving shock wave with Mach 1.22 in air located at $x = 64$ mm impacts a stationary R22 gas bubble or Helium gas bubble with radius $r_0 = 25$ mm with center $(x_c = 89, y_c = 44.5)$ mm as shown in figure 5.7. Reflected boundary conditions are applied at the upper and lower walls, and constant extrapolation are imposed at the left and right boundaries. A uniform grid of $1200 \times 400$ is used for both air-R22 and air-He cases with the CFL number is 0.2.

**Air-R22 test problem:** In this test, both air and R22 gas are modeled as perfect gas with $\gamma_{air} = 1.4$ and $\gamma_{R22} = 1.249$. Inside the R22 gas bubble, the state variables are as in [113]

$$(\rho_1, \rho_2, u, v, p, \alpha_1) = (4.415\text{kg/m}^3, 1.4\text{kg/m}^3, 0, 0, 1.0 \times 10^5\text{Pa}, 1 - \varepsilon)\,,$$

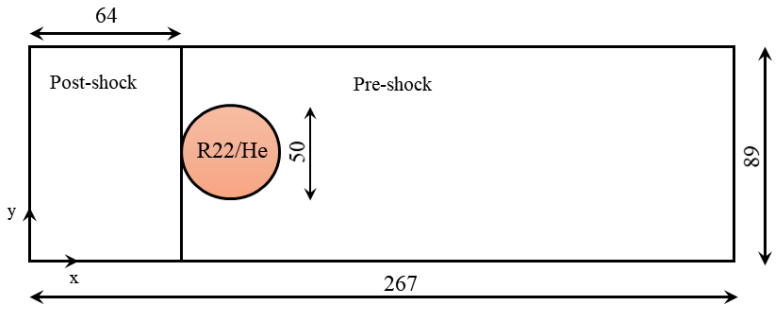


Figure 5.7: Schematic diagram of the computational domain (mm) for the shock-bubble interactions (air-R22 and air-He) cases.

while outside the bubble they are

$$(\rho_1, \rho_2, u, v, p, \alpha_1) = (4.415\text{kg/m}^3, 1.4\text{kg/m}^3, 0, 0, 1.0 \times 10^5\text{Pa}, \varepsilon)\,,$$

and

$$(\rho_1, \rho_2, u, v, p, \alpha_1) = (4.415\text{kg/m}^3, 1.927\text{kg/m}^3, 114.42, 0, 1.57 \times 10^5\text{Pa}, \varepsilon)$$

in the pres-hock and post-shock region respectively, where $\varepsilon = 10^{-8}$. The numerical results for density at four different time instants are presented in figure 5.8 computed by the multi-stage BVD-MOOD scheme. The present scheme can maintain the compact thickness of the material interfaces and provides large-scale structures which comparable to other existing high-order shock-capturing schemes [29, 113] as well as small-scale structures even in low grid of computation. Moreover, it is observed that the numerical results are in good agreement with experimental study as in [46], their figure 11, for instance the clear shock structures and the deformation of R22 gas. Another important feature in the flow field is the Kelvin-Helmholtz instability develops along the interface, which then rolls up small-scale structures in agreements with the results from [100, 113].

**Air-Helium test problem:** Similarly to previous test, both air and Helium gas are modeled as perfect gas with $\gamma_{air} = 1.4$ and $\gamma_{He} = 1.648$. Inside the Helium gas bubble, the state variables are as in [113]

$$(\rho_1, \rho_2, u, v, p, \alpha_1) = (0.255\text{kg/m}^3, 1.4\text{kg/m}^3, 0, 0, 1.0 \times 10^5\text{Pa}, 1 - \varepsilon)\,,$$

while outside the bubble they are

$$(\rho_1, \rho_2, u, v, p, \alpha_1) = (0.255\text{kg/m}^3, 1.4\text{kg/m}^3, 0, 0, 1.0 \times 10^5\text{Pa}, \varepsilon)\,,$$

and

$$(\rho_1, \rho_2, u, v, p, \alpha_1) = (0.255\text{kg/m}^3, 1.927\text{kg/m}^3, 114.42, 0, 1.57 \times 10^5\text{Pa}, \varepsilon)$$

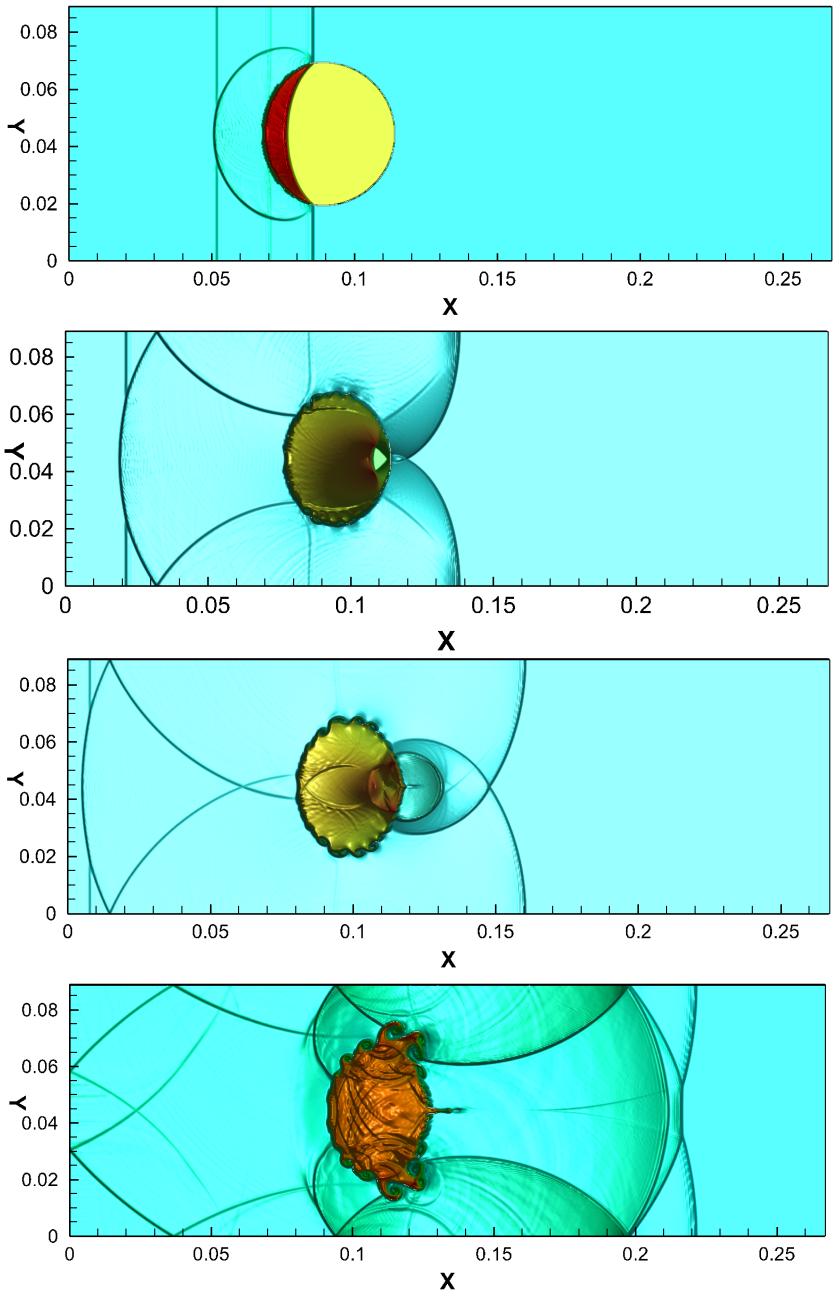


Figure 5.8: Numerical results for density computed by present scheme of air-R22 problem at four different time instants – From top to bottom: $55\mu s$, $190\mu s$, $250\mu s$, and $420\mu s$.

in the pres-hock and post-shock region respectively, where $\varepsilon = 10^{-8}$. The numerical results for density at four different time instants are presented in figure 5.9 computed by the multi-stage BVD-MOOD scheme. Similarly, the numerical results are qualitatively in good agreement with the experiment in [46], their figure 7. In this case, the incident shock is transmitted and reflected when it impacts the Helium cylinder and clearly captured by the present scheme. The upstream wall is compressed and the transverse jet

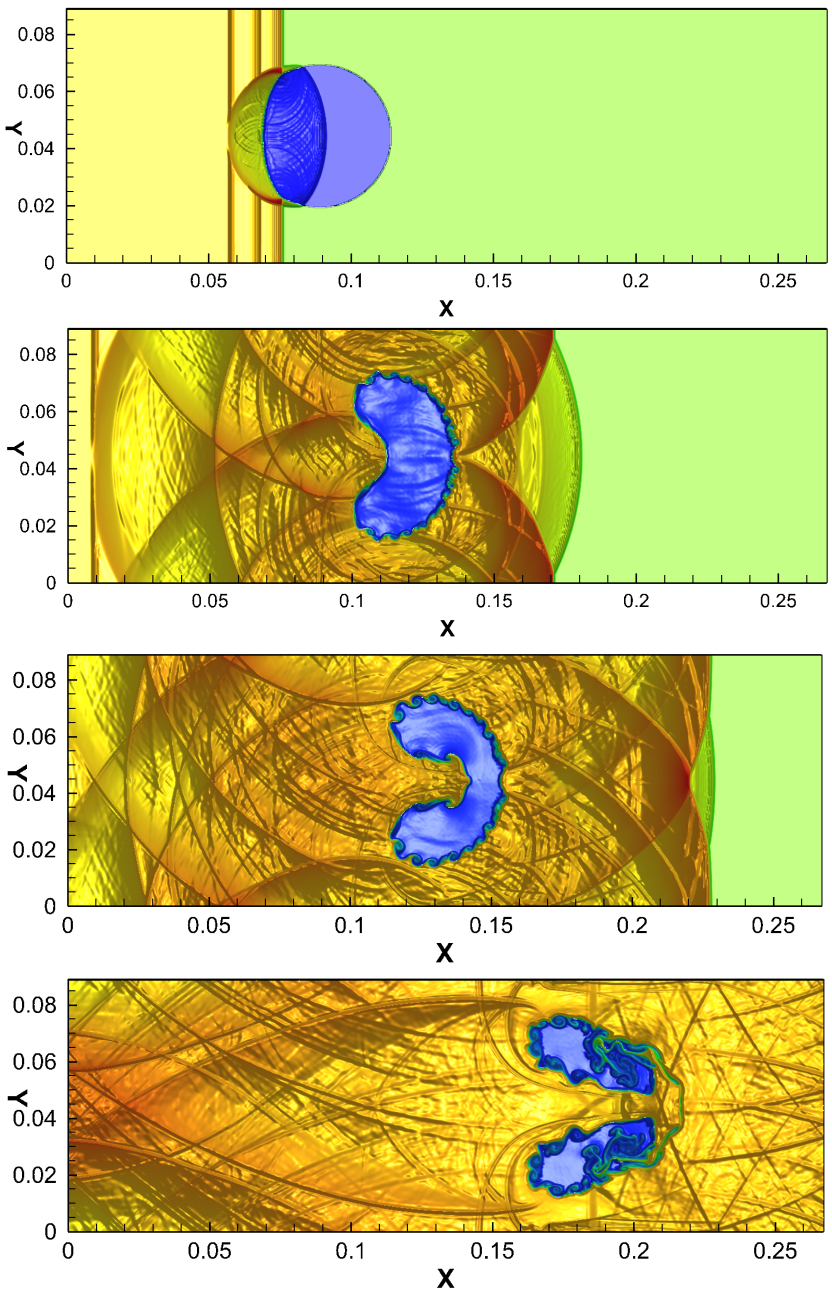


Figure 5.9: Numerical results for density computed by present scheme of air-Helium problem at four different time instants – From top to bottom: $30\mu s$, $245\mu s$, $380\mu s$, and $834\mu s$.

forms. Again, the air-He interface rolls up due to Kelvin-Helmholtz instability, similar to air-R22 case. Furthermore, the rolling-up structures are consistent with other existing high-order shock-capturing schemes [28, 59, 100, 113].

**Note:** We only solve the compressible Euler equations to produce the numerical results do not consider including the physical viscosity and surface tension. It is difficult to differentiate between the physically-real structures and those provided by numerical

methods. For instance, as in [64], the solution of compressible Euler equations does not converges, and the vortices will be continuously imposed when refine the grid resolution according to the absence of physical viscosity. The significance of low numerical dissipation schemes [29] lies in real-case or engineering applications where the physical dissipation (due to molecular or turbulent mixing) plays an important role. Under the effects of the physical dissipation, the real flow structures can be more precisely regenerated by the low numerical dissipation.

### 5.3.8 Two dimensional collapse of an air cavity in water

In this subsection, the collapse of an air cavity in water is considered. According to its importance in a wide range of physical and practical phenomena, for instance luminescence, lithotripsy, and hot-spot formation in explosives, this test has been extensively investigated [18, 47, 52, 53, 81, 113]. The computational domain $\Omega = [0, 10] \times [-2.5, 2.5]$ with an air bubble of unit radius placing in water and its center at $(4.375, 0)$, and the shock wave with Mach 1.72 is initially located at $x = 1$ at time $t = 0$ as in figure 5.10. The initial condition is given as [95]

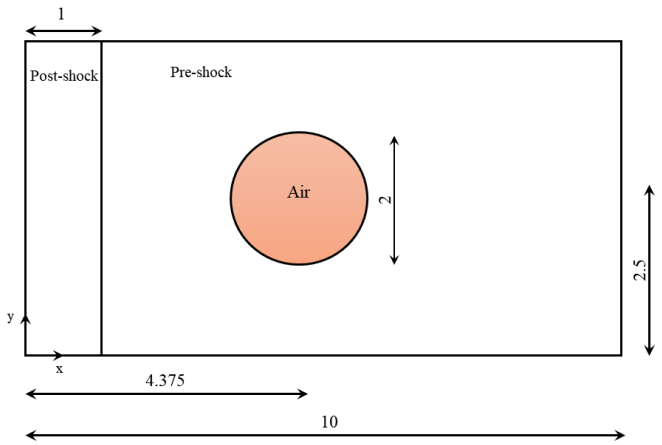


Figure 5.10: Schematic diagram of the computational domain for the collapse of an air cavity in water.

$$(\alpha_1\rho_1, \alpha_2\rho_2, u_0, v_0, p_0, \alpha_1) = \begin{cases} (10^{-3}, 0, 0, 0, 1, 1-\epsilon) & \text{for bubble,} \\ (0, 1.325, 68.52, 0, 19150, \epsilon) & \text{for post-shock,} \\ (0, 1, 0, 0, 1, \epsilon) & \text{for pre-shock.} \end{cases} \tag{5.27}$$

To model the thermodynamic behavior of gas and liquid, we use the stiffened gas equation of state where the parameter material-dependent parameters appeared in Eq.(5.3) are

$$\Gamma_k = \gamma_k - 1, \quad p_{\infty,k} = \gamma_k \mathcal{B}_k, \quad e_{\infty,k} = 0$$

with the parameter values taken in turn for the air with $\gamma_1 = 1.4$ and $P_1^{\infty} = 0$, and the water is modeled with $\gamma_2 = 4.4$ and $P_2^{\infty} = 6000$.

The computation is made by a uniform grid of $1000 \times 500$ with the CFL number is 0.3. The numerical results for density at various time instants are shown in figure 5.11 computed by the present scheme. We observe that the numerical results are in consistency and good agreement with numerical results in literature [47, 50, 52, 53, 81, 95, 113]. At early stage, the incident shock hits the bubble, creating a strong reflected rarefaction wave in the water, and the bubble gets compressed and deforms. As shown in figure 5.11 with the time evolution, the bubble is splitting (cavity fragment) due to the formation of a high speed jet while interface remains thin throughout the simulation. Finally, the flow structures become more complex due to the shock interaction. The computed solution shows no spurious oscillations.

### 5.3.9 Underwater explosion

In the present subsection, we consider the underwater explosion problem which has been extensively employed in [18, 29, 62, 81, 95]. This test case involves the interactions of an air cavity produced by a highly compressed cylindrical air bubble placed in water beneath a free surface (water-air interface). An significant challenge of this test is the topological change in the interface as the bubble bursts through the free surface. The computational domain is $\Omega = [-2, 2] \times [-1.5, 2.5]$ m$^2$. At $t = 0$, the horizontal water surface that separates air and water is located at $y = 0$ and below this surface line, a bulk of high compressed air lies surrounded by water. The cylindrical air cavity of $0.12$ m in radius is initially centered at $(x_c = 0, y_c = -0.3)$. The initial condition is given as

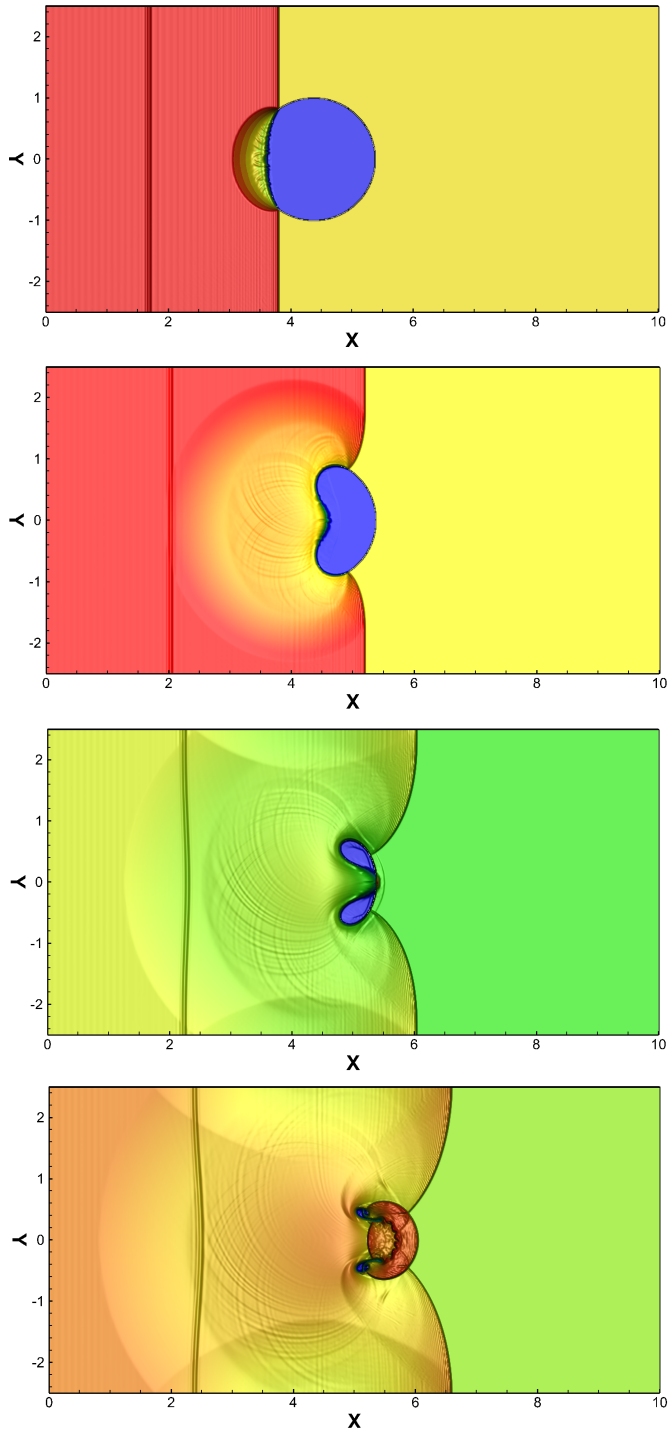


Figure 5.11: Numerical results for density computed by present scheme of collapse of an air cavity in water problem at four different time instants – From top to bottom: $10ms$, $15ms$, $18ms$, and $20ms$.

[95]

$$(\alpha_1\rho_1, \alpha_2\rho_2, u_0, v_0, p_0, \alpha_1) = \begin{cases} (0, 1250, 0, 0, 10^9, \epsilon) & \text{for air bubble,} \\ (1000, 0, 0, 0, 101325, 1-\epsilon) & \text{for below the surface,} \\ (0, 1.25, 0, 0, 101325, \epsilon) & \text{for above the surface.} \end{cases} \tag{5.28}$$

The units of density and pressure are in $\mathrm{kg}/\mathrm{m}^3$ and Pa, respectively. The thermodynamic behavior of water and air is modeled by the stiffened gas with the same equation of state as in Section 5.3.1. Gravity effects are neglected, the transparent boundary condition is imposed for the top, left and right boundaries, while for the bottom boundary the reflection condition is implemented. We conducted the simulation on a coarse uniform mesh with $600 \times 600$ with the CFL number is 0.2.

We demonstrate the color-map plots for density and VOF function at the time instants $t \in [0.2, 0.95, 1.26, 1.90]$ ms in figure 5.12. After the explosion, there are two circular pressure waves depart from the interface: a main shock wave travels outward into the water and a rarefaction wave simultaneously travels inside the air bulk (explosion zone). As soon as, a traveling shock impacts the free surface, causing the formation of wave diffraction phenomenon, a weak shock transmitted air shock and the shape of the gas bubble evolves into an oval shape. From the numerical results, we observe that the present scheme can sharply capture the interface throughout the computation while the conventional shock-capturing schemes (MUSCL and WENO-JS) smear out the water-air interfaces as reported in [29]. Furthermore, the flow structures including transmitted and reflected waves are well resolved by the present scheme. However, there is an instability effect on roll-up-like of the interface where is near the free surface presented by the present scheme. We also illustrate the distribution of VOF function along $x = 0$ cross-section in figure 5.13. The present scheme can keep the compact thickness of the transition layer of the interface even in coarse grid.

## 5.4 Summary

In this chapter, we implement the multi-stage BVD-MOOD scheme to solve compressible multi-phase flows by using the five-equation model. The approach relies on several type of reconstructions: fifth order accurate polynomials, viscous nonlinear THINC, low dissipation nonlinear ones, and peicewise constant scheme. The numerical model is formulated under a standard finite volume method with HLLC Riemann solver in the wave propagation form. The present scheme can capture sharply the discontinuous solutions

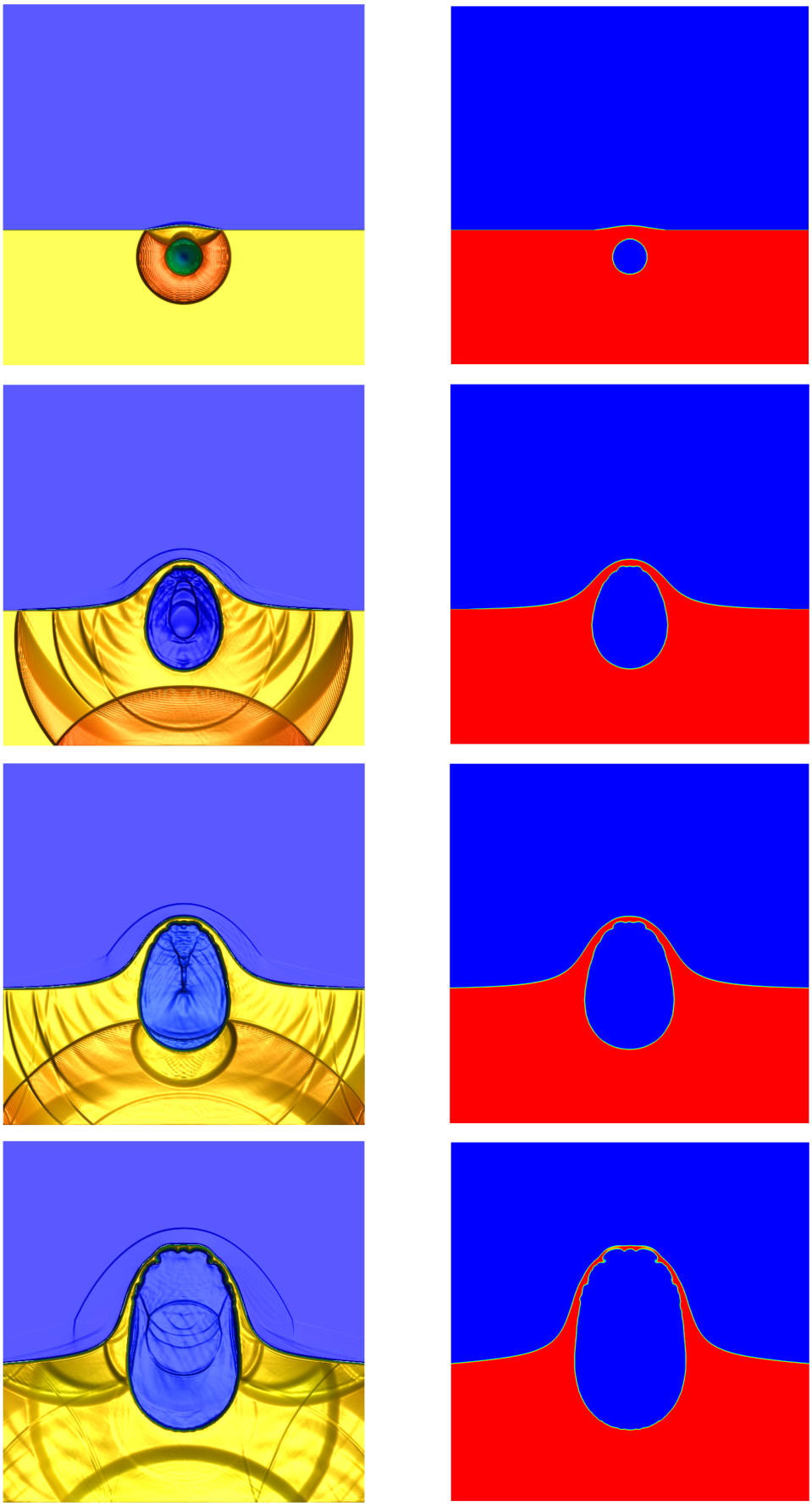

Figure 5.12: Numerical results for density and volume fraction for underwater explosion computed by the present scheme — From top to bottom: $0.2ms$, $0.95ms$, $1.26ms$ and $1.90ms$ — Left: Density; Right: Volume fraction.

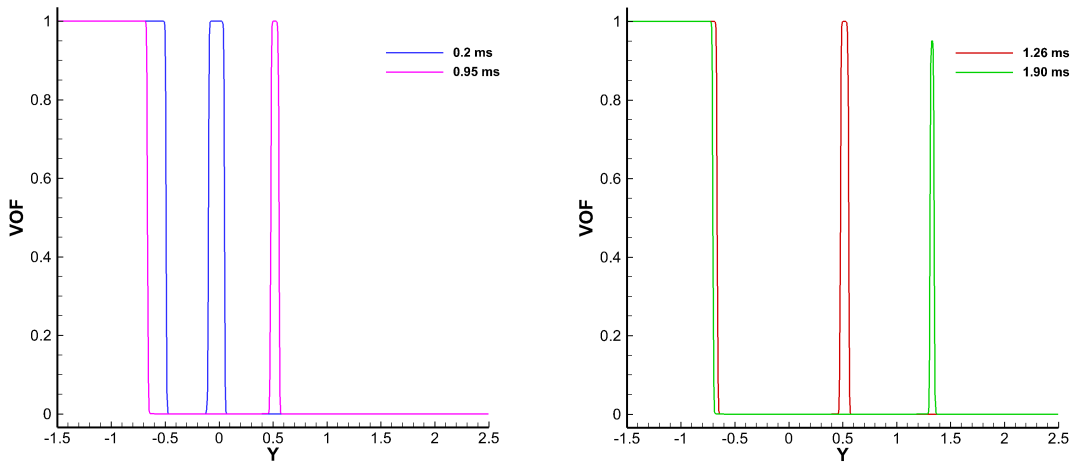


Figure 5.13: Distribution of VOF function along $x = 0$ cross-section for underwater explosion test — Left: $0.2ms$, $0.95ms$; Right: $1.26ms$, $1.90ms$.

as well as material interface without implementing interface-sharpening techniques. The novel scheme can realize thermodynamical-consistent reconstruction straightforwardly. The numerical results of the scheme show an improvement in the high-solution quality, and provide competitive or even better results compared with high-order shock-capturing schemes. This work is to provides an efficient approach with a simple procedure in implementation for simulating compressible interfacial multi-phase flows.

# Chapter 6

# Conclusions and future work

## 6.1 Problems and research purposes

In the numerical simulation of compressible gas dynamics, there are two critical problems such as numerical oscillations and numerical dissipation that highly demand the development of high-fidelity numerical scheme. The numerical oscillations always occur in high-order schemes. However, several standard high-order shock-capturing schemes were developed for suppressing numerical oscillations by feeding extra dissipative errors or projecting to lower order. Therefore, the numerical schemes suffer from numerical diffusion when the strong discontinuities occur, which noticed that still a significant problem in the solution. For instance, the so-called WENO schemes that can achieve very high-order accuracy but in some cases they still generate numerical dissipation in vicinity of strong discontinuities.

In recent years, high-order shock-capturing schemes were developed to handle both smooth and discontinuous solutions with less numerical dissipation such as a boundary variation diminishing (BVD) algorithm. Nevertheless, one main issue of original high-order schemes is that they may generate non-physical properties in the solution (negative density or pressure), which leads to a blow-up of the numerical computation and subsequent code crash. The negative values provided by classical high-order schemes due to interpolation errors when the solution involving very strong shock waves, or when vacuum or near vacuum states occur and very high Mach number.

In reactive Euler equations, there are several difficulties in designing stable/robust and high-resolution numerical schemes to accurately resolve a general hyperbolic system with source terms. For stiff source term, some high-order shock-capturing schemes may predict wrong wave propagation speed of detonation fronts or may generate spurious numerical propagation phenomenon of the shock waves in the flow structures. For example, the numerical dissipation smears out some discontinuities which, in return incorrectly trigger the reaction of the source term and then produce a wrong numerical solution. An other main issue in the reaction flow simulation is positivity-preserving when gaseous detonation propagating through different geometries or low density cases. For instance, the occurrence of negative density or pressure (non-physical properties) is quite often encounter during the time evolution, which leads to a blow-up the computation.

In compressible multi-phase flow, the development of numerical method is more challenging than in compressible single phase flow. The flow structures become complex when involve material interfaces between two gaseous or two materials of different physical natures. In literature, TVD and MUSCL schemes can solve discontinuities without spurious oscillations, however, they still suffer from excessive numerical dissipation. The excessive numerical dissipation smears out the flow fields as well as the discontinuities in mass or volume fraction which represents the material interfaces. Otherwise, WENO scheme can generously reduce numerical dissipation, capture well for the moving interfaces and provide high accuracy in smooth regions. However, it may generate numerical oscillations for compressible multi-phase flows with complex EOS as discussed in [28].

To deal with numerical oscillations and numerical dissipation, we design a new numerical under multi-dimensional optimal order detection (MOOD) framework which is an *a posteriori* limiting scheme. The concept of this method is replacing the first-order scheme to then tangent of hyperbola interface capturing (THINC) function to capture sharply the discontinuities without spurious oscillations and obtain possible highest order of accuracy.

Furthermore, in order to achieve high fidelity, the numerical methods should preserve

the solution properties such as: Accuracy on both smooth and discontinuous profile, non-oscillatory behavior and fail-safe behavior (positivity-preserving) we develop a general formulation of reconstruction in finite volume method by integrating the boundary variation diminishing (BVD) and multi-dimensional optimal order detection (MOOD) methodologies by blending of high-/low-order polynomials and hyperbolic tangent reconstructions. As a concrete example, we propose a high-resolution scheme under a three-stage cascade. For BVD reconstruction strategy, the linear fifth-order upwind or piecewise quartic method (PQM) on fourth-degree of polynomial (P4) [116] is implemented as one of the candidate reconstruction functions to capture smooth solutions. Other candidate reconstruction functions use tangent of hyperbola interface capturing (THINC) functions with different controlling the slope (jump thickness) to eliminate the numerical oscillation and to capture sharply all discontinuities. Furthermore, a MOOD algorithm performs and detects a candidate solution by PAD ensuring as such the positivity-preserving property.

We further extend our new approach (multi-stage BVD-MOOD) for the compressible Euler equations supplemented with source terms (e.g. gravity, chemical reaction). In addition, we also apply the present scheme to solve the five-equation model for interface two-phase flow under finite volume wave propagation method. The present method is able to capture both smooth and discontinuous solution in Euler equations, reactive Euler equations for compressible gas dynamics as well as five-equation model with excellent solution quality competitive and superior solution to other existing schemes.

## 6.2 Major contributions of the current study

The impacts and significances of the current study are summarized as follows

1. We introduce a novel finite volume scheme to solve hyperbolic systems under the multi-dimensional optimal order detection (MOOD) framework. We replace the first-order finite volume method to the tangent of hyperbola interface capturing (THINC) function. We obtain the numerical results for both scalar conservation laws and Euler equations which are comparable to original MOOD schemes as well as other existing

methods.

2. We present a reconstruction strategy to be employed in finite volume method which differs from classical polynomial based with a *priori* limiting strategy. Our approach differs because our cell-based reconstruction procedure relies on several types of reconstructions:

(1) Fifth order accurate polynomials for smooth solutions,

(2) Viscous nonlinear THINC functions to add dissipation,

(3) Sharp nonlinear ones to handle discontinuity and steep gradients,

(4) No reconstruction at all for extreme situations.

The fundamental mechanism in our approach is to choose between these reconstructions relies on the BVD strategy. For instance, the present scheme must choose among several reconstructions, the most appropriate one according to goodness criteria. Some criteria are set *a priori* with BVD, some are verified *a posteriori* with MOOD algorithm to preserve the positivity of physical properties.
The proposed scheme is performed via the numerical experiments of benchmark test problems which involve vacuum or near vacuum states, strong discontinuities and also smooth flows. It is demonstrated that the present scheme is able to maintain a high accuracy in smooth profile, eliminate the spurious oscillations in vicinity of discontinuity, capture sharply discontinuous solution, and preserve some physical properties like the positivity of density and pressure for the Euler equations of compressible gas dynamics.

3. The present scheme is applicable to non-homogeneous compressible Euler equations (e.g. gravity and chemical reaction as source terms). Some existing shock-capturing methods may predict incorrectly the position of the donation fronts or may generate excessive numerical dissipation. The numerical dissipation smears out the discontinuities, then incorrectly trigger the reaction of the stiff source term produces a wrong numerical solution. An other main issue is the occurrence of negative density or pressure is quite often encounter during the time evolution. The present scheme can resolve these problems in integrating the BVD and MOOD methodologies. We obtain superior quality results competitive to other existing shock-capturing schemes by sharply capturing

the detonation fronts and material interfaces without any treatment. Moreover, due to the small but sufficient numerical dissipation, the small-scale structures are well represented, simultaneously with the prevention of the occurrence of spurious oscillations.

4. The implementation of the multi-stage BVD-MOOD scheme for solving the five-equation model in compressible multi-phase flows. With BVD principle, the novel scheme can capture sharply the material interfaces by reducing numerical dissipation without implementation interface-sharpening approach. The current study can realize thermodynamical-consistent reconstruction straightforwardly. The designed schemes are simple, however they produce much better performance and can be interested using in complex compressible flows.

5. According to the low-dissipation property of the scheme, the present scheme is suitable for turbulent flows. More precisely, existing schemes have excessive numerical dissipation, so they cannot be used for DNS of high Reynold number flows. By reducing the numerical dissipation, BVD-MOOD scheme can be applied for DNS of flows with wider-range Reynold number. Moreover, in the implementation of LES the excessive numerical dissipation in current methods will contaminant (pollute) the physical turbulent viscosity of the LES sub-grid scale model. By reducing the numerical dissipation, BVD-MOOD scheme allows LES model to work more properly.

## 6.3 Future work

There are several areas that the present study has not yet covered. Further research could be usefully conducted to improve the effectiveness in numerical schemes and to understand some physical phenomena. The directions of future which will be considered as follows:

1. We wish to extend the present approach to three-dimensions straightforward. A three-dimensional numerical model is more realistic in calculation of complex compressible flows and transports phenomena in natural geometries. Moreover, three-dimensional numerical models are often employed in numerous different applications in aerospace engineering as well as other engineering fields.

2. We also wish to implement the BVD-MOOD methodologies in solving the compressible Navier-Stoke equations for the simulations of multi-component flows as well as phase-change phenomenon. In the computation of compressible Navier-Stoke equations, the viscosity is included which will effect on accuracy of the numerical solution. The current numerical model is robust and low dissipation schemes. Thus, the high-resolution positivity-preserving schemes are expected to solve these advanced numerical models.

3. Since the multistage BVD-MOOD algorithm uses several reconstruction operators and MOOD is an *a posteriori* limiting projection, therefore the MPI parallel computation should be considered. However, when we have such problem where trouble cell exists, the parallel computation will be affected by waiting the recomputing process for trouble cell which expected to occur in the rare events. On the other hand, the BVD algorithm is suitable for MPI parallel computation to simultaneously compute the reconstruction operators as well as GPU process for saving computational cost.

4. Turbulent flow is stilled considered one of unresolved challenging problems of physical phenomena. The investigation of shock turbulence interaction should be made by introducing higher-order shock-capturing schemes. The interaction between shocks and turbulence produces the flow structures even more complex such as shocks, discontinuities and turbulent features. Other existing schemes can achieve high accuracy in smooth solution, however, they commonly still suffer from stability or numerical dissipation in discontinuities. Thus, our high-resolution positivity-preserving schemes are suitable in applications of turbulent model.

5. High-resolution positivity-preserving schemes should be further explored on unstructured grids to handle more complex geometrical configurations. An development of the proposed scheme on unstructured grids is preferable for practical simulations. Two issues of high-order numerical schemes for compressible multi-phase flow on unstructured grids are numerical oscillations and positivity-preserving. Therefore, we plan to extend our limiter-free and robust schemes to unstructured grids, which are expected to be adequate to prevent numerical oscillations and fail-safe behavior.

# Bibliography


[1] R. Abgrall. How to prevent pressure oscillations in multicomponent flow calculations: A quasi conservative approach. *J. Comput. Phys.*, 125(1):150 – 160, 1996.

[2] R. Abgrall and S. Karni. Computations of compressible multifluids. *J. Comput. Phys.*, 169(2):594 – 623, 2001.

[3] F. Acker, R. Borges, and B. Costa. An improved WENO-Z scheme. *J. Comput. Phys.*, 313:726–753, 2016.

[4] G. Allaire, S. Clerc, and S. Kokh. A five-equation model for the simulation of interfaces between compressible fluids. *J. Comput. Phys.*, 181(2):577 – 616, 2002.

[5] D.S. Balsara. Multidimensional HLLE Riemann solver: Application to Euler and magnetohydrodynamic flows. *J. Comput. Phys.*, 229:1970–1993, 2010.

[6] D.S. Balsara. A two-dimensional HLLC Riemann solver for conservation laws: Application to euler and magnetohydrodynamic flows. *J. Comput. Phys.*, 231:7476–7503, 2012.

[7] D.S. Balsara, M. Dumbser, and R. Abgrall. Multidimensional HLLC Riemann Solver for Unstructured Meshes - With Application to Euler and MHD Flows. *J. Comput. Phys.*, 261:172–208, 2014.

[8] W. Bao and S. Jin. The random projection method for hyperbolic conservation laws with stiff reaction terms. *J. Comput. Phys.*, 163(1):216 – 248, 2000.

[9] W. Bao and S. Jin. The random projection method for stiff detonation capturing. *SIAM Journal on Scientific Computing*, 23(3):1000–1026, 2001.

[10] A.C. Berkenbosch, E.F. Kaasschieter, and R. Klein. Detonation capturing for stiff combustion chemistry. *Combust. Theor. Model.*, 2(3):313–348, 1998.

[11] B.L. Bihari and D. Schwendeman. Multiresolution schemes for the reactive euler equations. *J. Comput. Phys.*, 154(1):197 – 230, 1999.

[12] F. Blachère and R. Turpault. An admissibility and asymptotic preserving scheme for systems of conservation laws with source term on 2D unstructured meshes with high-order mood reconstruction. *Computer Methods in Applied Mechanics and Engineering*, 317:836 – 867, 2017.

[13] J.P. Boris and D.L. Book. Flux-corrected transport. I. SHASTA, a fluid transport algorithm that works. *J. Comput. Phys.*, 11(1):38 – 69, 1973.

[14] W. Boscheri, M. Dumbser, R. Loubère, and P.H. Maire. A second-order cell-centered lagrangian ader-mood finite volume scheme on multidimensional unstructured meshes for hydrodynamics. *J. Comput. Phys.*, 358:103 – 129, 2018.

[15] W. Boscheri, R. Loubère, and M. Dumbser. Direct arbitrary-Lagrangian-Eulerian ADER-MOOD finite volume schemes for multidimensional hyperbolic conservation laws. *J. Comput. Phys.*, 292:56 – 87, 2015.

[16] A. Bourlioux, A.J. Majda, and V. Roytburd. Theoretical and numerical structure for unstable one-dimensional detonations. *SIAM J. Appl. Math.*, 51(2):303–343, 1991.

[17] G. Capdeville. Local maximum principles in high-order non-oscillatory schemes for non-linear hyperbolic equations. *Computers & Fluids*, 131:102 – 122, 2016.

[18] C.H. Chang and M.S. Liou. A robust and accurate approach to computing compressible multiphase flow: Stratified flow model and ausm+-up scheme. *J. Comput. Phys.*, 225(1):840 – 873, 2007.

[19] H. Chen and S. Liang. Flow visualization of shock/wave column interactions. *Shock Waves*, 17(2):309 – 321, 2008.

[20] A.J. Chorin. Random choice solution of hyperbolic systems. *J. Comput. Phys.*, 22(4):517 – 533, 1976.

[21] A.J. Chorin. Random choice methods with applications to reacting gas flow. *J. Comput. Phys.*, 25(3):253 – 272, 1977.

[22] S. Clain, S. Diot, and R. Loubère. A high-order finite volume method for systems of conservation laws - Multi-dimensional Optimal Order Detection (MOOD). *J. Comput. Phys.*, 230:4028–4050, 2011.

[23] S. Clain and J. Figueiredo. The mood method for the non-conservative shallow-water system. *Computers & Fluids*, 145:99 – 128, 2017.

[24] J.P. Cocchi, R. Saurel, and J.C. Loraud. Treatment of interface problems with godunov-type schemes. *Shock Waves*, 5:347 – 357, 1996.

[25] B. Cockburn and C.W. Shu. The runge–kutta discontinuous galerkin method for conservation laws v: Multidimensional systems. *J. Comput. Phys.*, 141(2):199 – 224, 1998.

[26] P. Colella, A. Majda, and V. Roytburd. Theoretical and numerical structure for reacting shock waves. *SIAM Journal on Scientific and Statistical Computing*, 7(4):1059–1080, 1986.

[27] P. Colella and P. Woodward. The piecewise parabolic method (ppm) for gas-dynamical simulations. *J. Comput. Phys.*, 54(1):174 – 201, 1984.

[28] V. Coralic and T. Colonius. Finite-volume weno scheme for viscous compressible multicomponent flows. *J. Comput. Phys.*, 274:95 – 121, 2014.

[29] X. Deng, S. Inaba, B. Xie, K.M. Shyue, and F. Xiao. High fidelity discontinuity-resolving reconstruction for compressible multiphase flows with moving interfaces. *J. Comput. Phys.*, 371:945 – 966, 2018.

[30] X. Deng, Y. Shimizu, and F. Xiao. Constructing high-order discontinuity-capturing schemes with linear-weight polynomials and boundary variation diminishing algorithm. *arXiv preprint*, arXiv:1811.08316, 2018.

[31] X. Deng, Y. Shimizu, and F. Xiao. A fifth-order shock capturing scheme with two-stage boundary variation diminishing algorithm. *J. Comput. Phys.*, 386:323–349, 2019.

[32] X. Deng, B. Xie, R. Loubère, Y. Shimizu, and F. Xiao. Limiter-free discontinuity-capturing scheme for compressible gas dynamics with reactive fronts. *Computers & Fluids*, 171:1–14, 2018.

[33] X. Deng, B. Xie, F. Xiao, and H. Teng. New accurate and efficient method for stiff detonation capturing. *AIAA Journal*, 56(10):4024–4038, 2018.

[34] S. Diot, S. Clain, and R. Loubère. Improved detection criteria for the Multi-dimensional Optimal Order Detection (MOOD) on unstructured meshes with very high-order polynomials. *Comput Fluids*, 64:43–63, 2012.

[35] M. Dumbser and R. Loubère. A simple robust and accurate a posteriori sub-cell finite volume limiter for the discontinuous galerkin method on unstructured meshes. *J. Comput. Phys.*, 319:163 – 199, 2016.

[36] M. Dumbser, O. Zanotti, R. Loubère, and S. Diot. A posteriori subcell limiting of the discontinuous Galerkin finite element method for hyperbolic conservation laws. *J. Comput. Phys.*, 278:47–75, 2014.

[37] B. Engquist and B. Sjögreen. *Robust difference approximations of stiff inviscid detonation waves*. Department of Mathematics, University of California, Los Angeles, 1991.

[38] P. Fan, Y. Shen, B. Tian, and C. Yang. A new smoothness indicator for improving the weighted essentially non-oscillatory scheme. *J. Comput. Phys.*, 269:329 – 354, 2014.

[39] L. Fu, X.Y. Hu, and N.A. Adams. A family of high-order targeted eno schemes for compressible-fluid simulations. *J. Comput. Phys.*, 305:333 – 359, 2016.

[40] C.L. Gardner, J. Glimm, O. McBryan, R. Menikoff, D.H. Sharp, and Q. Zhang. The dynamics of bubble growth for Rayleigh-Taylor unstable interfaces. *Phys. Fluids*, 31(3):447–465, 1988.

[41] I. Glassman. *Combustion*. Academic Press, 2nd edition edition, 1987.

[42] S.K. Godunov. A difference method for numerical calculation of discontinuous solutions of the equations of hydrodynamics. *Matematicheskii Sbornik*, 89:271–306, 1959.

[43] S. Gottlieb. On high order strong stability preserving runge-kutta and multi step time discretizations. *J. Sci. Comput.*, 25:105–128, 2005.

[44] Y. Ha and C. Gardner. Positive scheme numerical simulation of high mach number astrophysical jets. *J. Sci. Comput.*, 34:247–259, 03 2008.

[45] Y. Ha, C. Gardner, A. Gelb, and C.W. Shu. Numerical simulation of high mach number astrophysical jets with radiative cooling. *J. Sci. Comput.*, 24(1):29–44, Jul 2005.

[46] J.-F. Haas and B. Sturtevant. Interaction of weak shock waves with cylindrical and spherical gas inhomogeneities. *J. Fluid Mech.*, 181:41–76, 1987.

[47] R. K.S. Hankin. The euler equations for multiphase compressible flow in conservation form: Simulation of shock–bubble interactions. *Journal of Computational Physics*, 172(2):808 – 826, 2001.

[48] A. Harten. High resolution schemes for hyperbolic conservation laws. *J. Comput. Phys.*, 49(3):357 – 393, 1983.

[49] A. Harten, P. Lax, and B. van Leer. On upstream differencing and godunov-type schemes for hyperbolic conservation laws. *SIAM Rev*, 25:35–61, 01 1983.

[50] N.A. Hawker and Y. Ventikos. Interaction of a strong shockwave with a gas bubble in a liquid medium: a numerical study. *J. Fluid Mech.*, 701:59–97, 2012.

[51] C. Helzel, R.J. Leveque, and G. Warnecke. A modified fractional step method for the accurate approximation of detonation waves. *SIAM J. Sci. Comput.*, 22(4):1489–1510, 2000.

[52] X.Y. Hu and B.C. Khoo. An interface interaction method for compressible multifluids. *Journal of Computational Physics*, 198(1):35 – 64, 2004.

[53] X.Y. Hu, B.C. Khoo, N.A. Adams, and F.L. Huang. A conservative interface method for compressible flows. *Journal of Computational Physics*, 219(2):553 – 578, 2006.

[54] H.T. Huynh. Schemes and constraints for advection time stepping method with flux reconstruction view project. *Art. Lec. Notes Phys.*, 1997.

[55] R. Jeltsch and P. Klingenstein. Error estimators for the position of discontinuities in hyperbolic conservation laws with source terms which are solved using operator splitting. *Computing and Visualization in Science*, 1(1):231 – 249, 1999.

[56] G.S. Jiang and C.W. Shu. Efficient implementation of weighted ENO schemes. *J. Comput. Phys.*, 126:202–228, 1996.

[57] Z.H. Jiang, X. Deng, F. Xiao, C. Yan, and J. Yu. A high order interpolation scheme of finite volume method for compressible flow on curvilinear grids. *Commun. Comput. Phys. (in press)*, 2020.

[58] Z.H. Jiang, C. Yan, and J. Yu. Efficient methods with higher order interpolation and mood strategy for compressible turbulence simulations. *J. Comput. Phys.*, 371:528 – 550, 2018.

[59] E. Johnsen and T. Colonius. Implementation of weno schemes in compressible multicomponent flow problems. *J. Comput. Phys.*, 219(2):715 – 732, 2006.

[60] C.Y. Jung and T.B. Nguyen. Fine structures for the solutions of the two-dimensional Riemann problems by high-order WENO schemes. *Adv. Comput. Math.*, 44(1):147–174, Feb 2018.

[61] D.I. Ketcheson, M. Parsani, and R.J. LeVeque. High-order wave propagation algorithms for hyperbolic systems. *SIAM Journal on Scientific Computing*, 35(1):A351–A377, 2013.

[62] S. Kokh and F. Lagoutière. An anti-diffusive numerical scheme for the simulation of interfaces between compressible fluids by means of a five-equation model. *J. Comput. Phys.*, 229(8):2773 – 2809, 2010.

[63] A. Kurganov and E. Tadmor. Solution of two-dimensional Riemann problems for gas dynamics without Riemann problem solvers. *Numer. Methods Partial Differential Equations*, 18:584–608, 2002.

[64] P.D. Lax and X.D. Liu. Solution of two-dimensional Riemann problems of gas dynamics by positive schemes. *SIAM J. Sci. Comput.*, 19(2):319–340, 1998.

[65] B. Van Leer. Towards the ultimate conservative difference scheme. iv. a new approach to numerical convection. *J. Comput. Phys.*, 23(3):276 – 299, 1977.

[66] B. Van Leer. Towards the ultimate conservative difference scheme. v. a second-order sequel to Godunov's method. *J. Comput. Phys.*, 32(1):101 – 136, 1979.

[67] R.J. LeVeque. Wave propagation algorithms for multidimensional hyperbolic systems. *J. Comput. Phys.*, 131(2):327 – 353, 1997.

[68] R.J. LeVeque. *Finite Volume Methods for Hyperbolic Problems*. Cambridge Texts in Applied Mathematics. Cambridge University Press, 2002.

[69] P. Li, W.S. Don, C. Wang, and Z. Gao. High order positivity- and bound-preserving hybrid compact-WENO finite difference scheme for the compressible Euler equations. *J. Sci. Comput.*, 74(2):640–666, Feb 2018.

[70] Q. Li, P. Liu, and H. Zhang. Piecewise polynomial mapping method and corresponding weno scheme with improved resolution. *Commun. Comput. Phys.*, 18(5):1417–1444, 2015.

[71] T. Linde and P.L. Roe. Robust Euler codes. *in: Thirteenth Computational Fluid Dynamics Conference*, pages AIAA–97–2098, 1997.

[72] R. Liska and B. Wendroff. Comparison of several difference schemes on 1d and 2d test problems for the euler equations. *SIAM J. Sci. Comput.*, 25(3):995–1017, 2003.

[73] W. Liu, J. Cheng, and C.W. Shu. High order conservative lagrangian schemes with lax-wendroff type time discretization for the compressible euler equations. *J. Comput. Phys.*, 228(23):8872–8891, December 2009.

[74] C. Lohmann and D. Kuzmin. Synchronized flux limiting for gas dynamics variables. *J. Comput. Phys.*, 326:973 – 990, 2016.

[75] R. Loubère, M. Dumbser, and S. Diot. A new family of high order unstructured mood and ader finite volume schemes for multidimensional systems of hyperbolic conservation laws. *Commun. Comput. Phys.*, 16(3):718–763, 2014.

[76] R. Loubère and M.J. Shashkov. A subcell remapping method on staggered polygonal grids for arbitrary-lagrangian–eulerian methods. *J. Comput. Phys.*, 209(1):105 – 138, 2005.

[77] S.P. Marsh. *LASL SHOCK HUGONIOT DATA*. Univ of California Press, 1980.

[78] B. Matania. The generalized Riemann problem for reactive flows. *J. Comput. Phys.*, 81(1):70 – 101, 1989.

[79] W. Mulder, S. Osher, and J. A. Sethian. Computing interface motion in compressible gas dynamics. *J. Comput. Phys.*, 100(2):209 – 228, 1992.

[80] D. Nguyen, F. Gibou, and R. Fedkiw. A fully conservative ghost fluid method and stiff detonation waves. In *12th Int. Detonation Symposium, San Diego, CA*, 2002.

[81] R.R. Nourgaliev, T.N. Dinh, and T.G. Theofanous. Adaptive characteristics-based matching for compressible multifluid dynamics. *Journal of Computational Physics*, 213(2):500 – 529, 2006.

[82] S. Pirozzoli. On the spectral properties of shock-capturing schemes. *J. Comput. Phys.*, 219(2):489 – 497, 2006.

[83] J.J. Quirk and S. Karni. On the dynamics of a shock–bubble interaction. *J. Fluid Mech.*, 318:129–163, 1996.

[84] A. Rault, G. Chiavassa, and R. Donat. Shock-vortex interactions at high mach numbers. *J. Sci. Comput.*, 19:347–371, 2003.

[85] J. Reisner, J. Serencsa, and S. Shkoller. A space–time smooth artificial viscosity method for nonlinear conservation laws. *J. Comput. Phys.*, 235:912 – 933, 2013.

[86] Y.X. Ren, M. Liu, and H. Zhang. Efficient implementation of weighted ENO schemes. *J. Comput. Phys.*, 192:365–386, 2003.

[87] V. Rusanov. Calculation of interaction of non-steady shock waves with obstacles. 1961.

[88] S.J. Ruuth. Global optimization of explicit strong-stability-preserving runge-kutta methods, 2006.

[89] R. Saurel and R. Abgrall. A multiphase godunov method for compressible multifluid and multiphase flows. *J. Comput. Phys.*, 150(2):425 – 467, 1999.

[90] C.W. Schulz-Rinne. Classification of the Riemann problem for two-dimensional gas dynamics. *SIAM J. Math. Anal.*, 24:76–88, 1993.

[91] L.I. Sedov. *Similarity and Dimensional Methods in Mechanics*. Academic Press, New York, 1959.

[92] Z. Shen, W. Yan, and G. Yuan. A robust HLLC-type Riemann solver for strong shock. *J. Comput. Phys.*, 309:185 – 206, 2016.

[93] C.W. Shu and S. Osher. Efficient implementation of essentially non-oscillatory shock-capturing schemes. *J. Comput. Phys.*, 77:439–471, 1988.

[94] C.W. Shu and S. Osher. Efficient implementation of essentially non-oscillatory shock-capturing schemes, ii. *J. Comput. Phys.*, 83:32–78, 1989.

[95] R.K. Shukla, C. Pantano, and J.B. Freund. An interface capturing method for the simulation of multi-phase compressible flows. *J. Comput. Phys.*, 229(19):7411 – 7439, 2010.

[96] K.M. Shyue. An efficient shock-capturing algorithm for compressible multicomponent problems. *J. Comput. Phys.*, 142(1):208 – 242, 1998.

[97] K.M. Shyue. A fluid-mixture type algorithm for compressible multicomponent flow with van der waals equation of state. *J. Comput. Phys.*, 156(1):43 – 88, 1999.

[98] K.M. Shyue. A fluid-mixture type algorithm for compressible multicomponent flow with Mie-Grüneisen equation of state. *J. Comput. Phys.*, 171(2):678 – 707, 2001.

[99] K.M. Shyue and F. Xiao. An eulerian interface sharpening algorithm for compressible two-phase flow: The algebraic thinc approach. *J. Comput. Phys.*, 268:326 – 354, 2014.

[100] K.K. So, X.Y. Hu, and N.A. Adams. Anti-diffusion interface sharpening technique for two-phase compressible flow simulations. *J. Comput. Phys.*, 231(11):4304 – 4323, 2012.

[101] R.J. Spiteri and S.J. Ruuth. A new class of optimal high-order strong-stability-preserving time discretization methods. *SIAM J. Numer. Anal.*, 40(2):469–491, February 2002.

[102] G. Strang. On the construction and comparison of difference schemes. *SIAM J. Numer. Anal.*, 5(3):506–517, 1968.

[103] Z. Sun, S. Inaba, and F. Xiao. Boundary variation diminishing (BVD) reconstruction: A new approach to improve Godunov schemes. *J. Comput. Phys.*, 322:309–325, 2016.

[104] P.K. Sweby. High resolution schemes using flux limiters for hyperbolic conservation laws. *J. Comput. Phys.*, 21(5):995 – 1011, 1984.

[105] S. Tann, X. Deng, R. Loubère, and F. Xiao. Solution property preserving reconstruction bvd+mood scheme for compressible euler equations with source terms and detonations. *Computers & Fluids*, 206:104594, 2020.

[106] S. Tann, X. Deng, Y. Shimizu, R. Loubère, and F. Xiao. Solution property preserving reconstruction for finite volume scheme: a boundary variation diminishing+multidimensional optimal order detection framework. *Int J Numer Meth Fluids*, 92(6):603–634, 2020.

[107] V.A. Titarev and E.F. Toro. ADER schemes for three-dimensional non-linear hyperbolic systems. *J. Comput. Phys.*, 204(2):715 – 736, 2005.

[108] E.F. Toro. *Riemann solvers and numerical methods for fluid dynamics: a practical introduction*. Springer Verlag, 2009.

[109] L. Tosatto and L. Vigevano. Numerical solution of under-resolved detonations. *J. Comput. Phys.*, 227(4):2317 – 2343, 2008.

[110] R. Turpault and T.H. Nguyen Bui. A high order mood method for compressible navier-stokes equations: application to hypersonic viscous flows. *Progress in Computational Fluid Dynamics,*, 2019. in press.

[111] B. van Leer. Towards the ultimate conservative difference scheme. ii. monotonicity and conservation combined in a second-order scheme. *J. Comput. Phys.*, 14(4):361 – 370, 1974.

[112] F. Vilar. A posteriori correction of high-order discontinuous galerkin scheme through subcell finite volume formulation and flux reconstruction. *J. Comput. Phys.*, 2018.

[113] B. Wang, G. Xiang, and X.Y. Hu. An incremental-stencil weno reconstruction for simulation of compressible two-phase flows. *Int. J. Multiphase Flow*, 104:20 – 31, 2018.

[114] C. Wang, X. Zhang, C.W. Shu, and J. Ning. Robust high order discontinuous Galerkin schemes for two-dimensional gaseous detonations. *J. Comput. Phys.*, 231(2):653 – 665, 2012.

[115] W. Wang, C.W. Shu, H.C. Yee, and B. Sjögreen. High order finite difference methods with subcell resolution for advection equations with stiff source terms. *J. Comput. Phys.*, 231(1):190 – 214, 2012.

[116] L. White and A. Adcroft. A high-order finite volume remapping scheme for nonuniform grids: The piecewise quartic method (PQM). *J. Comput. Phys.*, 227(15):7394–7422, 2008.

[117] P. Woodward and P. Colella. The numerical simulation of two-dimensional fluid flow with strong shocks. *J. Comput. Phys.*, 54:115–173, 1984.

[118] F. Xiao, K. Honma, and T. Kono. A simple algebraic interface capturing scheme using hyperbolic tangent function. *int. J. Methods Fluids*, 48:1023–1040, 2005.

[119] F. Xiao, S. Ii, and C. Chen. Revisit to the thinc scheme: A simple algebraic vof algorithm. *J. Comput. Phys.*, 230:7086–7092, 2011.

[120] Z. Xu and C.W. Shu. Anti-diffusive flux corrections for high order finite difference WENO schemes. *J. Comput. Phys.*, 205(2):458 – 485, 2005.

[121] Z. Xu and X. Zhang. Chapter 4 - bound-preserving high-order schemes. In R. Abgrall and C.W. Shu, editors, *Handbook of Numerical Methods for Hyperbolic Problems*, volume 18 of *Handbook of Numerical Analysis*, pages 81 – 102. Elsevier, 2017.

[122] H.C. Yee, D.V. Kotov, W. Wang, and C.W. Shu. Spurious behavior of shock-capturing methods by the fractional step approach: Problems containing stiff source terms and discontinuities. *J. Comput. Phys.*, 241:266 – 291, 2013.

[123] Y.N. Young, H. Tufo, A. Dubey, and R. Rosner. On the miscible Rayleigh-Taylor instability: two and three dimensions. *J. Fluid Mech.*, 447:377–408, 2001.

[124] S.T. Zalesak. Fully multidimensional flux-corrected transport algorithms for fluids. *J. Comput. Phys.*, 31(3):335 – 362, 1979.

[125] O. Zanotti, F. Fambri, M. Dumbser, and A. Hidalgo. Space–time adaptive ADER discontinuous Galerkin finite element schemes with a posteriori sub-cell finite volume limiting. *Comput Fluids*, 118:204 – 224, 2015.

[126] B. Zhang, H. Liu, F. Chen, and J.H. Wang. The equilibrium state method for hyperbolic conservation laws with stiff reaction terms. *J. Comput. Phys.*, 263:151 – 176, 2014.

[127] X. Zhang and C.W. Shu. On positivity-preserving high order discontinuous galerkin schemes for compressible euler equations on rectangular meshes. *J. Comput. Phys.*, 229:8918–8934, 2010.

[128] X. Zhang and C.W. Shu. Maximum-principle-satisfying and positivity-preserving high-order schemes for conservation laws: survey and new developments. *Proceedings of the Royal Society A: Mathematical, Physical and Engineering Sciences*, 467(2134):2752–2776, 2011.

[129] X. Zhang and C.W. Shu. Positivity-preserving high order discontinuous galerkin schemes for compressible euler equations with source terms. *J. Comput. Phys.*, 230(4):1238–1248, 2011.

[130] X. Zhang and C.W. Shu. Positivity-preserving high order finite difference weno schemes for compressible euler equations. *J. Comput. Phys.*, 231:2245–2258, 2012.

[131] H. Zhu and Z. Gao. An h-adaptive RKDG method for two-dimensional detonation wave simulations. *E Asian J Appl Math*, 9(1):165–184, 2019.